Politecnico di Bari

Repository Istituzionale dei Prodotti della Ricerca del Politecnico di Bari

Control strategies for energy harvesting systems

This is a PhD Thesis

Original Citation:
Control strategies for energy harvesting systems / Tesso Woafo, Paul Christian. - ELETTRONICO. - (2026).

Availability:
This version is available at http://hdl.handle.net/11589/295880 since: 2026-01-19

Published version
DOI:

Publisher: Politecnico di Bari

Terms of use:

(Article begins on next page)

23 April 2026

Italian National Ph.D. Program in Autonomous Systems

ACADEMIC DISCIPLINE: SYSTEMS AND CONTROL ENGINEERING (IINF-04/A)

Final Dissertation

Control strategies for energy harvesting systems

by

Paul Christian Tesso Woafo

Administrative Headquarters:

Politecnico di Bari – Department of Electrical and Information Engineering

Hosting University:

University of Calabria – Department of Computer Engineering, Modeling, Electronics, and Systems

Referees:

Prof. Olivier Sename

Prof. Biswajit Basu

Supervisors:

Prof. Alessandro Casavola

Prof. Francesco Tedesco

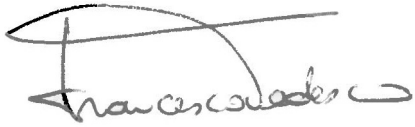

Coordinator of Ph.D Program

Prof. Mariagrazia Dotoli

Course no. 38, 01/11/2022-31/10/2025

LIBERATORIA PER L'ARCHIVIAZIONE DELLA TESI DI DOTTORATO

Al Magnifico Rettore
del Politecnico di Bari

Il sottoscritto Paul Christian Tesso Woafo nato in CAMERUN il 01/07/1998
residente a Rende in via Tito Flavio 2 e-mail tessowoafopaulchristian@gmail.com
iscritto al 3° anno di Corso di Dottorato di Ricerca in Autonomous Systems (DAuSy) ciclo XXXVIII
ed essendo stato ammesso a sostenere l'esame finale con la prevista discussione della tesi dal titolo:
Control strategies for energy harvesting systems

DICHIARA

1) di essere consapevole che, ai sensi del D.P.R. n. 445 del 28.12.2000, le dichiarazioni mendaci, la falsità negli atti e l'uso di atti falsi sono puniti ai sensi del codice penale e delle Leggi speciali in materia, e che nel caso ricorressero dette ipotesi, decade fin dall'inizio e senza necessità di nessuna formalità dai benefici conseguenti al provvedimento emanato sulla base di tali dichiarazioni;
2) di essere iscritto al Corso di Dottorato di ricerca Autonomous Systems (DAuSy) ciclo XXXVIII, corso attivato ai sensi del "*Regolamento dei Corsi di Dottorato di ricerca del Politecnico di Bari"*, emanato con D.R. n.286 del 01.07.2013;
3) di essere pienamente a conoscenza delle disposizioni contenute nel predetto Regolamento in merito alla procedura di deposito, pubblicazione e autoarchiviazione della tesi di dottorato nell'Archivio Istituzionale ad accesso aperto alla letteratura scientifica;
4) di essere consapevole che attraverso l'autoarchiviazione delle tesi nell'Archivio Istituzionale ad accesso aperto alla letteratura scientifica del Politecnico di Bari (IRIS-POLIBA), l'Ateneo archivierà e renderà consultabile in rete (nel rispetto della Policy di Ateneo di cui al D.R. 642 del 13.11.2015) il testo completo della tesi di dottorato, fatta salva la possibilità di sottoscrizione di apposite licenze per le relative condizioni di utilizzo (di cui al sito http://www.creativecommons.it/Licenze), e fatte salve, altresì, le eventuali esigenze di "embargo", legate a strette considerazioni sulla tutelabilità e sfruttamento industriale/commerciale dei contenuti della tesi, da rappresentarsi mediante compilazione e sottoscrizione del modulo in calce (Richiesta di embargo);
5) che la tesi da depositare in IRIS-POLIBA, in formato digitale (PDF/A) sarà del tutto identica a quelle **consegnate**/inviate/da inviarsi ai componenti della commissione per l'esame finale e a qualsiasi altra copia depositata presso gli Uffici del Politecnico di Bari in forma cartacea o digitale, ovvero a quella da discutere in sede di esame finale, a quella da depositare, a cura dell'Ateneo, presso le Biblioteche Nazionali Centrali di Roma e Firenze e presso tutti gli Uffici competenti per legge al momento del deposito stesso, e che di conseguenza va esclusa qualsiasi responsabilità del Politecnico di Bari per quanto riguarda eventuali errori, imprecisioni o omissioni nei contenuti della tesi;
6) che il contenuto e l'organizzazione della tesi è opera originale realizzata dal sottoscritto e non compromette in alcun modo i diritti di terzi, ivi compresi quelli relativi alla sicurezza dei dati personali; che pertanto il Politecnico di Bari ed i suoi funzionari sono in ogni caso esenti da responsabilità di qualsivoglia natura: civile, amministrativa e penale e saranno dal sottoscritto tenuti indenni da qualsiasi richiesta o rivendicazione da parte di terzi;
7) che il contenuto della tesi non infrange in alcun modo il diritto d'Autore né gli obblighi connessi alla salvaguardia di diritti morali od economici di altri autori o di altri aventi diritto, sia per testi, immagini, foto, tabelle, o altre parti di cui la tesi è composta.

Luogo e data Rende,15/01/2026 Firma

Il/La sottoscritto, con l'autoarchiviazione della propria tesi di dottorato nell'Archivio Istituzionale ad accesso aperto del Politecnico di Bari (POLIBA-IRIS), pur mantenendo su di essa tutti i diritti d'autore, morali ed economici, ai sensi della normativa vigente (Legge 633/1941 e ss.mm.ii.),

CONCEDE

- al Politecnico di Bari il permesso di trasferire l'opera su qualsiasi supporto e di convertirla in qualsiasi formato al fine di una corretta conservazione nel tempo. Il Politecnico di Bari garantisce che non verrà effettuata alcuna modifica al contenuto e alla struttura dell'opera.
- al Politecnico di Bari la possibilità di riprodurre l'opera in più di una copia per fini di sicurezza, back-up e conservazione.

Luogo e data Rende,15/01/2026 Firma

Paul Christian Tesso Woafo

Control strategies for energy harvesting systems

Thesis submitted for the degree of Philosophiae Doctor

Italian National Ph.D. Program in Autonomous Systems
University of Calabria

Tutors
Prof. Engr. *Alessandro Casavola*
Prof. Engr. *Francesco Tedesco*

UNIVERSITÀ DELLA CALABRIA

2026

The doctoral scholarship was funded by the European Union - Next Generation EU, Mission 4 Component 1 CUP *D93C22000850005* (PNRR - 351).

Dissertation submitted for the degree of *Philosophiae Doctor*
Italian National Ph.D. Program in Autonomous Systems

Cycle:
38th

Administrative Headquarters:
Politecnico di Bari

Hosting University:
Università della Calabria

Title:
Control strategies for energy harvesting systems

Ph.D Candidate:
Paul Christian Tesso Woafo, Università della Calabria (Rende, Italy)

Tutors:
Prof. Engr. Alessandro Casavola, Università della Calabria (Rende, Italy)
Prof. Engr. Francesco Tedesco, Università della Calabria (Rende, Italy)

Coordinator:
Prof. Engr. Mariagrazia Dotoli, Politecnico di Bari (Bari, Italy)

External Reviewers:
Prof. Engr. Olivier Sename, Grenoble INP/ University Grenoble Alpes (Grenoble, France)
Prof. Engr. Biswajit Basu, Trinity College Dublin (Dublin, Ireland)

Last version:
December 20th, 2025

All rights reserved. No part of this publication may be reproduced or transmitted, in any form or by any means, without permission.

Abstract

This thesis presents the development and evaluation of advanced control strategies for energy harvesting systems, focusing on vehicle regenerative suspensions and wave energy converters. The main goal is to design controllers that maximize energy collected from external disturbances, like road profiles or ocean waves, while adhering to physical and operational constraints. A central challenge addressed is the design of effective causal approximations for optimal control solutions, which are often anti-causal because they depend on the future of external signals.

To achieve these objectives, the thesis develops several novel control frameworks. These include H_∞/H_2 output feedback controllers that use the Maximum Induced Power Control (MIPC) strategy; a new multi-objective Linear Quadratic Regulator (LQR) that incorporates an H_∞ formulation to enforce a bound on the Ride Index (RI); and Economic Model Predictive Control (EMPC). The EMPC framework is explored in two forms: a predictive controller for wave energy converters that relies on wave forecasts, and a stochastic version for regenerative suspensions that operates without needing a road preview.

The investigation of these strategies leads to several key findings. The H_2 MIPC controller proved more effective than its H_∞ counterpart, and the Inerter Pendulum Vibration Absorber (IPVA) was identified as the best actuator for regenerative suspensions. The new LQR strategy significantly increased harvested energy, showing improvements of 37.3% and 27.8% over the regenerative damper and H_2 MIPC state feedback methods, respectively. This LQR approach also has lower computational overhead, making it well-suited for real-time implementation. Furthermore, EMPC strategies achieved the highest levels of energy harvesting and superior constraint satisfaction for both regenerative suspensions without road preview and wave energy converters using wave prediction. All developed control strategies were rigorously validated through extensive numerical simulations and comparative analyses.

Keywords: Economic Model Predictive Control(EMPC), Regenerative suspension systems, Wave Energy Converters, Linear Quadratic Regulator.

I dedicate this work to my family and my fiancée Merveille who have always believed in me and have encouraged me to go far.

Contents

List of Figures **vi**

List of Tables **xi**

Preface **xvi**

List of Papers Written by the Author **xvi**

1 Introduction and literature review **1**
1.1 Introduction 1
1.2 Background and motivation 1
1.3 Literature review 3
1.4 Problem statement of the work 13
1.5 Contributions 13
1.6 Thesis outline 15

2 Regenerative suspension configuration **17**
2.1 Introduction 17
2.2 Suspension modeling 17
2.3 Actuators modeling 23
2.4 Power flow analysis 32
2.5 Conclusion 35

3 Wave energy converters configuration **37**
3.1 Introduction 37
3.2 Point Absorber (PAs) classification 37
3.3 Power Take Off (PTO) mechanisms 39
3.4 PA dynamics modeling and wave forecasting models . 43
3.5 Conclusion 48

4 H_∞ and H_2 MIPC dynamic output feedback control **50**
4.1 Introduction 50
4.2 Control specifications 50
4.3 State space realization 52
4.4 H_∞ and H_2 dynamic output feedback control LMI design 55
4.5 Results and discussion 57
4.6 Conclusion 71

5 H_2 MIPC state feedback and LQR with a non-standard cost **73**
5.1 Introduction 73

5.2 Vehicle regenerative suspension systems 73
5.3 Simulations on Carsim 2025.1 103
5.4 Wave energy converters 107
5.5 Conclusion 117

6 Economic Model Predictive Control (EMPC) 119
6.1 Introduction 119
6.2 EMPC design for vehicles regenerative suspension systems 120
6.3 EMPC design for Wave Energy Converters 140
6.4 Conclusion 157

7 Conclusions and future works 160
7.1 Summary of the thesis 160
7.2 Future works 163

Appendices 167

A Vehicles, actuators and wave energy converters data 168
A.1 Vehicles data 168
A.2 Actuators data 169
A.3 Wave Energy Converters data 169

B Plots on CarSim 2025.1 172

List of Figures

1.1 Hydraulic regenerative suspension 3
1.2 Scheme of the vehicle energy harvesting suspension system layout 4
1.3 Classification of wave energy converter (WEC) extraction technology: (a) oscillating water column, (b) overtopping devices, and (c) oscillating bodies 8
1.4 The various wave energy technologies 9
1.5 Classification of control strategies for WECs 12

2.1 Full-car schematic- passive setup 19
2.2 Full-car schematic- active setup 20
2.3 Full-car schematic- regenerative setup 22
2.4 Quarter car model for a regenerative setup 23
2.5 Linear Permanents Magnets Actuator. 23
2.6 Simulink model of the LPMA 25
2.7 Rack-Pinion Energy Harvesting Shock Absorber (RPEHSA): 1) Rack; 2) Roller; 3) Pinion; 4) Planetary gears and motors; 5) Thrust bearings; 6) Roller clutches; 7) Ball bearings; 8) Bevel gears. 25
2.8 Electric circuit of the RP-EHSA 26
2.9 Simulink model of the RPEHSA 27
2.10 Diagram of the equivalent mechanical system of the SPEHSA 28
2.11 CAD design of the SPEHSA prototype with its electromechanical components 28
2.12 Simplified electric circuit diagram of the SPEHSA shock absorber. 30
2.13 Simulink model of the SPEHSA 31
2.14 IPVA internal structure and IPVA electric schematic 31
2.15 Simulink model of the IPVA 33
2.16 Power flow in the suspension system 34

3.1 Classification of Point absorber wave energy converters according to the design geometry, manner of installation and operating mode 38
3.2 One body point absorber working principle: a)floating type b)submerged type 38
3.3 Multi body point absorber working principle: a)self-reacting b) self-contained c)multi-point PAs 39
3.4 Four types of power take-off mechanisms used for point absorber wave energy converters. 40

3.5 Hydraulic power take-off mechanisms with a schematic plot (a) and a hydraulic PTO system under tank testing (b). . . 40
3.6 Ball screw PTO 42
3.7 Direct Drive PTO 43
3.8 Schematic diagram of the working principle of a point absorber 44
3.9 Dynamic diagram of a point absorber 44
3.10 Jonswap spectrum 46
3.11 Small wave signal 47
3.12 Big wave signal 47

4.1 Full car simulink model 57
4.2 System's dynamics 57
4.3 Class C road for the full car model 58
4.4 RI = 0.25 - Suspension deflections $z_{s_i} - z_{u_i}(t)$ for the four wheels 60
4.5 RI = 0.25 - Tire deflections $z_{u_i} - z_{r_i}(t)$ for the four wheels . 60
4.6 RI = 0.25 - Roll $\varphi(t)$, Pitch $\theta(t)$ and vertical motion z_s of the vehicle 61
4.7 RI = 0.25 - Accelerations $\ddot{z}_{s_i}(t)$ for the four wheels 61
4.8 RI = 0.25 - Angular speeds $\omega_i(t)$ for the four wheels 61
4.9 RI = 0.25 - Control currents $u_i(t)$ for the four wheels 62
4.10 RI = 0.25 - Electrical powers $P_{e_i}(t)$ for the four wheels . . . 62
4.11 RI = 0.25 - Mechanical powers $P_{m_i}(t)$ for the four wheels . 62
4.12 RI = 0.25 - Road induced powers $P_{s_i}(t)$ for the four wheels 63
4.13 RI = 0.40 - Suspension deflections $z_{s_i} - z_{u_i}(t)$ for the four wheels 63
4.14 RI = 0.40 - Tire deflections $z_{u_i} - z_{r_i}(t)$ for the four wheels . 64
4.15 RI = 0.40 - Roll $\varphi(t)$, Pitch $\theta(t)$ and vertical motion z_s of the vehicle 64
4.16 RI = 0.40 - Accelerations $\ddot{z}_{s_i}(t)$ for the four wheels 64
4.17 RI = 0.40 - Angular speeds $\omega_i(t)$ for the four wheels 65
4.18 RI = 0.40 - Control currents $u_i(t)$ for the four wheels 65
4.19 RI = 0.40 - Electrical powers $P_{e_i}(t)$ for the four wheels . . . 65
4.20 RI = 0.40 - Mechanical powers $P_{m_i}(t)$ for the four wheels . 66
4.21 RI = 0.40 - Road induced powers $P_{s_i}(t)$ for the four wheels 66
4.22 RI = 0.70 - Suspension deflections $z_{s_i} - z_{u_i}(t)$ for the four wheels 66
4.23 RI = 0.70 - Tire deflections $z_{u_i} - z_{r_i}(t)$ for the four wheels . 67
4.24 RI = 0.70 - Roll $\varphi(t)$, Pitch $\theta(t)$ and vertical motion z_s of the vehicle 67
4.25 RI = 0.70 - Accelerations $\ddot{z}_{s_i}(t)$ for the four wheels 67
4.26 RI = 0.70 - Angular speeds $\omega_i(t)$ for the four wheels 68
4.27 RI = 0.70 - Control currents $u_i(t)$ for the four wheels 68
4.28 RI = 0.70 - Electrical powers $P_{e_i}(t)$ for the four wheels . . . 68
4.29 RI = 0.70 - Mechanical powers $P_{m_i}(t)$ for the four wheels . 69
4.30 RI = 0.70 - Road induced powers $P_{s_i}(t)$ for the four wheels 69

5.1 Control architecture 75
5.2 Signal characterizing the road profile. 85
5.3 Sensitivity of the Ride index to α and ρ 87
5.4 Sensitivity of the electrical power to α and ρ 88
5.5 Scenario 1: Acceleration $\ddot{z}_s(t)$, actuation current $u(t)$, harvested electrical power $P_e(t)$ and harvested electrical energy $E_e(t)$ 89
5.6 Convergence analysis for $\lambda \geq 0$ 90
5.7 Convergence analysis for $\lambda \geq -10$. 91
5.8 LQR approach's Ride Index heatmap accross different road conditions 92
5.9 Scenario 2: Acceleration $\ddot{z}_s(t)$, actuation current $u(t)$, harvested electrical power $P_e(t)$ and harvested electrical energy $E_e(t)$ 93
5.10 Scenario 3: Acceleration $\ddot{z}_s(t)$, actuation current $u(t)$, harvested electrical power $P_e(t)$ and harvested electrical energy $E_e(t)$ 94
5.11 Scenario 4: Acceleration $\ddot{z}_s(t)$, actuation current $u(t)$, harvested electrical power $P_e(t)$ and harvested electrical energy $E_e(t)$ 96
5.12 Sensitivity of P_e to ρ for $\alpha = 39$ 99
5.13 Sensitivity of P_e to α for $\rho = 0.25$ 99
5.14 Sensitivity of the electrical power to the vehicle speed . . . 99
5.15 C-class vehicle in CarSim 104
5.16 Simulink model of the LQ control with CarSim S-function . 104
5.17 Straight driving road's roughness 105
5.18 Double lane changing road's roughness 106
5.19 Sine bumps roughness 107
5.20 Average mechanical and electrical energies with respect to λ 115
5.21 Average mechanical and electrical energies with respect to bigger values of λ 115
5.22 Absorbed power, PTO force, heave position and heave velocity obtained with the small WEC 116

6.1 Regenerative quarter car model 120
6.2 Signal characterizing the road profile. 128
6.3 Performance with respect to λ, $\lambda \in [0; 10^6]$ 129
6.4 Performance with respect to N_T, $N_T \in [1; 30]$ with a step of 1 129
6.5 Constrained EMPC 0 vs. LQR 131
6.6 Constrained EMPC 1 vs. LQR 133
6.7 Constrained EMPC 2 vs. LQR 133
6.8 Constrained EMPC 3 vs. LQR 134
6.9 Constrained EMPC 0 vs. LQR for vehicle parameters variations 136
6.10 Constrained EMPC 1 vs. LQR for vehicle parameters variations 137
6.11 Drag coefficient 144
6.12 Radiation resistance 145

6.13 Monochromatic wave $w(k)$ vs Harvey's model wave $w(t)$ . . 147
6.14 Power for the ideal case during 500 s simulation (a) and in the interval [200-500] s (b) 148
6.15 Ideal case: Heave position (a) and Heave velocity (b) . . . 149
6.16 Ideal case constrained: Absorbed power, control input, heave position and heave velocity 149
6.17 Non ideal case: Absorbed power, control input, heave position and heave velocity 150
6.18 Non ideal case constrained: Absorbed power, control input, heave position and heave velocity 151
6.19 Corpower WEC Device 152
6.20 Absorbed power, PTO force, heave position and heave velocity obtained with the small WEC 152
6.21 Absorbed power, PTO force, heave position and heave velocity obtained with the big WEC 153
6.22 Probability (%) of sea conditions for the chosen site (data from AMETS Berth B wave buoy offshore north west coast of Ireland). 155
6.23 Power absorbed with the constrained EMPC under various sea conditions 155
6.24 Position obtained with the constrained EMPC under various sea conditions 156
6.25 Velocity obtained with the constrained EMPC under various sea conditions 156
6.26 Control input force obtained with the constrained EMPC under various sea conditions 157

B.1 Test 1- Chassis acceleration with LQ 172
B.2 Test 1- Pitch with LQ 173
B.3 Test 1- Roll with LQ 173
B.4 Test 1- Tire deflections with LQ 174
B.5 Test 1- Suspension deflections with LQ 174
B.6 Test 1- Actuation currents with LQ 175
B.7 Test 1- Electrical power with LQ 175
B.8 Test 1- Mechanical power with LQ 176
B.9 Test 1- Chassis acceleration with MIPC H_2 176
B.10 Test 1- Pitch with MIPC H_2 177
B.11 Test 1- Roll with MIPC H_2 177
B.12 Test 1- Tire deflections with MIPC H_2 178
B.13 Test 1- Suspension deflections with MIPC H_2 178
B.14 Test 1- Actuation currents with MIPC H_2 179
B.15 Test 1- Electrical power with MIPC H_2 179
B.16 Test 1- Mechanical power with MIPC H_2 180
B.17 Test 2- Chassis acceleration with LQ 180
B.18 Test 2- Pitch with LQ 181
B.19 Test 2- Roll with LQ 181

B.20 Test 2- Tire deflections with LQ 182
B.21 Test 2- Suspension deflections with LQ 182
B.22 Test 2- Actuation currents with LQ 183
B.23 Test 2- Electrical power with LQ 183
B.24 Test 2- Mechanical power with LQ 184
B.25 Test 2- Chassis acceleration with MIPC H_2 184
B.26 Test 2- Pitch with MIPC H_2 185
B.27 Test 2- Roll with MIPC H_2 185
B.28 Test 2- Tire deflections with MIPC H_2 186
B.29 Test 2- Suspension deflections with MIPC H_2 186
B.30 Test 2- Actuation currents with MIPC H_2 187
B.31 Test 2- Electrical power with MIPC H_2 187
B.32 Test 2- Mechanical power with MIPC H_2 188
B.33 Test 3- Chassis acceleration with LQ 188
B.34 Test 3- Pitch with LQ 189
B.35 Test 3- Roll with LQ 189
B.36 Test 3- Tire deflections with LQ 190
B.37 Test 3- Suspension deflections with LQ 190
B.38 Test 3- Actuation currents with LQ 191
B.39 Test 3- Electrical power with LQ 191
B.40 Test 3- Mechanical power with LQ 192
B.41 Test 3- Chassis acceleration with MIPC H_2 192
B.42 Test 3- Pitch with MIPC H_2 193
B.43 Test 3- Roll with MIPC H_2 193
B.44 Test 3- Tire deflections with MIPC H_2 194
B.45 Test 3- Suspension deflections with MIPC H_2 194
B.46 Test 3- Actuation currents with MIPC H_2 195
B.47 Test 3- Electrical power with MIPC H_2 195
B.48 Test 3- Mechanical power with MIPC H_2 196

List of Tables

1.1 Comparison of the most popular energy conversion mechanisms in automotive suspension 5

2.1 Advantages, limitations, and applications of different suspension types 21

4.1 Knobs tuning – RI=0.25 (Excellent comfort/Smallest harvesting), RI = 0.40 (Trade-off between comfort/harvesting) and RI=0.70 (Perceivable discomfort/largest harvesting) with the H_2 dynamic output feedback control 59
4.2 MIPC Parameters – RI=0.25 (Excellent comfort/Smallest harvesting), RI = 0.40 (Trade-off between comfort/harvesting) and RI=0.70 (Perceivable discomfort/largest harvesting) with the H_2 dynamic output feedback control. 59
4.3 Average Harvested Electrical Power for RI=0.25, RI=0.40 and RI=0.70 - A single EHSA with the H_2 MIPC dynamic output feedback control 69
4.4 Generator Average Angular (Linear) Velocities for RI=0.25, RI=0.40 and RI=0.70 - A single EHSA with the H_2 MIPC dynamic output feedback control. 70
4.5 Average Harvested Electrical Power for RI=0.25, RI=0.40 and RI=0.70 - A single EHSA with the H_∞ MIPC dynamic output feedback 70

5.1 Amplitude of PSD according to ISO classification. 74
5.2 MIPC H_2 static state feedback tuning parameters – $RI = 0.25$ (not uncomfortable), $RI = 0.47$ (a little uncomfortable) and $RI = 0.70$ (fairly uncomfortable). 86
5.3 LQR tuning parameters – $RI = 0.25$ (not uncomfortable), $RI = 0.47$ (a little uncomfortable) and $RI = 0.70$ (fairly uncomfortable). 86
5.4 Harvested energy using different controllers with MOSEK/SEDUMI solvers and stability analysis 90
5.5 Stability analysis and execution time for different road conditions and $\lambda \geq 0$. 92
5.6 Electrical Energy for $RI = 0.25$, $RI = 0.47$ and $RI = 0.70$. 94
5.7 Road handling for $RI = 0.25$, $RI = 0.47$ and $RI = 0.70$ . . 94
5.8 Suspension stroke for $RI = 0.25$, $RI = 0.47$ and $RI = 0.70$ 95
5.9 Acceleration for $RI = 0.25$, $RI = 0.47$ and $RI = 0.70$ . . . 95

5.10 Average Electrical Power for $RI = 0.25$, $RI = 0.47$ and $RI = 0.70$ . . . 95
5.11 Electrical Energy for $RI = 0.25$, $RI = 0.47$ and $RI = 0.70$ considering the new system's parameters . . . 95
5.12 MIPC H_2 static state feedback tuning parameters – $RI = 0.25$ (not uncomfortable), $RI = 0.47$ (a little uncomfortable) and $RI = 0.70$ (fairly uncomfortable) with IPVA actuator . . . 100
5.13 LQR tuning parameters – $RI = 0.25$ (not uncomfortable), $RI = 0.47$ (a little uncomfortable) and $RI = 0.70$ (fairly uncomfortable) with IPVA actuator . . . 100
5.14 Average Electrical Power for $RI = 0.25$, $RI = 0.47$ and $RI = 0.70$ with IPVA actuator . . . 100
5.15 Electrical Energy for $RI = 0.25$, $RI = 0.47$ and $RI = 0.70$ with IPVA actuator . . . 101
5.16 Acceleration for $RI = 0.25$, $RI = 0.47$ and $RI = 0.70$ with IPVA actuator . . . 101
5.17 Road handling for $RI = 0.25$, $RI = 0.47$ and $RI = 0.70$ with IPVA actuator . . . 101
5.18 Suspension stroke for $RI = 0.25$, $RI = 0.47$ and $RI = 0.70$ with IPVA actuator . . . 101
5.19 Electrical Energy harvested considering full-vehicle dynamics 102
5.20 Electrical Energy with the second road signal for $RI = 0.25$, $RI = 0.47$ and $RI = 0.70$ . . . 102
5.21 Test 1: Total electrical power harvested with CarSim . . . 105
5.22 Test 2: Total electrical power harvested with CarSim . . . 106
5.23 LQR and MIPC H_2 for a WEC . . . 116

6.1 Active constraints in LQR and Constrained EMPC 0 . . . 131
6.2 Outputs of LQR and Constrained EMPC 0 . . . 132
6.3 Active constraints in LQR and Constrained EMPC 1 . . . 132
6.4 Outputs of LQR and Constrained EMPC 1 . . . 132
6.5 Active constraints in LQR and Constrained EMPC 2 . . . 132
6.6 Outputs of LQR and Constrained EMPC 2 . . . 132
6.7 Active constraints in LQR and Constrained EMPC 3 . . . 133
6.8 Outputs of LQR and Constrained EMPC 3 . . . 134
6.9 Summary of the results . . . 135
6.10 Constrained EMPC 0 results obtained with vehicle parameters variations . . . 136
6.11 Active constraints in LQR and Constrained EMPC 1 with vehicle parameters variations . . . 136
6.12 Constrained EMPC 1 results obtained with vehicle parameters variations . . . 136
6.13 Active constraints in LQR and Constrained EMPC 3 for $n_{00} = 0.1m^{-1}$ . . . 137
6.14 Constrained EMPC 3 results obtained for $n_{00} = 0.1m^{-1}$ . . . 137

6.15 Active constraints in LQR and Constrained EMPC 3 for $G(n_0) = 20 \times 10^{-6}$ . . . 138
6.16 Constrained EMPC 3 results obtained for $G(n_0) = 20 \times 10^{-6}$ 138
6.17 Active constraints in LQR and Constrained EMPC 1 for a full-car model . . . 140
6.18 LQR on a full car model . . . 140
6.19 Constrained EMPC 1 on a full car model . . . 140
6.20 Ideal case: values obtained without constraints . . . 147
6.21 Ideal case: values obtained with constraints . . . 148
6.22 Non ideal case: values obtained without constraints . . . 150
6.23 Non ideal case: values obtained with constraints . . . 150
6.24 Values obtained with the small WEC . . . 152
6.25 Values obtained with the big WEC . . . 154
6.26 Mean value of the computation time for each time step . . . 154

A.1 Vehicle 1 data . . . 168
A.2 Vehicle 2 data . . . 169
A.3 Quarter car parameters . . . 169
A.4 LPMA data. . . . 169
A.5 RPEHSA data. . . . 170
A.6 SPEHSA data . . . 170
A.7 IPVA data . . . 170
A.8 Actuator data . . . 171
A.9 The parameters used for the small WEC . . . 171
A.10 The parameters used for the big WEC . . . 171

Acronyms

AWS *Archimedes Wave Swing*. 42, 140

BMI *Bilinear Matrix Inequalities*. 122

DARE *Discrete time Algebraic Ricatti Equation*. 144
DHR *Dynamic Harmonic Regression*. 47, 160
DoF *Degrees-of-Freedom*. 18, 23
DSWP *Deterministic Sea Wave Prediction*. 12

EHSA *Energy Harvesting Shock Absorber*. 3, 4
EHSAs *Energy Harvesting Shock Absorbers*. 160, 161
EMPC *Economic Model Predictive Control*. 14, 162

HIL *Hardware-in-the-Loop*. 164

ICC *Inner Current Controller*. 74
IPVA *Inerter Pendulum Vibration Absorber*. 4, 14, 30

JONSWAP *Joint North Sea Wave Analysis Project*. 45

LMI *Linear Matrix Inequalities*. 55
LNOC *Linear Noncausal Optimal Control*. 142
LPMA *Linear Permanents Magnets Actuator*. 23
LPV *Linear Parameters Varying*. 164
LQ *Linear Quadratic*. 14
LQR *Linear Quadratic Regulator*. 14
LTI *Linear Time Invariant*. 164

MIPC *Maximum Induced Power Control*. 6, 13
MIT *Massachusetts Institute of Technology*. 2
MMLA *Moving Magnets Linear Actuator*. 23
MPC *Model Predictive Control*. 6, 7

NMPC *Nonlinear Model Predictive Control*. 13, 144

O&M *Operation&Maintenance*. 41

OPT *Ocean Power Technologies*. 41

ORC *Outer Regenerative Controller*. 74

OTD *Overtopping Device*. 8, 10

OWCs *Oscillating Water Columns*. 8, 10

PID *Proportional Integral Derivative*. 7

PMLG *Permanent Magnet Linear Generator*. 42

PSD *Power Spectral Density*. 73

PTO *Power-Take-Off*. 9, 10

R&D *Research&Development*. 37

RESs *Renewable Energy Sources*. 13

RI *Ride Index*. 161

RPEHSA *Rack Pinion Energy Harvesting Shock Absorber*. 4, 24

SPEHSA *Synchronous Pulley Energy Harvesting Shock Absorber*. 4, 27

WECs *Wave Energy Converters*. 2, 8, 162

Preface

This thesis is submitted in partial fulfillment of the requirements for the degree of *Philosophiae Doctor* in Control Engineering.

The full list of papers written by the author is reported hereafter.

List of Papers Written by the Author

- Gagliardi G, Manna P, Tesso PCW, Casavola A. Performance Analysis of Linear and Rotary Energy Harvesting Shock Absorber Systems. IEEE Vehicle Power and Propulsion Conference (VPPC) 2023:1-6.https://ieeexplore.ieee.org/document/10403168
- Tesso PCW, Gagliardi G, Casavola A, Tedesco F. Energy Harvesting Optimization in Vehicle Suspension Systems via a Non Standard LQ Control Strategy. Proceedings of I4SDG Workshop 2025 - IFToMM for Sustainable Development Goals;180: 2025. https://doi.org/10.1007/978-3-031-91179-8_31
- Tesso PCW, Gagliardi G, Casavola A, Tedesco F. A novel multi objective optimal LQ control strategy for energy harvesting in vehicle suspension systems. ISA Transactions; 2025. https://doi.org/10.1016/j.isatra.2025.09.010
- Tesso PCW, Angeli D, Casavola A, Tedesco F. Novel LQR and Economic MPC Control Strategies for Energy Harvesting in Wave Energy Converters. 10th IFAC Symposium on Mechatronics-14th IFAC Symposium on Robotics; 2025.
- Tesso PCW, Casavola A, Tedesco F. Comparison of promising control design approaches for energy harvesting in Wave Energy Converters. 6^{th} International Conference on Offshore Renewable Energy (CORE); 2025.
- Tesso PCW, Angeli D, Casavola A, Tedesco F. A Stochastic Economic Model Predictive Control for Regenerative Suspension Systems. International Journal of Control; under review.
- Tesso PCW, Gagliardi G, Lupia Marco, Casavola A. Economic Model Predictive Control for electric vehicles off-grid charging station's optimization including battery's lifetime; under preparation.
- Gagliardi G, Casavola A, Gianni C, Lupia M, Manna P, Tesso PCW. H_2 Multiobjective Control Strategies for Linear and Rotary Vehicular Regenerative Suspension Systems; under preparation.

Acknowledgements

First of all, I would like to thank the Lord Almighty for the strength given every day to accomplish this thesis. It is also an opportunity to thank all those who have contributed in any way to the development of this work. I think particularly to:

- Prof. Alessandro Casavola and Prof. Francesco Tedesco, my PhD supervisors who gave me the opportunity to join their team. I sincerely thank them for their attention and their availability. I also thank them for the encouragements, advices, orientations, and supports in all aspects of this research and during the writing of this thesis.
- DAuSy Programme. Grateful acknowledgements to the European Union-Next Generation Eu under the National Recovery and Resilience Plan (NRRP) Mission 4 Component 1 Investment 4.1-Decree No.351 (09th April 2022) of Italian Ministry of University and Research-Concession Decree No.2152(28th December 2022) of the Italian Ministry of University and Research, Project code D93C22000850005, within the Italian National Program PhD Programme in Autonomous Systems (DAuSy) and by the European Union - Next Generation EU under the Italian National Recovery and Resilience Plan (NRRP), Mission 4, Component 2, Investment 1.3, CUP E63C22002070006, partnership on "Telecommunications of the Future" (PE00000001 - program "RESTART").
- Dr. Gianfranco Gagliardi who can be considered as another supervisor for my thesis. I thank him for the research we carried together and for all his orientations since my arrival in Italy.
- Prof. David Angeli at Imperial College London for his availability and advices which helped me gaining a good knowledge of Model Predictive Control techniques.
- All the jury's members for the examination of this thesis.
- All the DAuSy board of professors.
- All my friends and colleagues either in DAUSY or at the University of Calabria.
- All the teaching and administrative staff of the University of Calabria and Polytechnic of Bari.

- My family for their support and advices. Special thanks to my dad who proof-read my thesis and my fiancée Merveille who was on my side despite the distance.

All those whose names have not been mentioned here, but who have contributed in one way or another to the success of this work should hereby receive my sincere gratitude.

Chapter 1

Introduction and literature review

I

Contents

1.1 Introduction 1
1.2 Background and motivation 1
1.3 Literature review 3
1.4 Problem statement of the work 13
1.5 Contributions 13
1.6 Thesis outline 15

1.1 Introduction

This chapter is made up of five sections. Section 1.2 provides the motivation behind the research conducted in the thesis and also presents some general background to the work. Section 1.3 depicts the state-of-the-art of the main notions studied in this thesis and the problem statement is presented in section 1.4. The contributions are hightlighted in section 1.5 and the chapter concludes with an overview of the structure of the thesis.

1.2 Background and motivation

Growing fossil fuel consumption has made automobile manufacturers to focus on innovative design to improve overall fuel efficiency of the vehicle. Vertical movement in the vehicle shock absorber is an important energy loss. It is estimated that vertical kinetic energy consumes about 30–50 % of the drive train energy and reduces the fuel efficiency [1]. Therefore, power lost in the vehicle shock absorbers cannot be ignored. In an attempt to reduce these losses, regenerative suspension systems have been developed. They can convert the energy from road disturbances into electrical energy. If an electric or hybrid car featured one of these, the energy it collected could be put toward charging the battery, extending the range of the car. On the other hand, using the collected energy to power the electrical subsystems in traditional cars could reduce the workload of the internal combustion engine [2]. Although in its infancy, yet both industrial prototypes and academic

projects have already proven that electricity can be harvested during normal driving. Academic innovators like Tufts University patented a high-power yet bulky regenerative shock absorber [3], while *Massachusetts Institute of Technology* (MIT) spin-off Levant Power and Stony Brook University focused on more streamlined, cost-effective second-generation designs [4]. More recent developments from 2023 to 2025 further illustrate the field's maturation. Audi's eROT prototype, unveiled around 2016 and evolving through 2025, uses electromechanical rotary dampers powered by a 48 V vehicle network and a 0.5 kWh battery. It generates an average of 100˘150 W ranging from just 3 W on smooth highways to around 613 W on rough roads. Audi has integrated the eROT system into its adaptive electromechanical suspension architecture introduced in production models in 2017 [5].

Nevertheless, these systems should not affect passengers comfort and handling of the vehicle. In fact, vehicle suspensions serve several conflicting purposes. Suspensions must isolate the passenger compartment from road irregularities. For driving safety, a permanent contact between the tires and the road should be assured [6]. This requires the use of appropriate controllers.

Another alternative to reduce the reliability upon fossil fuels is renewable energy. Wave energy is a kind of this clean energy. Waves offer the highest energy density compared to other renewable energy sources [7]. In fact, the total power of waves breaking around the world's coastlines is estimated at 2–3 million megaWatts [8] and *Wave Energy Converters* (WECs) (WECs) have been developed to harvest that energy [9]. However, higher energy density though, requires the devices to be more resistant to be able to withstand the harsh and at times possibly damaging sea environment. Moreover, the most energetic areas are usually in remote parts of the sea, quite far away from the coast. This increases dramatically the costs of installation, operation and maintenance as well, given the necessity for moorings for deeper waters and longer power transmission cables to reach shore. In order to make wave energy commercially viable, it is important to optimize energy harvesting in wave energy converters.

Therefore, the motivation of this thesis is in developing novel control design methodologies that can be readily applied to increase the efficiency of regenerative suspensions and wave energy converters. That means that the control algorithms must optimize energy harvesting in those devices while satisfying the main operative constraints. The interest of the writer is to outperform some existing control strategies used in these devices. Hence, the algorithms presented in this thesis have been developed to be suited for real-time implementation.

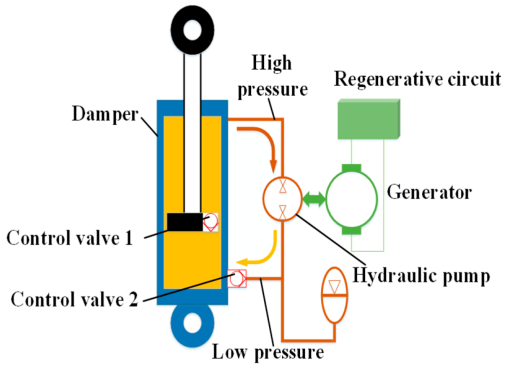

Figure 1.1: Hydraulic regenerative suspension

1.3 Literature review

1.3.1 Vehicle Energy Harvesting Shock Absorbers and their control strategies

Although energy efficiency has been a major concern in the automotive industry since the mass production in the 1900s, researchers realized that the energy dissipated in traditional hydraulic shock absorbers is worthy of being recovered only in the middle of 1990s. Since then, many different types of *Energy Harvesting Shock Absorber* (EHSA) were conceptualized and prototyped [10]. Regenerative shock absorber systems are mainly divided into hydraulic and electromagnetic according to working principles.

Hydraulic transmission-based energy harvester is a promising energy harvesting suspension system despite its relatively high cost compared to other systems. Hydraulic regenerative actuators include an energy recovery device for collecting the energy generated by shock absorbers. They can be single- or double-tube damping with an electronic control valve. Traditional hydraulic shock absorbers convert vibrational energy into heat and then dissipate heat into the environment [11]. With the discovery of the benefits of energy recovery and reuse, hydraulic regenerative suspension has been extensively developed. The mechanical energy of hydraulic suspension vibration is recovered and stored in the form of hydraulic energy. Hydraulic regenerative suspension is shown in Figure 1.1. It depends mainly on the hydraulic fluid to transfer the up-down displacement of the cylinder to the hydraulic pump/motor that is attached to an electrical generation circuit for power extraction out of the translated rotational motion [12]. To achieve stability in the hydraulic regenerative based damper performance, some necessary components are used in the system such as gas accumulators and hydraulic check valves as motion rectifiers.

On the other side, the working principle of electromagnetic energy-regenerative suspension is to replace traditional shock absorbers with electromagnetic actuators [13]. The energy generated by the mechanical vibration is converted into electrical energy and stored into energy storage

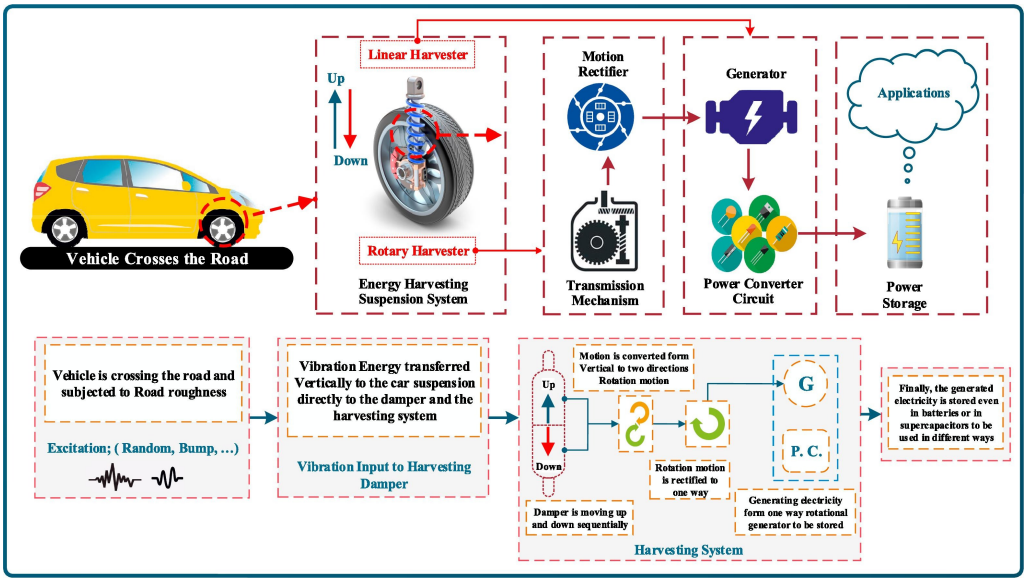

Figure 1.2: Scheme of the vehicle energy harvesting suspension system layout

devices. If the energy can be regenerated directly because of the linear movement between the two oscillators, namely the wheel's assembly and the vehicle's body, it can be categorized as a direct-drive regenerative shock absorber system or a linear EHSA.

If the energy can't be regenerated directly, the system is categorized as an indirect drive regenerative shock absorber. It relies on a certain mechanism to achieve the conversion between the linear motion of the shock absorber and the rotary motion of the generator. During this process the input speed can be amplified by the mechanism. Many mechanisms have been developed: ball screw, *Rack Pinion Energy Harvesting Shock Absorber* (RPEHSA) and their variants. Fig.1.2 summarizes the working principle of this energy's conversion.

Table 1.1 provides a comparison between the most popular energy conversion mechanisms in automotive suspension. New mechanisms have been recently developed with better characteristics. The *Synchronous Pulley Energy Harvesting Shock Absorber* (SPEHSA) uses synchronous pulleys and belts to convert the suspension's alternating motion into rotational motion, which is then amplified for power generation [14]. An alternative design uses an *Inerter Pendulum Vibration Absorber* (IPVA) with a planetary gear set and an electromagnetic rotary EHSA [15]. The efficiency of a vehicle's regenerative suspension system can be defined as the fraction of mechanical vibration energy dissipated in the suspension that is converted into useful electrical energy. In a broader perspective, it is the fraction of the road disturbance energy converted into useful electrical energy. Energy losses occur at different stage of the system :

- Friction in moving parts : Bearings, seals, and sliding interfaces generate frictional resistance, dissipating energy as heat.

Table 1.1: Comparison of the most popular energy conversion mechanisms in automotive suspension

Energy Conversion System	**Advantages**	**Limitations**
Rack-Pinion transmission based electromagnetic rotary energy harvesting suspension	It has a considerable potential energy and power density. Highest energy conversion efficiency. High assembly accuracy achievable. The ability of motion and force magnification.	It requires accurate system design and torque transmission capability limited by the gear module. Input and output axis perpendicular to each other and limited for the large space designs. Short operation life cycle for small designs due to easily damage and hard to offer a good lubrication for the mechanical meshing parts.
Ball-Screw transmission based electromagnetic rotary energy harvesting suspension	Easy to be designed with simple construction with quiet and smooth operation. High mechanical advantages and high mechanical efficiency with lower power consumption and power losses. High positional accuracy and smooth operation and it has good durability properties comparing to rack pinion. It can hold a large force comparing to the rack-pinion which could be used for large-scale systems.	Relative lower conversion efficiency than the rack pinion. High relative cost compared to the rack-pinion mechanism. Risk of buckling in the region between supports. It requires more parts for ball recirculating.
Linear electromagnetic based energy harvesting suspension	Being easily and reliably integrated into most existing vibration systems without the requirement of transmission mechanisms. It can generate power in compression and rebound stroke and can get the power for small velocities. It is more applicable to a real vehicle and easy to be fabricated and used as a self-power controllable damper. It is the best choice for achieving good vehicle dynamics behavior as a semi-active or active suspension (easy to be controlled).	Low conversion efficiency due to the continuous changing in the motor direction leading to a high inertia power loss. High production cost which requires accurate system design to make the magnetic hold the excitation force. Low power density for small-scale units and the magnetic field affected by surroundings. Its size is still large because of the relatively low vibration velocity.

- Gear train losses : If the absorber uses rack-and-pinion, ball-screw, or other transmissions, gear meshing and backlash cause inefficiencies.
- Viscous damping in fluids : Hydraulic or magnetorheological fluids resist motion, converting part of the energy into heat rather than electricity.
- Structural deformation : Elastic components (springs, bushings, mounts) store and release energy, but some is lost through hysteresis and material damping.
- Generator inefficiency : Copper losses (heating), iron losses (eddy currents, hysteresis), and mechanical drag reduce net output.
- Power electronics losses : Rectifiers, converters, and controllers dissipate energy during switching and conduction.

However, the performance of the overall regenerative suspension system also relies on the control strategies used to satisfy the control requirements. Unlike traditional methods that use electric motors as virtual dampers, [16]-[17] proposed an H_∞ multi-objective control strategy, the *Maximum Induced Power Control* (MIPC), to improve energy harvesting while maintaining ride comfort and road stability. In [18], an energy harvesting system using a linear electromagnetic generator in a shock absorber is examined. The system employs a perturb and observe Maximum Power Point Tracking algorithm to deliver consistent power to the battery, avoiding the need for expensive sensors. Another study in [19] implements two *Model Predictive Control* (MPC) strategies for a nonlinear IPVA in a quarter-car model. These strategies improve both vibration control and energy harvesting efficiency, demonstrating the potential of advanced control techniques. The use of the H_2 norm for performance evaluation is explored in [20], focusing on power generation, ride comfort, and road handling at different speeds and road conditions. Simulations suggest that a vehicle traveling at 60 mph on class B or C roads could produce 100 to 400 W, highlighting the feasibility of energy harvesting in real-world conditions. Recent studies have also explored multi-objective control strategies to optimize energy management in vehicular suspensions. For example, [21] employs the H_∞ norm within a multi-objective framework for electromagnetic suspension energy management. This approach is robust to uncertainties and external disturbances, ideal for the dynamic nature of vehicular environments. Further advancements include the gain-scheduled MIPC approach in [22], which adapts controller parameters in real time based on operating conditions. This adaptability is crucial for maintaining high performance and energy efficiency across varied road and driving scenarios. [23] extends the MIPC strategy to a full car model, applying both H_∞ and H_2 control strategies to balance ride comfort, road handling, and energy efficiency.

In [24], the authors develop a novel stochastic linearization model predictive control approach in which they employ stochastic linearization to approximate the nonlinear dynamics of the EHSA that has superior accuracy

compared to standard linearization. This leads to a MPC problem that is much more computationally efficient than the nonlinear MPC counterpart with no major performance degradation. Also, the effect of different road preview configurations on control performance is investigated, which is shown to have a significant impact on the control performance. In [25], a genetic algorithm optimization technique is used to find a balance between the rider's comfort and vehicle handling. In [26], the effect of the road profile towards the vehicle suspension travel is examined by using a state-feedback controller. The state-feedback controller's purpose is to decrease the continuous damping in the suspension system. Suspension travel and ride comfort are significantly improved by using the state-feedback controller as compared to the passive controller and the *Proportional Integral Derivative* (PID) controller. In [27], a semi-active control is applied to coordinate the energy-regenerative performance and the vehicle vibration isolation performance. The relation between semi-active control force and the maximum electromagnetic damping force in frequency domain is theoretically analyzed to increase the effective bandwidth of controllable semi-active force. Simulations demonstrate that the regenerative suspension with proposed circuit and semi-active control strategy improve the vehicle's ride comfort obviously on random excitation road while slightly deteriorate road handling performance. The regenerative suspension ensures 20.53 W that charges the battery on D-class road when the vehicle's velocity is 60 km/h.

According to this literature review on regenerative suspensions, it appears that few control methods optimize electrical power directly in their objective function. However, this approach can prove interesting and can open up a new field of possibilities. Moreover, we have introduced the concept of MIPC (Maximum Induced Power Control) which is an approach in the literature that optimizes energy harvesting while maintaining ride comfort and road stability (see [16], [17], [22], [23]). Nevertheless this MIPC has been investigated in a state feedback control formulation. In reality, it is not always possible to have full states information even using an observer, hence there is a need to explore the potential of MIPC from an output feedback perspective. On the other hand, many MPC methods of the literature are primarily based on the road preview. This non-causality leads to the necessity of prediction devices and a more or less high computing power. Therefore, the investigation of a new MPC approach which doesn't rely on road preview, is of interest. In addition, few works in the literature investigate the application of control strategies on vehicle suspensions's nonlinear models which are closer to reality than pure linear models. It is to address all these limitations that we are developing new control strategies for vehicle's regenerative suspensions in this thesis.

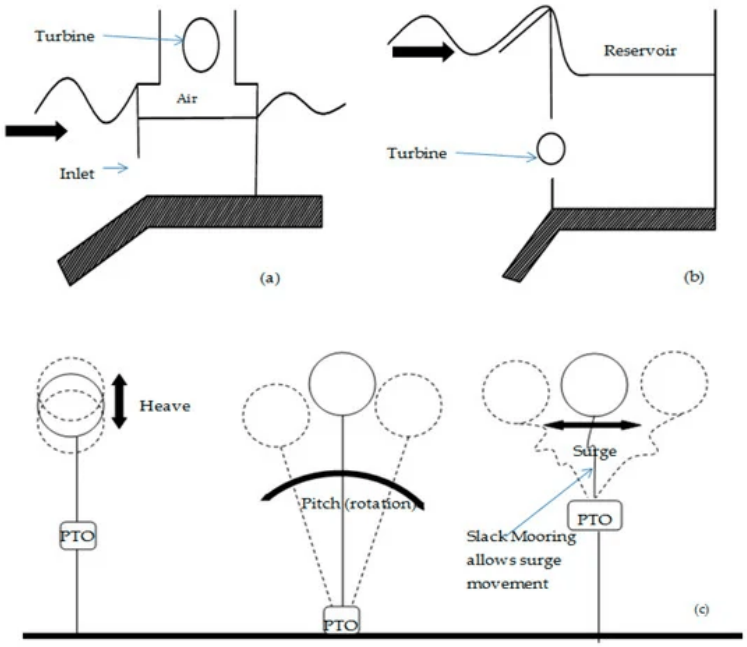

Figure 1.3: Classification of wave energy converter (WEC) extraction technology: (a) oscillating water column, (b) overtopping devices, and (c) oscillating bodies

1.3.2 Wave Energy Converters(WECs) and their control strategies

WECs are devices that convert the oscillatory motion from ocean waves into electricity [9]. Ocean wave energy converter technologies can be categorized into three systems, based on their working principles [28] and can be seen in Fig.1.3.

The first type of WEC is called *Oscillating Water Columns* (OWCs), where a chamber is put semi-submerged into the ocean water, and the air pressure change caused by the ocean wave induced water level change is used to drive air turbines to generate electricity. For instance, a research was conducted on the air turbine choice and the optimization of the power output in [29]. The second type of WEC is the oscillating body devices where the devices are either fully submerged or floating on the surface of the ocean to oscillate under the excitation of the wave. The kinematic energy is then harvested through various types of generators [28]. The third type of WEC is the *Overtopping Device* (OTD) where the water in the crest area of the ocean wave is stored and put into the reservoir, then the water is released and potential energy stored is used to generate electricity [30]. Oscillating body devices can be classified based on the wave motion they exploit. Among them, Point absorbers use a floating buoy to harvest energy through the heave motion induced by ocean waves, where the buoy's motion reacts against a fixed frame or a submerged body to generate power [31]-[32]. These devices can be either placed along the coastlines as fixed structures or used as floating structures in offshore areas.

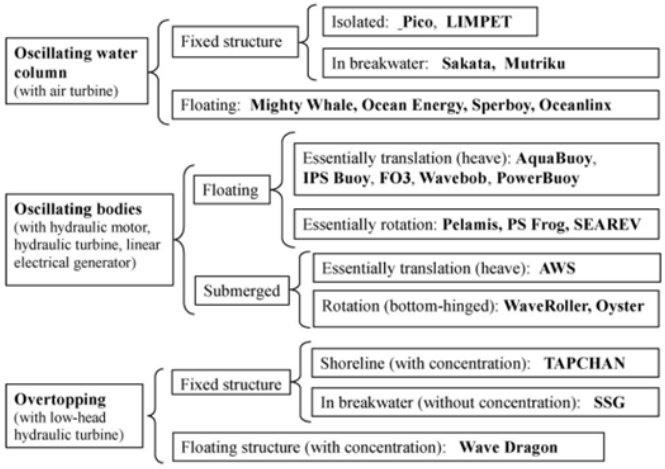

Figure 1.4: The various wave energy technologies

The examples shown in Fig.1.4 are not intended to form an exhaustive list [33] and were chosen among the projects that reached the prototype stage or at least were the object of extensive development effort.

In [33], a framework has been adopted to compare the hydrodynamic power efficiency of the three WECs categories. The efficiency is the ratio of the power capture to the power available within the width of the primary interacting part of the device and it is obtained with:

$$\eta = \frac{\text{Power absorbed}}{\text{Power available device width}} \tag{1.1}$$

Using this method to estimate the power absorbing efficiency is almost straightforward for WECs in oscillating water columns and oscillating body systems categories. For overtopping devices, there is a big challenge when using this method because their mode of operation is more like that of conventional hydropower systems technically [33]. In addressing this challenge, a modified method is used to estimate the hydrodynamic performance of overtopping converters, in which the hydrodynamic efficiency is represented by the ratio of power in the crest of the overtopping water after it encounters the converter to the power available in the ocean waves. The power in the crest of the overtopping device will depend on the width as well as the depth between the top and the turbine. This method may be able to give an estimate of the amount of average power absorbed from the power available in ocean waves during a specific period by the overtopping devices [33].

The efficiencies of wave energy converters can be classified by the efficiencies at the different stages of their energy conversion processes [33]:

1. Pneumatic/hydrodynamic efficiency: This is the ratio of the primary energy absorbed by the device to the energy resource available within the interacting section of the device with the ocean wave.

2. Turbine/mechanical efficiency: This is the ratio of the absorbed energy by the device to the mechanical energy through the *Power-Take-Off* (PTO)

device.

3. Electrical efficiency: This is the ratio of mechanical energy to electrical energy through the appropriate generator.

4. Transmission efficiency: This occurs during the conversion of the unstable electrical energy by the device to stable grid-acceptable electric energy.

Like the regenerative vehicle suspension system, the overall performance of wave energy converters also depends on the control strategies used to satisfy the control requirements. Although improvements to WEC mechanical and PTO systems can increase the economic feasibility of wave power, appropriate controller design has been shown to significantly increase the harvested energy of WECs [34].

In [35], an holitic techno-economic optimization of a wave energy converter is performed to minimize the cost of electricity, as opposed to simply maximize the converted energy at the early design stages. The objective function, which the genetic algorithm tries to minimize, is the ratio between capital cost and annual energy production.

In [36], a comprehensive literature review on the progress of classical and modern control strategies, including latching control, declutch control, reactive control, model predictive control, state space control, etc. has been done for the three major types of ocean wave energy converters, i.e. oscillating-body wave energy converter (including point absorber, attenuator and terminator), OWCs and OTD. Since point absorber is widely adopted for WEC (due to its high flexibility and efficiency), the research on control methods for point absorbers is more extensive than other types of WECs. Attenuator is not so common, but it still has Pelamis, the first utility-scale WEC, as a typical representative WEC in this category [36]. It may take some time to develop good control strategies for attenuator and evaluate their efficiency in the long run. The control strategies for OWCs and OTDs also experienced a prosperous time but they have less variation compared to point absorbers due to their similar structure and PTOs.

In [37], it has been shown that a gain scheduling control can directly address the two main issues often cited in the WEC controller design: noncausality and nonlinearities. The proposed approach retains most of the advantages of using linear models, which simplify the identification and design of the controllers.

In [38], the authors propose an adaptive hierarchical model predictive control scheme for wave energy converters. The proposed control law consists of two layers: On the top layer, an efficient cascaded estimation algorithm is developed to online identify and update the WEC model adaptively according to the change of sea states; on the bottom layer, a specially tailored MPC controller is implemented based on the updated WEC model to maximize the energy output subject to constraints for safe operation requirements.

In [39], the authors propose an economic feedback model predictive control scheme to improve energy conversion efficiency of wave energy converters and guarantee their safe operation over a wide range of sea

conditions. The proposed MPC control law consists of two terms: one state feedback gain designed offline to maximize operating range and one term calculated online to maximize the energy output.

In [40], the authors consider the incorporation into the model of all the conversion stages from ocean waves to the electricity network, referred to as wave-to-wire models, and identify the necessary components and their dynamics and constraints, including grid constraints. In addition, the authors identify different control inputs for the different components of the PTO system and how these inputs are articulated to the dynamics of the system.

In [41], it has been proposed the design of an energy-maximizing optimal controller for a single WEC device by employing the moment-based phasor transform, describing a pioneering application of this novel moment-matching mathematical scheme to an optimal control problem. Under this framework, the energy-maximizing optimal control formulation is shown to be a strictly concave quadratic program, allowing the application of well-known efficient real-time algorithms.

In [42], a strategy has been proposed to improve the computational performance of Nonlinear Pseudo spectral Control of Wave Energy Converters. A sliding mode control has been proposed in [43]. A nonlinear Constrained Optimal Control With Adaptive Dynamic Programming has been proposed in [44] and a robust optimal control with adaptive dynamic programming has been proposed in [45].

Controllers for WECs are sometimes designed assuming single-frequency waves [46]-[47]; however, true sea states are far from narrowband phenomena, and such controllers are consequently suboptimal in realistic applications. These controllers can be extended to the broadband situation by implementing a complex conjugate control [48].

Some control strategies for WEC include passive control [49], damping control, reactive control, latching control [50]-[51], phase control [52], and declutching control [53]. Damping control, usually constant damping control, is the best approach for technology developers willing to test an industrial scale WEC device, given the simplicity of implementation and the safety of operation. Reactive control is the natural evolution from damping control, presenting an affordable tabular approach for any WEC prototype being deployed for a demonstration phase. Latching control solves the PTO limitation of reactive control, but it requires an additional clamping mechanism to be installed and energized in the WEC, generating extra costs while also lowering the reliability. However, most of these control strategies are only effective for regular waves and become very complicated to implement for irregular waves in real sea conditions.

Other suboptimal control strategies have been recently developed for the WEC control problem, e.g., a nonstandard linear quadratic Gaussian control [54] and the noncausal control proposed in [55]. Although the implementation of these causal optimal controllers avoids the hardware cost for wave prediction, this extra hardware cost can be trivial compared with the increased energy output gained by incorporating wave prediction into

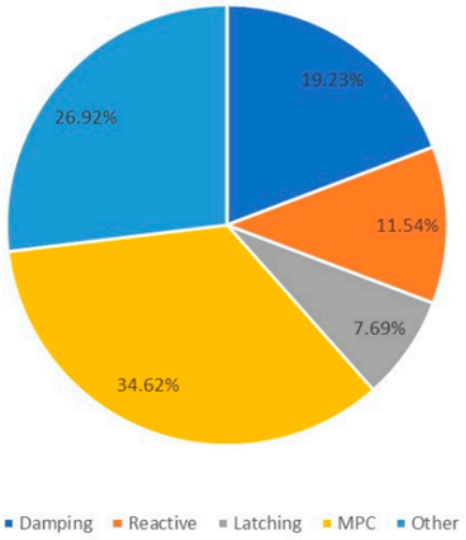

Figure 1.5: Classification of control strategies for WECs

control in some scenarios [56].

Wave prediction has been incorporated in some works [56]-[57]. It has been demonstrated in [58] that the noncausal optimal WEC control with wave prediction based on the concept of model predictive control (MPC) can at least double the energy output than the energy converted by the traditional causal WEC control methods. MPC solutions represent the best approach to optimal control. Enabling excitation force prediction applies at each time step the optimum PTO force for maximum energy absorption while still considering constraints. In Fig.1.5, we can see a classification of recent studies for different WEC control strategies from 2017 to 2019. MPC has been found to be the most interesting topic among the scientific community over the recent years, given the good results presented in different articles. This is due to the growing experience in simulated and tank-testing environments, the incremental available advances in computational capacity and the improved expertise with environments based on neural networks. Nevertheless, the complexity of implementation and absence of industry scale demonstration projects disfavored MPC solutions for WEC technology developers [59].

Many wave prediction techniques have been developed such as the *Deterministic Sea Wave Prediction* (DSWP) technology [60] and the Harvey's model [61]. These techniques can be incorporated to the control strategies for WECs. There is a constant need for control strategies which can incorporate wave predictions into the controller and satisfy the imposed constraints.

When looking at the literature, one finds that the researchers who are focusing on the mechanical aspects of the WEC systems and the associated energy capturing mechanisms are working apart from considering the electrical systems and vice versa [62]. It is obvious now that more interdisciplinary research efforts between mechanical, electrical, and control

engineers are required to achieve mature research in WEC systems. Moreover, the private companies who are active in the field of wave systems do not share their results with the scientific community because of commercial reasons and hence it becomes difficult for researchers to include the real conditions and challenges in their analyses and experiments.

According to this literature review on WECs, it appears that most control strategies are based on MPC, latching control, reactive control, damping control and so on.... Moreover, most of the methods in the literature are non-causal, meaning they require wave prediction. These strategies have advantages and limitations such as the need of wave prediction devices and a high computational power. It seems necessary to develop new causal control strategies different from the aforementioned ones. Furthermore, MPC methods are rarely developed in the form of EMPC and do not optimize energy recovery directly in their objective function. However EMPC offers a broad range of possibilities for energy systems in general. It is to address these limitations that we are developing new control strategies for WECs in this thesis. In addition, few works in the literature focus on the design of control strategies considering nonlinear hydrodynamic effects faced by WECs. This is due to the fact that considering these nonlinear effects in the control laws design always require experimental studies on WEC's prototypes which are not available. In this thesis, the question won't be to include nonlinear hydrodynamic effects into the control laws design but to compare our control strategies designed for WECs to an existing *Nonlinear Model Predictive Control* (NMPC) of the literature.

1.4 Problem statement of the work

This thesis is embedded in the fields of control and *Renewable Energy Sources* (RESs). The aim of the present research is to design control strategies that maximize the energy harvested by the aforementioned devices while satisfying safe operative constraints. Regarding regenerative suspensions, these constraints are passengers comfort, good road handling and suspension stroke. Regarding wave energy converters, these constraints are good buoy's displacement, buoy's velocity and actuator's force.

The objectives of the thesis are the following:

- **to develop causal and noncausal control strategies suitable for energy harvesting optimization and constraints satisfaction;**
- **to investigate the performance of the control strategies by simulations on the devices.**

1.5 Contributions

The contributions of the present work are as follows.

Firstly, two control laws are investigated: H_∞ and H_2 dynamic output feedback control designed with the MIPC strategy to compare the performances of the main actuators used in vehicle's regenerative suspension literature. The aim of this first study is to determine the best actuator and the best control law. It is shown that the IPVA is the best actuator for regenerative suspension systems and the MIPC H_2 dynamic output feedback control is better than its H_∞ counterpart to optimize energy harvesting, suspension stroke, road handling and passenger's comfort.

Secondly, it is well known that classical *Linear Quadratic Regulator* (LQR) methods, although the quadratic cost function can be adapted to reflect different objectives, are generally ill-suited for multi-objective optimization and for enforcing hard constraints. As a result, even though LQR offers optimality in a theoretical sense, practical implementations often require careful tuning, since there is no inherent guarantee that the system variables will remain within acceptable bounds during operation. To address these limitations, a novel solution to a non-standard optimal LQR control design problem is developed with a cost function that maximizes directly the electrical power generated by the regenerative suspension system using an appropriate approach, rather than being the standard integral of the sum of state and input norms. Additionally, a bound on the passenger's comfort is taken into consideration as a secondary objective to be optimized through H_∞ norm, together with the energy harvesting requirement to demonstrate how the LQR synthesis problem can handle multi objective optimization problems. It is demonstrated on multiple roads and driving scenarios that this novel strategy outperforms the MIPC H_2 static state feedback and the Regenerative damper control strategies which are references in the domain.

Thirdly, the same multi objective *Linear Quadratic* (LQ) control strategy is investigated for wave energy converters and similar conclusions are obtained. Fourthly, an *Economic Model Predictive Control* (EMPC) based on the same non standard cost function is developed. In the regenerative suspension context, a Stochastic Model Predictive Control is developed because road disturbance is assumed to be unpredictable. The controller is applied without road preview and the main difficulty here is to use the right condition for recursive feasibility assuming a stochastic disturbance.

In the wave energy converter context, this control strategy is applied to optimize energy harvesting, to ensure recursive feasibility at each time step and to ensure safe operative constraints (limitation on the buoy displacement, buoy velocity and actuator's force). Wave prediction is incorporated into the controller and investigations are undertaken using different models of wave energy converters and wave scenarios. The control strategies designed in this thesis are based on linear models. However, vehicle's regenerative suspension systems are not perfectly linear and wave energy converters can exhibit significant nonlinear hydrodynamic effects in harsh seas. To address this issue, additional studies are undertaken using more realistic nonlinear models of vehicle suspensions on CarSim's software. Moreover, the economic model predictive control strategy designed for WECs is compared to a

nonlinear model predictive control strategy which includes some nonlinear hydrodynamic forces often neglected in the controller's design.

1.6 Thesis outline

The thesis is organized in six chapters following this one.

Chapter 2 introduces the main vehicle's regenerative suspension configurations studied in this thesis and their dynamics. This includes vehicles suspension modeling, actuators modeling and power flow analysis.

Chapter 3 introduces wave energy converters configurations. In particular, the emphasis is on the point absorber classification, power take off mechanisms, point absorber dynamics and wave forecasting models.

H_∞ and H_2 MIPC dynamic output feedback control strategies are designed in chapter 4. The control strategies are applied on four actuators and comparison is undertaken. The aim is to determine the best actuator for vehicles regenerative suspensions configuration and the best control strategy among the two proposed.

Chapter 5 presents H_2 MIPC state feedback and a novel LQR control strategy with a non-standard cost. The two control strategies are applied on vehicles regenerative suspensions and wave energy converters. Regarding regenerative suspensions, the novel LQR strategy is compared to the H_2 MIPC state feedback and the regenerative damper control strategy considering a quarter car model, a full-car model and two road signals. The robustness of the control strategies to some parameters uncertainties is also investigated. In addition, simulations on the mechanical simulation software CarSim 2025.1 are undertaken to show the effectiveness of the novel LQR control strategy on more realistic nonlinear suspension models assuming different driving scenarios and vehicles parameters. Regarding wave energy converters, four control strategies, including the H_2 MIPC state feedback and the LQR, are designed for a standard point absorber and simulations are presented.

Chapter 6 introduces Economic Model Predictive Control based on the same non standard cost. The control strategy is applied to vehicles regenerative suspensions assuming a non deterministic road disturbance and simulations are undertaken on two car models. Four constraint approaches are investigated and a comparison with the LQR strategy is presented. On the other hand, the same Economic Model Predictive Control is redefined for wave energy converters with the incorporation of wave prediction into the controller's scheme. A comparison to the Linear Noncausal Optimal Control strategy (LNOC) and to the Nonlinear Model Predictive Control strategy (NMPC) with moment based approach is presented. Many simulations are undertaken: perfect wave prediction and imperfect wave prediction, application on a small wave energy converter (a standard point absorber) and a big wave energy converter (Corpower device), application under many waves scenarios.

Chapter 7 concludes the thesis presenting the main findings and provides future research directions.

Chapter 2

Regenerative suspension configuration

Contents

2.1 Introduction 17
2.2 Suspension modeling 17
2.3 Actuators modeling 23
2.4 Power flow analysis 32
2.5 Conclusion 35

2.1 Introduction

The aim of this chapter is to detail regenerative suspension configuration. It is important to understand the methodology used in this work to harvest energy in suspension system. Section 2.2 presents the vehicle suspension modeling. Section 2.3 introduces actuators modeling. Power flow analysis is detailed in section 2.4 and a conclusion ends the chapter in section 2.5.

2.2 Suspension modeling

Whether a suspension model is passive, active or semi-active, a mathematical model is needed to describe the dynamics of the vehicle when it is subjected to excitation. As there are many variables involved in these dynamics equations, it is appropriate to introduce simplifications, considering only the most relevant dynamics.

On a mechanical level, the suspension dynamics can be divided into vertical, roll and pitch motions. Among the three motions, the predominant one is the vertical dynamics, i.e. the translational motion of the vehicle along the axis perpendicular to the direction of the longitudinal motion.

Depending on the degree of accuracy desired, it is possible to consider all three motions or only some of them. Clearly, these considerations affect the equations complexity and lead to different models which will be presented in the following paragraphs.

2.2.1 Full car suspension model

The 7 *Degrees-of-Freedom* (DoF) mathematical model proposed in [63] is employed here to describe the vehicle's dynamic behavior, specifically its pitch (θ_s) and roll (φ_s) rotational motions, as well as the vertical motion of the sprung mass (m_s). The model encompasses a set of coupled linear differential equations that govern these motions. For simplicity, the dependence on time is omitted in the equations. The pitch motion (θ_s) describes the rotation around the vehicle's lateral axis, typically influenced by acceleration and braking forces. The roll motion (φ_s) involves rotation around the longitudinal axis, primarily affected by cornering forces. The vertical motion (z_s) refers to the up and down movement of the vehicle's sprung mass, influenced by road irregularities and the vehicle's suspension system. The next paragraphs will present the different kind of suspension systems : passive suspensions, active suspensions, semi-active suspensions and regenerative suspensions.

2.2.1.1 Passive full-car model

Fig. 2.1 shows the passive full-car model. It includes all three aforementionned dynamics i.e. vertical, roll and pitch motions [23]. In conventional suspension systems, passive viscous dampers are used for all four wheels to absorb shocks and maintain vehicle stability [23]. The following equations encapsulate these dynamics, illustrating how the pitch, roll, and vertical motions are linked :

$$\begin{cases} I_r\ddot{\varphi}_s &= -b_f t_f(\dot{z}_{s_1}-\dot{z}_{u_1}) + b_f t_f(\dot{z}_{s_2}-\dot{z}_{u_2}) - b_r t_r(\dot{z}_{s_3}-\dot{z}_{u_3}) + b_r t_r(\dot{z}_{s_4}-\dot{z}_{u_4}) \\ & \quad -k_f t_f(z_{s_1}-z_{u_1}) + k_f t_f(z_{s_2}-z_{u_2}) - k_r t_r(z_{s_3}-z_{u_3}) + k_r t_r(z_{s_4}-z_{u_4}) \\ I_p\ddot{\theta}_s &= -b_f a(\dot{z}_{s_1}-\dot{z}_{u_1}) - b_f a(\dot{z}_{s_2}-\dot{z}_{u_2}) + b_r b(\dot{z}_{s_3}-\dot{z}_{u_3}) + b_r b(\dot{z}_{s_4}-\dot{z}_{u_4}) \\ & \quad -k_f a(z_{s_1}-z_{u_1}) - k_f a(z_{s_2}-z_{u_2}) + k_r b(z_{s_3}-z_{u_3}) + k_r b(z_{s_4}-z_{u_4}) \\ m_s\ddot{z}_s &= -b_f(\dot{z}_{s_1}-\dot{z}_{u_1}) - b_f(\dot{z}_{s_2}-\dot{z}_{u_2}) - b_r(\dot{z}_{s_3}-\dot{z}_{u_3}) - b_f(\dot{z}_{s_4}-\dot{z}_{u_4}) \\ & \quad -k_f(z_{s_1}-z_{u_1}) - k_f(z_{s_2}-z_{u_2}) - k_r(z_{s_3}-z_{u_3}) - k_r(z_{s_4}-z_{u_4}) \end{cases} \tag{2.1}$$

where I_p and I_r represent the moments of inertia associated with pitch and roll motions respectively and z_{u_i}, $i = 1, \ldots, 4$ the vertical motions of the four unsprung masses described by

$$\begin{cases} m_{u_1}\ddot{z}_{u_1} &= b_f(\dot{z}_{s_1}-\dot{z}_{u_1}) + k_f(z_{s_1}-z_{u_1}) - b_{tf}(\dot{z}_{u_1}-\dot{z}_{r_1}) - k_{tf}(z_{u_1}-z_{r_1}) \\ m_{u_2}\ddot{z}_{u_2} &= b_f(\dot{z}_{s_2}-\dot{z}_{u_2}) + k_f(z_{s_2}-z_{u_2}) - b_{tf}(\dot{z}_{u_2}-\dot{z}_{r_2}) - k_{tf}(z_{u_2}-z_{r_2}) \\ m_{u_3}\ddot{z}_{u_3} &= b_r(\dot{z}_{s_3}-\dot{z}_{u_3}) + k_r(z_{s_3}-z_{u_3}) - b_{tr}(\dot{z}_{u_3}-\dot{z}_{r_3}) - k_{tr}(z_{u_3}-z_{r_3}) \\ m_{u_4}\ddot{z}_{u_4} &= b_r(\dot{z}_{s_4}-\dot{z}_{u_4}) + k_r(z_{s_4}-z_{u_4}) - b_{tr}(\dot{z}_{u_4}-\dot{z}_{r_4}) - k_{tr}(z_{u_4}-z_{r_4}) \end{cases} \tag{2.2}$$

Moreover, z_{s_i}, $i = 1, \ldots, 4$ represent the vertical motions of the body corners. Assuming small pitch and roll angles, they are related to φ_s, θ_s and z_s by

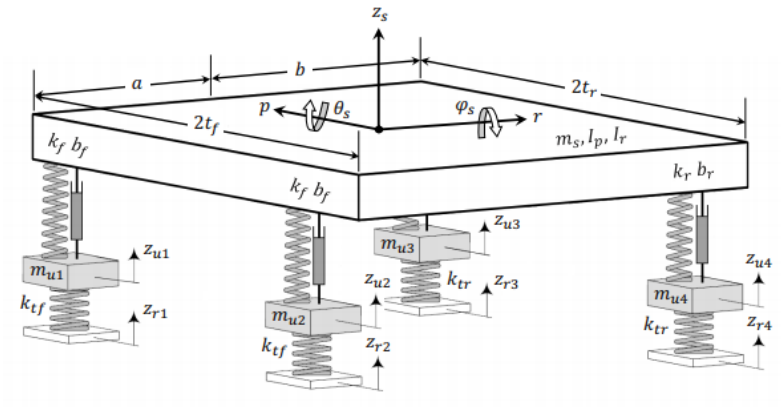

Figure 2.1: Full-car schematic- passive setup

the following equations

$$\begin{cases} z_{s_1} = t_f\varphi_s + a\theta_s + z_s & \dot{z}_{s_1} = t_f\dot{\varphi}_s + a\dot{\theta}_s + \dot{z}_s \\ z_{s_2} = -t_f\varphi_s + a\theta_s + z_s & \dot{z}_{s_2} = -t_f\dot{\varphi}_s + a\dot{\theta}_s + \dot{z}_s \\ z_{s_3} = t_r\varphi_s - b\theta_s + z_s & \dot{z}_{s_3} = t_r\dot{\varphi}_s - b\dot{\theta}_s + \dot{z}_s \\ z_{s_4} = -t_r\varphi_s - b\theta_s + z_s & \dot{z}_{s_4} = -t_r\dot{\varphi}_s - b\dot{\theta}_s + \dot{z}_s \end{cases} \tag{2.3}$$

In the above equations, the following notation has been used:

- a, b, t_f and t_r are geometric parameters that characterize the body of the car;
- z_{r_i}, $i = 1, \ldots, 4$ denote the road profiles;
- $z_{s_i} - z_{u_i}$, $i = 1, \ldots, 4$ denote the suspension strokes;
- $z_{u_i} - z_{r_i}$, $i = 1, \ldots, 4$ model the tire deflections.
- m_{u_1} and m_{u_2} are the masses of the front wheels, while m_{u_3} and m_{u_4} are the masses of the rear wheels;
- k_{tf} and k_{tr} are the tire elastic stiffnesses;
- k_f and k_r are the front and rear suspension stiffnesses respectively.

2.2.1.2 Active full-car model

In an active full-car model, it is necessary to add on each wheel the effect of an actuator placed in parallel to the springs and dampers, modulable by appropriate forces f_1, f_2, f_3 and f_4. Fig.2.2 shows the full-car mechanical system in active configuration, where the actuators are present [23]. It is shown that the previous equations 2.1 and 2.2 must be rewritten including the actuation forces as follows :

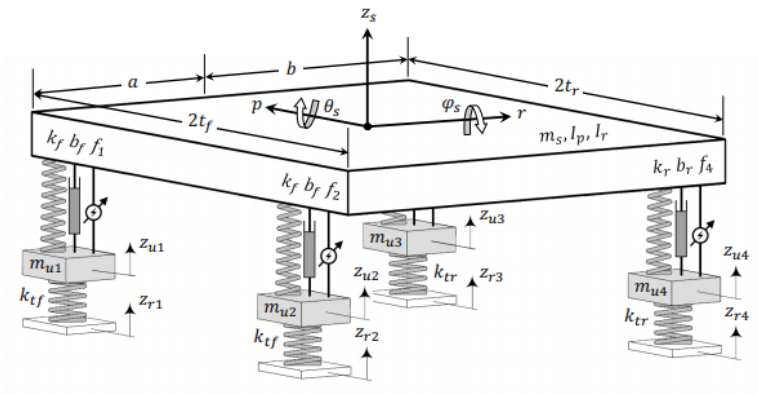

Figure 2.2: Full-car schematic- active setup

$$\begin{cases} I_r\ddot{\varphi}_s &= -b_f t_f(\dot{z}_{s_1}-\dot{z}_{u_1})+b_f t_f(\dot{z}_{s_2}-\dot{z}_{u_2})-b_r t_r(\dot{z}_{s_3}-\dot{z}_{u_3})+b_r t_r(\dot{z}_{s_4}-\dot{z}_{u_4}) \\ & \quad -k_f t_f(z_{s_1}-z_{u_1})+k_f t_f(z_{s_2}-z_{u_2})-k_r t_r(z_{s_3}-z_{u_3})+k_r t_r(z_{s_4}-z_{u_4}) \\ & \quad +t_f f_1-t_f f_2+t_r f_3-t_r f_4 \\ I_p\ddot{\theta}_s &= -b_f a(\dot{z}_{s_1}-\dot{z}_{u_1})-b_f a(\dot{z}_{s_2}-\dot{z}_{u_2})+b_r b(\dot{z}_{s_3}-\dot{z}_{u_3})+b_r b(\dot{z}_{s_4}-\dot{z}_{u_4}) \\ & \quad -k_f a(z_{s_1}-z_{u_1})-k_f a(z_{s_2}-z_{u_2})+k_r b(z_{s_3}-z_{u_3})+k_r b(z_{s_4}-z_{u_4}) \\ & \quad +af_1+af_2-bf_3-bf_4 \\ m_s\ddot{z}_s &= -b_f(\dot{z}_{s_1}-\dot{z}_{u_1})-b_f(\dot{z}_{s_2}-\dot{z}_{u_2})-b_r(\dot{z}_{s_3}-\dot{z}_{u_3})-b_f(\dot{z}_{s_4}-\dot{z}_{u_4}) \\ & \quad -k_f(z_{s_1}-z_{u_1})-k_f(z_{s_2}-z_{u_2})-k_r(z_{s_3}-z_{u_3})-k_r(z_{s_4}-z_{u_4}) \\ & \quad +f_1+f_2+f_3+f_4 \end{cases} \tag{2.4}$$

where z_{u_i}, $i=1,\ldots,4$ are described by

$$\begin{cases} m_{u_1}\ddot{z}_{u_1} &= b_f(\dot{z}_{s_1}-\dot{z}_{u_1})+k_f(z_{s_1}-z_{u_1})-b_{tf}(\dot{z}_{u_1}-\dot{z}_{r_1})-k_{tf}(z_{u_1}-z_{r_1})-f_1 \\ m_{u_2}\ddot{z}_{u_2} &= b_f(\dot{z}_{s_2}-\dot{z}_{u_2})+k_f(z_{s_2}-z_{u_2})-b_{tf}(\dot{z}_{u_2}-\dot{z}_{r_2})-k_{tf}(z_{u_2}-z_{r_2})-f_2 \\ m_{u_3}\ddot{z}_{u_3} &= b_r(\dot{z}_{s_3}-\dot{z}_{u_3})+k_r(z_{s_3}-z_{u_3})-b_{tr}(\dot{z}_{u_3}-\dot{z}_{r_3})-k_{tr}(z_{u_3}-z_{r_3})-f_3 \\ m_{u_4}\ddot{z}_{u_4} &= b_r(\dot{z}_{s_4}-\dot{z}_{u_4})+k_r(z_{s_4}-z_{u_4})-b_{tr}(\dot{z}_{u_4}-\dot{z}_{r_4})-k_{tr}(z_{u_4}-z_{r_4})-f_4 \end{cases} \tag{2.5}$$

and the vertical motions z_{s_i}, $i=1,\ldots,4$ remain unchanged.

2.2.1.3 Semi-active full-car model

The semi-active suspension system bridges the gap between passive and active suspensions, offering enhanced damping performance compared to passive suspensions while consuming less energy than active counterparts. During vehicle operation, the controller of a semi-active suspension adjusts the stiffness of elastic components or the damping coeffiient of dampers in response to variations in road conditions, thereby suppressing vibrations in the suspension system. In the event of control algorithm failure, it can function as a passive suspension [64]. Semi-active suspensions retain the inherent characteristics of passive suspensions without the addition of external actuators, often replacing traditional passive dampers with units that feature adjustable damping coefficients. This design

Table 2.1: Advantages, limitations, and applications of different suspension types

Suspension type	Advantages	Limitations	Applications
Passive	Simple, reliable, low cost	Fixed damping, less effective in varying conditions	Most common, entry-level vehicles
Semi-active	Improved damping, energy-effiient, reliable	Complex design, control-dependent	Mid to high-end vehicles, aerospace
Active	Best performance, real-time adjustment	High energy consumption, expensive, less reliable	High-end vehicles, racing cars, limited use.

addresses the structural complexities, energy consumption, costs, and reliability issues associated with active suspensions, while achieving damping effects comparable to active suspensions. In summary, semi-active suspension systems exhibit superior damping effectiveness compared to passive suspensions, featuring faster response speed and enhanced adaptability to varying road conditions. When appropriate control strategies are implemented, semi-active suspensions achieve damping performance comparable to active suspensions, alongside benefits such as simpler structure and reduced energy consumption. Considering cost constraints and development expenses, semi-active suspensions combine the reliability of passive suspensions with well-balanced handling stability and ride comfort, thus presenting promising prospects. Researchers have extensively researched semi-active suspensions, thus establishing them as the most widely deployed controllable suspension system in today's market [65]-[66]. In particular, [66] presents a comprehensive discussion of designing control algorithms for semi-active suspensions. It also covers performance analysis and control design. Moreover, it evaluates approaches to different control theories, and it includes methods needed for analyzing and evaluating suspension performances, while identifying optimal performance bounds.

As shown in Table 2.1, the performance advantages, limitations, and application ranges of the three types of suspensions mentioned above are listed. The table provides a clear illustration of the distinct strengths and weaknesses of passive and active suspensions. In contrast, semi-active suspensions integrate the structural simplicity of passive suspensions with the variable damping capability of active suspensions [64].

2.2.1.4 Regenerative full-car model

In the regenerative set-up, the passive dampers are substituted with electromechanical actuators. These are designed to generate forces on the four wheels of the vehicle. The primary function of these actuators is to provide an active damping effect, which is more efficient and responsive than passive damping. By generating the necessary forces in real-time, the

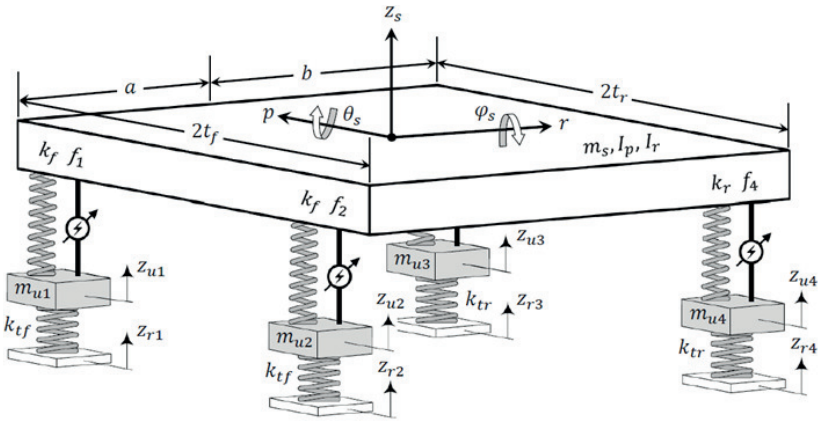

Figure 2.3: Full-car schematic- regenerative setup

actuators can effectively mitigate the vertical, pitch, and roll motions of the car's body. The schematic of the full-car regenerative suspension system is illustrated in Fig.2.3. By employing this model, the complex dynamics of the vehicle can be analyzed, enabling the design of control strategies to optimize ride comfort, stability, and handling performance. The dynamics equations are given :

$$\begin{cases} I_r\ddot{\varphi}_s &= -k_f t_f(z_{s_1}-z_{u_1}) + k_f t_f(z_{s_2}-z_{u_2}) - k_r t_r(z_{s_3}-z_{u_3}) + k_r t_r(z_{s_4}-z_{u_4}) + \\ & \quad t_f f_1 - t_f f_2 + t_r f_3 - t_r f_4 \\ I_p\ddot{\theta}_s &= -k_f a(z_{s_1}-z_{u_1}) - k_f a(z_{s_2}-z_{u_2}) + k_r b(z_{s_3}-z_{u_3}) + k_r b(z_{s_4}-z_{u_4}) + \\ & \quad a f_1 + a f_2 - b f_3 - b f_4 \\ m_s\ddot{z}_s &= -k_f(z_{s_1}-z_{u_1}) - k_f(z_{s_2}-z_{u_2}) - k_r(z_{s_3}-z_{u_3}) - k_r(z_{s_4}-z_{u_4}) + \\ & \quad f_1 + f_2 + f_3 + f_4 \end{cases} \tag{2.6}$$

with z_{u_i}, $i = 1, \ldots, 4$ the vertical motions of the four unsprung masses described by

$$\begin{cases} m_{u_1}\ddot{z}_{u_1} &= k_f(z_{s_1}-z_{u_1}) - k_{tf}(z_{u_1}-z_{r_1}) - f_1 \\ m_{u_2}\ddot{z}_{u_2} &= k_f(z_{s_2}-z_{u_2}) - k_{tf}(z_{u_2}-z_{r_2}) - f_2 \\ m_{u_3}\ddot{z}_{u_3} &= k_r(z_{s_3}-z_{u_3}) - k_{tr}(z_{u_3}-z_{r_3}) - f_3 \\ m_{u_4}\ddot{z}_{u_4} &= k_r(z_{s_4}-z_{u_4}) - k_{tr}(z_{u_4}-z_{r_4}) - f_4 \end{cases} \tag{2.7}$$

and the vertical motions z_{s_i}, $i = 1, \ldots, 4$ remain unchanged.

2.2.2 Half car suspension model

The half-car model is a simplified version of the previous one. There are two types of half-car models depending on the application: one takes into account vertical and pitch motions while the other takes into account vertical and roll motions [27]. In fact, in addition to the vertical motion that cannot be excluded as it is the predominant one, it may be necessary to take into account one of the two other motions but not both. This is the case where the half-car suspension model can be particularly useful.

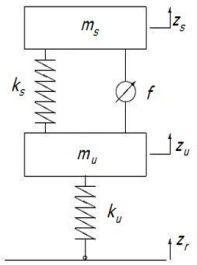

Figure 2.4: Quarter car model for a regenerative setup

2.2.3 Quarter car suspension model

The 2-DoF quarter-car model is depicted in Fig.2.4. In such a system, the passive viscous damper is replaced by an electromechanical actuator that generates a force $f(t)$ to be used to suitably dampen the vertical motion only. The dynamics of the model is described by the following equations.

$$\begin{cases} m_s\ddot{z}_s(t) &= -k_s(z_s(t) - z_u(t)) + f(t) \\ m_u\ddot{z}_u(t) &= k_s(z_s(t) - z_u(t)) - k_u(z_u(t) - z_r(t)) - f(t) \end{cases} \tag{2.8}$$

In Fig.2.4., k_s and k_u denote respectively the suspension and tire stiffness, m_s and m_u respectively the sprung and unsprung masses, z_s and z_u their positions and z_r the road profile. Moreover, $z_s - z_u$ represents the suspension stroke and $z_u - z_r$ the tire deflection.

2.3 Actuators modeling

2.3.1 Linear Permanents Magnets Actuator(LPMA) or Moving Magnets Linear Actuator (MMLA)

Linear Permanents Magnets Actuator (LPMA) or *Moving Magnets Linear Actuator* (MMLA) are electromagnetic devices that generate direct short travel oscillatory or progressive linear motion (Fig.2.5). They are beneficial in a wide range of applications, including compressors, pumps, electromagnetic valve actuators, active shock absorbers, and vibrators.

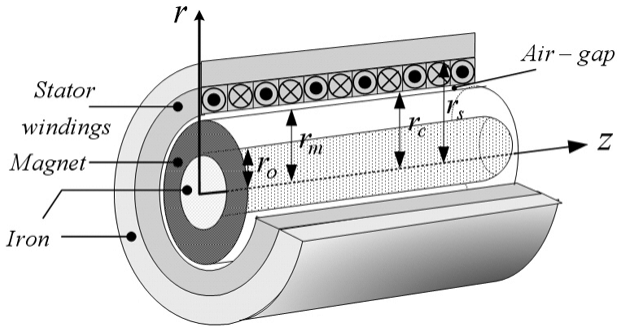

Figure 2.5: Linear Permanents Magnets Actuator.

From a mathematical point of view, the LPMA model can be derived by accounting for the Kirchoff's law [23]

$$v_{a_i}(t) = R_{a_i} i_i(t) + L_{a_i} \frac{di_i(t)}{dt} + K_v v_i(t) \tag{2.9}$$

$$v_i(t) = \dot{z}_{s_i}(t) - \dot{z}_{u_i}(t) \tag{2.10}$$

$$f_i(t) = K_v i_i(t) \tag{2.11}$$

for each of the four identical actuators considered ($i = 1, \ldots, 4$) where

- v_i represent the suspension stroke's velocities;
- f_i are the damping forces;
- v_{a_i} are the armature voltages;
- i_i represent the armature currents;
- R_{a_i} and L_{a_i} are the armature resistances and inductances respectively;
- $K_v v_i(t)$ represents the counter-electromotive force;
- K_v is the force constant.

The electrical power delivered by the i^{th} actuator is defined as $P_{e_i}(t) = v_{a_i}(t) i_i(t)$ and it is given by

$$P_{e_i}(t) = i_i(t) v_{a_i}(t) = P_{d_i}(t) + P_{c_i}(t) + P_{m_i}(t), \quad i = 1, \ldots, 4 \tag{2.12}$$

where

- $P_{d_i}(t) = R_{a_i} i_i^2(t)$ represents the power dissipated by the Joule effect;
- $P_{c_i}(t) = L_{a_i} \frac{di_i(t)}{dt} i_i(t)$ the reactive electrical power stored in the inductance L_{a_i};
- $P_{m_i}(t) = K_v v_i(t) i_i(t)$ the mechanical power acting on the i-th actuator.

Fig.2.6 depicts this actuartor's configuration in Simulink.

2.3.2 Rack Pinion Energy Harvesting Shock Absorber (RPEHSA)

The RPEHSA falls into the category of mechanical transmission-based electromagnetic rotary harvesters. Fig.2.7 shows the RPEHSA configuration. This system features a pair of rack and pinion, a single shaft, and three bevel gears. Mounted between the shaft (gray) and the two larger bevel gears (purple) are two roller clutches (blue). The larger bevel gears (purple) remain engaged with the small bevel gear (green) all times. When the rack moves up and down, the pinion and shaft rotate in clockwise and counterclockwise directions. At any instant, only one large bevel gear will be engaged and driven by the shaft, while the roller clutch will disengage the other large

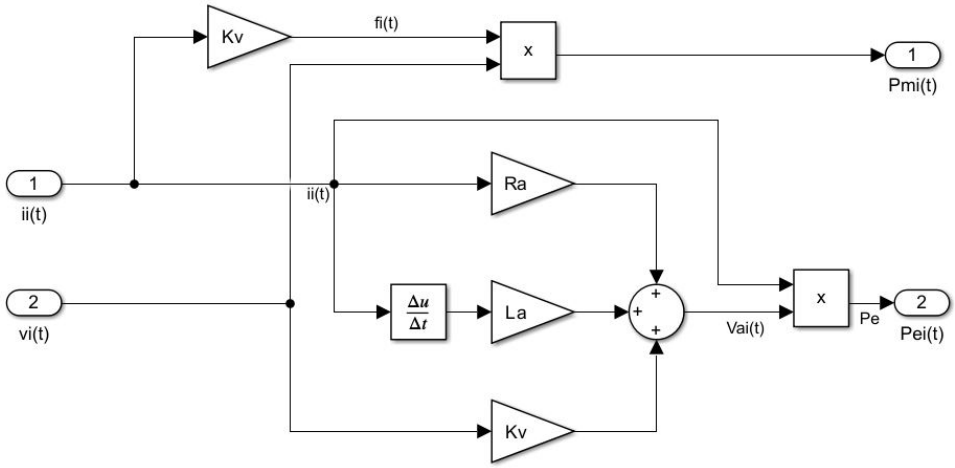

Figure 2.6: Simulink model of the LPMA

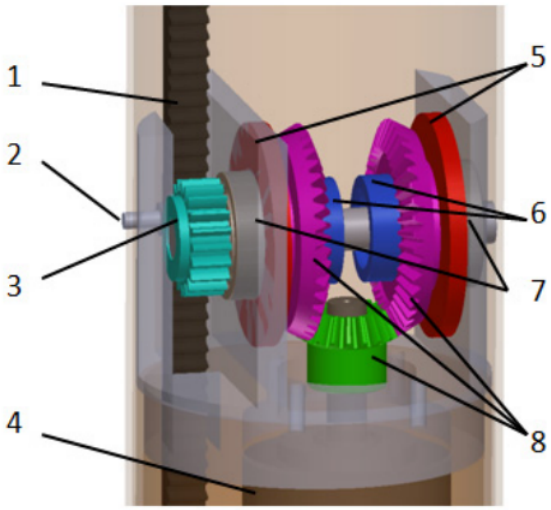

Figure 2.7: Rack-Pinion Energy Harvesting Shock Absorber (RPEHSA): 1) Rack; 2) Roller; 3) Pinion; 4) Planetary gears and motors; 5) Thrust bearings; 6) Roller clutches; 7) Ball bearings; 8) Bevel gears.

bevel gear from the shaft. This setup causes the shaft to drive the two larger bevel gears in opposite directions. Regardless of the rack's movement direction, the smaller bevel gear (and the generator) attached to it will always rotate in a single direction [67]. To define the mathematical model of RPEHSA, it is possible to refer to Fig.2.8 where its electric circuit is shown. From this figure, it can be noted that when the DC generator rotates, it generates a back electromotive force (back EMF) represented by the voltage

$$V_{emf} = K_e \frac{d\theta}{dt} \tag{2.13}$$

with K_e the electromotive force constant. This voltage is directly proportional to the rotational speed of the generator $\frac{d\theta}{dt}$. The electric current

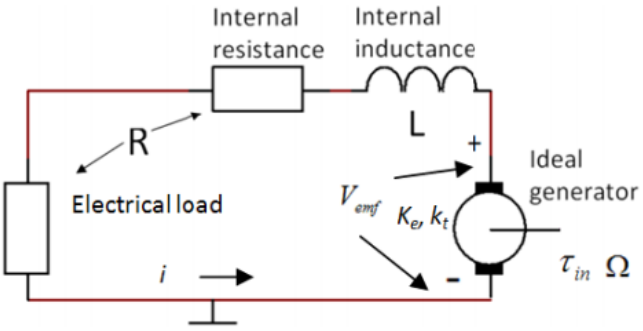

Figure 2.8: Electric circuit of the RP-EHSA

i of the motor will produce a torque

$$\tau_e = K_t i(t) \tag{2.14}$$

with K_t being the torque constant. By considering the generator's mechanical properties (with τ_{in} being the mechanical input of the generator), it is possible to write down the dynamic equation of the motion of the device

$$\tau_{in} - \tau_e = J_m \frac{d^2\theta}{dt^2} \tag{2.15}$$

with the electrical relation expressed by the following equation

$$V_{emf} + L\frac{di(t)}{dt} + Ri(t) = V(t) \tag{2.16}$$

where L denotes the internal inductance and R characterize the internal resistance. Finally, by putting together Eq.(2.13)-(2.16), it is possible to obtain the RPEHSA's mathematical characterization for each wheel:

$$K_e\frac{d\theta_i}{dt} + \frac{L}{K_t}\frac{d}{dt}(\tau_{in_i} - J_m\frac{d^2\theta_i}{dt^2}) + \frac{R}{K_t}(\tau_{in_i} - J_m\frac{d^2\theta_i}{dt^2}) = V_i(t)\ , i = 1, 2, ..., 4 \tag{2.17}$$

We obtain the expression of the electrical power as follows:

$$P_{ei}(t) = P_{di}(t) + P_{ci}(t) + P_{mi}(t), \quad i = 1, \ldots, 4 \tag{2.18}$$

where

- $P_{di}(t) = Ri_i^2(t)$ is the power lost;
- $P_{mi}(t) = K_e\frac{d\theta_i}{dt}i_i(t)$ the mechanical power acting on the i-th actuator;
- $P_{ci}(t) = L\frac{di_i(t)}{dt}i_i(t)$ the reactive electrical power stored in the inductance L.

More details can be found in [67]. Fig.2.9 depicts the RPEHSA actuator's configuration in Simulink.

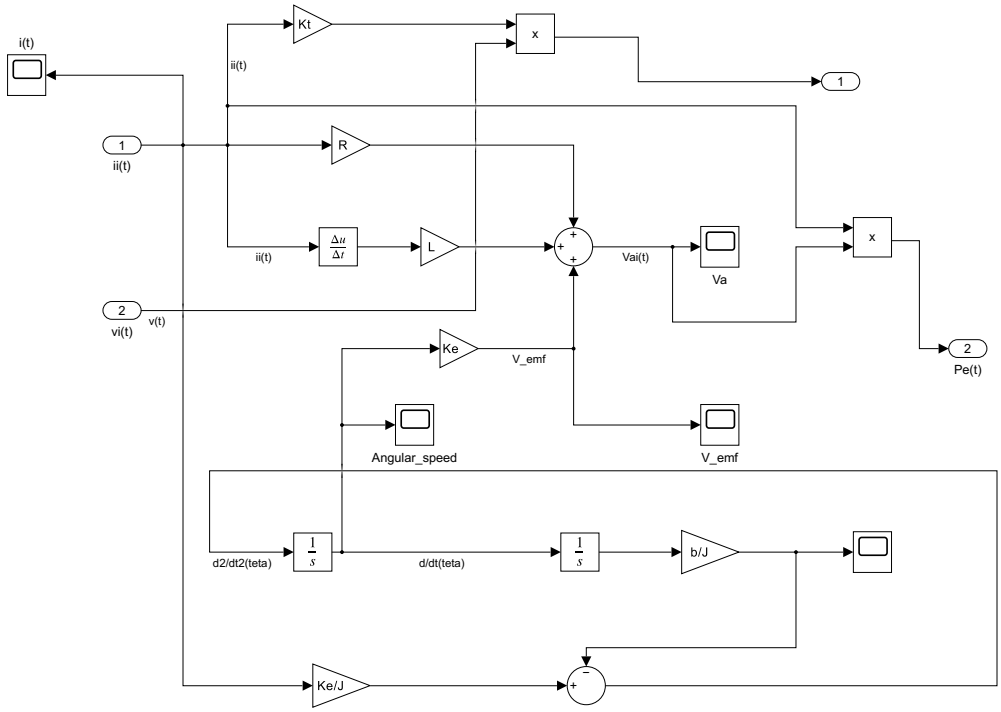

Figure 2.9: Simulink model of the RPEHSA

2.3.3 Synchronous Pulley Energy Harvesting Shock Absorber(SPEHSA)

Fig.2.10 presents the diagram and components of the SPEHSA system. The linear reciprocating movement, characterized by force F_1 and displacement x, is transformed into rotational motion through a synchronous pulley and belt system, producing torque τ_{pp} and angular displacement θ_{pp} [14]. This rotational movement is redirected along a perpendicular axis by two 1:1 ratio bevel gears, resulting in torque τ_{ec} and angular displacement θ_{ec} on the new shaft. Subsequently, a gearbox is used to amplify the revolutions entering the generator. It adjusts the torque and angular displacement from the bevel gears to τ_{mul} and θ_{mul}, serving as inputs for the generator. The system's mechanics also includes a synchronous belt with stiffness k_c, and the tensioner characterized by stiffness k_p and damping coefficient c_c. Belt tensions T_1, T_2, and T_3 are noted, along with the idler pulley's angular speed $\dot{\theta}_l$ and radius r_{pl}, and the generating pulley's radius r_{pp} [14]. Hereafter, the inertias of the freewheel, power pulley, bevel gears, multiplier, and generator are referred to as J_{pl}, J_{pp}, J_{ec}, J_{mul}, and J_{gen}, respectively. The efficiencies of the power pulley, bevel gears, and multiplier are represented by η_{pp}, η_{ec}, and η_{mul}, while k_{ec} and k_{mul} indicate the multiplication factors for the bevel gears and the planetary gearbox, respectively.

Additionally, as depicted in Fig.2.11, the mechanism converting linear

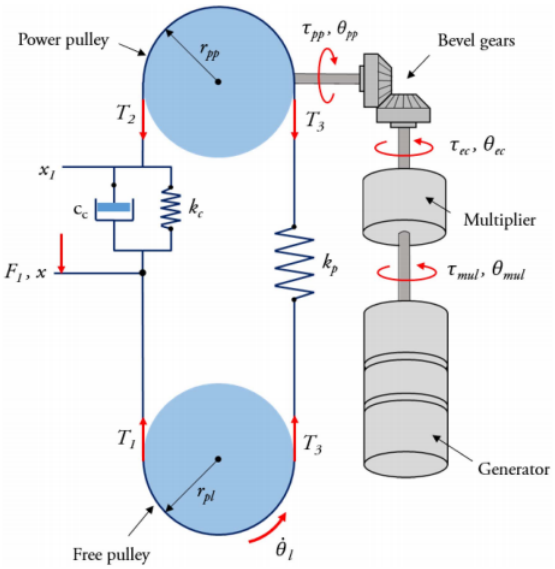

Figure 2.10: Diagram of the equivalent mechanical system of the SPEHSA

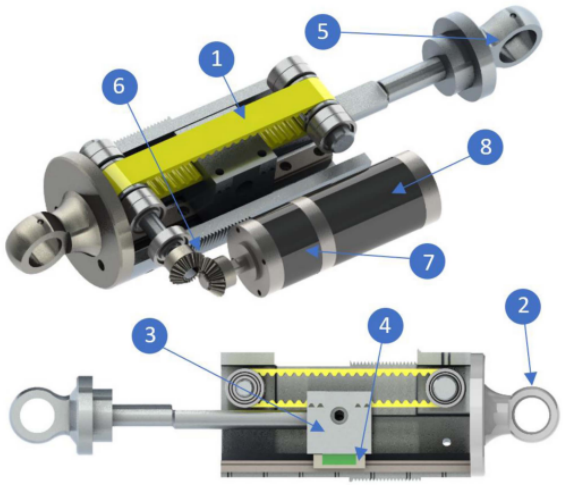

Figure 2.11: CAD design of the SPEHSA prototype with its electromechanical components

motion to rotary movement is integrated within the main cylinder of the shock absorber. This conversion is achieved through a system of pulleys and synchronous belts (1). A spherical joint facilitates the oscillatory movement of the suspension arm (2). The linear motion is transmitted to a piston connected to the crimping block of the strap (3), which is in turn linked to a linear ball guide system (4). This guide system is mounted on the suspension cylinder, which is attached to the lower suspension bracket via another spherical joint (5). The belt is positioned between two synchronous pulleys; the first rotates freely while the second transmits power. These pulleys are mounted on two shafts that rotate within a bearing system. The crankshaft transfers energy to a pair of bevel gears (6), which adjust the rotation axis by 90º. The gear system then delivers power to a planetary

gearbox (7), whose output powers the DC generator (8).

The mechanical system equations for SPEHSA shock absorbers are outlined in [14], [68]. In this respect, the relationship between the input force (F_1) and the tensions (T_1, T_2) is given by:

$$F_1 = T_2 - T_1 \tag{2.19}$$

The moments balance in the driven pulley is defined as

$$(T_1 - T_3)r_{pl} = J_{pl}\ddot{\theta}_{pl} \tag{2.20}$$

while the energy balance in the power pulley is

$$\eta_{pp}(T_2 - T_3)r_{pp}\ddot{\theta}_{pp} = J_{pp}\ddot{\theta}_{pp}\dot{\theta}_{pp} + \tau_{pp}\dot{\theta}_{pp} \tag{2.21}$$

The relationships between the angular velocity of the pulleys and the displacements is defined as:

$$\dot{\theta}_{pp} = \frac{x}{r_{pp}} \tag{2.22}$$

while the torques balance in the bevel gears is given by

$$\tau_{ec} = \frac{\eta_{ec}}{k_{ec}} * \tau_{pp} \tag{2.23}$$

where

$$\eta_{ec} = \frac{\tau_{ec}\dot{\theta}_{ec}}{\tau_{pp}\dot{\theta}_{pp}}, \qquad k_{ec} = \frac{\dot{\theta}_{ec}}{\dot{\theta}_{pp}} \tag{2.24}$$

The energy balance in the multiplier is given by

$$\eta_{mul}\tau_{ec}\dot{\theta}_{ec} = J_{mul}(\ddot{\theta}_{mul} - \ddot{\theta}_{ec})(\dot{\theta}_{mul} - \dot{\theta}_{ec}) + \tau_{gen}\dot{\theta}_{mul} \tag{2.25}$$

Moreover, knowing that

$$\theta_{mul} = \theta_{gen} \tag{2.26}$$

the dynamic behavior of the generator is modeled as

$$\tau_{mul} - \tau_r = J_{gen}\ddot{\theta}_{mul} \tag{2.27}$$

where

$$\tau_{mul} = J_{gen}\ddot{\theta}_{mul} + k_i i(t) \tag{2.28}$$

is the mechanical input to the generator (the torque from the multiplier) and

$$\tau_r = k_i i(t) \tag{2.29}$$

is the resistant torque generated by the current flowing in the generator. From the above equations, we can obtain the generator's torque

$$\tau_{gen} = \eta_{mul}\frac{\tau_{ec}}{k_{mul}} - J_{mul}(1 - \frac{1}{k_{mul}})^2\ddot{\theta}_{mul} \tag{2.30}$$

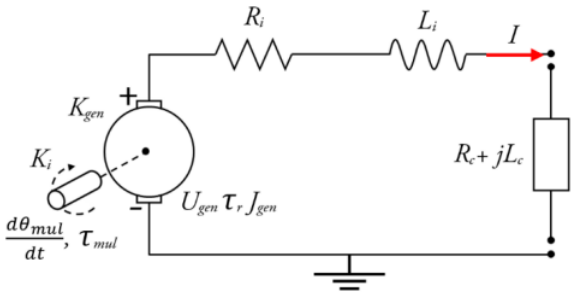

Figure 2.12: Simplified electric circuit diagram of the SPEHSA shock absorber.

where

$$k_{mul} = \frac{\dot{\theta}_{mul}}{\dot{\theta}_{ec}} \tag{2.31}$$

Together with the electrical system equations, Eqs. (2.19)-(2.31) allow one to write down the equivalent electromechanical system of the shock absorber [68]. In particular, by considering Fig.2.12, one can write the Kirchhoff equation for each actuator.

$$U_{gen_i} + L_i \frac{di_i(t)}{dt} + R_i i_i(t) = V_{a_i}(t) \quad i = 1, \ldots, 4 \tag{2.32}$$

with

$$U_{gen_i} = K_{gen} \frac{d\theta_{mul_i}}{dt} \tag{2.33}$$

in which K_{gen} represents the electromotive force constant. By using the above equalities, the Kirchhoff equation becomes

$$K_{gen} \frac{d\theta_{mul_i}}{dt} + \frac{L_i}{K_i} \frac{d}{dt}(\tau_{mul_i} - J_{gen} \ddot{\theta}_{mul_i}) + \frac{R_i}{K_i}(\tau_{mul_i} - J_{gen} \ddot{\theta}_{mul_i}) = V_{a_i} \tag{2.34}$$

By multiplying both sides of Eq.(2.32) by $i_i(t)$, we obtain

- The total electrical power: $P_{e_i} = V_{a_i}(t) * i_i(t) \quad i = 1, \ldots, 4$;
- The mechanical power: $P_{m_i} = K_{gen} \frac{d\theta_{mul_i}}{dt} * i_i(t) \quad i = 1, \ldots, 4$;
- The power dissipated by Joule effect: $P_{d_i} = R_i i_i(t)^2 \quad i = 1, \ldots, 4$;
- The reactive electrical power stored in the inductance: $P_{c_i} = L_i \frac{di_i(t)}{dt} * i_i(t) \quad i = 1, \ldots, 4$.

Fig.2.13 depicts the SPEHSA actuator's configuration in Simulink.

2.3.4 Inerter Pendulum Vibration Absorber Model

The IPVA is an electromagnetic rotary energy harvester that utilizes the inertial nonlinear effects of a pendulum vibration absorber. Fig.2.14 shows the IPVA internal structure and the related electric schematic. It features a pendulum mass and arm that convert linear motion into rotational motion

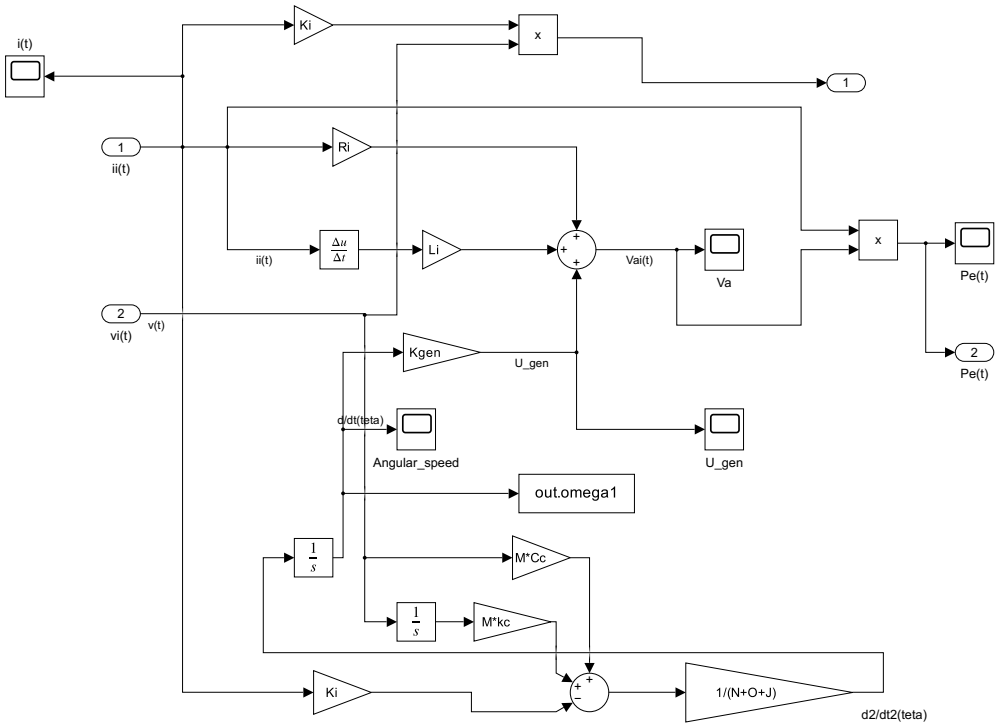

Figure 2.13: Simulink model of the SPEHSA

around a pivot point, allowing free oscillation. A nut and screw mechanism is included to adjust the pendulum's position and tension. An inerter element produces force proportional to relative acceleration, enhancing damping. The electromagnetic harvester converts mechanical energy into electrical energy through electromagnetic induction. In addition, a gearbox modifies rotational speed and torque for optimal energy harvesting [19].

The electrical power delivered by the i-th IPVA, $i = 1, \ldots, 4$, can be mathematically characterized with reference to Fig.2.14, which illustrates the IPVA electrical circuit. Note that the section of the circuit inside the dashed rectangle in Fig.2.14 is approximated using a variable resistance R_a.

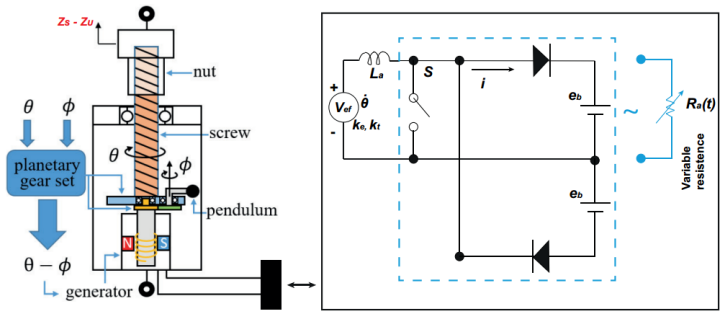

Figure 2.14: IPVA internal structure and IPVA electric schematic

A counter-electromotive force is generated and characterized by the

voltage

$$V_{ef} = K_e \frac{d\theta}{dt} \tag{2.35}$$

where K_e is the voltage constant. A twisting moment is produced by the current

$$\tau_e = K_t i(t) \tag{2.36}$$

where K_t is the mechanical constant of the torque. By applying the Newton second law for rotating masses we obtain the following result

$$\tau_m - \tau_e = J_m \frac{d^2\theta}{dt^2} \tag{2.37}$$

where J_m and τ_m are the inertia and the mechanical input of the generator. Finally, the Kirchhoff's law gives

$$V_{ef} + L_a \frac{di(t)}{dt} + R_a i(t) = V_a(t) \tag{2.38}$$

Both sides of Eq.(2.38) can be multiplied by the current to determine the electrical power [69]

$$P_{ei}(t) = P_{di}(t) + P_{ci}(t) + P_{mi}(t), \quad i = 1, \ldots, 4 \tag{2.39}$$

where

- $P_{di}(t) = R_a i_i^2(t)$ is the power lost;
- $P_{mi}(t) = K_e \omega_i i_i(t)$ the mechanical power acting on the i-th actuator, with ω_i the generator's angular velocity;
- $P_{ci}(t) = L_a \frac{di_i(t)}{dt} i_i(t)$ the reactive electrical power stored in the inductance L_a.

More details can be found in [19]. Fig.2.15 depicts the IPVA actuator's configuration in Simulink.

2.4 Power flow analysis

A comprehensive power flow analysis of the regenerative suspension system is performed to outline the key strategies for maximizing the harvestable electrical energy. The case study in this power flow analysis is the IPVA actuator but a similar analysis can be undertaken for each aformentioned actuator. The total energy of the suspension system is given by

$$E = K + V \tag{2.40}$$

where K indicates the kinetic energy of the masses, defined as

$$\begin{aligned} K = & \tfrac{1}{2} J_r \left(\dot{\varphi}_s - \dot{\theta}_s\right)^2 + \tfrac{1}{2} J_p \left(\dot{\varphi}_s + \dot{\theta}_s\right)^2 + \tfrac{1}{2} J \dot{\theta}_s^2 + \tfrac{1}{2} I_r \dot{\varphi}_s^2 \\ & + \tfrac{1}{2} I_p \dot{\theta}_s^2 + \tfrac{1}{2} m_s \dot{z}_s^2 + \tfrac{1}{2} m_{uf} (\dot{z}_{u1}^2 + \dot{z}_{u2}^2) + \tfrac{1}{2} m_{ur} (\dot{z}_{u3}^2 + \dot{z}_{u4}^2) \\ & + \tfrac{m}{2} \left[R_p^2 \dot{\theta}_s^2 + r^2 \left(\dot{\theta}_s + \dot{\varphi}_s\right)^2 + 2 R_p r cos(\varphi_s) \dot{\theta}_s \left(\dot{\theta}_s + \dot{\varphi}_s\right) \right] \end{aligned} \tag{2.41}$$

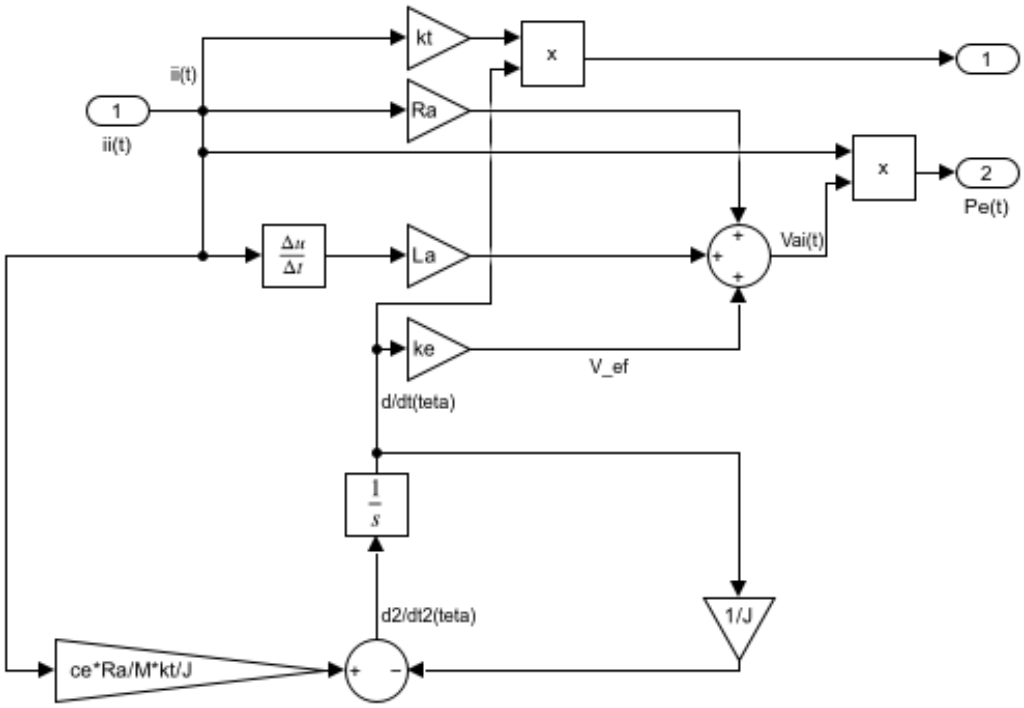

Figure 2.15: Simulink model of the IPVA

and V is the potential energy of the springs, defined as

$$\begin{aligned} V=&\frac{k_f}{2}\left[\left(z_{s_1}-z_{u_1}\right)^2+\left(z_{s_2}-z_{u_2}\right)^2\right]+\frac{k_r}{2}\left[\left(z_{s_3}-z_{u_3}\right)^2+\left(z_{s_4}-z_{u_4}\right)^2\right] \\ &+\frac{k_{tf}}{2}\left[\left(z_{u_1}-z_{r_1}\right)^2+\left(z_{u_2}-z_{r_2}\right)^2\right]+\frac{k_{tr}}{2}\left[\left(z_{u_3}-z_{r_3}\right)^2+\left(z_{u_4}-z_{r_4}\right)^2\right] \end{aligned} \tag{2.42}$$

Working under the assumption that the pendulum mass m is a point mass (rendering J_p, J_r, and J negligible) [19], the power can be derived as follows:

$$\begin{aligned} \dot{E}=&m_s\dot{z}_s\ddot{z}_s+m_{uf}(\dot{z}_{u_1}\ddot{z}_{u_1}+\dot{z}_{u_2}\ddot{z}_{u_2})+m_{ur}(\dot{z}_{u_3}\ddot{z}_{u_3}+\dot{z}_{u_4}\ddot{z}_{u_4}) \\ &+I_r\dot{\varphi}_s\ddot{\varphi}_s+I_p\dot{\theta}_s\ddot{\theta}_s \\ &+k_f\left[\left(z_{s_1}-z_{u_1}\right)\left(\dot{z}_{s_1}-\dot{z}_{u_1}\right)+\left(z_{s_2}-z_{u_2}\right)\left(\dot{z}_{s_2}-\dot{z}_{u_2}\right)\right] \\ &+k_r\left[\left(z_{s_3}-z_{u_3}\right)\left(\dot{z}_{s_3}-\dot{z}_{u_3}\right)+\left(z_{s_4}-z_{u_4}\right)\left(\dot{z}_{s_4}-\dot{z}_{u_4}\right)\right] \\ &+k_{tf}\left[\left(z_{u_1}-z_{r_1}\right)\left(\dot{z}_{u_1}-\dot{z}_{r_1}\right)+\left(z_{u_2}-z_{r_2}\right)\left(\dot{z}_{u_2}-\dot{z}_{r_2}\right)\right] \\ &+k_{tr}\left[\left(z_{u_3}-z_{r_3}\right)\left(\dot{z}_{u_3}-\dot{z}_{r_3}\right)+\left(z_{u_4}-z_{r_4}\right)\left(\dot{z}_{u_4}-\dot{z}_{r_4}\right)\right] \end{aligned} \tag{2.43}$$

By replacing $m_s\ddot{z}_s$, $I_r\ddot{\varphi}_s$ and $I_p\ddot{\theta}_s$ with their expressions in Eq.2.6, one

obtains:

$$\begin{aligned}\dot{E}=&k_f\left[(z_{s_1}-z_{u_1})\left(-t_f\dot{\varphi}_s-a\dot{\theta}_s-\dot{z}_s\right)\right]+k_f\left[(z_{s_2}-z_{u_2})\left(t_f\dot{\varphi}_s-a\dot{\theta}_s-\dot{z}_s\right)\right]\\&+k_r\left[(z_{s_3}-z_{u_3})\left(-t_r\dot{\varphi}_s+b\dot{\theta}_s-\dot{z}_s\right)\right]+k_r\left[(z_{s_4}-z_{u_4})\left(t_r\dot{\varphi}_s+b\dot{\theta}_s-\dot{z}_s\right)\right]\\&+f_1\left(t_f\dot{\varphi}_s+a\dot{\theta}_s+\dot{z}_s\right)+f_2\left(-t_f\dot{\varphi}_s+a\dot{\theta}_s+\dot{z}_s\right)\\&+f_3\left(t_r\dot{\varphi}_s-b\dot{\theta}_s+\dot{z}_s\right)+f_4\left(-t_r\dot{\varphi}_s-b\dot{\theta}_s+\dot{z}_s\right)-\textstyle\sum_{i=1}^{4}f_i\dot{z}_{u_i}\\&+k_f\left[(z_{s_1}-z_{u_1})\,\dot{z}_{s_1}+(z_{s_2}-z_{u_2})\,\dot{z}_{s_2}\right]\\&+k_r\left[(z_{s_3}-z_{u_3})\,\dot{z}_{s_3}+(z_{s_4}-z_{u_4})\,\dot{z}_{s_4}\right]\\&+k_{tf}\left[(z_{u_1}-z_{r_1})\,(-\dot{z}_{r_1})+(z_{u_2}-z_{r_2})\,(-\dot{z}_{r_2})\right]\\&+k_{tr}\left[(z_{u_3}-z_{r_3})\,(-\dot{z}_{r_3})+(z_{u_4}-z_{r_4})\,(-\dot{z}_{r_4})\right]\end{aligned}\tag{2.44}$$

From Eq.2.3, we have the expression of $\dot{z}_{s_i}, i = 1...4$ with respect to $\dot{\varphi}_s$, $\dot{\theta}_s$ and $\dot{z}_s$ which allows one to simplify the above equation. The total instantaneous power $\dot{E}$ can be expressed as

$$\begin{aligned}\dot{E}=&f_1(\dot{z}_{s_1}-\dot{z}_{u_1})+f_2(\dot{z}_{s_2}-\dot{z}_{u_2})+f_3(\dot{z}_{s_3}-\dot{z}_{u_3})+f_4(\dot{z}_{s_4}-\dot{z}_{u_4})\\&-k_{tf}\left[(z_{u_1}-z_{r_1})\,\dot{z}_{r_1}+(z_{u_2}-z_{r_2})\,\dot{z}_{r_2}\right]-k_{tr}\left[(z_{u_3}-z_{r_3})\,\dot{z}_{r_3}+(z_{u_4}-z_{r_4})\,\dot{z}_{r_4}\right]\end{aligned}\tag{2.45}$$

which can also be rewritten as

$$\dot{E} = P_s(t) + P_m(t) \tag{2.46}$$

where P_s is the power exchanged with the road (due to road irregularities z_{r_i}) and P_m is the mechanical power exchanged with the actuators.

In addition, the power contributions due to road profiles and actuators can be determined as:

$$P_s(t)=-k_{tf}\sum_{i=1}^{2}(z_{u_i}-z_{r_i})\dot{z}_{r_i}-k_{tr}\sum_{i=3}^{4}(z_{u_i}-z_{r_i})\dot{z}_{r_i};\quad P_m(t)=\sum_{i=1}^{4}f_i(\dot{z}_{s_i}-\dot{z}_{u_i})\tag{2.47}$$

Fig.2.16 depicts the power flow in the suspension system.

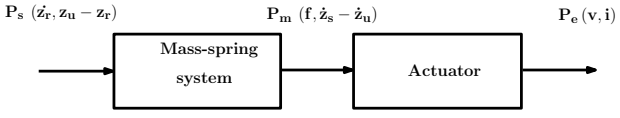

Figure 2.16: Power flow in the suspension system

The aforementioned expressions for P_m and P_s originate from the formulations in [17] and can be summarized as follows:

1. Ideally, one would aim to implement a control action that ensures both quantities to remain large and to have a consistent sign over time:

$$P_m(t) << 0; \quad P_s(t) >> 0; \qquad P_m(t) = -P_s(t) \tag{2.48}$$

Achieving this would mean $\dot{E}(t) = 0$, guaranteeing an ideal energy transfer from the road to the electrical batteries.

2. Because $f_i(t)$ can be directly manipulated, it becomes quite simple to make $P_m(t) < 0$ consistently sign-defined. However

$$\int_0^T |P_m(t)| \leq \int_0^T |P_s(t)| \tag{2.49}$$

This clearly limits the energy that can be harvested within any interval $[0, T]$ to the amount provided by the road. Consequently, it might be pointless to try maximizing P_m through control actions if P_s is low and there's no control degree of freedom to enhance it further.

3. It should be noted first that P_s is zero when the road profiles are perfectly flat ($\dot{z}_{r_i} = 0; i = 1, \ldots, 4$) or when the tire deflections are non-existent ($z_{u_i}(t) - z_{r_i}(t) = 0; i = 1, \ldots, 4$). Thus, high energy harvesting on flat roads is incompatible with good road handling performance. From a control viewpoint, note that P_s depends on the regulated variables z_{u_i}. Applying a suitable control law to make $P_s \gg 0$ would increase harvested energy regardless of P_m. In simple terms, making $P_s \gg 0$ would prevent the system's internal energy from flowing back to the road.

2.5 Conclusion

The aim of this chapter was to present the models of vehicle's regenerative suspension. Suspensions models and actuators have been studied. Power flow analysis has also been conducted to show the energy conversion. These models will be used in the design of the control strategies. The next chapter will focus on wave energy converter configuration.

Chapter 3

Wave energy converters configuration

III

Contents

3.1 Introduction 37
3.2 Point Absorber (PAs) classification 37
3.3 Power Take Off (PTO) mechanisms 39
3.4 PA dynamics modeling and wave forecasting models . 43
3.5 Conclusion 48

3.1 Introduction

This chapter is devoted to wave energy converters configuration. In particular, point absorber classification is presented in section 3.2. Power Take off mechanisms are detailed in section 3.3. Point Absorber dynamics and wave forecasting models are explained in section 3.4 and a conclusion ends the chapter in section 3.5.

3.2 Point Absorber (PAs) classification

In section 1.3.2, we introduced the different wave energy converters technologies. In this thesis, we will focus on point absorbers(PAs) because this kind of WECs presents the following advantages:

- The PA concept is one of the simplest concepts in system structures [70]. Thus, PAs may be easy to manufacture, reliable to operate and economical to maintain.

- The PA concept is one of the most broad-based concepts with intensive *Research&Development* (R&D) activities. More than half of the R&D activities of wave energy are based on the PA concept [71].

- PAs are appropriate for developing and testing novel ideas, including new modeling methods, novel PTO mechanisms and creative control strategies [72].

- PAs are applicable to a wide range of sea states in various deployment sites, and PAs sizes can be easily optimized to fit the wave climates of certain

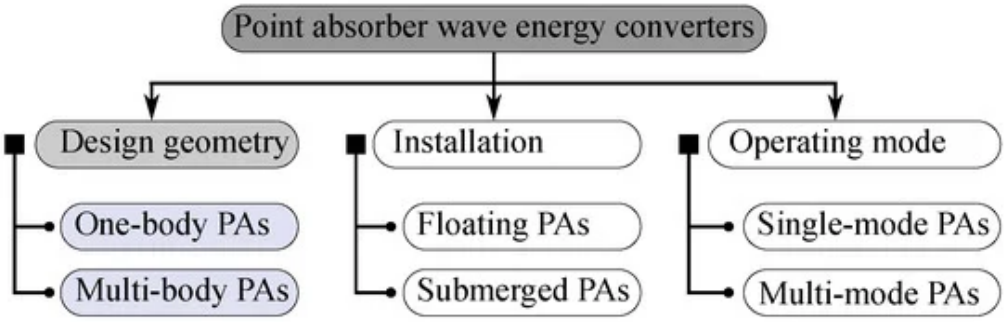

Figure 3.1: Classification of Point absorber wave energy converters according to the design geometry, manner of installation and operating mode

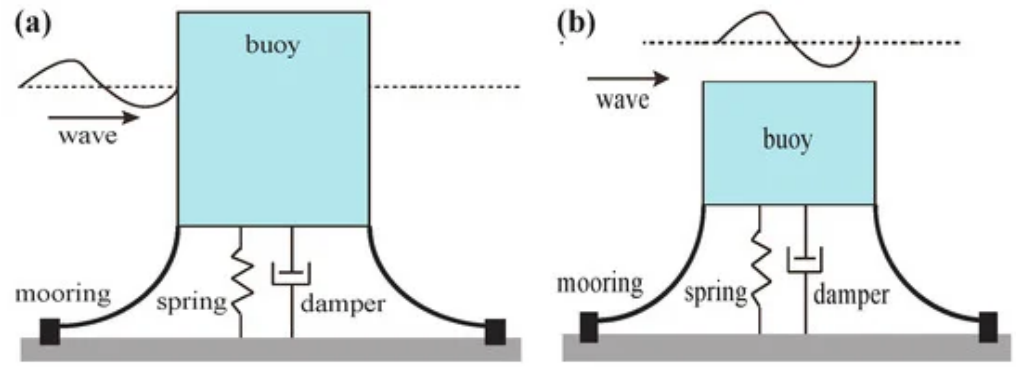

Figure 3.2: One body point absorber working principle: a)floating type b)submerged type

sites. In general, PAs are small and thus expected to be more economical [73].

As shown in Fig.3.1, PAs can be further classified as (1) one-body and multi-body PAs according to design geometry, (2) floating and submerged devices according to the deployment manner, and (3) single-DoF and multi-DoF prototypes according to the operating DoFs.

3.2.1 One-Body Point Absorbers

A one-body PA device is referenced to a fixed or absolute point (e.g. the sea bed). There are two main subtypes of one-body PAs: the floating one-body PAs and the submerged one-body PAs, as shown in Fig.3.2.

A floating PA comprises a floating body interacting with surface waves and a PTO unit referenced or anchored to the sea bed. The floating body oscillates under the excitation of waves, and its motion drives the PTO mechanism to generate electricity [73].

The working principle of a submerged one-body PA is similar to its floating counterpart, and the only difference lies in the status of the body, which can stand on or anchor to the sea bed with positive buoyancy.

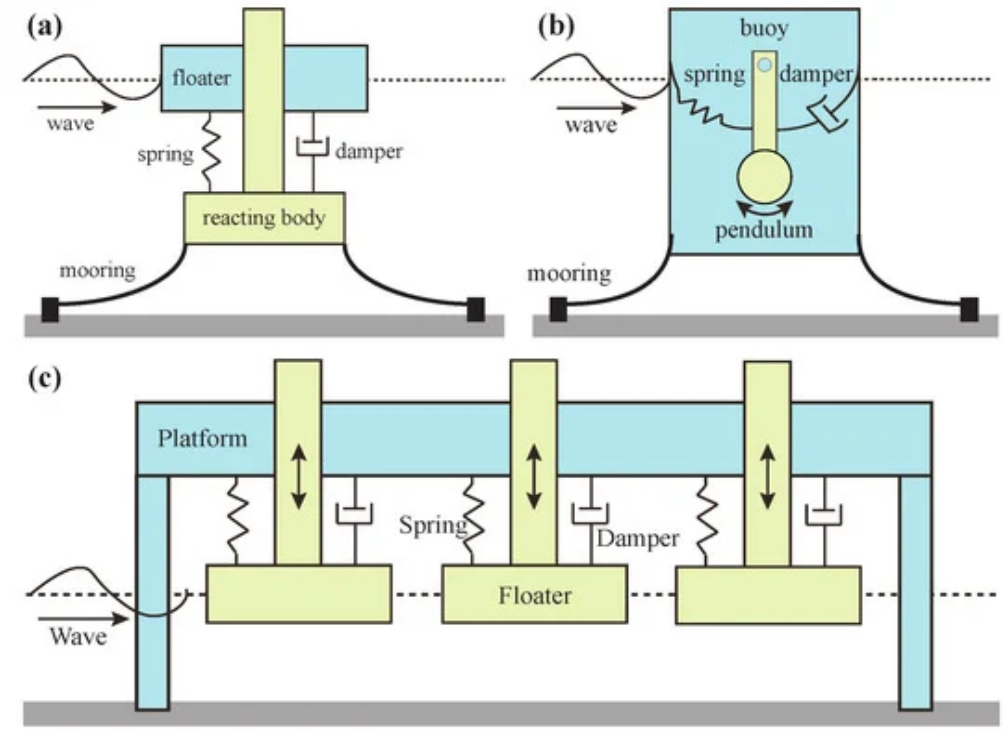

Figure 3.3: Multi body point absorber working principle: a)self-reacting b) self-contained c)multi-point PAs

3.2.2 Multi-Body Point Absorbers

Multi-body PAs can be further divided into two-body PAs and multi-point WECs, as shown in Fig.3.3. In general, a two-body PA is self-referenced, and its relative motion between the two bodies is used to drive the PTO system for electricity production. The multi-point absorber device is referred to a WEC consisting of several floaters referenced to a large offshore platform, and the floaters' motion drives the PTO units to generate electricity[73].

Two-body PAs can be further divided into self-reacting PAs and self-contained PAs. A self-reacting two-body device has a floater, mainly to interact with surface waves for wave power capture, and a reacting body, mainly to provide a reference point. The relative motion between these two bodies drives a PTO system to generate electricity. A self-contained PA only uses its hull to interact with surface waves and a pendulum structure to generate electricity.

For multi-point absorbers, a jacked-up structure or a semi-submersible platform is used to host several floating bodies to harvest wave power. The floating bodies can operate in heave, pitch and other modes.

3.3 Power Take Off (PTO) mechanisms

For a PA device, the PTO mechanism is one of the most important components which generates electrical power and, simultaneously, works as

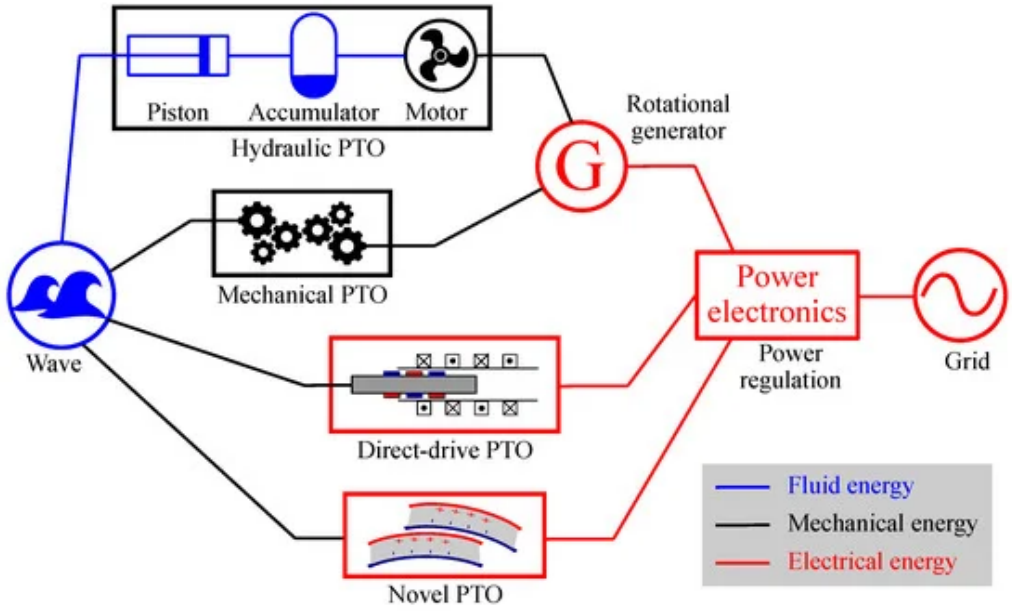

Figure 3.4: Four types of power take-off mechanisms used for point absorber wave energy converters.

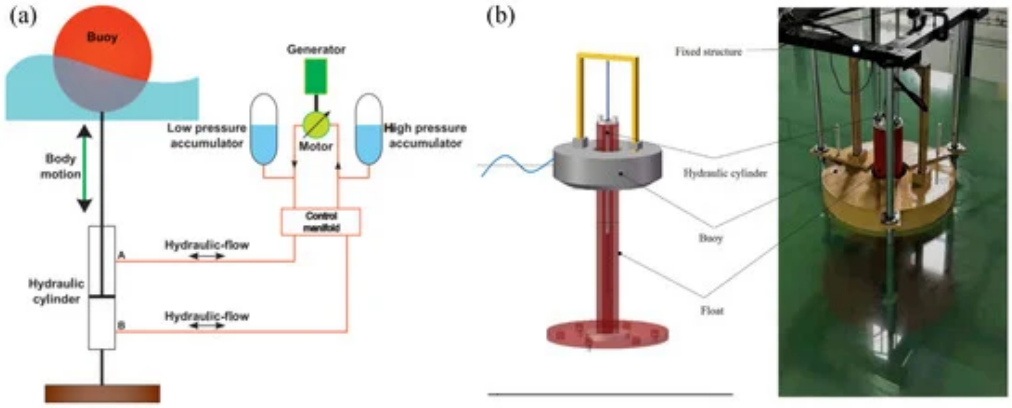

Figure 3.5: Hydraulic power take-off mechanisms with a schematic plot (a) and a hydraulic PTO system under tank testing (b).

an actuator for control implementation. PTO mechanisms can be classified as hydraulic PTOs [74], mechanical PTOs [75], direct-drive PTOs [76] and some novel PTOs [77], as shown in Fig.3.4.

3.3.1 Hydraulic PTO mechanisms

The hydraulic PTO mechanism is the most mature one for wave energy conversion, comprising hydraulic cylinders, pipes, regulating valves, accumulators, hydraulic motors, rotary generators, etc [73]. The working principle and a case study of hydraulic PTO systems are shown in Fig.3.5.

Compared with the other PTO mechanisms, the hydraulic PTO has shown some unique advantages: (1) The hydraulic technology is mature and

broadly used in the industrial sector[73]. (2) Hydraulic systems are capable of providing a large force at a low speed, and this feature suits the wave energy application scenarios well since wave force has a large amplitude and a low frequency. (3) Hydraulic PTO systems can be feasibly and flexibly used for a variety of PA devices regardless of the operating DoFs, installation manners or geometries. Finally, (4) with the assistance of the regulating valves and accumulators, a hydraulic PTO system is able to overcome the variation in wave power and provide stable electrical power.

However, the application of the hydraulic PTO mechanism for PA devices is constrained by some drawbacks: (1) Compared with the other PTO systems, the overall efficiency of a hydraulic PTO system is low, mainly due to the friction and viscous loss in the hydraulic system [78]. In addition, the energy conversion steps are complex. (2) In general, a hydraulic PTO system requires regular maintenance, and hence, the *Operation&Maintenance* (O&M) cost may be high, considering the harsh offshore environment. The hydraulic oil should be replaced after some thousand hours of operation; that is, the hydraulic oil should be refilled once or twice a year. Finally, (3) there exists a pollution risk as hydraulic oil is used. Thus, it is challenging to seal a hydraulic PTO system in an effective and efficient manner. From the viewpoint of control, the properties of hydraulic PTO systems are manifold. Some control strategies (e.g., latching, declutching and bang-bang control approaches) can be easily realized by hydraulic PTO systems[79]. On the other hand, the features of hydraulic PTO units also limit the control strategies in the discrete time domain. More hydraulic rams and accumulators are required to smooth out the control performance, which will increase the system complexity significantly.

3.3.2 Mechanical PTO mechanisms

Mechanical PTO systems are broadly used in PA devices. For instance, a rack and pinion mechanism is used by the CorPower device, belt drive mechanisms are used by the LifeSaver device and the CETO 6 device, and a ball screw mechanism is used by the *Ocean Power Technologies* (OPT) PowerBuoy device in order to convert reciprocating motion to rotation for driving rotary generators[79]. To demonstrate the working principle of the mechanical PTO mechanism, a ball screw unit is shown in Fig.3.6.

Compared with the other PTO mechanisms, the mechanical PTO mechanism shows some technical advantages: (1) The mechanical transmission is mature and broadly applied in industrial applications. (2) In general, the energy loss of a mechanical PTO system is low, and the efficiency of a mechanical transmission system is high. For instance, a rack and pinion mechanism can achieve an efficiency up to 97% [73]. Lastly, (3) a variety of mechanical transmission mechanisms provides flexible means to regulate the reciprocating motion of WEC bodies into unidirectional rotation, which is more friendly for driving conventional rotary generators. However, there are still some drawbacks that hinder the commercial application of WECs

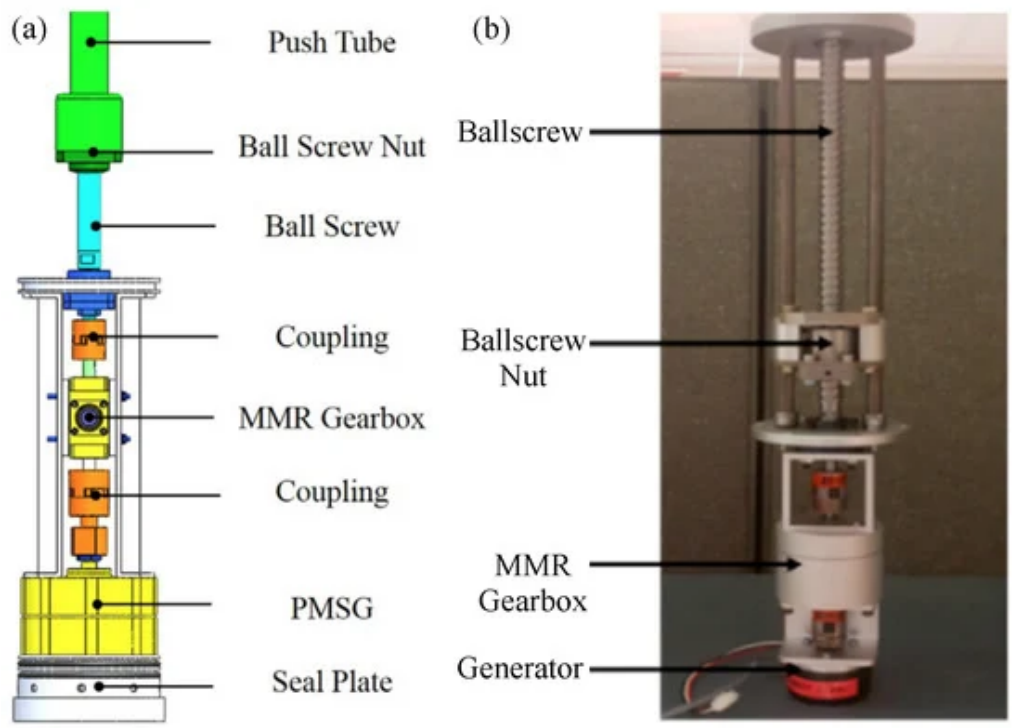

Figure 3.6: Ball screw PTO

with mechanical PTO systems: (i) The mechanical transmission systems suffer from a fatigue problem, and they are prone to structure failures. Their reliability and lifespan should be improved. (2) In general, a mechanical PTO system itself is complex. Considering the dynamics of a mechanical PTO system, the complexity of a PA device will be critically high. (3) The mechanical PTO systems suffer from various nonlinear dynamics (friction, backslashing, etc.). Finally, (4) regular O&M work is required (e.g., lubrication) to keep the mechanical PTO systems operating under an ideal condition.

3.3.3 Direct drive PTO mechanisms

Direct-drive PTO systems have been successfully used for wind turbines, and some experience is portable for WEC devices. The *Permanent Magnet Linear Generator* (PMLG) concept was proposed in [80] to produce electrical power from sea waves. A PMLG, as shown in Fig. 3.7, was designed and tested in [81] as PTO mechanism for the *Archimedes Wave Swing* (AWS) device and the Seabased device. A variety of PMLGs was compared in [82]. In addition, a rotary generator is used as the direct-drive PTO system for the Columbia Power PA device [83].

Compared with the other PTO systems, the main advantages of the direct-drive PTO units are as follows: (1) The direct-drive mechanism can provide high efficiency, since it can convert the buoy motion into electricity directly with only two energy conversion stages [84]. (2) The reliability

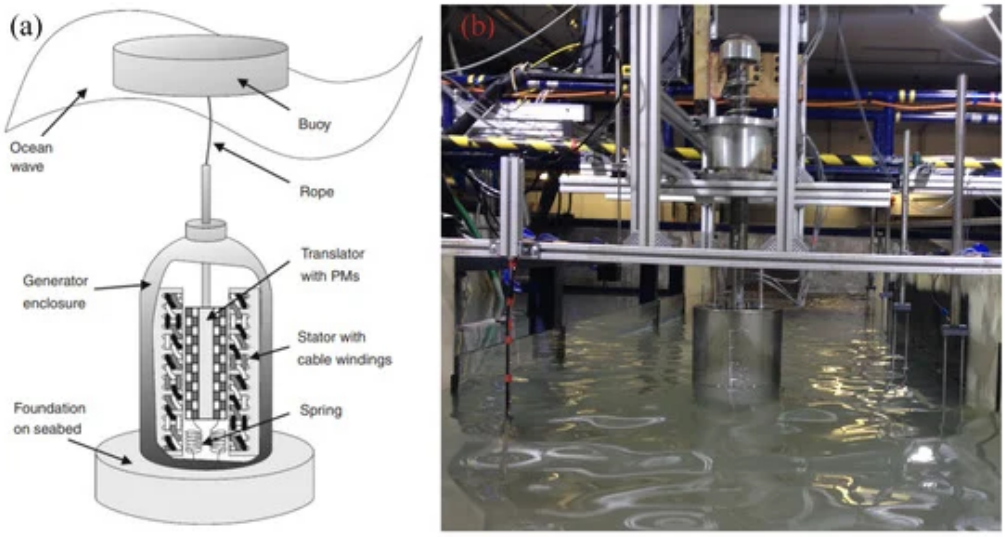

Figure 3.7: Direct Drive PTO

is expected to be high since a direct-drive PTO unit compromises fewer components. (3) The maintenance requirement is low, mainly due to its simple topological structure. (4) The direct-drive PTO system is feasible for control via electrical approaches, which have been generally used in the electricity industry[85]. Lastly, (5) direct-drive PTO systems can operate reliably, even when the peak-to-average power ratio is up to 20 [86].

On the other hand, the drawbacks of direct-drive PTO systems are as follows: (1) The power or force density is low, and hence, the PTO volume and weight should be large enough to achieve a certain power rating [71], and (2) the manufacturing cost of a direct-drive PTO system is relatively high compared with the hydraulic PTO systems due to the high cost of the permanent magnets [87]. The permanent magnet materials have advanced significantly, resulting in a larger force density and a lower cost[88]. However, the force density and manufacturing cost of direct-drive PTO systems are still relatively higher than those of hydraulic PTO systems.

3.4 PA dynamics modeling and wave forecasting models

3.4.1 PA dynamic modeling

Fig.3.8 recalls the working principle of a point absorber. z_w is the wave level; The buoy is floating on the sea surface, whose heave position is z_v. Below the buoy, is a hydraulic cylinder fixed to the seabed. The persistent wave excitation force drives the buoy, which provides relative motion between the piston fixed to the buoy and the cylinder fixed to the seabed. The kinetic energy of the relative motion can be captured by a power take-off (PTO) mechanism to generate electricity. The piston moves together with the buoy

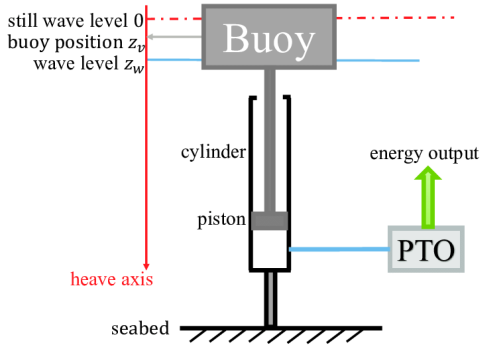

Figure 3.8: Schematic diagram of the working principle of a point absorber

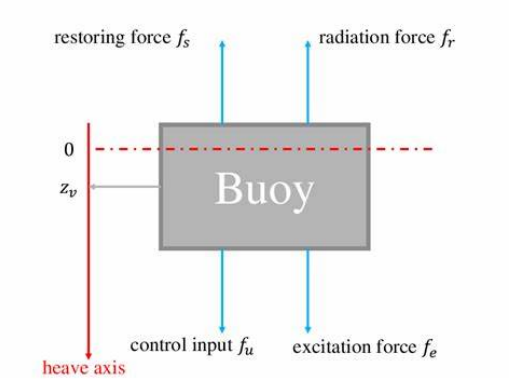

Figure 3.9: Dynamic diagram of a point absorber

at a heave velocity $\dot{z}_v$. The potential power that can be captured by the PTO at time t is

$$P(t) = -f_u(t)v(t) \tag{3.1}$$

and the energy absorbed in a time interval $[T_1, T_2]$ can be expressed by

$$E = \int_{T_1}^{T_2} -f_u(t)v(t)dt \tag{3.2}$$

The dynamic modeling of the point absorber is illustrated in Fig.3.9. By applying Newton's second law, the dynamics can be modeled by

$$m_s\ddot{z}_v(t) = f_e - f_s - f_r + f_u \tag{3.3}$$

where m_s is the mass of the buoy with the attached piston; f_s is the restoring force that can be computed by

$$f_s = k_s z_v \tag{3.4}$$

with the hydro-stiffness coefficient given by $k_s = \rho g S$. Here ρ is the water density; g is the acceleration of gravity; S is the cross sectional area of the floating buoy. f_u is the force provided by PTO and is treated as the control

input. f_r and f_e are the frequency dependent radiation force and excitation force, respectively. The radiation force is determined by

$$f_r = m_\infty \ddot{z}_v + f_R \tag{3.5}$$

where m_∞ is called frequency-independent added mass; f_R is the noncausal convolutional part of the radiation force and can be computed by

$$f_R = \int_{-\infty}^{\infty} h_r(\tau)\dot{z}_v(t-\tau)d\tau \tag{3.6}$$

where the kernel of the radiation force h_r can be approximated by a causal state-space representation [20]

$$\begin{cases} \dot{x}_r &= A_r x_r + B_r \dot{z}_v \\ f_R &\approx C_r x_r \end{cases} \tag{3.7}$$

where $D_r(s) \sim (A_r,\ B_r,\ C_r,\ 0)$ and x_r are the state-space realization and the associated state respectively. Following the similar route as the above derivation, the persistent wave excitation force can be modeled by

$$f_e = \int_{-\infty}^{\infty} h_e(t-t_c-\tau)z_w(\tau)d\tau \tag{3.8}$$

with h_e being the excitation kernel, which can be approximated by the following state-space formulation

$$\begin{cases} \dot{x}_e &= A_e x_e + B_e z_w \\ f_e &= C_e \tilde{x}_e \end{cases} \tag{3.9}$$

with $\tilde{x}_e = x_e(t+t_c)$ with t_c as a positive constant non-causal time shift, $D_e(s) \sim (A_e,\ B_e,\ C_e,\ 0)$ and x_e are the state-space realization and the associated state respectively.

3.4.2 Wave forecasting models

Real wave data are gathered off the coast of UK (Latitude 54.228027, Longitude -10.149796) on the 13th October 2024 [89]. Among all waves scenarios that will be used for simulations in this thesis, let us introduce the two main wave signals. The first wave has a significant wave height of $H_s = 0.5m$ and a peak period of $T_p = 15.38s$ and it will be used on a small WEC. The second wave signal has a significant wave height and a peak period of $H_s = 2.1m$ and $T_p = 10.53s$ respectively and it will be used on a big WEC. These data satisfy the *Joint North Sea Wave Analysis Project* (JONSWAP) spectrum as depicted in Fig.3.10 for the first wave signal. The timeseries $\eta(t)$ are derived from the JONSWAP spectrum with application of a random phase through a wave forecasting model [28].

The most straightforward forecasting model is a cyclical model, where the wave elevation is expressed as a superposition of a number M of linear harmonic components.

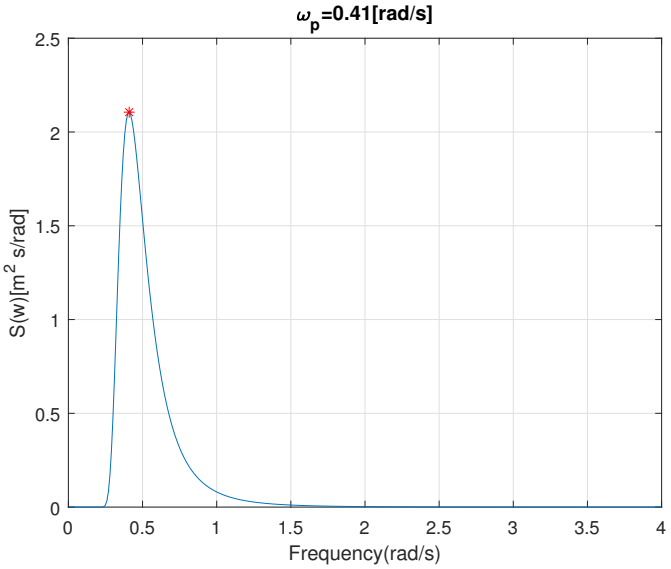

Figure 3.10: Jonswap spectrum

$$W(k) = \sum_{i=1}^{M} \alpha_i cos(\omega_i k) + \beta_i sin(\omega_i k) + \tau(k) \tag{3.10}$$

An error term τ has been introduced as a Gaussian white noise, while the phase and amplitude information for each harmonic component is contained in the parameters α_i and β_i. This model is completely characterized by the parameters α_i, β_i and by the frequencies ω_i. The choice of the frequencies is a crucial one. In [29], it was pointed out how, while the range of frequencies is easy to determine, the distribution inside this range is more problematic. A robust choice would be a constant spacing over all the range, with the spacing as small as possible in order to give an accurate coverage of the spectrum. Alternative nonhomogeneous solutions may be considered, for example, with the frequencies more densely distributed around the energy peaks. Such more efficient solutions, however, would be unreliable, in the context of a model with fixed frequencies, due to the time variations of the energy distribution in wave spectra (which can be verified through the wavelet transform [30]).

A methodology could be a set of regularly spaced frequencies. The smaller the $d\omega$ the more the complexity of the model, but even the greater are the numerical problems that can be encountered in the estimation procedure. A good value for it has been found to be $d\omega = 0.01 rad/s$ [31]. Once the frequencies are determined, a model for the amplitude variations has to be chosen. The cyclical structural model proposed by Harvey [9] is adopted

$$W(k) = \sum_{i=1}^{M} \psi_i(k) + \tau(k) \tag{3.11}$$

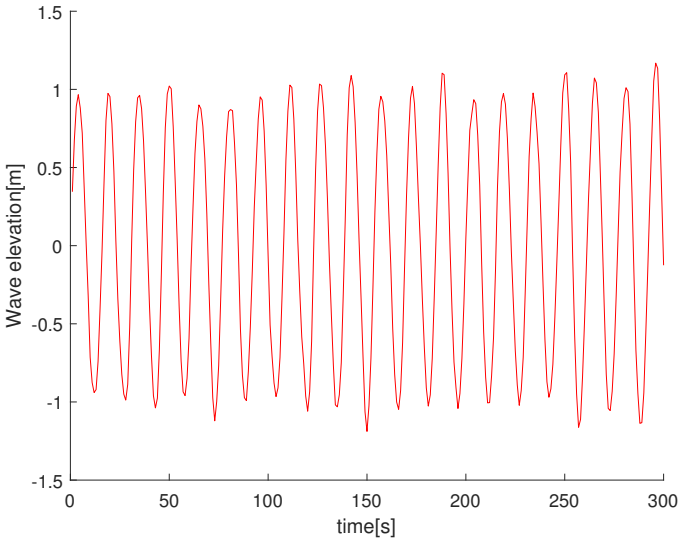

Figure 3.11: Small wave signal

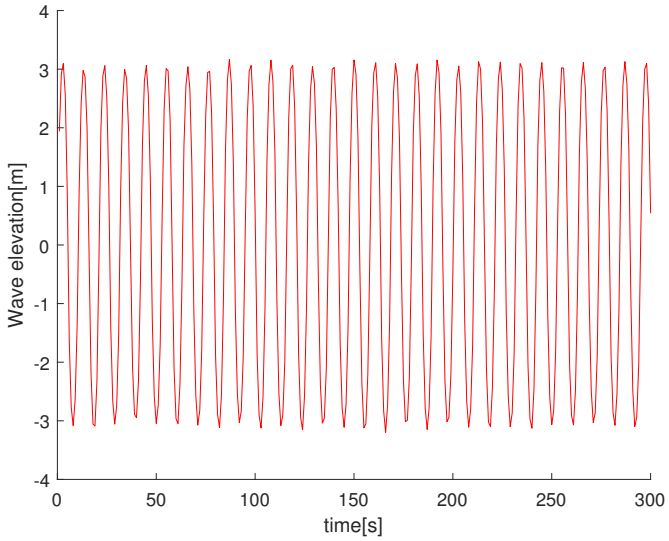

Figure 3.12: Big wave signal

and

$$\begin{bmatrix} \psi_i(k+1) \\ \psi_i^*(k+1) \end{bmatrix} = \begin{bmatrix} cos(\omega_i T_s) & sin(\omega_i T_s) \\ -sin(\omega_i T_s) & cos(\omega_i T_s) \end{bmatrix} \begin{bmatrix} \psi_i(k) \\ \psi_i^*(k) \end{bmatrix} + \begin{bmatrix} \omega_i(k) \\ \omega_i^*(k) \end{bmatrix}, i = 1...M \tag{3.12}$$

where T_s is the sampling time, vectors $[\psi_i(k), \psi_i^*(k)]^T$ model the M cyclical components. The Gaussian white disturbance $[\omega_i(k), \omega_i^*(k)]^T$ models the amplitude and phases variation. It is good to remind that the Harvey's model is initialized with the real data aformentioned. In [9], an alternative stochastic model for the amplitudes $\alpha_i(k)$ and $\beta_i(k)$ is proposed: the *Dynamic Harmonic Regression* (DHR) model. However, the higher complexity required (four state variables for each harmonic against two of the Harvey's model)

is not justified by an improvement of the modeling ability, so the DHR model will not be considered in this thesis. More details about the Harvey's forecasting model can be found in [31]-[9]. It is important to notice that this model incorporates error predictions in its scheme (the error term $\tau(k)$). In other words the controllers designed for WECs in this thesis, are developed under realistic prediction inaccuracies.

One can see the timeseries of the two waves $W(t)$ obtained in Fig. 3.11 and Fig. 3.12.

3.5 Conclusion

In this chapter, we have described the point absorber type of WEC and some wave forecasting models. In the next chapter, we will introduce the first control strategies we designed for regenerative suspension systems.

Chapter 4

H_∞ and H_2 MIPC dynamic output feedback control

Contents

4.1 Introduction 50
4.2 Control specifications 50
4.3 State space realization 52
4.4 H_∞ and H_2 dynamic output feedback control LMI design 55
4.5 Results and discussion 57
4.6 Conclusion 71

4.1 Introduction

This chapter is devoted to the design of H_∞ and H_2 MIPC dynamic output feedback control strategies and to the comparison of the most used actuators in vehicles regenerative suspensions. In other words, the goal is to determine the best actuator for vehicles regenerative suspensions and the best control law among the two aforementioned ones that satisfy the control specifications. Section 4.2 depicts these control specifications, section 4.3 introduces the state space realization, section 4.4 depicts the control laws design, section 4.5 presents the simulations results then the chapter's conclusion is in section 4.6.

4.2 Control specifications

In classical passive and active suspension systems, traditional control involves finding an appropriate balance between ride comfort and road handling requirements. To eliminate subjectivity in ride comfort specifications, the ISO-2631 standard introduces an index known as the Ride Index (RI) [90], defined as follows:

$$RI = \sqrt{a_{wx}^2 + a_{wy}^2 + a_{wz}^2} \tag{4.1}$$

$$a_{i,RMS} = \sqrt{\frac{1}{T}\int_0^T a_{wi}^2(t)dt} \quad i = x, y, z \tag{4.2}$$

where a_{wi} represents the acceleration along the i-th axis, weighted by the following filter:

$$W_k(s) = \frac{81.89s^3 + 796.6s^2 + 1937s + 0.14}{s^4 + 80s^3 + 2264s^2 + 7172s + 21196} \tag{4.3}$$

Better vibration attenuation is reflected by lower Ride Index values. Road handling and suspension stroke are another crucial objectives, closely related to the safety of both the vehicle and its passengers. This aspect becomes especially important in sports and racing cars. Road handling can typically be represented by the tire deflection $z_u - z_r$ and suspension stroke by $z_s - z_u$ which need to be minimized according to certain norms.

In addition, a regenerative suspension system must be capable of harvesting energy from road unevenness. This requirement is achieved by applying the MIPC(Maximum Induced Power Control) strategy [69]. In this strategy, the power flowing from the road P_s is made sign-defined and as large as possible. According to section 2.4, achieving this condition involves enforcing the following conditions on tire deflections within a closed-loop system:

$$z_{u_i}(t) - z_{r_i}(t) = -\alpha \dot{z}_{r_i}(t), \quad i = 1, \ldots, 4 \tag{4.4}$$

with $\alpha > 0$ a design parameter. Provided that all these conditions are fulfilled at every instant, the power P_s would be determined based on Eq.2.47.

$$\begin{aligned} P_s &= -\left[k_f \sum_{i=1}^{2} \left(z_{u_i} - z_{r_i}\right) \dot{z}_{r_i} + k_{tr} \sum_{i=3}^{4} \left(z_{u_i} - z_{r_i}\right) \dot{z}_{r_i}\right] \\ &= \alpha k_{tf} \left(\dot{z}_{r_1}^2(t) + \dot{z}_{r_2}^2(t)\right) + \alpha k_{tr} \left(\dot{z}_{r_3}^2(t) + \dot{z}_{r_4}^2(t)\right) \end{aligned} \tag{4.5}$$

In this manner, theoretically, $P_s(t)$ would always be positive (ensuring power consistently flows from the road to the suspension system) and large by selecting a suitably large α. Nonetheless, it is worth mentioning that making tire deflections large conflicts with good road handling performance. Moreover, achieving high levels of harvested energy requires high armature currents, which increase electrical losses in the actuators. Therefore, depending on the application, a suitable trade-off among these conflicting control specifications must be addressed in designing the MIPC controller, which can naturally be approached as a multi-objective optimal control problem. Indeed, conditions (4.4) can be recast as the following model reference errors $z_{pi}(t)$ that should be minimized

$$z_{p_i}(t) = z_{u_i}(t) - z_{r_i}(t) + \alpha(s)\dot{z}_{r_i}(t), \quad i = 1, \ldots, 4 \tag{4.6}$$

with

$$\alpha(s) = \frac{K_\alpha}{s\tau + 1} \tag{4.7}$$

where the gain K_α and the time constant τ are design parameters.

4.3 State space realization

To address the requirement of using the derivatives $\dot{z}_{ri}$ instead of z_{ri} as exogenous signals for causally realizing z_{pi} in Eq.(4.6), an alternative state-space representation of the full-car model can be used. The following state-space representation results

$$\begin{cases} \dot{x}(t) &= Ax(t) + Bu(t) + E\dot{z}_r(t) \\ y(t) &= C_y x(t) + D_{yu}u(t) + F_{yw}\dot{z}_r(t) \\ z(t) &= C_z x(t) + D_{zu}u(t) + F_{zw}\dot{z}_r(t) \end{cases} \tag{4.8}$$

where the matrices A, B, C_y, C_z, D_{yu}, D_{zu}, E, F_{yw}, F_{zw} are of appropriate dimensions, $x(t)$ is the system state, $u(t)$ the input, $y(t)$ the measured output, $\dot{z}_r(t)$ the exogenous input and $z(t)$ the performance output corresponding to the following system vectors

$$x = \begin{bmatrix} z_{s_1} - z_{u_1} \\ z_{s_2} - z_{u_2} \\ z_{s_3} - z_{u_3} \\ z_{s_4} - z_{u_4} \\ \dot{\varphi}_s \\ \dot{\theta}_s \\ \dot{z}_s \\ z_{u_1} - z_{r_1} \\ z_{u_2} - z_{r_2} \\ z_{u_3} - z_{r_3} \\ z_{u_4} - z_{r_4} \\ \dot{z}_{u_1} \\ \dot{z}_{u_2} \\ \dot{z}_{u_3} \\ \dot{z}_{u_4} \end{bmatrix} \quad u = \begin{bmatrix} i_1 \\ i_2 \\ i_3 \\ i_4 \end{bmatrix} \quad \dot{z}_r = \begin{bmatrix} \dot{z}_{r_1} \\ \dot{z}_{r_2} \\ \dot{z}_{r_3} \\ \dot{z}_{r_4} \end{bmatrix} \tag{4.9}$$

$$y = \left[(z_{s_1} - z_{u_1}) \;\; (z_{s_2} - z_{u_2}) \;\; (z_{s_3} - z_{u_3}) \;\; (z_{s_4} - z_{u_4}) \;\; \ddot{z}_{s_1} \;\; \ddot{z}_{s_2} \;\; \ddot{z}_{s_3} \;\; \ddot{z}_{s_4}\right]^T \tag{4.10}$$

$$z = \left[\ddot{z}_{s_1} \;\; \ddot{z}_{s_2} \;\; \ddot{z}_{s_3} \;\; \ddot{z}_{s_4} \;\; i_1 \;\; i_2 \;\; i_3 \;\; i_4 \;\; z_{p_1} \;\; z_{p_2} \;\; z_{p_3} \;\; z_{p_4}\right]^T \tag{4.11}$$

In particular $z(t)$ collects:

- the accelerations $\ddot{z}_{s_i}$, $i = 1, \ldots, 4$, accounting for the drive comfort requirements;
- the control actions i_i, $i = 1, \ldots, 4$, used to moderate the control energy so as to mitigate the electrical losses;
- the four variables z_{p_i}, $i = 1, \ldots, 4$, defined in (4.6) related to the energy harvesting specifications.

4.3.1 Open cycle analysis and structural properties

The analysis of the internal stability of the system is carried out by studying the eigenvalues of A. We know that if all the eigenvalues of the matrix A have negative real part then the system is asymptotically stable.

$$\lambda = \begin{bmatrix} 0 \\ 0 + 6.20628i \\ 0 - 6.20628i \\ 0 + 9.34256i \\ 0 - 9.34256i \\ 0 + 8.37592i \\ 0 - 8.37592i \\ 0 + 59.0777i \\ 0 - 59.0777i \\ 0 + 58.9937i \\ 0 - 58.9937i \\ 0 + 58.0359i \\ 0 - 58.0359i \\ 0 + 58.1034i \\ 0 - 58.1034i \end{bmatrix} \tag{4.12}$$

As we can see in Eq.4.12, the system is stable, not asymptotically stable given the presence of the zero eigenvalues. It expresses the existence of a geometric constraint between the state variables. We need to check the properties of reachability, controllability and observability. The reachability problem is to **"find the set of all the final states** $x(t_1)$ **reachable starting from a given initial state** $x(t_0)$**."** The controllability problem is **"to find the set of all the initial states** $x(t_0)$ **controllable to a given final state** $x(t_1)$**".** Let R be the reachability matrix.

$$R = \begin{bmatrix} B & AB & A^2B & ... & A^{n-1}B \end{bmatrix} \tag{4.13}$$

A system is said to be reachable if the rank of the matrix R is equal to n (the order of the system). In our case, we have "complete reachability" because $rank(R) = 15$. Furthermore, since the model is continuous time, we will also obtain "complete controllability". The reachability always implies the controllability.

A system is said to be completely observable if and only if each state, not null, gives rise to a free exit which is not identically null, that is, when the observability matrix has maximum rank.

The observability matrix is defined as:

$$O = \begin{bmatrix} C_y \\ C_yA \\ C_yA^2 \\ ... \\ C_yA^{n-1} \end{bmatrix} \tag{4.14}$$

Obtaining $rank(O) = 15$, we have "complete observability".

4.3.2 Frequency shaping of the state space realization

A common approach in designing optimal control laws involves shaping control objectives in the frequency domain to either penalize or enhance performance within specific frequency bands of interest. This can be done by filtering the control signals. Denoting with $W_{a_i}(s),\ i = 1, \ldots, 4$ the filter shaping the vertical acceleration of the body corner $\ddot{z}_{s_i}(t)$, with $W_{u_i}(s)$ the filter related to the current $i_i(t)$ and with

$$W_z(s) = diag\left\{W_a(s), W_u(s), I_4\right\} \tag{4.15}$$

the multivariable filter related to the objective vector $z(t)$, it is possible to introduce the following aggregate filters

$$W_a(s) = diag\left\{W_{a_1}(s), W_{a_2}(s), W_{a_3}(s), W_{a_4}(s)\right\}, \tag{4.16}$$

$$W_u(s) = diag\left\{W_{u_1}(s), W_{u_2}(s), W_{u_3}(s), W_{u_4}(s)\right\} \tag{4.17}$$

and for simplicity they are assumed identical

$$\begin{aligned} W_{a1}(s) &= W_{a2}(s) = W_{a3}(s) = W_{a4}(s) \\ W_{u1}(s) &= W_{u2}(s) = W_{u3}(s) = W_{u4}(s) \end{aligned} \tag{4.18}$$

Note that, these filters can be selected according to the characteristics reported in the *ISO-2636 Mechanical vibration and shock* standard [90]. Furthermore, the energy of the road profiles is optionally shaped by a suitable bank of filters as well:

$$W_d(s) = diag\left\{W_{d_1}(s), W_{d_2}(s), W_{d_3}(s), W_{d_4}(s)\right\} \tag{4.19}$$

$$W_{d1}(s) = W_{d2}(s) = W_{d3}(s) = W_{d4}(s) \tag{4.20}$$

Denoting by $(A_{wd}, B_{wd}, C_{wd}, D_{wd})$ and $(A_{wz}, B_{wz}, C_{wz}, D_{wz})$ the state representations of the filters $W_d(s)$ and $W_z(s)$, with x_d and x_z the corresponding states, it is possible to introduce the following augmented state

$$x_g = \begin{bmatrix} x^T & x_z^T & x_d^T \end{bmatrix}^T \tag{4.21}$$

that allows one to define the extended state-space representation

$$\left\{\begin{array}{rcl} \dot{x}_g(t) &=& A_g x_g(t) + B_{gu} u(t) + B_{gw} \dot{z}_r(t) \\ \tilde{z}(t) &=& C_{gz} x_g(t) + D_{gzu} u(t) + D_{gzw} \dot{z}_r(t) \end{array}\right. \tag{4.22}$$

where

$$A_g = \begin{bmatrix} A & 0_{19\times 20} & EC_{wd} \\ B_{wz}C_z & A_{wz} & B_{wz}FC_{wd} \\ 0_{4\times 19} & 0_{4\times 20} & A_{wd} \end{bmatrix}, \quad B_{gu} = \begin{bmatrix} B \\ B_{wz}D_{zu} \\ 0_{4\times 4} \end{bmatrix},$$

$$B_{gw} = \begin{bmatrix} ED_{wd} \\ B_{wz}F_{zw}D_{wd} \\ B_{wd} \end{bmatrix}, \quad C_{gz} = \begin{bmatrix} D_{wz}C_z & C_{wz} & D_{wz}F_{zw}C_{wd} \end{bmatrix}, \tag{4.23}$$

$$D_{gzu} = D_{wz}D_{zu}, \qquad D_{gzw} = D_{zu}F_{zw}D_{wd}$$

4.4 H_∞ and H_2 dynamic output feedback control LMI design

Considering the augmented state system (4.22), the system's output (4.10), and the performance output (4.11), our objective is to design a dynamic feedback controller of the form

$$K := \left\{ \begin{array}{rcl} \dot{\xi} & = & A_k\xi + B_k y \\ u & = & C_k\xi + D_k y \end{array} \right. \tag{4.24}$$

By substituting (4.24) into the system (4.22), the resulting closed-loop system is obtained as follows [69]:

$$\begin{array}{l} \begin{bmatrix} \dot{x} \\ \dot{\xi} \end{bmatrix} = \underbrace{\begin{bmatrix} A_g + B_{gu}D_kC_y & B_{gu}C_k \\ B_kC & A_k \end{bmatrix}}_{A_{cl}} \begin{bmatrix} x \\ \xi \end{bmatrix} + \underbrace{\begin{bmatrix} B_{gw} + B_{gu}D_kD_{yu} \\ B_kD_{yu} \end{bmatrix}}_{B_{cl}} \dot{z}_r \\ \tilde{z} = \underbrace{\begin{bmatrix} (C_{gz} + D_{gzu}D_kC_y) & D_{gzu}C_k \end{bmatrix}}_{C_{cl}} \begin{bmatrix} x \\ \xi \end{bmatrix} + \underbrace{(D_{gzu}D_kD_{yu} + D_{gzw})}_{D_{cl}} \dot{z}_r \end{array} \tag{4.25}$$

with:

$$T(s) = C_{cl}(sI - A_{cl})^{-1}B_{cl} + D_{cl} \tag{4.26}$$

being the closed-loop transfer matrix between $\dot{z}_r(t)$ and $\tilde{z}(t)$.

A multi-objective optimal H_2 output feedback control law can be determined by solving the following *Linear Matrix Inequalities* (LMI) based optimization problem [69]-[91]:

$$\left\{ \begin{array}{l} \min_{X,Y,Q,\hat{A}_k,\hat{B}_k,\hat{C}_k,\hat{D}_k,v} v \\ \begin{bmatrix} A_1 & A_2 & A_3 \\ A_4 & A_5 & A_6 \\ A_7 & A_8 & -I \end{bmatrix} < 0, \\ \begin{bmatrix} Q & (C_{gz}Y + D_{gzu}\hat{C}_k)^T & (C_{gz} + D_{gzu}\hat{D}_kC_y)^T \\ C_{gz}Y + D_{gzu}\hat{C}_k & Y & I \\ C_{gz} + D_{gzu}\hat{D}_kC_y & I & X \end{bmatrix} > 0, \\ tr(Q) < v^2, \\ \begin{bmatrix} Y & I \\ I & X \end{bmatrix} > 0 \end{array} \right.$$

with

- $A_1 = (A_gY + B_{gu}\hat{C}_k) + (A_gY + B_{gu}\hat{C}_k)^T$;
- $A_2 = \hat{A}_k^T + (A_g + B_{gu}\hat{D}_kC_y)$;
- $A_3 = B_{gw} + B_{gu}\hat{D}_kD_{yu}$;
- $A_4 = \hat{A}_k + (A_g + B_{gu}\hat{D}_kC_y)$;

- $A_5 = (XA_g + \hat{B}_k C_y) + (XA_g + \hat{B}_k C_y)^T$;
- $A_6 = XB_{gw} + \hat{B}_k D_{yu}$;
- $A_7 = (B_{gw} + B_{gu}\hat{D}_k D_{yu})^T$;
- $A_8 = (XB_{gw} + \hat{B}_k D_{yu})^T$.

In addition, A_{cl} is asymptotically stable and $||T||_{H_\infty} < \gamma_f$ if and only if $\exists X = X^T > 0$, $\exists Y = Y^T > 0$, $\exists(\hat{A}_k, \hat{B}_k, \hat{C}_k, \hat{D}_k)$ such that

$$\begin{cases} \min_{X,Y,\hat{A}_k,\hat{B}_k,\hat{C}_k,\hat{D}_k} \gamma_f \\ \begin{bmatrix} B_1 & B_2 & B_3 & B_4 \\ B_2^T & B_5 & B_6 & B_7 \\ B_3^T & B_6^T & -\gamma_f I & B_8 \\ B_4^T & B_7^T & B_8^T & -\gamma_f I \end{bmatrix} < 0, \end{cases}$$

with

- $B_1 = (A_g Y + B_{gu}\hat{C}_k) + (A_g Y + B_{gu}\hat{C}_k)^T$;
- $B_2 = \hat{A}_k^T + (A_g + B_{gu}\hat{D}_k C_y)$;
- $B_3 = B_{gw} + B_{gu}\hat{D}_k D_{yu}$;
- $B_4 = (C_{gz}Y + D_{gzu}\hat{C}_k)^T$;
- $B_5 = (XA_g + \hat{B}_k C_y) + (XA_g + \hat{B}_k C_y)^T$;
- $B_6 = XB_{gw} + \hat{B}_k D_{yu}$;
- $B_7 = (C_{gz} + D_{gzu}\hat{D}_k C_y)^T$;
- $B_8 = (D_{gzw} + D_{gzu}\hat{D}_k D_{yu})^T$.

When the matrices $X, Y, \hat{A}_k, \hat{B}_k, \hat{C}_k, \hat{D}_k$ are found for both control laws, it remains the problem of finding the matrices A_k, B_k, C_k, D_k of the controller. To this end, it can be done easily by considering the inverse relationships:

$D_k = \hat{D}_k$

$C_k = (\hat{C}_k - D_k C_y Y)M^{-T}$

$B_k = N^{-1}(\hat{B}_k - XB_{gu}D_k)$

$A_k = N^{-1}[\hat{A}_k - NB_k C_y Y - XB_{gu}C_k M^T - X(A_g + B_{gu}D_k C_y)Y]M^{-T}$

where N and M are computed by exploiting the factorization $NM^T = I - XY$.

A way to force N and M to be invertible consists of adding the LMI

$$\begin{bmatrix} Y & I \\ I & X \end{bmatrix} > 0$$

in the synthesis problem if it is not already present among the LMIs.

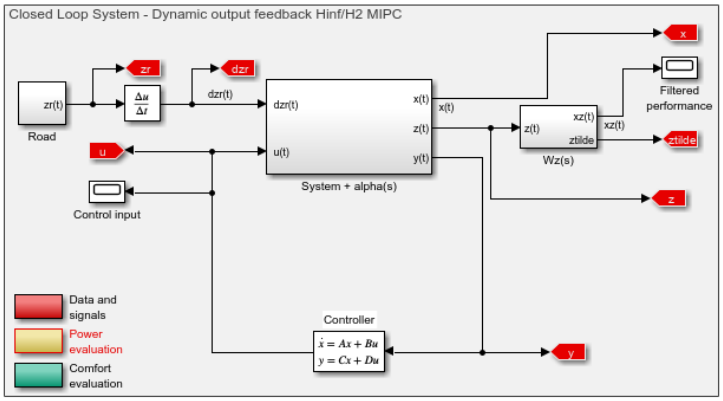

Figure 4.1: Full car simulink model

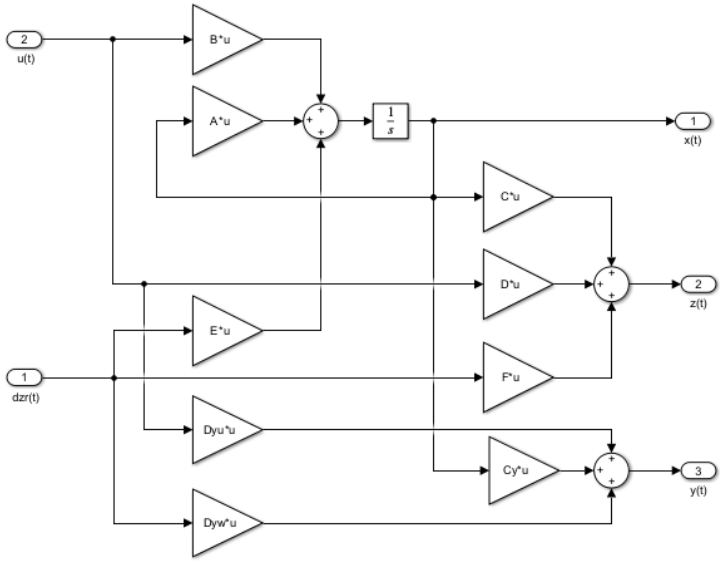

Figure 4.2: System's dynamics

4.5 Results and discussion

A simulation study on MATLAB Simulink has been conducted to evaluate the performance of the proposed control architecture. In this context, comparisons between the four regenerative suspension actuators described in section 2.3 have been performed. As shown in Fig.4.1, there are two inputs namely the road profile and the actuation signal. Indeed, the road profile is the disturbance that must be rejected by the control algorithms and whose energy must be recovered. The second input corresponds to the control current sent as input to the shock absorbers. The "system+alpha(s)" block describes the system's dynamics and it is explicited in Fig.4.2.

Road profiles complying with the ISO-8608 standard are used in the simulations. In particular, all simulations have been undertaken by assuming

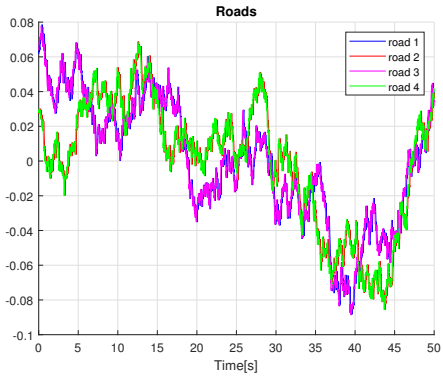

Figure 4.3: Class C road for the full car model

to drive on a **C** class straight road at $70km/h$. Fig.4.3 depicts the corresponding profiles.

The vehicle chosen for the simulation and performance evaluation of all suspension's actuators (LPMA, RPEHSA, SPEHSA, IPVA) is a standard Class **C** car, with its parameters detailed in Table A.1 of the appendix A. The data corresponding to the actuators are provided in Tables A.4, A.5, A.6 and A.7 of the appendix A. It is noteworthy that the electrical parameters of the four actuators, including armature resistance, armature inductance, EMF constant, and torque constant, are kept identical to ensure a fair and objective comparison. Moreover, the optimal H_2 and H_∞ dynamic output feedback controllers are designed for all four suspension configurations to enable consistent and reliable performance comparisons. For brevity, the results obtained with the H_2 dynamic output feedback control are detailed and the results obtained with the H_∞ dynamic output feedback control are summarized.

We consider three values of the Ride Index (RI): $RI = 0.25$, $RI = 0.40$, and $RI = 0.70$, which, according to the ISO 2631 Ride Index classification [90], correspond to the likely passenger reactions of *not uncomfortable*, *slightly uncomfortable*, and *uncomfortable*, respectively. In order to design the optimal controller, the filters (4.16), (4.17), and ((4.19)) have been properly designed as follows:

$$W_{ai}(s) = \rho \frac{81.89s^3 + 796.6s^2 + 1937s + 0.1446}{s^4 + 80s^3 + 2264s^2 + 7172s + 21196} \tag{4.27}$$

$$W_{ui}(s) = \beta \frac{s+1}{s+10} \tag{4.28}$$

$$W_{di}(s) = \gamma \frac{10}{s+1000} \tag{4.29}$$

and the filters tuning parameters ρ, β and γ have been chosen to adjust the Ride Index according to the ISO 2631 RI classification. The values of these design parameters used in the simulations for $RI = 0.25$, $RI = 0.40$, and $RI = 0.70$ are presented in Table 4.1 while the MIPC parameters values are given in Table 4.2.

Table 4.1: Knobs tuning – RI=0.25 (Excellent comfort/Smallest harvesting), RI = 0.40 (Trade-off between comfort/harvesting) and RI=0.70 (Perceivable discomfort/largest harvesting) with the H_2 dynamic output feedback control

	RI=0.25			**RI=0.40**			**RI=0.70**		
MOTOR	ρ	β	γ	ρ	β	γ	ρ	β	γ
LPMA	0,0715	0,1055	1	0,6155	0,2055	1	0,2585	0,0805	1
RP-EHSA	0,0105	0,0723	1	0,0468	0,1575	1	0,0455	0,1963	1
SP-EHSA	0,0105	0,0723	1	0,0468	0,1575	1	0,0455	0,1963	1
IPVA	0,0106	0,0804	1	0,0445	0,1463	1	0,0515	0,2063	1

Table 4.2: MIPC Parameters – RI=0.25 (Excellent comfort/Smallest harvesting), RI = 0.40 (Trade-off between comfort/harvesting) and RI=0.70 (Perceivable discomfort/largest harvesting) with the H_2 dynamic output feedback control.

	RI=0.25	**RI=0.40**	**RI=0.70**
	τ=0.0005		
MOTOR	K_α		
LPMA	0.00012	0.0001	0.0005
RP-EHSA	0.2	0.19	0.22
SP-EHSA	0.2	0.19	0.22
IPVA	0.198	0.195	0.23

In the configuration corresponding to $RI = 0.25$, classified as "not uncomfortable", the energy-harvesting shock absorber is designed to prioritize passenger comfort. This results in an optimal ride experience with minimal vibrations and enhanced vehicle stability. However, this emphasis on comfort significantly reduces the energy-harvesting potential of the system. In this configuration, the system absorbs a larger proportion of road-induced disturbances to achieve superior ride quality, leading to the smallest amount of energy being harvested. While this setup excels in terms of comfort, it inherently sacrifices energy regeneration efficiency, as the focus is shifted away from converting vibrational energy into usable power.

Figs.4.4 - 4.12 present the simulation results for the RI=0.25 configuration, which corresponds to excellent comfort and minimal energy harvesting. The plots are drawn for the four wheels and for the four actuators(LPMA, RPEHSA, IPVA, SPEHSA) under the H_2 control law.

Suspension deflections and tire deflections are good. Roll, pitch and vertical motions have good values. The accelerations are in the range [-1;1] $[m/s^2]$ which means excellent comfort. In Fig.4.8, one notices the RPEHSA's angular speed is the highest on the fourth wheel. This is a direct consequence

of the highest mechanical power of the RPEHSA on the same wheel in Fig. 4.11. We have low control currents in Fig. 4.9. The electrical and road's induced powers are depicted in Fig.4.10 and 4.12.

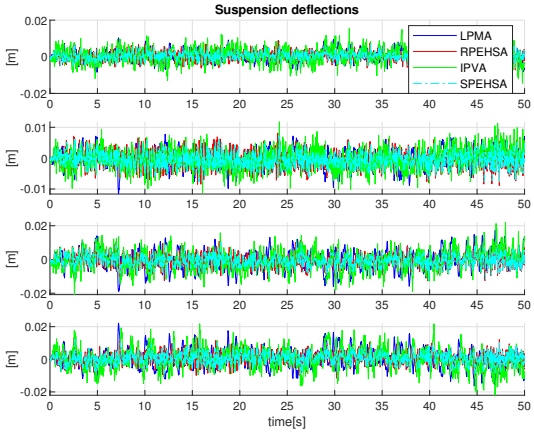

Figure 4.4: RI = 0.25 - Suspension deflections $z_{s_i} - z_{u_i}(t)$ for the four wheels

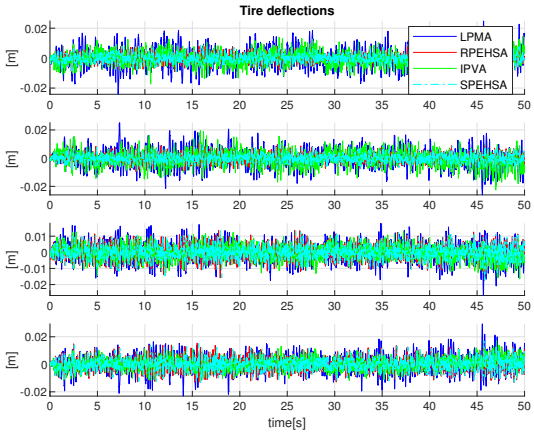

Figure 4.5: RI = 0.25 - Tire deflections $z_{u_i} - z_{r_i}(t)$ for the four wheels

In the configuration corresponding to RI=0.40, classified as "slightly uncomfortable" according to the ISO 2631 standard, the energy harvesting shock absorber strikes a balance between passenger comfort and energy harvesting efficiency. This configuration represents a trade-off where the system allows for a moderate level of discomfort in exchange for an increase in energy harvesting potential. While the ride quality remains acceptable, the system is designed to convert more road-induced vibrations into electrical energy, improving the overall efficiency of energy recovery. This trade-off is particularly useful in scenarios where maintaining a reasonable level of comfort is important, but enhanced energy regeneration is also desired to maximize the benefits of the regenerative suspension system.

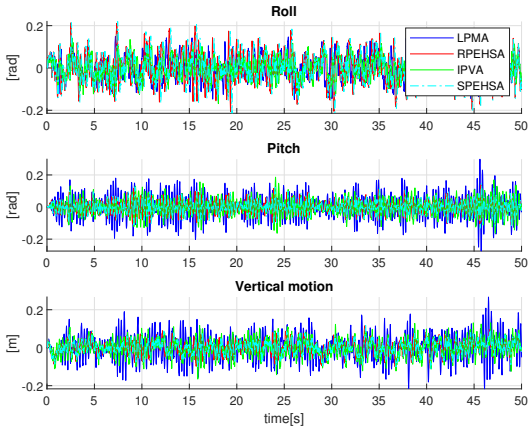

Figure 4.6: RI = 0.25 - Roll $\varphi(t)$, Pitch $\theta(t)$ and vertical motion z_s of the vehicle

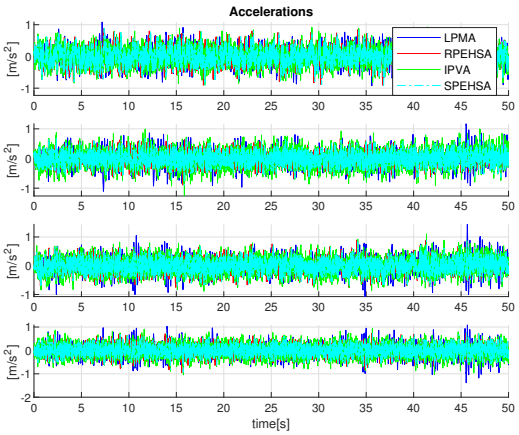

Figure 4.7: RI = 0.25 - Accelerations $\ddot{z}_{s_i}(t)$ for the four wheels

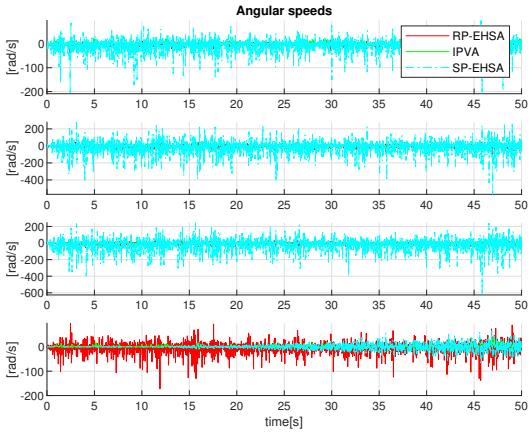

Figure 4.8: RI = 0.25 - Angular speeds $\omega_i(t)$ for the four wheels

Figs.4.13 - 4.21 present the simulation results for the RI=0.40 configuration, which corresponds to tradeoff between comfort and energy harvesting. The plots are drawn for the four wheels and for the four actuators(LPMA,

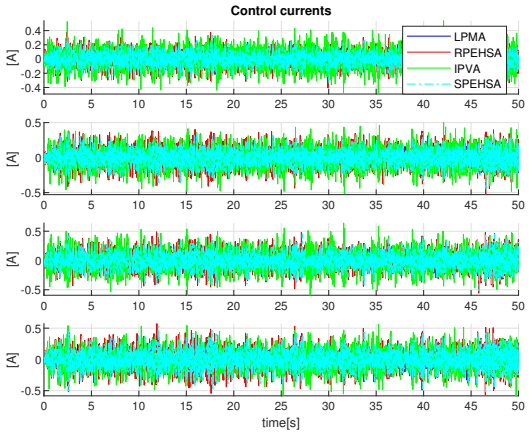

Figure 4.9: RI = 0.25 - Control currents $u_i(t)$ for the four wheels

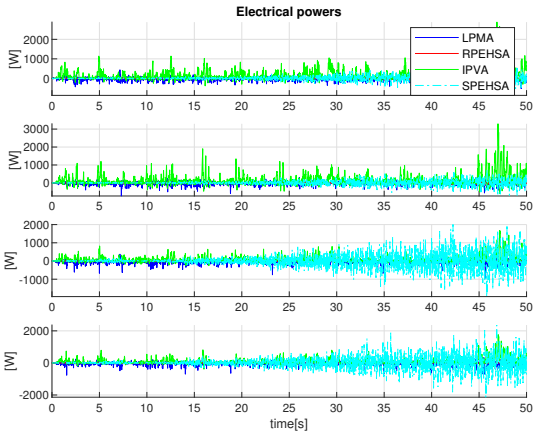

Figure 4.10: RI = 0.25 - Electrical powers $P_{e_i}(t)$ for the four wheels

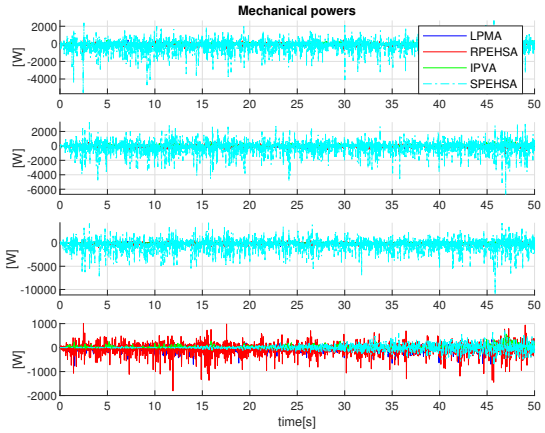

Figure 4.11: RI = 0.25 - Mechanical powers $P_{m_i}(t)$ for the four wheels

RPEHSA, IPVA, SPEHSA) under the H_2 control law.

We notice that suspension deflections and tire deflections increase a little when compared with the case RI=0.25. Roll, pitch and vertical motions don't

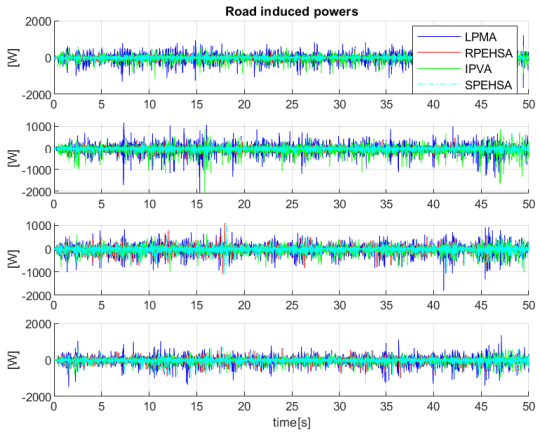

Figure 4.12: RI = 0.25 - Road induced powers $P_{s_i}(t)$ for the four wheels

vary much. In Figs.4.16, 4.17, 4.18, 4.19 and 4.20, we notice an increase of the accelerations, angular speeds, control currents, electrical and mechanical powers.

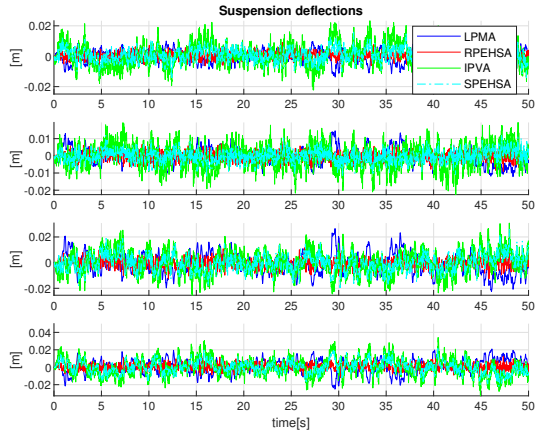

Figure 4.13: RI = 0.40 - Suspension deflections $z_{s_i} - z_{u_i}(t)$ for the four wheels

In the configuration corresponding to RI=0.70, classified as "uncomfortable" according to the ISO 2631 standard, the energy-harvesting shock absorber prioritizes maximizing energy recovery at the expense of passenger comfort. This setup leads to perceivable discomfort due to the increased transmission of road vibrations to the vehicle's occupants. However, this discomfort allows for the largest amount of energy to be harvested, as more of the vibrational energy is converted into electrical power rather than being absorbed by the suspension system. The RI=0.70 configuration is most suitable for scenarios where energy regeneration is prioritized over ride comfort, making it ideal for applications where maximizing energy efficiency is critical, and the trade-off of reduced comfort is acceptable.

Figs.4.22 - 4.30 present the corresponding simulation results. The plots are drawn for the four wheels and for the four actuators(LPMA, RP-EHSA,

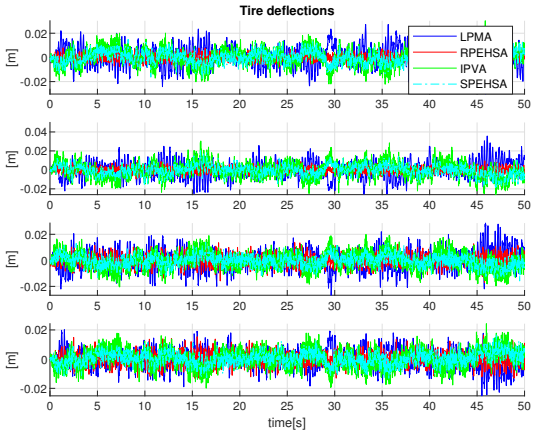

Figure 4.14: RI = 0.40 - Tire deflections $z_{u_i} - z_{r_i}(t)$ for the four wheels

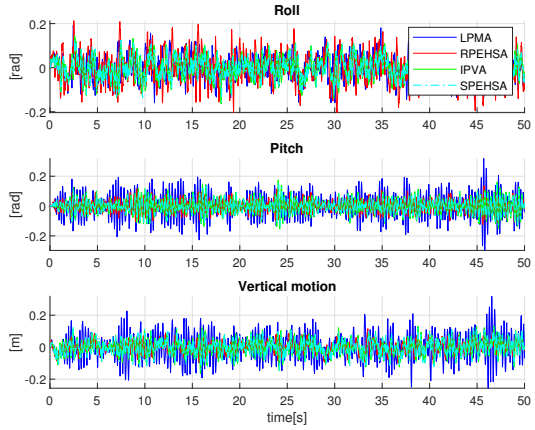

Figure 4.15: RI = 0.40 - Roll $\varphi(t)$, Pitch $\theta(t)$ and vertical motion z_s of the vehicle

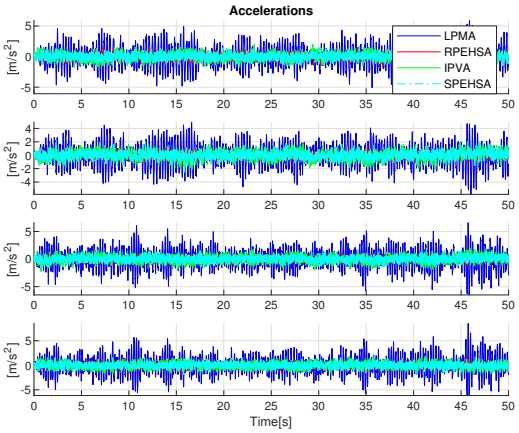

Figure 4.16: RI = 0.40 - Accelerations $\ddot{z}_{s_i}(t)$ for the four wheels

IPVA, SP-EHSA) under the H_2 control law.

We notice that suspension deflections and tire deflections don't increase when compared with the case RI=0.40 but we note a remarkable increase in

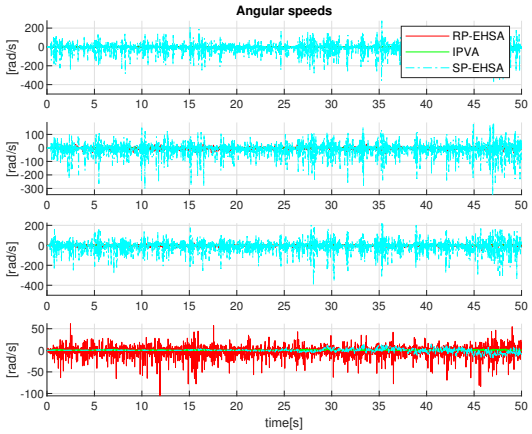

Figure 4.17: RI = 0.40 - Angular speeds $\omega_i(t)$ for the four wheels

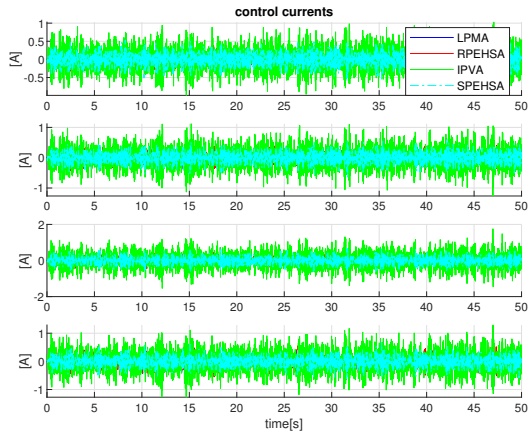

Figure 4.18: RI = 0.40 - Control currents $u_i(t)$ for the four wheels

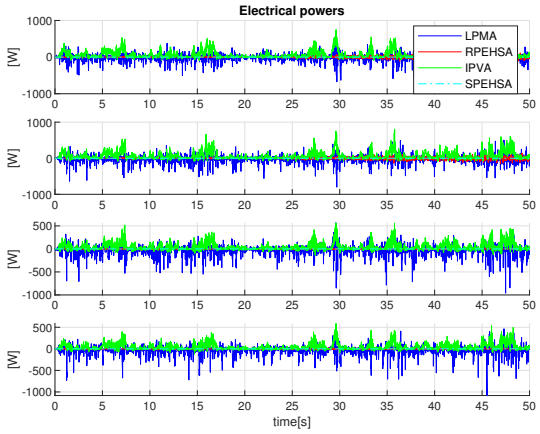

Figure 4.19: RI = 0.40 - Electrical powers $P_{e_i}(t)$ for the four wheels

vehicle's pitch and vertical motion. In Figs.4.25, 4.26, 4.27, 4.28 and 4.29, we notice an increase of the accelerations, angular speeds, control currents, electrical and mechanical powers.

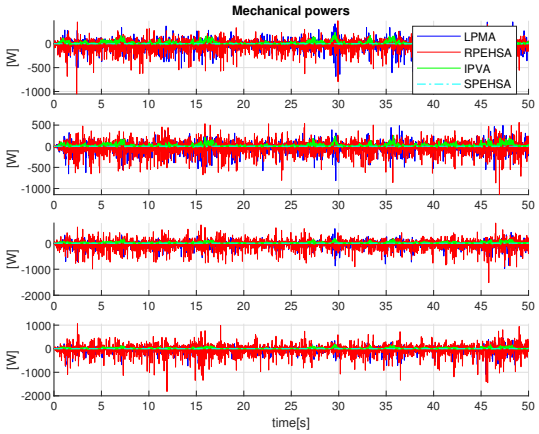

Figure 4.20: RI = 0.40 - Mechanical powers $P_{m_i}(t)$ for the four wheels

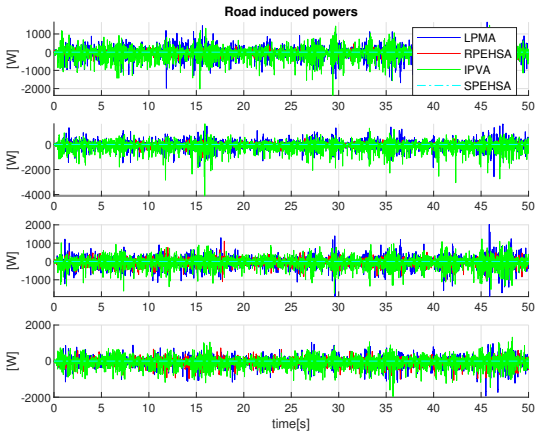

Figure 4.21: RI = 0.40 - Road induced powers $P_{s_i}(t)$ for the four wheels

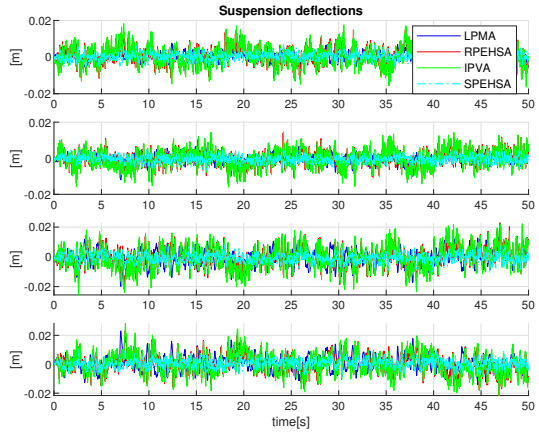

Figure 4.22: RI = 0.70 - Suspension deflections $z_{s_i} - z_{u_i}(t)$ for the four wheels

For a more detailed quantitative comparison, Tables 4.3 and 4.4 present the average harvested electrical power and the average angular (or linear) velocities calculated for the four wheels. The results demonstrate that rotary

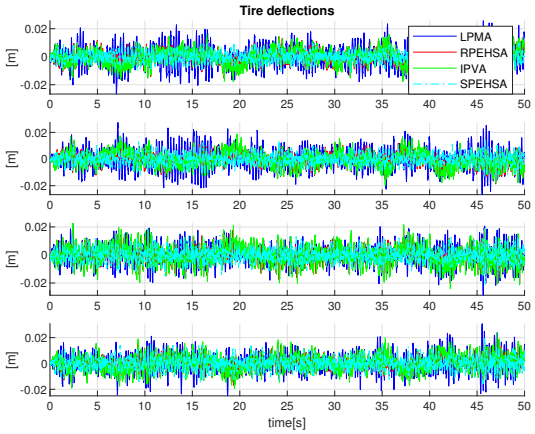

Figure 4.23: RI = 0.70 - Tire deflections $z_{u_i} - z_{r_i}(t)$ for the four wheels

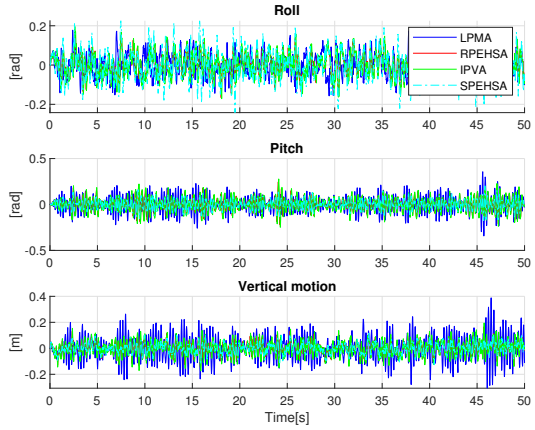

Figure 4.24: RI = 0.70 - Roll $\varphi(t)$, Pitch $\theta(t)$ and vertical motion z_s of the vehicle

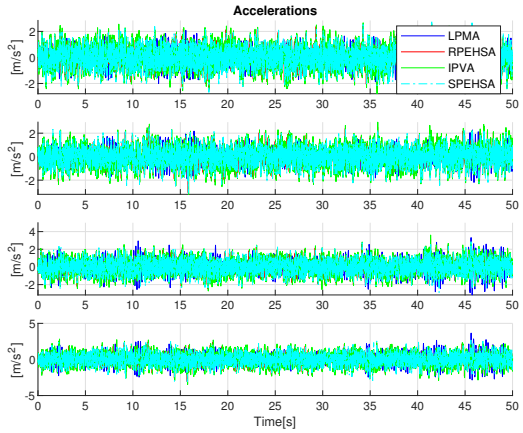

Figure 4.25: RI = 0.70 - Accelerations $\ddot{z}_{s_i}(t)$ for the four wheels

EHSAs effectively convert the suspension's linear motion to the angular motion of the rotor, enabling higher angular speeds and, consequently, inducing larger electrical currents. By achieving higher speeds, rotary

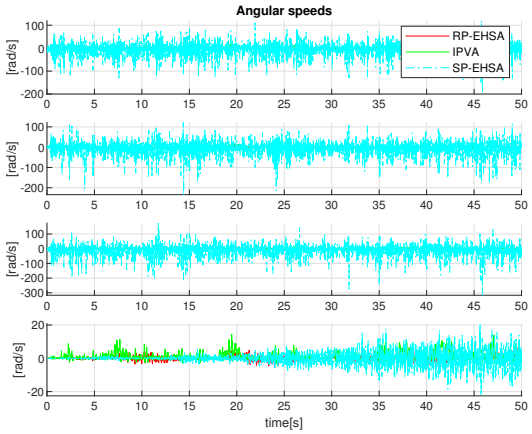

Figure 4.26: RI = 0.70 - Angular speeds $\omega_i(t)$ for the four wheels

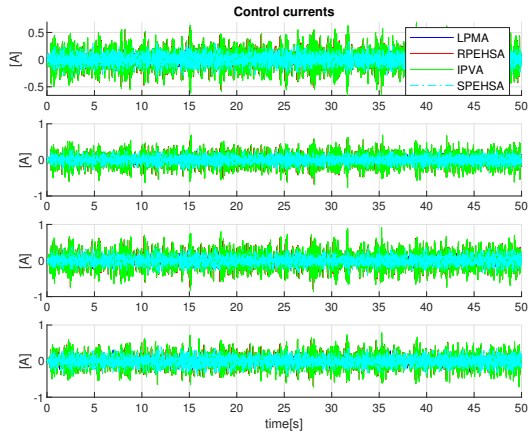

Figure 4.27: RI = 0.70 - Control currents $u_i(t)$ for the four wheels

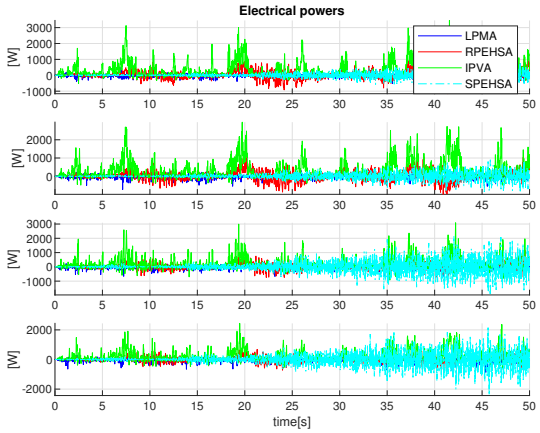

Figure 4.28: RI = 0.70 - Electrical powers $P_{e_i}(t)$ for the four wheels

EHSAs are able to optimize energy conversion, providing a clear advantage over systems that rely solely on linear motion for energy recovery.

When comparing the performance of the four regenerative suspension

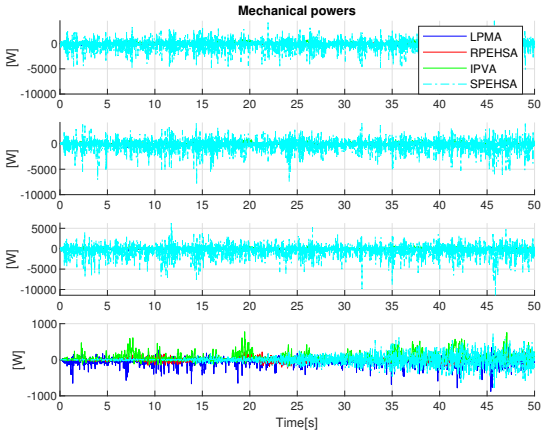

Figure 4.29: RI = 0.70 - Mechanical powers $P_{m_i}(t)$ for the four wheels

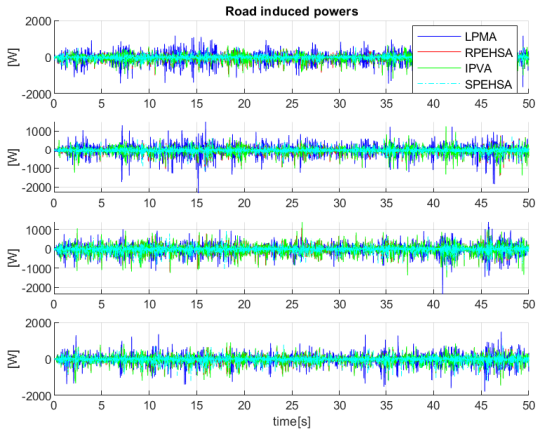

Figure 4.30: RI = 0.70 - Road induced powers $P_{s_i}(t)$ for the four wheels

Table 4.3: Average Harvested Electrical Power for RI=0.25, RI=0.40 and RI=0.70 - A single EHSA with the H_2 MIPC dynamic output feedback control

Average Harvested Electrical Power with H_2			
Motor	**RI=0.25**	**RI=0.40**	**RI=0.70**
LPMA	45.70 W	49.36 W	57.64 W
RPEHSA	65.48 W	118.75 W	187.97 W
SPEHSA	79.85 W	143.28 W	233.22 W
IPVA	**89.29 W**	**168.24 W**	**354.32 W**

configurations IPVA, RPEHSA, LPMA, and SPEHSA, it is evident that the IPVA, due to its unique structural and mechanical characteristics, generates significantly higher angular speeds than the RPEHSA and SPEHSA configurations. This higher angular velocity directly translates into increased generator's power output, resulting in a substantial improvement in the amount of energy harvested. The design of the IPVA allows for more

Table 4.4: Generator Average Angular (Linear) Velocities for RI=0.25, RI=0.40 and RI=0.70 - A single EHSA with the H_2 MIPC dynamic output feedback control.

Average Angular (Linear) Velocity - A Single EHSA			
Motor	**RI=0.25**	**RI=0.40**	**RI=0.70**
RPEHSA	1.2911 rad/s	1.0983 rad/s	1.3249 rad/s
SPEHSA	1.7923 rad/s	1.3279 rad/s	1.6449 rad/s
IPVA	**1.8650 rad/s**	**1.7503 rad/s**	**2.0222 rad/s**
LPMA	0.1127 m/s	0.1093 m/s	0.1139 m/s

Table 4.5: Average Harvested Electrical Power for RI=0.25, RI=0.40 and RI=0.70 - A single EHSA with the H_∞ MIPC dynamic output feedback

Average Harvested Electrical Power with H_∞			
Motor	**RI=0.25**	**RI=0.40**	**RI=0.70**
LPMA	18.31 W	26.27 W	41.34 W
RPEHSA	24.54 W	36.92 W	52.91 W
SPEHSA	62.22 W	67.05 W	95.83 W
IPVA	**70.73 W**	**73.9 W**	**97.68 W**

efficient transformation of the suspension's linear motion into rotational motion, capitalizing on the rotary generator's ability to harness kinetic energy more effectively.

In particular, the IPVA's ability to outperform both the RPEHSA and SPEHSA systems can be attributed to its enhanced mechanical transmission system, which is specifically optimized to convert linear displacement into rotary movement with minimal energy loss. This structural efficiency is critical for maximizing the energy recovery potential in dynamic vehicle environments, where varying road conditions can influence both the frequency and amplitude of suspension movement.

Furthermore, when comparing the IPVA to the LPMA, the performance differential is even more pronounced. While the LPMA operates effectively by utilizing linear motion directly for energy recovery, the IPVA's ability to convert this motion into a faster rotational speed provides a distinct advantage. The higher rotational speeds achieved by the IPVA (see Table 4.4) result in greater energy capture, as the associated increase in angular velocity directly impacts the EMF generated, thereby enhancing the overall energy harvesting efficiency. This makes the IPVA a more suitable choice in applications where maximizing energy recovery is a priority, especially in environments where vehicle dynamics produce frequent or large suspension displacements.

In addition, Table 4.5 presents the average harvested electrical powers obtained using the H_∞ dynamic output feedback control with the MIPC strategy. One notices that the H_2 outperforms the H_∞ in terms of energy

harvesting. The IPVA remains the best energy harvester followed respectively by the SPEHSA, RPEHSA and LPMA.

4.6 Conclusion

In conclusion, the results indicate that among the examined configurations, the IPVA offers the highest potential for energy recovery due to its superior conversion of linear to rotary motion, allowing it to achieve higher power outputs. This advantage underscores the importance of selecting the appropriate suspension architecture depending on the desired trade-off between comfort and energy harvesting, with the IPVA standing out as an optimal solution for applications that prioritize energy efficiency without significantly compromising ride quality. We also notice that the H_2 dynamic output feedback control applied with the MIPC strategy outperforms its H_∞ counterpart. This confirms the results of [23] where a comparative study between MIPC H_2 and H_∞ static state feedback has been performed on a LPMA regenerative suspension configuration. In the next chapter, we will introduce a novel multiobjective LQR control strategy for regenerative suspensions and wave energy converters.

Chapter 5

H_2 MIPC state feedback and LQR with a non-standard cost

V

Contents

5.1 Introduction 73
5.2 Vehicle regenerative suspension systems 73
5.3 Simulations on Carsim 2025.1 103
5.4 Wave energy converters 107
5.5 Conclusion 117

5.1 Introduction

In this chapter, we aim to develop a novel multi-objective LQR control law for energy harvesting maximization. Regarding regenerative suspension systems, an additional bound on the ride index is incorporated into the LQR's LMI design and comparison to existing control strategies is undertaken. Regarding wave energy converters, the same LQR control law is reformulated in many ways and compared to H_2 MIPC state feedback also reformulated to tackle the challenges associated to wave energy. Section 5.2 presents the control strategies for the regenerative suspension case, section 5.3 presents simulations on the mechanical simulation software Carsim 2025.1, section 5.4 presents the wave energy converter case and a conclusion ends the chapter in section 5.5.

5.2 Vehicle regenerative suspension systems

5.2.1 Road profile

In general, a road profile can be seen as a stochastic process but rarely can be considered a simple Gaussian white noise. Thus, in some case studies, it is necessary to provide detailed mathematical representations characterized by a deep knowledge of the road profile's *Power Spectral Density* (PSD)[92]. These mathematical models have been described in the ISO 6808 standard

Type of road	$G(n_0)10^{-6}$	β_1
A(very good)	< 8	< 0.1018
B(good)	8-32	0.1018-0.2035
C(average)	32-128	0.2036-0.4072
D(poor)	128-512	0.4073-0.8145
E(very poor)	512-2048	0.8146-1.6295
F	2048-8192	1.6296-3.2582
G	8192-32768	3.2583-6.5166
H	> 32768	> 6.5166

Table 5.1: Amplitude of PSD according to ISO classification.

and are based on the assumption that the road roughness must present the same statistical properties in all sections of the road. The expression of the PSD envisaged by the model ISO 8608, can be traced back in the following form [92]:

$$G_d(n) = G(n_0)(\frac{n}{n_0})^{-2} \tag{5.1}$$

Where n is the wavelength in cycles per meter and n_0 is equal to 0.1 cycles/m. The constant $G(n_0)$ characterizes in amplitude the degree of roughness of the road and this parameter identifies the class to which the road profile belongs.

The ISO 8608 standard subdivides the roads in several classes depicted in Table 5.1 ([92]- [93]).

A further useful contribution in modeling the road profile z_r is [93] where, based on experimental work, models of the form

$$\dot{z}_r = \alpha_1 u z_r + \beta_1 \sqrt{u} w \tag{5.2}$$

have been determined, where u denotes the longitudinal velocity of the car and w is a zero-mean unitary-variance white noise. The parameter $\alpha_1 = -3.96$ is a constant for all kind of road whereas β_1 depends on road class and is tabled hereafter in Table 5.1.

5.2.2 Overall control architecture

A schematic of a possible implementation and control architecture is shown in Fig.5.1 and consists of two nested control loops, governed respectively by the *Inner Current Controller* (ICC) and the *Outer Regenerative Controller* (ORC). In order to create the proper bidirectional electrical power flows between the energy storage (battery) and the actuator, ICC regulates the armature current loop of the four-quadrant DC-DC converter. It usually consists of a PI control law which is used to maintain the armature current at suitable reference values provided by the outer ORC controller. Its design is not considered here for brevity but, being its time constants expected to be small, the inner current loop dynamics can be neglected during the ORC

design. On the contrary, the ORC controller is in charge of implementing active control strategies that ensure standard suspension performance while maximizing energy harvesting.

In Fig.5.1, the red arrows indicate an exchange of energy flows, while black arrows indicate information. Notice that, because the proposed strategy requires a bidirectional flow of electrical energy between the battery and the actuator, a four-quadrant DC-DC converter must be used as an interface. Within this control architecture, one can then focus on the design of active control strategies for the ORC block that are expected to provide both control performance of standard active suspension systems and energy harvesting capabilities.

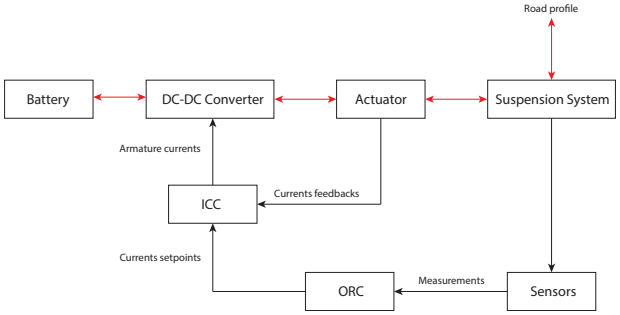

Figure 5.1: Control architecture

5.2.3 State space realization

Regarding the specified road profile, moving-magnet linear actuator depicted in section 2.3.1, and control specifications depicted in section 4.2, the aim is to design an ORC controller on the basis of the LQR approach to simultaneously meet requirements for passenger comfort, system stability and energy harvesting optimization. To this end, let the quarter-car system (Eq.(2.8)) and the moving-magnet linear actuator (Eq.(2.9)) jointly model by the following state-space representation

$$\begin{cases} \dot{x}(t) &= Ax(t) + Bu(t) + Ew(t) \\ z(t) &= C_z x(t) + D_{zu} u(t) + F_{zw} w(t) \end{cases} \tag{5.3}$$

with system matrices

$$A = \begin{bmatrix} \alpha_1 u & 0 & 0 & 0 & 0 \\ 0 & 0 & 1 & 0 & 0 \\ 0 & -\frac{k_s}{m_s} & 0 & \frac{k_s}{m_s} & 0 \\ 0 & 0 & 0 & 0 & 1 \\ \frac{k_u}{m_u} & \frac{k_s}{m_u} & 0 & -\frac{k_u+k_s}{m_u} & 0 \end{bmatrix} \quad B = \begin{bmatrix} 0 \\ 0 \\ \frac{K_v}{m_s} \\ 0 \\ -\frac{K_v}{m_u} \end{bmatrix} \tag{5.4}$$

$$E = \begin{bmatrix} \beta_1\sqrt{u} \\ 0 \\ 0 \\ 0 \\ 0 \end{bmatrix}, \quad C_z = \begin{bmatrix} 0 & -\frac{k_s}{m_s} & 0 & \frac{k_s}{m_s} & 0 \end{bmatrix} \tag{5.5}$$

$$D_{zu} = \frac{K}{m_s}, \quad F_{zw} = 0$$

with α_1 and β_1 the parameters of the road profile defined in the section 5.2.1.

In Eq.(5.3), $x(t)$ denotes the system state, $u(t)$ the input, $z(t)$ the objective vector and $w(t)$ a zero-mean, unitary-variance white noise that models the road profile z_r. Specifically, the following system vectors are obtained

$$x = \begin{bmatrix} z_r \\ z_s \\ \dot{z}_s \\ z_u \\ \dot{z}_u \end{bmatrix}, \quad u = i, \quad z = \ddot{z}_s \tag{5.6}$$

The attention here is on limiting the vertical acceleration in the objective vector in order to maintain a certain level of ride comfort while maximizing the amount of energy harvested.

5.2.4 Frequency shaping of the state space

In order to quantify the ride comfort adequately, the above state-space representation is extended by introducing dynamic weighting filters to better shape in frequency the vector z according to the ISO 2631 standard [90]. In particular, if the $W_k(s)$ filter introduced in Eq.(4.3) is used, the filtered objective vector $\tilde{z} = W_k z$ can be used to enforce conditions directly on the Ride Index defined in section 4.2.

Denoting by (A_k, B_k, C_k, D_k) the state-space representation of the filter $W_k(s)$

$$\begin{aligned} \dot{x}_k &= A_k x_k + B_k z \\ \tilde{z} &= C_k x_k + D_k z \end{aligned} \tag{5.7}$$

with state x_k, one has the extended state

$$x_g = \begin{bmatrix} x^T & x_k^T \end{bmatrix}^T \tag{5.8}$$

and, accordingly, the extended state-space representation of the system is obtained as

$$\begin{aligned} \dot{x}_g(t) &= A_g x_g(t) + B_{gu} u(t) + B_{gw} w(t) \\ \tilde{z}(t) &= C_{gz} x_g(t) + D_{gzu} u(t) + D_{gzw} w(t) \end{aligned} \tag{5.9}$$

where

$$A_g = \begin{bmatrix} A & 0_{5\times4} \\ B_k C_z & A_k \end{bmatrix}, \quad B_{gu} = \begin{bmatrix} B \\ B_k D_{zu} \end{bmatrix},$$
$$B_{gw} = \begin{bmatrix} E \\ B_k F_{zw} \end{bmatrix}, \quad C_{gz} = \begin{bmatrix} D_k C_z & C_k \end{bmatrix}, \tag{5.10}$$
$$D_{gzu} = D_k D_{zu}, \quad D_{gzw} = D_k F_{zw}$$

For the above model, one wants to find the optimal LQR state-feedback control law

$$u(t) = -K_{LQ} x_g(t) \tag{5.11}$$

that minimizes a suitable cost related to the harvestable energy subject to a bound on the Ride Index.

5.2.5 The unconstrained LQR approach via LMI

Notation: In the sequel, $E(\cdot)$ will denote the expected value of a variable under stationary conditions, $tr(.)$ the trace of a matrix, $||\cdot||_2$ and $||\cdot||_\infty$ denote the 2-norm and the ∞-norm of a signal respectively.

In traditional Linear Quadratic Regulator (LQR) designs applied to suspension systems, the objective is typically to minimize a quadratic performance index of the form:

$$J = \int_0^\infty \left(x^T Q x + u^T R u + 2 x^T N u \right) dt \tag{5.12}$$

where Q penalizes state deviations from zero, R penalizes control effort, and N is a cross-weighting matrix - commonly set to zero in standard implementations. This formulation is well suited for regulating state trajectories and minimizing energy or acceleration, but does not directly address objectives such as energy harvesting [94]. By considering that under stationary conditions the expected value of the electrical power is given by [54]

$$J := E(v_{emf} i + R_a i^2) \tag{5.13}$$

in our approach, the LQR cost function is reformulated to explicitly maximize the electrical power harvested by the suspension actuator. This is accomplished by setting $Q = 0$, and designing the weighting matrices $R = R_a$ and $N = N_a = 0.5$ such that the cost function becomes proportional to the expected harvested power which is negative. As stated before in section 2.3.1, P_e represents the fraction of mechanical power P_m produced when the actuator operates as a generator (that is, $P_m(t) < 0$). In other words, P_e is negative. Then, the objective of maximizing the harvested energy can be converted in the minimization of the expected value of P_e. As a consequence, the following cost index can be considered

$$J := E(2 v_{emf}^T N_a i + i^T R_a i) \tag{5.14}$$

where v_{emf} is the back EMF voltage. This is a particular instance of the LQ cost where the first term is the electrical power directly generated by the mechanical power P_m and $i^T R_a i$ represents the Joule power loss. Notice that the reactive power P_c stored in the inductance is not considered in the cost since it is zero under stationary conditions. Notice also that $R_a > 0$ is the generator's resistance.

Moreover, note that Eqs. (5.13) and (5.14) describe the same cost index J, provided that the weighting factor N_a is set to 0.5. This specific value highlights the equivalence between the two formulations and corresponds to the condition under which the harvested electrical power is maximized, balancing the contribution of the electromotive force and resistive losses. Let us recall that K_v is the actuator's force constant. By noting that

$$v_{emf} = K_v(\dot{z}_s - \dot{z}_u) \tag{5.15}$$

$$i = -K_{LQ} x_g \tag{5.16}$$

$$\dot{z}_s - \dot{z}_u = G^T x_g, \text{with } G^T = [0,\ 0,\ 1,\ 0,\ -1,\ 0,\ 0,\ 0,\ 0] \tag{5.17}$$

the following developments are obtained

$$\begin{aligned} J &= E[(2K_v(\dot{z}_s - \dot{z}_u))^T N_a(-K_{LQ}x_g) + (-K_{LQ}x_g)^T R_a(-K_{LQ}x_g)] \\ &= E[(K_v G^T x_g)^T 2N_a(-K_{LQ}x_g) + x_g^T K_{LQ}^T R_a K_{LQ} x_g] \\ &= E[x_g^T(-2K_v G N_a K_{LQ} + K_{LQ}^T R_a K_{LQ})x_g] \end{aligned} \tag{5.18}$$

By using the trace property $a^T H b = tr(Hba^T)$ for square matrice H with a and b vectors, Eq.(5.18) can be rewritten as

$$J = tr((-2K_v G N K_{LQ} + K_{LQ}^T R_a K_{LQ})E[x_g x_g^T]) \tag{5.19}$$

by noting also that for a random square matrix A, $E[tr(A)] = tr(E[A])$.

Let denote $E[x_g x_g^T] = P$, which represents the state covariance matrix. Clearly, P is a symmetric positive definite matrix that has to satisfy the Lyapunov equation for the asymptotical stability of the closed-loop system [94]

$$(A_g - B_{gu}K_{LQ})P + P(A_g - B_{gu}K_{LQ})^T < 0$$

Then, the cost assumes the following new expression

$$J = tr(-2K_v G N_a K_{LQ} P + K_{LQ}^T R_a K_{LQ} P) \tag{5.20}$$

By introducing the new matrix Y and denoting $Y = K_{LQ}P$, one can rewrite the cost in the following way

$$J = (tr(-2K_v G N Y) + tr(K_{LQ}^T R_a Y)) \tag{5.21}$$

Next, by observing that the term R_a is a constant scalar, one obtains $tr(K_{LQ}^T R_a K_{LQ} P) = R_a tr(K_{LQ}^T K_{LQ} P)$ and noticing that $K_{LQ}^T = P^{-1}Y^T$, one arrives to

$$J = (tr(-2K_v G N_a Y) + R_a tr(Y P^{-1} Y^T)) \tag{5.22}$$

because $tr(YP^{-1}Y^T) = tr(P^{-1}Y^TY)$.

The nonlinear term $tr(YP^{-1}Y^T)$ in the cost can be replaced by a second auxiliary variable X using Schur's complements, such that [95]

$$X > YP^{-1}Y^T \Leftrightarrow \begin{bmatrix} X & Y \\ Y^T & P \end{bmatrix} > 0 \tag{5.23}$$

and the cost can bounded by

$$J' = (tr(-2K_vGN_aY) + R_atr(X)) \geq J \tag{5.24}$$

The objective of this work is to develop a control strategy that enhances energy harvesting performance while maintaining low computational complexity. By formulating the LQR design as a Linear Matrix Inequality (LMI) problem, a solution can be efficiently obtained using convex optimization techniques.Therefore, the controller can be determined by solving the following semi-definite convex optimization problem expressed by LMIs

$$\begin{cases} [P_{LQ}, Y_{LQ}] = argmin_{P,X,Y}(tr(-2K_vGN_aY) + R_atr(X)) \\ s.t \\ P > 0; \\ A_gP - B_{gu}Y + PA_g^T - Y^TB_{gu}^T < 0; \\ \begin{bmatrix} X & Y \\ Y^T & P \end{bmatrix} > 0 \end{cases} \tag{5.25}$$

If a solution exists, the optimal controller is given by

$$K_{LQ} = Y_{LQ}P_{LQ}^{-1} \tag{5.26}$$

It is important to note that, in the classical free-endpoint linear-quadratic (LQ) framework with a positive semi-definite cost functional, the optimal solution is given by the smallest extremal, positive semi-definite, real symmetric, and stabilizing solution of the associated algebraic Riccati equation. However, when the cost functional is indefinite, this relationship no longer holds, and the solution may deviate significantly from the classical Riccati-based interpretation. Consequently, optimality cannot be formally asserted in this case. Nonetheless, the resulting design procedure remains a powerful and practical approach for synthesizing stabilizing state-feedback controllers that exhibit high performance in energy harvesting applications. For details about the resolution of the free-end point LQR control problem with indefinite cost, refer to [95]. A further difference with the Riccati approach to be pointed out is that the matrix P of the LMI optimization problem needs not to converge to the smallest extremal solution of the corresponding Riccati equation at the optimum because the indefinite cost of Eq.(5.25) is unbounded. As a consequence, the solution of the LMI described

above is different from the solution of the corresponding Algebraic Riccati equation.

Moreover with our approach, many controllers can be determined Eq.(5.25) with costs arbitrarily large if forced by adding additional conditions on P_e in Eq.(5.25). This can be done by introducing a bound λ on the cost and in reformulating the LMI design optimization problem as follows

$$\begin{cases} [P_{LQ}, Y_{LQ}] = argmin_{P,X,Y}(\lambda) \\ s.t \\ P > 0; \\ A_g P - B_{gu} Y + P A_g^T - Y^T B_{gu}^T < 0; \\ tr(-2K_v G N_a Y) + R_a tr(X) < \lambda; \\ \lambda > 0; \\ \begin{bmatrix} X & Y \\ Y^T & P \end{bmatrix} > 0 \end{cases} \tag{5.27}$$

5.2.6 Condition on the RI and constrained LQR

The unconstrained LQR design seeks to maximize the harvested electrical power by minimizing a cost function subject to standard LMI stability conditions. This formulation prioritizes energy recovery without explicitly accounting for ride comfort. To address passenger comfort, the Ride Index constraint is introduced as a bound on the energy of

$$\|\tilde{z}\|_2^2 \leq \eta \tag{5.28}$$

where $\tilde{z}$ denotes the filtered vertical acceleration, and η is a threshold corresponding to acceptable ride quality (e.g., RI = 0.25 for "not uncomfortable", RI = 0.47 for "a little uncomfortable", etc.).

By denoting with $T(s)$ the closed-loop transfer function between $w(t)$ and $\tilde{z}$, the following inequalities are achieved

$$||\tilde{z}||_2^2 \leq ||T||_\infty^2 ||w||_2^2 \leq \eta \tag{5.29}$$

$$||T||_\infty^2 \leq \frac{\eta}{||w||_2^2} \tag{5.30}$$

Notice that $T(s)$ depends on the choice of the controller. Then, condition (5.28) would be satisfied if the controller is designed so as to satisfy (5.29). Thus, for the system

$$\begin{cases} \dot{x}_g(t) &= (A_g - B_{gu}K)x_g(t) + B_{gw}w(t) \\ \tilde{z} &= (C_{gz} - D_{gzu}K)x_g(t) + D_{gzw}w(t) \end{cases} \tag{5.31}$$

under the static state-feedback control law of the form

$$u(t) = -Kx_g(t) \tag{5.32}$$

the KYP lemma [96] ensures that $A_g - B_{gu}K$ is asymptotically stable and

$$||T(s)||_\infty < \alpha$$

if and only if exists $P = P^T > 0$, $P \in \mathbb{R}^{9\times 9}$ and $Y \in \mathbb{R}^{1\times 9}$ such that

$$\begin{bmatrix} A_gP - B_{gu}Y + (A_gP - B_{gu}Y)^T & B_{gw} & (C_{gz}P - D_{gzu}Y)^T \\ B_{gw}^T & -\alpha I & D_{gzw}^T \\ C_{gz}P - D_{gzu}Y & D_{gzw} & -\alpha I \end{bmatrix} < 0 \tag{5.33}$$

for a state-feedback gain parameterized as $K = YP^{-1}$. Notice that in our case, α should be selected as

$$\alpha = \sqrt{\frac{\eta}{||w||_2^2}} \tag{5.34}$$

As a conclusion, because the controller of the unconstraint LQR synthesis problem is parameterized by the same matrices Y and P, the following constrained LQR synthesis algorithm can be directly derived

$$\begin{cases} \begin{array}{c} [P_{LQC}, Y_{LQC}] = argmin_{P,Y,X}(tr(-2K_vGN_aY) + R_atr(X)) \\ s.t \\ P > 0; \\ A_gP - B_{gu}Y + PA_g^T - Y^TB_{gu}^T < 0; \\ \begin{bmatrix} X & Y \\ Y^T & P \end{bmatrix} > 0 \end{array} \\ \\ \begin{bmatrix} A_gP - B_{gu}Y + (A_gP - B_{gu}Y)^T & B_{gw} & (C_{gz}P - D_{gzu}Y)^T \\ B_{gw}^T & -\alpha I & D_{gzw}^T \\ C_{gz}P - D_{gzu}Y & D_{gzw} & -\alpha I \end{bmatrix} < 0 \end{cases} \tag{5.35}$$

This formulation allows for the exploration of trade-offs between ride comfort and energy harvesting by adjusting the threshold η, and therefore provides flexibility not available in classical LQR formulations. While the RI is not part of the cost function, it is embedded into the control design through a rigorously derived LMI constraint, enabling a structured and computationally tractable way to balance comfort and energy harvesting within the same control framework. If a solution exists, the optimal controller is given by

$$K_{LQC} = Y_{LQC}P_{LQC}^{-1} \tag{5.36}$$

5.2.7 Other control laws used for comparison

In this section, two alternative control laws are recalled and they will be used here for comparison. The first has been denoted in the literature as the Maximum Induced Power Control in [16] and [23], where static state-feedback and dynamic output feedback designs were considered for full-car models optimal in both H_∞ and H_2 sense. The second strategy is the classic

approach to regulate the mechanical device to mimic the effect of a standard passive viscous damper. This control strategy will be denoted hereafter as the regenerative viscous damper control [16].

5.2.7.1 H_2 MIPC state feedback

The principles used to derive the MIPC control law are based on the analysis of the energy fluxes (see Fig.2.16). The road profile z_r is the only exogenous signal in the system which excites the suspension and it is the only source of power to be harvested. The energy of the road can be absorbed by the system, such as when the springs release their energy, or it can be introduced by its unevenness.

From power fluxes analysis (section 2.4), it is determined that

$$P_s(t) := -k_u \dot{z}_r(t)(z_u(t) - z_r(t)) \tag{5.37}$$

is the power generated by the road unevenness and z_s and z_u (and their derivatives) are controlled variables. Notice that P_s could be made sign defined ($P_s > 0$) if a suitable reference model

$$z_u(t) - z_r(t) = -\alpha(s)\dot{z}_r(t) \tag{5.38}$$

could be enforced in closed-loop, where $\alpha(s) > 0$ is a stable filter such as

$$\alpha(s) = \frac{K_\alpha}{s\tau + 1} \tag{5.39}$$

In this case, one would have that $P_s(t) = k_u \alpha \dot{z}_r^2(t)$ and condition (5.38) would provide a control design objective for energy harvesting maximization. To this end, we introduce the following output z_p

$$z_p(t) = z_u(t) - z_r(t) + \alpha \dot{z}_r(t) \tag{5.40}$$

and we observe that $z_p(t) = 0, \forall t$ would imply that the condition (5.38) holds true. The tuning parameters in this control strategy are only the gain K_α and the time constant τ. More details can be found in [16] and [23].

- **H_2 MIPC control design**

  Consider the following state-space realization

$$\begin{array}{rcl} \dot{x}(t) & = & Ax(t) + Bu(t) + Ew(t) \\ z(t) & = & C_z x(t) + D_{zu} u(t) + F_{zw} w(t) \end{array} \tag{5.41}$$

  with matrices

$$A = \begin{bmatrix} \alpha_1 u & 0 & 0 & 0 & 0 & 0 \\ 0 & 0 & 1 & 0 & 0 & 0 \\ 0 & -\frac{k_s}{m_s} & 0 & \frac{k_s}{m_s} & 0 & 0 \\ 0 & 0 & 0 & 0 & 1 & 0 \\ \frac{k_u}{m_u} & \frac{k_s}{m_u} & 0 & -\frac{k_u+k_s}{m_u} & 0 & 0 \\ K_\alpha \alpha_1 \frac{u}{\tau} & 0 & 0 & 0 & 0 & -\frac{1}{\tau} \end{bmatrix}, \quad B = \begin{bmatrix} 0 \\ 0 \\ \frac{K_v}{m_s} \\ 0 \\ -\frac{K_v}{m_u} \\ 0 \end{bmatrix},$$

$$E = \begin{bmatrix} \beta_1\sqrt{u} \\ 0 \\ 0 \\ 0 \\ 0 \\ K_\alpha\beta_1\frac{sqrt(u)}{\tau} \end{bmatrix}, C_z = \begin{bmatrix} 0 & -\frac{k_s}{m_s} & 0 & \frac{k_s}{m_s} & 0 & 0 \\ 0 & 0 & 0 & 0 & 0 & 0 \\ -1 & 0 & 0 & 1 & 0 & 0 \\ -1 & 0 & 0 & 1 & 0 & 1 \end{bmatrix},$$

$$D_{zu} = \begin{bmatrix} \frac{K_v}{m_s} \\ 1 \\ 0 \\ 0 \end{bmatrix}, F_{zw} = \begin{bmatrix} 0_{4*1} \end{bmatrix},$$

$x(t)$ denotes the system state, $u(t)$ the input, $z(t)$ the objective vector and w a zero-mean unitary variance white noise hereafter defined

$$x = \begin{bmatrix} z_r \\ z_s \\ \dot{z}_s \\ z_u \\ \dot{z}_u \\ \tilde{z}_r \end{bmatrix} \quad u = i \;\; z = \begin{bmatrix} \ddot{z}_s \\ i \\ z_u - z_r \\ z_p \end{bmatrix} \tag{5.42}$$

In $z(t)$, the control design specifications are included.

- **Frequency shaping of the state-space realization**

  One denotes with $W_a(s)$ the filter shaping the vertical acceleration $\ddot{z}_s(t)$, with $W_u(s)$ the one shaping the current $i(t)$ and with

  $$W_z(s) = diag\left\{W_a(s), W_u(s), 1, 1\right\} \tag{5.43}$$

  the overall filter for $z(t)$. In addition, one can also shape the energy of the road profile by introducing a filter $W_d(s)$.

  By calling $(A_{wd}, B_{wd}, C_{wd}, D_{wd})$ and $(A_{wz}, B_{wz}, C_{wz}, D_{wz})$ the state representations of the filters $W_d(s)$ and $W_z(s)$,the following augmented state can be obtained

  $$x_g = \begin{bmatrix} x^T & x_z^T & x_d^T \end{bmatrix}^T \tag{5.44}$$

  and the overall state space representation (Eq.5.9) can be characterized by the following state-space matrices [17]:

  $$A_g = \begin{bmatrix} A & 0 & EC_{wd} \\ B_{wz}C_z & A_{wz} & B_{wz}FC_{wd} \\ 0 & 0 & A_{wd} \end{bmatrix}, \quad B_{gu} = \begin{bmatrix} B \\ B_{wz}D_{zu} \\ 0 \end{bmatrix},$$

  $$B_{gw} = \begin{bmatrix} ED_{wd} \\ B_{wz}F_{zw}D_{wd} \\ B_{wd} \end{bmatrix}, \quad C_{gz} = \begin{bmatrix} D_{wz}C_z & C_{wz} & D_{wz}F_{zw}C_{wd} \end{bmatrix}, \tag{5.45}$$

  $$D_{gzu} = D_{wz}D_{zu}, \quad D_{gzw} = D_{zu}F_{zw}D_{wd}$$

- H_2 **MIPC state feedback control**

  By using a standard Kalman filter as the observer, a state-feedback controller

  $$u(t) = -K_2 x_g(t) \tag{5.46}$$

  can be used and the following closed-loop system results

  $$\begin{cases} \dot{x}_g(t) &= \underbrace{(A_g - B_{gu}K_2)}_{A_{cl}} x_g(t) + \underbrace{B_{gw}}_{B_{cl}} w(t) \\ \tilde{z} &= \underbrace{(C_{gz} - D_{gzu}K_2)}_{C_{cl}} x_g(t) + \underbrace{D_{gzw}}_{D_{cl}} w(t) \end{cases} \tag{5.47}$$

  with:

  $$T(s) = C_{cl}(sI - A_{cl})^{-1}B_{cl} + D_{cl} \tag{5.48}$$

  being the closed-loop transfer matrix between $w(t)$ and $\tilde{z}(t)$. Then, a multi-objective H_2 control law can be determined by solving the following LMI optimization problem.

  $$\begin{cases} [X_2, Y_2] = argmin_{X,Y,Q,\gamma}\ \gamma \\ s.t \\ Q > 0; \\ \gamma > 0; \\ tr(Q) \leq \gamma; \\ X = X^T > 0; \\ \begin{bmatrix} A_g X - B_{gu}Y + (A_g X - B_{gu}Y)^T & B_{gw} \\ * & -I \end{bmatrix} < 0; \\ \\ \begin{bmatrix} X & (C_{gz}X - D_{gzu}Y)^T \\ * & Q \end{bmatrix} > 0 \end{cases} \tag{5.49}$$

  If a solution exists, the optimal controller is given by

  $$K_2 = Y_2 X_2^{-1} \tag{5.50}$$

5.2.7.2 Regenerative damper strategy

This kind of control strategy is the most natural in this kind of applications. It consists of regulating the motion of the actuator to mimic the behaviour of a passive viscous damper [16]. Specifically, the actuator provides a force $f(t)$ according to the following law

$$f(t) = K_v i(t) = -c(\dot{z}_s(t) - \dot{z}_u(t)) \tag{5.51}$$

This equation leads directly to the following control law

$$i(t) = -\frac{c}{K_v}(\dot{z}_s(t) - \dot{z}_u(t)) \tag{5.52}$$

that is simply to implement requiring only a sensor that measures the relative speed between the sprung and the unsprung masses. The tuning of this control law consists to select a value for the viscous parameter c that should be chosen as a compromise among ride comfort, road handling and energy harvesting objectives.

5.2.8 Results and discussions

To comprehensively assess and contrast the regenerative damper, H_2 MIPC, and LQR control methodologies, several Matlab/Simulink simulations have been performed. The simulations have been undertaken via MATLAB R2022b running on a 64-bit Windows 10 with 3.5GHz Intel(R) Xeon(R) W-2265 CPU and 64 GB of RAM. The optimization problems have been solved using the solver MOSEK. Alternatively, Sedumi solver has also been used and the results are almost the same with both solvers.

To evaluate robustness under realistic operating conditions, the following non-idealities have been introduced into the simulation framework:

- Sensor noise, modeled as zero-mean Gaussian white noise, as described in [97],
- Actuator saturation, imposed with current limits in the range $[-10, 10]$ A.

Each control strategy was evaluated under identical conditions, including the same LPMA actuator (refers to Table A.8 of the appendix A for actuator's data), driving scenario, and quarter car model. The vehicle selected for these simulations is a typical class **C** car, with detailed specifications provided in Tables A.2 and A.3 of the appendix A. To effectively characterize the road profile, the signal presented in Fig.5.2 has been considered. This signal is instrumental in depicting the diverse road conditions that the vehicle will face during the simulation tests.

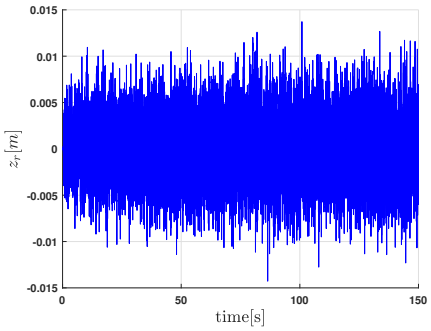

Figure 5.2: Signal characterizing the road profile.

The Ride Index (RI) threshold values used in this study are selected based on the guidelines provided by the ISO 2631 standard [90], which defines acceptable limits for human exposure to whole-body vibration in

$RI = 0.25$			$RI = 0.47$			$RI = 0.70$		
$K_\alpha = 0.03, \tau = 0.0005$			$K_\alpha = 0.07, \tau = 0.0005$			$K_\alpha = 0.1, \tau = 0.0005$		
ρ	β	γ	ρ	β	γ	ρ	β	γ
0.4	0.1	1	0.72	0.2	1	0.95	0.36	1

Table 5.2: MIPC H_2 static state feedback tuning parameters – $RI = 0.25$ (not uncomfortable), $RI = 0.47$ (a little uncomfortable) and $RI = 0.70$ (fairly uncomfortable).

	$RI = 0.25$	$RI = 0.47$	$RI = 0.70$
ρ	0.25	0.40	0.45
α	39	105	200

Table 5.3: LQR tuning parameters – $RI = 0.25$ (not uncomfortable), $RI = 0.47$ (a little uncomfortable) and $RI = 0.70$ (fairly uncomfortable).

terms of comfort perception. Specifically, the standard classifies passenger responses as follows: $RI = 0.25$ corresponds to a condition that is "not uncomfortable", $RI = 0.47$ is considered "a little uncomfortable"', and $RI = 0.70$ is associated with a "fairly uncomfortable" experience. These thresholds are used to assess and constrain ride comfort within the control design, ensuring that the proposed strategy maintains vibration levels within acceptable human tolerance limits under various operating conditions.

Moreover, it is essential to emphasize that the maximum suspension deflection for an automobile shock absorber during typical running conditions is between 50 and 80 mm. This specification must be met to guarantee the vehicle's performance and to maintain passenger comfort [97]-[98].

The following dynamical weights have been used for the H_2 MIPC control

$$W_a(s) = \rho \frac{81.89s^3 + 796.6s^2 + 1937s + 0.1446}{s^4 + 80s^3 + 2264s^2 + 7172s + 21196} \tag{5.53}$$

$$W_u(s) = \beta \frac{s + 100}{s + 10000} \tag{5.54}$$

$$W_d(s) = \gamma \frac{10}{s + 10} \tag{5.55}$$

where filters tuning parameters ρ, β and γ have been chosen to adjust the Ride Index.

Table 5.2 presents the values of the design knobs (ρ, β, γ) used in all the simulations for the quarter car model under the MIPC strategy. On the other side, Table 5.3 lists the tuning parameters for the LQR strategy. In particular, the tuning parameters include ρ, which affects the filter on acceleration, and α that is used in the LMI condition related to the Ride Index. Adjusting these parameters is essential to obtain different Ride Index values and achieve the desired vehicle performance and comfort levels.

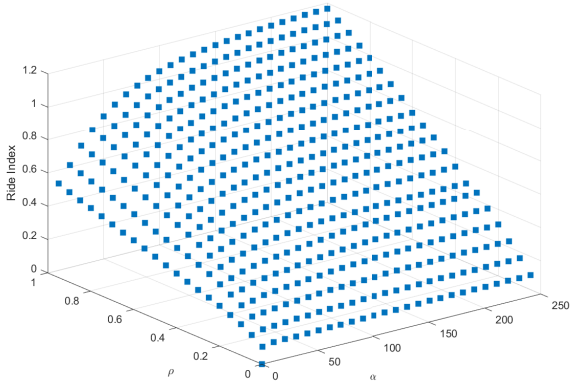

Figure 5.3: Sensitivity of the Ride index to α and ρ

In the context of ride comfort optimization, the tuning of control parameters, specifically α and ρ in the proposed LQR formulation, plays a critical role in balancing energy harvesting and passenger comfort. These parameters, analogous to hyperparameters in machine learning, are not learned automatically but must be selected to achieve the desired system behavior. Grid search has been employed in this work as a systematic and exhaustive tuning methodology. It allows to evaluate the performance over a predefined range of values for α and ρ, allowing us to explore the trade-off surface between electrical power and the Ride Index. This method, while computationally simple, is effective in identifying regions of the parameter space where comfort constraints (as defined by ISO 2631) are satisfied without severely compromising energy recovery. Proper tuning of α and ρ is essential for ensuring that the controller meets ride comfort specifications. The methodology chosen for tuning directly affects not only computational effort but also the ability to identify optimal trade-offs between comfort and energy efficiency. The effect of parameter tuning on ride comfort is further illustrated in Fig.5.3, which shows the variation of the Ride Index as a function of α and ρ. The figure highlights several combinations of these parameters that correspond to key comfort thresholds defined by the ISO 2631 standard namely RI = 0.25, 0.47, and 0.70. Fig.5.4 also depicts the corresponding variation in harvested electrical power across the same parameter space. This figure provides a valuable framework for selecting tuning parameter values that achieve the desired balance between ride comfort and energy harvesting efficiency. This supports an informed tuning process and demonstrates the sensitivity of the control outcome to proper parameter selection.

In what follows, four distinct simulation scenarios are presented. The first scenario considers a simulation without any constraints on the Ride Index. The other three scenarios are designed with specific Ride Index conditions of $RI = 0.25$, $RI = 0.47$ and $RI = 0.70$, respectively. These scenarios allow for a comprehensive evaluation of how varying Ride Index conditions affect

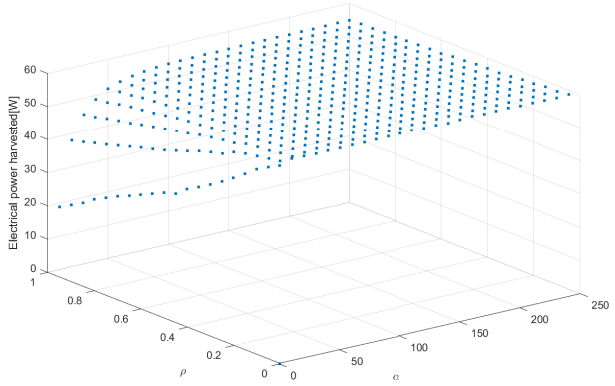

Figure 5.4: Sensitivity of the electrical power to α and ρ

vehicle performance and passenger comfort.

5.2.8.1 Scenario 1

The first scenario refers to a simulation where no constraints are imposed on the Ride Index. This scenario establishes a baseline, helping to evaluate the natural performance and comfort levels of the vehicle without any predetermined Ride Index conditions.

In this respect, Fig.5.5 illustrates the acceleration $\ddot{z}_s(t)$, actuation current $u(t)$, harvested electrical power $P_e(t)$, and harvested electrical energy $E_e(t)$ for the three control laws. Among these control laws, the LQR controller exhibits the highest acceleration, indicating the lowest level of passenger comfort. The control inputs for all three control laws are within the same range of $[-10; 10]$ A. In this scenario, the LQR strategy generates an average power of -58.6 W and an average energy of -8789 J. The resulting Ride Index value is 1.25, which indicates a relatively uncomfortable ride. This scenario highlights the trade-off between power generation and passenger comfort when no specific Ride Index constraints are imposed. Conversely, the Viscous Regenerative Damper yields an average power of -34.9 W and an average energy of -5235 J. The higher damping coefficient results in stronger damping forces, effectively mitigating oscillations and vibrations in the vehicle suspension. A damping coefficient of $c = 180$ N/(m/s) was selected for the regenerative damper, as it provides a good balance between energy harvesting and passenger comfort. It is worth noting that the unconstrained LQR strategy achieves the highest energy harvesting among the three control laws, followed by the H_2 MIPC in terms of energy harvesting efficiency. However, this comes at the cost of passenger comfort, as the LQR strategy provides the lowest comfort level. To enhance comfort, the LQR strategy can be refined by incorporating an appropriate constraint on the Ride Index. This adjustment helps to balance energy harvesting and passenger comfort more effectively.

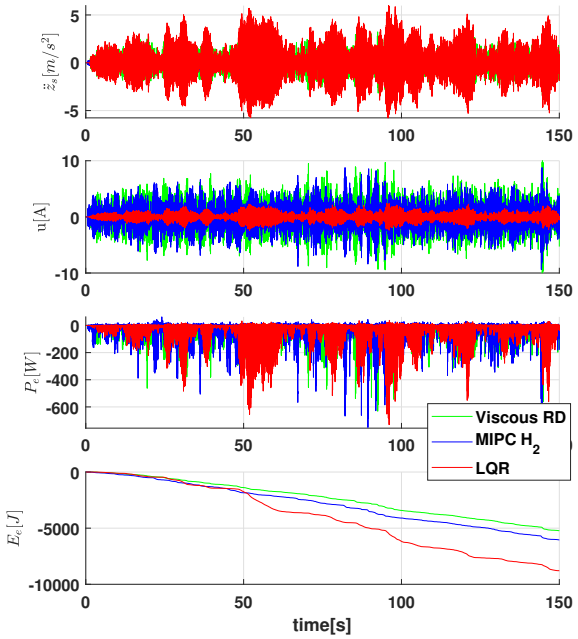

Figure 5.5: Scenario 1: Acceleration $\ddot{z}_s(t)$, actuation current $u(t)$, harvested electrical power $P_e(t)$ and harvested electrical energy $E_e(t)$

- Internal stability analysis

  The analysis of the internal stability of the system is carried out, for various values of λ, by looking at the poles of transfer function between the disturbance $w(t)$ and the objective $\tilde{z}(t)$ defined by Eq. (5.9). Table 5.4 presents the corresponding closed loop poles (real parts and imaginary parts) and stability margins of the closed-loop system (gain in *decibels* and phase in *degrees*), thereby confirming its stability across all configurations. It provides the range of real parts and imaginary parts of the closed-loop poles associated with each controller. In addition, Table 5.4 reports the harvested electrical energy E_e obtained by solving the optimization problem for multiple values of λ, using both the MOSEK and SEDUMI solvers. The results show that, regardless of the chosen λ, all synthesized controllers yield comparable performance in terms of harvested energy (approximately -8800 J), indicating limited sensitivity to this design parameter and reinforcing the robustness of the proposed control framework. Based on the results presented in Table 5.4, it can be concluded that the closed-loop system remains stable for all considered values of λ, thereby confirming the suitability of the proposed control design for energy harvesting applications.

  A convergence analysis of the LQR optimization process is provided in Fig.5.6 and Fig.5.7 corresponding to two different values of the cost bound: $\lambda \geq 0$ and $\lambda \geq -10$, respectively. These figures illustrate the

Bound	E_e (Mosek)	E_e (Sedumi)	Re(pole)	Im(pole)	Gain	Phase
$\lambda \geq 0$	-8789 J	-8842 J	[-77;-0.18]	[-84.75;84.75]	-21.5	27.5
$\lambda \geq -10$	-8779 J	-8851 J	[-77;-0.19]	[-84.76;84.76]	-20.7	27.1
$\lambda \geq -100$	-8721 J	-8862 J	[-77;-0.17]	[-84.8;84.8]	-18.7	26.2
$\lambda \geq -200$	-8794 J	-8851 J	[-77;-0.18]	[-84.8;84.8]	-18.5	26.1
$\lambda \geq -1000$	-8735 J	-8859 J	[-77;-0.18]	[-84.79;84.79]	-18.3	26.1

Table 5.4: Harvested energy using different controllers with MOSEK/SEDUMI solvers and stability analysis

evolution of the cost function across iterations of the optimization solver. In both cases, the solver successfully converges to the expected optimal value defined by the constraint ($\lambda = 0$ in the first case and $\lambda = -10$ in the second case) thus confirming the correctness and numerical stability of the LMI-based formulation.

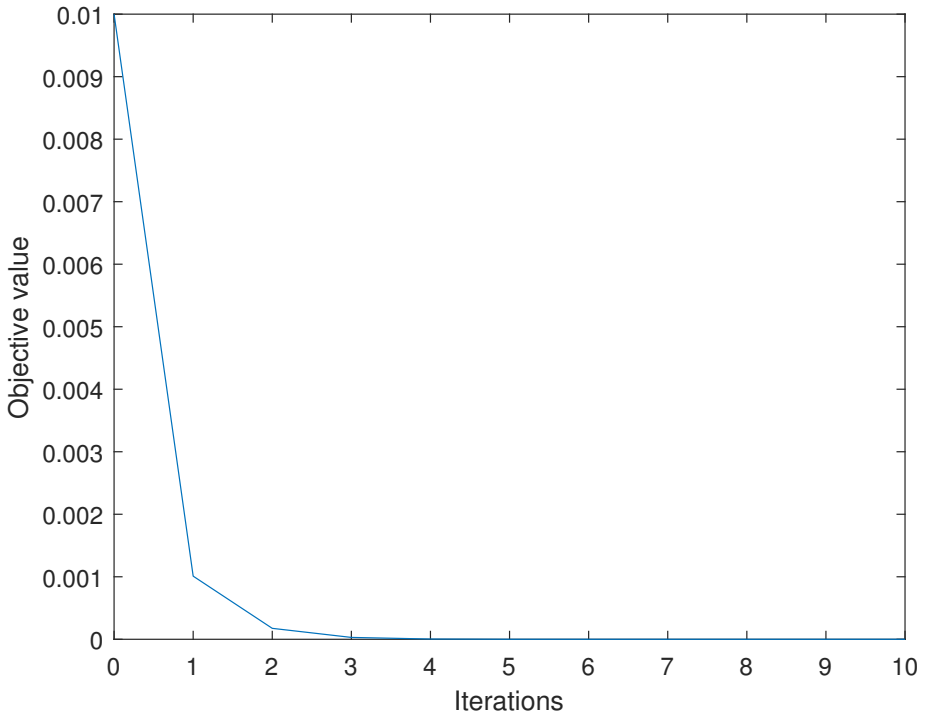

Figure 5.6: Convergence analysis for $\lambda \geq 0$

It is important to note that the dynamic load acting on the vehicle is strongly influenced by a range of factors, including pavement roughness, vehicle speed, tire pressure, tire dimensions, and the characteristics of the suspension system. These factors induce variations in both the frequency content and the magnitude of the load acting on the vehicle. In this context, it becomes essential to assess the stability of the proposed LQR-based control strategy across different road excitation

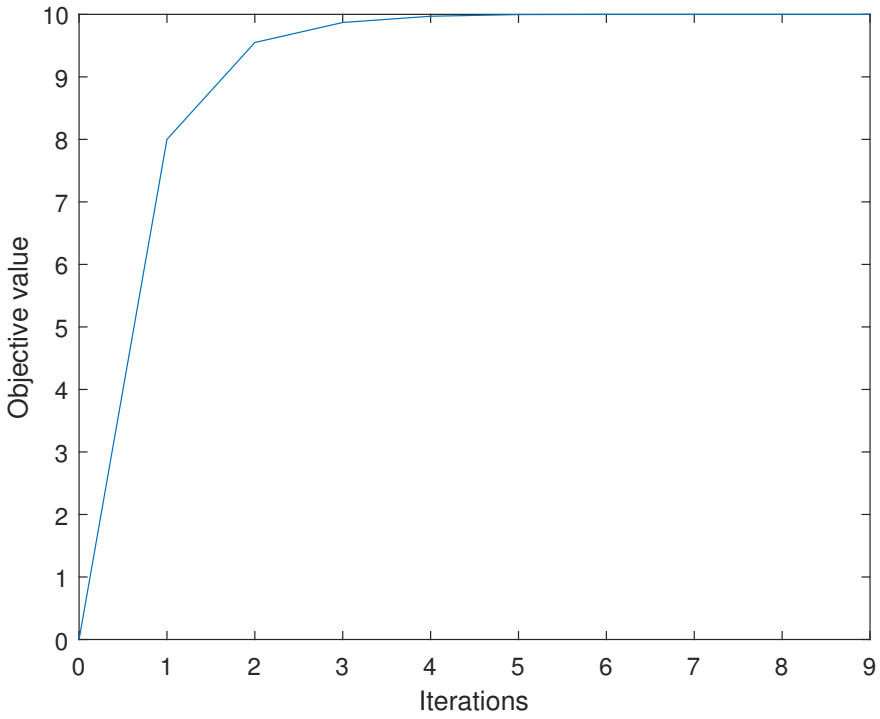

Figure 5.7: Convergence analysis for $\lambda \geq -10$.

scenarios. In particular, to evaluate stability, the analysis focuses on the eigenstructure of the closed-loop system, specifically examining the real parts of the poles of the associated transfer function. Table 5.5 reports the real parts of the dominant poles obtained under a range of road profiles, classified from Class A to Class H in accordance with the ISO 2631 standard and the duration required to solve the optimization problem. This analysis provides insight into the robustness of the control strategy when subjected to varying external disturbances representative of real-world driving conditions. For all considered road conditions, the closed-loop poles exhibit negative real parts, thereby confirming the internal stability of the LQR control law. The corresponding results provide an indication of the method's efficiency across varying road excitation conditions. From the presented results, it is possible to assess that LMIs can be viewed as an efficient framework for solving the proposed optimization problem, primarily due to their computational simplicity and the availability of well-established convex optimization solvers.

- Comfort vs. energy harvesting trade-offs across road conditions

  Fig.5.8 provides a heat-map that highlights the trade-off between ride comfort and energy harvesting under varying road conditions, classified from Class A (very good) to Class H (extremely poor) according to the ISO 2631 standard. The results show that harvested electrical

Type of roads	Re(eigenvalue)	Execution time in seconds
A	[-77;-0.18]	15.41
B	[-77;-0.18]	15.23
C	[-77;-0.18]	15.09
D	[-77;-0.18]	15.95
E	[-77;-0.18]	15.57
F	[-77;-0.18]	15.41
G	[-77;-0.18]	16.64
H	[-77;-0.18]	16.60

Table 5.5: Stability analysis and execution time for different road conditions and $\lambda \geq 0$.

power increases with road roughness, while ride comfort decreases accordingly. This emphasizes the importance of explicitly enforcing a Ride Index constraint within the control formulation. Furthermore, the visualization suggests that optimal values of the tuning parameters α and ρ must be adapted to each road type to maintain comfort within acceptable bounds. This analysis further supports the evaluation of practical feasibility and efficiency among the control strategies.

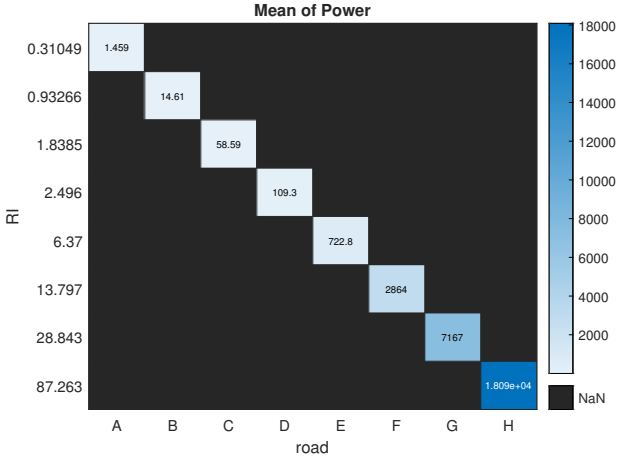

Figure 5.8: LQR approach's Ride Index heatmap accross different road conditions

5.2.8.2 Scenario 2

The second scenario illustrates the impact of imposing a strict Ride Index condition on the control strategies. By setting $RI = 0.25$, the focus shifts towards maximizing passenger comfort, resulting in the smallest energy harvesting among the scenarios. Fig.5.9 shows the plots of the three control laws' acceleration $\ddot{z}_s(t)$, actuation current $u(t)$, electrical power $P_e(t)$, and harvested electrical energy $E_e(t)$ for $RI = 0.25$.

It is observed that the acceleration for the regenerative viscous damper control law is the greatest, while the accelerations for the MIPC and LQR

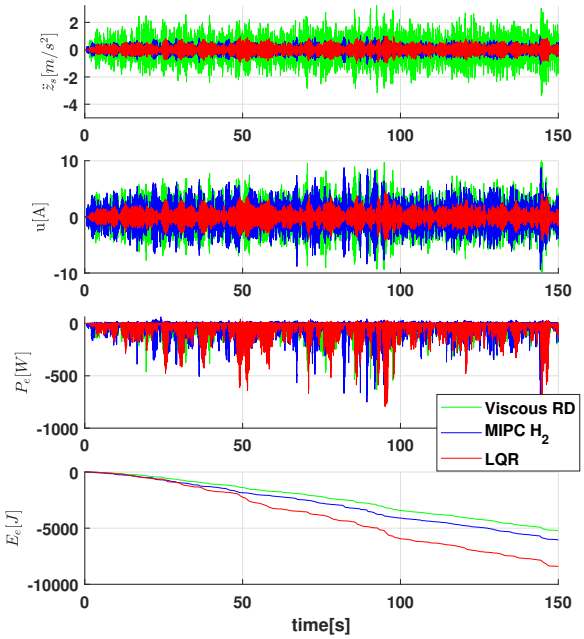

Figure 5.9: Scenario 2: Acceleration $\ddot{z}_s(t)$, actuation current $u(t)$, harvested electrical power $P_e(t)$ and harvested electrical energy $E_e(t)$

controllers are within the range of $[-1; 1]m/s^2$ that ensure excellent comfort for the passengers, as indicated by the low acceleration levels. Additionally, the control inputs for all three control laws remain within the same range of $[-10; 10]A$, ensuring the feasibility and stability of the system.

In terms of energy harvesting, as reported in Table 5.6 and Table 5.10, the LQR strategy achieves the highest energy, followed by the MIPC. Both strategies outperform the viscous regenerative damper controller in energy harvesting efficiency. This demonstrates that even with a focus on comfort, the LQR and MIPC strategies can still maintain relatively high energy harvesting performance compared to the viscous regenerative damper. This highlights the trade-off between comfort and energy harvesting efficiency, with the LQR and MIPC strategies being adjusted to prioritize comfort over energy generation.

5.2.8.3 Scenario 3

The third scenario is designed with a specific Ride Index condition of $RI = 0.47$, which represents a trade-off between comfort and energy harvesting. Fig.5.10 illustrates the acceleration $\ddot{z}_s(t)$, actuation current $u(t)$, electrical power $P_e(t)$, and harvested electrical energy $E_e(t)$ for the three control laws.

The third scenario demonstrates the trade-off between passenger comfort and energy harvesting. In fact, the control strategies (MIPC and LQR) achieve a balanced performance, ensuring that both comfort and energy

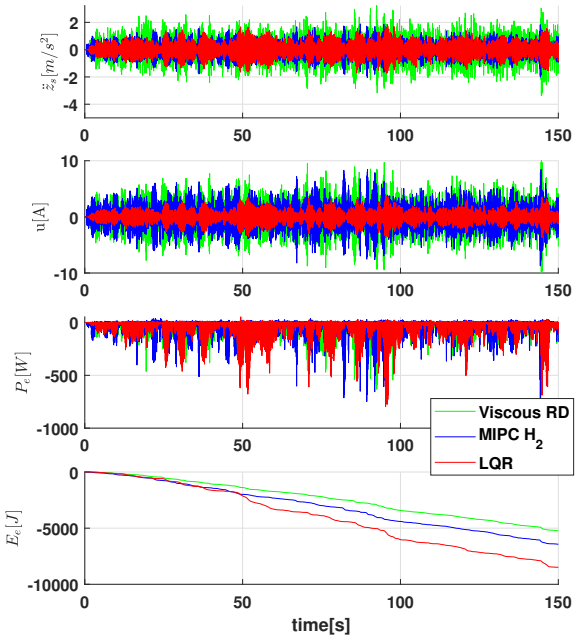

Figure 5.10: Scenario 3: Acceleration $\ddot{z}_s(t)$, actuation current $u(t)$, harvested electrical power $P_e(t)$ and harvested electrical energy $E_e(t)$

Harvested Electrical Energy			
	$RI = 0.25$	$RI = 0.47$	$RI = 0.70$
RD [J]	-5235	-5235	-5235
H_2 MIPC [J]	-6050	-6443	-7309
LQR [J]	-8411	-8491	-8559

Table 5.6: Electrical Energy for $RI = 0.25$, $RI = 0.47$ and $RI = 0.70$

Road handling			
	$RI = 0.25$	$RI = 0.47$	$RI = 0.70$
RD [cm]	[-3;3]	[-3;3]	[-3;3]
H_2 MIPC [cm]	[-3.5;3.5]	[-3.8;3.8]	[-4.2;4.2]
LQR [cm]	[-5;5]	[-5.4;5.4]	[-5.8;5.8]

Table 5.7: Road handling for $RI = 0.25$, $RI = 0.47$ and $RI = 0.70$

harvesting are optimized to a satisfactory level. This scenario highlights the ability to fine-tune control laws to meet specific objectives, balancing the needs for passenger comfort and energy efficiency.

Finally note that the acceleration for the regenerative damper control law remains the highest, while the accelerations for the MIPC and LQR controllers are greater than in the $RI = 0.25$ scenario. This increase in acceleration implies improved energy harvesting performance, while the

Suspension Stroke			
	$RI = 0.25$	$RI = 0.47$	$RI = 0.70$
RD [cm]	[-3;3]	[-3;3]	[-3;3]
H_2 MIPC [cm]	[-3.8;3.8]	[-4;4]	[-4.2;4.2]
LQR [cm]	[-5;5]	[-5.4;5.4]	[-5.8;5.8]

Table 5.8: Suspension stroke for $RI = 0.25$, $RI = 0.47$ and $RI = 0.70$

Acceleration			
	$RI = 0.25$	$RI = 0.47$	$RI = 0.70$
RD $[m/s^2]$	[-4;4]	[-4;4]	[-4;4]
H_2 MIPC $[m/s^2]$	[-1;1]	[-2;2]	[-3;3]
LQR $[m/s^2]$	[-1;1]	[-2;2]	[-3;3]

Table 5.9: Acceleration for $RI = 0.25$, $RI = 0.47$ and $RI = 0.70$

Average Electrical Power			
	$RI = 0.25$	$RI = 0.47$	$RI = 0.70$
RD [W]	-34.90	-34.90	-34.90
H_2 MIPC [W]	-40.33	-42.95	-48.73
LQR [W]	-56.07	-56.60	-57.06

Table 5.10: Average Electrical Power for $RI = 0.25$, $RI = 0.47$ and $RI = 0.70$

Harvested Electrical Energy			
	$RI = 0.25$	$RI = 0.47$	$RI = 0.70$
RD [J]	-5257	-5257	-5257
H_2 MIPC [J]	-6040	-6425	-7322
LQR [J]	-8548	-8621	-8641

Table 5.11: Electrical Energy for $RI = 0.25$, $RI = 0.47$ and $RI = 0.70$ considering the new system's parameters

control inputs remain within the same range of $[-10; 10]A$. Specifically, as reported in Tables 5.6 and 5.10, the LQR strategy harvests more effectively in this instance than in the $RI = 0.25$ scenario. Similarly, the MIPC strategy also shows enhanced energy harvesting performance. Both the LQR and MIPC strategies outperform the viscous regenerative damper control in terms of energy harvesting efficiency.

5.2.8.4 Scenario 4

In this scenario, the control strategies are tuned to achieve a Ride Index of $RI = 0.70$, prioritizing energy harvesting efficiency even at the expense of passenger comfort. Fig.5.11 illustrates the acceleration $\ddot{z}_s(t)$, actuation current $u(t)$, electrical power $P_e(t)$, and harvested electrical energy $E_e(t)$ for the three control laws.

In this scenario, it is observed that the accelerations of the three control laws are equivalent. The control inputs remain within the same range. The LQR strategy generates more power and energy compared to the previous case with $RI = 0.47$. It is followed by the MIPC H_2 control, and both outperform the Viscous Regenerative Damper in terms of energy harvesting efficiency.

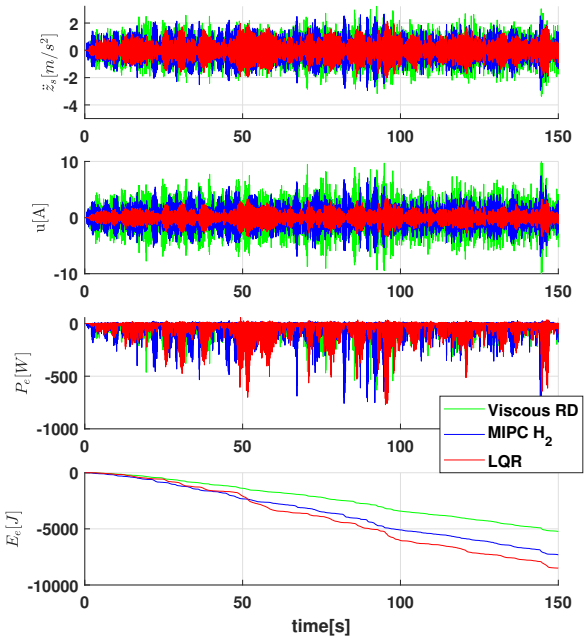

Figure 5.11: Scenario 4: Acceleration $\ddot{z}_s(t)$, actuation current $u(t)$, harvested electrical power $P_e(t)$ and harvested electrical energy $E_e(t)$

5.2.8.5 Comments to the simulation results

Fig.5.12 and Fig.5.13 depict the sensitivity of electrical power with respect to ρ and α, respectively. In particular, Fig.5.12 shows how the tuning parameter ρ influences both the Ride Index and the harvested electrical power. As ρ increases, the Ride Index consistently increases, indicating reduced ride comfort. In contrast, the harvested power varies with ρ in a non-uniform manner, reaching a maximum within a certain range before decreasing at higher values. This highlights the presence of a tuning region where an effective trade-off between comfort and energy efficiency can be achieved. Similarly (ref. to Fig.5.13), increasing α leads to simultaneous increases of both the Ride Index and the harvested electrical power, revealing a direct trade-off: improved energy recovery is associated with reduced ride quality. In this case, both performance indicators reach their peak values at the upper end of the considered α interval. Together, these analyses highlight the importance of careful parameter tuning to balance conflicting objectives in suspension control design.

The simulation outcomes, as summarized in Tables 5.6, 5.7, 5.8, 5.9, and 5.10, allow a comprehensive comparison of the performance metrics - harvested energy, road handling, suspension stroke, vertical acceleration and average electrical power - under various Ride Index constraints.

These results show that the LQR controller allows one to outperform both the H_2 MIPC and the regenerative damper strategies, achieving higher energy recovery while satisfying ride comfort specifications. It is important to recall that the regenerative damper strategy does not actively constrain acceleration and, therefore, fails to meet comfort requirements under these conditions. The proposed LQR approach demonstrates strong robustness against sensor noise and actuator limitations, while maintaining superior performance in both energy harvesting and ride comfort compared to the other approaches considered. Although road handling and suspension stroke are not directly enforced as constraints in the control formulation, the results demonstrate that the proposed method does not significantly compromise handling performance and suspension stroke, achieving an acceptable trade-off among the key performance objectives. Moreover, the inverse relationship between energy harvesting and ride comfort can be highlighted: higher energy recovery is typically associated with reduced comfort and increased tire deflection. This highlights the inherent conflict between energy harvesting and both ride comfort and handling.

Balancing safety and performance in control systems is a challenge that involves finding the right balance between keeping things safe and making sure they work well. Failure analysis of vehicle suspension system has been undertaken in [99]. It has been observed that a vehicle suspension system fails because of poor surface finish, poor operating conditions and excessive loading. In [100], the new concept of series active variable geometry suspension incorporates fail safe, since this system can switch back to the original passive suspension if the single-link actuator suffers power loss or

even failure. While road handling and suspension stroke cannot be directly integrated into the LQR control scheme, it is important to highlight that both energy harvesting and ride comfort have been markedly enhanced, without an important reduction in road handling or suspension stroke performance, which are more closely associated with the fatigue experienced by the actuators.

From a computational perspective, the regenerative damper strategy is the most efficient, requiring only 5 seconds per simulation, whereas the LQR and MIPC H_2 controllers require approximately 15 seconds due to their more complex optimization and feedback mechanisms. This comparative analysis confirms that the LQR approach not only achieves a superior balance between energy harvesting and comfort, but also does so with a lower tuning complexity than MIPC H_2, which requires four tuning parameters and multiple filters. Despite a slightly higher computational burden than the regenerative damper, the proposed strategy remains feasible for real-time implementation and offers a clear advantage in performance and flexibility.

The influence of vehicle speed on control performance is presented in Fig.5.14, which shows how harvested electrical power and the associated Ride Index vary across different speeds, without any comfort constraint. Electrical power increases with speed, reaching a peak of -59 W at 80 km/h (RI = 1.89), before decreasing slightly. The second-highest value, -58.22 W, occurs at 70 km/h with RI = 1.82. These results demonstrate a non-linear relationship between speed and energy harvesting efficiency.

Across all tested speeds, the proposed LQR-based strategy consistently outperforms both MIPC H_2 and the regenerative damper in terms of energy recovery, suggesting that the controller's effectiveness increases with speed up to an optimal point, beyond which performance may decline due to dynamic instability or reduced actuator efficiency.

Finally, while uncertainties are commonly introduced in control system analysis to reflect modeling inaccuracies [97]-[98], the physical system considered in this work does not include explicit parametric uncertainty. In this respect, the primary source of uncertainty is modeled through the external stochastic disturbance $w(t)$, which represents road excitations. This disturbance is treated as a zero-mean Gaussian white noise process, consistent with ISO 2631-based modeling of road roughness via Power Spectral Density (PSD) profiles. No parametric uncertainty has been introduced in the system matrices, as the scope of this work focuses on evaluating the performance and robustness of the proposed LQR-based control strategy under realistic stochastic excitations.

5.2.8.6 Robustness of the proposed control law

In addition to the added non-idealities, the robustness of the proposed control law to physical parameter variations has been assessed. While structured uncertainty has not been directly considered in the system matrices, a

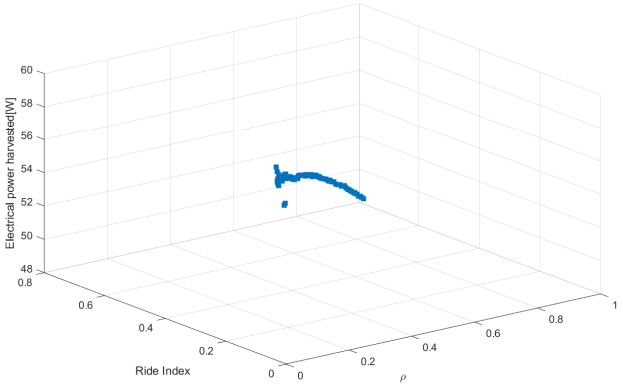

Figure 5.12: Sensitivity of P_e to ρ for $\alpha = 39$

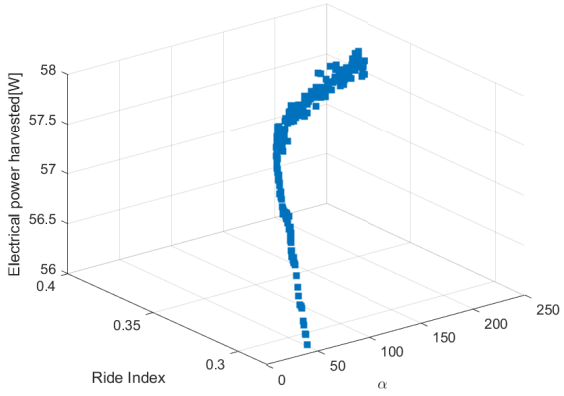

Figure 5.13: Sensitivity of P_e to α for $\rho = 0.25$

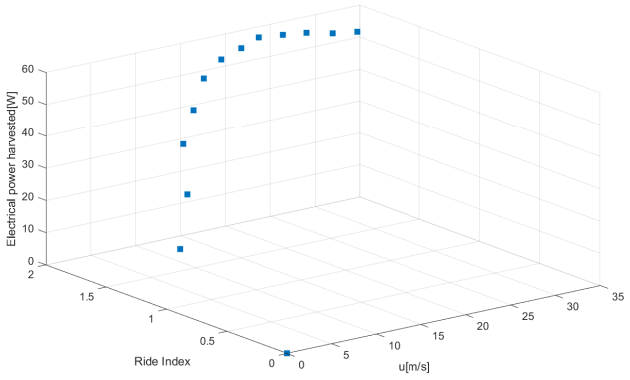

Figure 5.14: Sensitivity of the electrical power to the vehicle speed

sensitivity analysis has been conducted by modifying key parameters of the quarter-car model. In particular:

- The sprung mass was reduced from $m = 1274$ kg to $m = 1174$ kg,
- The suspension stiffness was reduced from $k_f = 27$ kN/m to $k_f = 25$

$RI = 0.25$			$RI = 0.47$			$RI = 0.70$		
$K_\alpha = 0.03, \tau = 0.0005$			$K_\alpha = 0.07, \tau = 0.0005$			$K_\alpha = 0.1, \tau = 0.0005$		
ρ	β	γ	ρ	β	γ	ρ	β	γ
0.95	0.36	1	0.7	4	1	1.3	4	1

Table 5.12: MIPC H_2 static state feedback tuning parameters – $RI = 0.25$ (not uncomfortable), $RI = 0.47$ (a little uncomfortable) and $RI = 0.70$ (fairly uncomfortable) with IPVA actuator

	$RI = 0.25$	$RI = 0.47$	$RI = 0.70$
ρ	0.60	0.45	2.5
α	39	10^3	10^2

Table 5.13: LQR tuning parameters – $RI = 0.25$ (not uncomfortable), $RI = 0.47$ (a little uncomfortable) and $RI = 0.70$ (fairly uncomfortable) with IPVA actuator

kN/m.

The results of this analysis are reported in Table 6.10, which shows the harvested energy under the new parameter set. Note also that the corresponding vertical accelerations remain consistent with those previously reported in Table 5.9. Despite the changes in physical parameters, the LQR control law remains the most effective strategy, confirming its robustness to moderate parameter uncertainties. In summary, the proposed LQR approach demonstrates strong robustness against sensor noise, actuator limitations, and parameter variations, while maintaining superior performance in both energy harvesting and ride comfort compared to the other approaches considered.

5.2.8.7 Application to the IPVA actuator on a quarter car model

Tables 5.12 to 5.18 present the results obtained with the use of the IPVA actuator described in Section 2.3.4. We note that in all control laws used in this section, the IPVA outperforms the LPMA actuator used previously in terms of energy harvesting. This confirms the results obtained in the previous chapter. In addition, the LQR is also the best control strategy for energy harvesting using the IPVA actuator.

5.2.8.8 Extension to a full-car model

The results obtained considering the full vehicle dynamics described in Eq.(2.6) and whose schematic is illustrated in Fig.2.3 with the LPMA actuator (refers to Table A.8 of the appendix A for actuator's data), are presented in Table 5.19. One notices that the LQR still outperforms the two other control laws.

Average Electrical Power with IPVA actuator			
	$RI = 0.25$	$RI = 0.47$	$RI = 0.70$
RD [W]	-319	-319	-319
H_2 MIPC [W]	-324	-325	328
LQR [W]	-325	-330	-331

Table 5.14: Average Electrical Power for $RI = 0.25$, $RI = 0.47$ and $RI = 0.70$ with IPVA actuator

Harvested Electrical Energy with IPVA actuator			
	$RI = 0.25$	$RI = 0.47$	$RI = 0.70$
RD [J]	-4.784*10^4	-4.784*10^4	-4.784*10^4
H_2 MIPC [J]	-4.854*10^4	-4.867*10^4	-4.924*10^4
LQR [J]	-4.866*10^4	-4.948*10^4	-4.964*10^4

Table 5.15: Electrical Energy for $RI = 0.25$, $RI = 0.47$ and $RI = 0.70$ with IPVA actuator

Acceleration with IPVA actuator			
	$RI = 0.25$	$RI = 0.47$	$RI = 0.70$
RD $[m/s^2]$	[-3.2;3.3]	[-3.2;3.3]	[-3.2;3.3]
H_2 MIPC $[m/s^2]$	[-1;1]	[-2;2]	[-3;3]
LQR $[m/s^2]$	[-1;1]	[-2;2]	[-3;3]

Table 5.16: Acceleration for $RI = 0.25$, $RI = 0.47$ and $RI = 0.70$ with IPVA actuator

Road handling with IPVA actuator			
	$RI = 0.25$	$RI = 0.47$	$RI = 0.70$
RD [cm]	[-3;3]	[-3;3]	[-3;3]
H_2 MIPC [cm]	[-3;3]	[-4;4]	[-5;5]
LQR [cm]	[-3;3]	[-3;3]	[-4;4]

Table 5.17: Road handling for $RI = 0.25$, $RI = 0.47$ and $RI = 0.70$ with IPVA actuator

Suspension stroke with IPVA actuator			
	$RI = 0.25$	$RI = 0.47$	$RI = 0.70$
RD [cm]	[-3;3]	[-3;3]	[-3;3]
H_2 MIPC [cm]	[-4;4]	[-4;4]	[-5;5]
LQR [cm]	[-3;3]	[-3;3]	[-4;4]

Table 5.18: Suspension stroke for $RI = 0.25$, $RI = 0.47$ and $RI = 0.70$ with IPVA actuator

Total Harvested Electrical Energy for the 4 wheels			
	$RI = 0.25$	$RI = 0.47$	$RI = 0.70$
RD [J]	-2.16*10^4	-2.16*10^4	-2.16*10^4
H_2 MIPC [J]	-2.61*10^4	-3.06*10^4	-3.64*10^4
LQR [J]	-3.49*10^4	-3.8*10^4	-4.05*10^4

Table 5.19: Electrical Energy harvested considering full-vehicle dynamics

Harvested Electrical Energy with the second road signal			
	$RI = 0.25$	$RI = 0.47$	$RI = 0.70$
RD [J]	-3196	-3196	-3196
H_2 MIPC [J]	-3839	-3949	-3993
LQR [J]	-4098	-4352	-4438

Table 5.20: Electrical Energy with the second road signal for $RI = 0.25$, $RI = 0.47$ and $RI = 0.70$

5.2.8.9 Second road signal

To validate the applicability to different scenarios of the proposed approach, an additional test was conducted using the road profile described in [16], the same LPMA actuator (refers to Table A.8 of the appendix A for actuator's data) and by accounting a vehicle characterized by the parameters reported in [69]. The corresponding results are presented in Table 5.20. These results show the capabilities of the proposed approach to overcome the performance of the Regenerative damper and the H_2 MIPC even using a different road signal. Moreover, it must be highlighted that the electrical energy harvested using the LQR without any RI condition is -4622 J.

Constraining the Ride Index and shaping the vertical acceleration have a significant impact on the performance of the control strategies. Notably, the LQR control consistently delivers the greatest amount of harvested energy in all scenarios. This underscores the LQR strategy's effectiveness in optimizing energy harvesting, even when balancing trade-offs with passenger comfort. In addition, the Ride Index constraint in the LQR strategy also improves the tire deflection (road handling) and suspension deflection (suspension stroke) when compared to the unconstrained LQR.

However one notices that with the LPMA actuator, the LQR has the worst characteristics in terms of road handling and suspension stroke even though these characteristics have not been significantly deteriorated. This could be explained by the fact the LQR strategy doesn't optimize directly tire deflection and suspension deflection. More advanced control strategies are needed to address this lack in the LQR strategy.

5.3 Simulations on Carsim 2025.1

5.3.1 Introduction to Carsim 2025.1 and Simulink model

The previous models used for simulations describe by means of a linear approximation the main motions of a vehicle suspension system. However in reality, things are much more complex. In fact there are phenomena that affect the trends of the main variables. Some of these phenomena are the non-linearities of the springs and shock absorbers, components' geometry, brake effects and many other aspects. These are neglected when designing the controller for the sake of simplicity. Otherwise we would have to deal with an excessively complex system on which it becomes extremely laborious to design a control algorithm. To assess the effectiveness of our control approaches, it is advisable to use models that are as accurate as possible. Therefore, we implement the previous control laws in the CarSim software. It is a well-known mechanical simulation tool from the Mechanical Simulation Company used to study vehicles dynamics. It is widely used at industrial level. It considers all the main components of a car, taking into account all the aspects listed above. It has many roads models to use in simulations. It is also possible to integrate CarSim's dynamic models with Simulink, in order to test feedback control systems such as ABS or any other control units. To do so, Simulink is used as a co-simulation software of CarSim.

Thanks to this tool, we can evaluate the effectiveness of our control laws on a car model very close to reality. The user does not see the dynamics equations directly. There are standard models of vehicles of different sizes integrated into CarSim. We define all the main parameters of the vehicle in the software's datasets. Then, we define the inputs and outputs we want to import and export from CarSim to Simulink.

The type of car chosen for the simulations is a class C vehicle depicted in Fig.5.15.

Figure 5.15: C-class vehicle in CarSim

This corresponds to a car of medium-large size (Audi A3, Chevrolet Cruze, Ford Focus, Opel Astra...). We use the default values for the main parameters of the vehicle. The inputs we define are four replacement forces

for the shock absorbers. In this context, CarSim has many forces to be used and one difficulty is to choose the good replacement forces for the shock absorbers. After discussion with the Mechanical Simulation Company, we choose the inputs called "Compressive force from damper" to replace the shock absorbers. The outputs are all those required for control, avoiding the use of observers here. We assume that we have sensors for the following quantities: the four ride spring compressions, roll, pitch, acceleration of the chassis, the four tire compressions, the four ride spring compression rates, the road profile, the four wheel speeds and the four wheel positions. With this software, it is possible to include the chassis acceleration along the x and y axis in the control law and not only along the z axis as in the previous simulations on Simulink. Fig.5.16 shows the Simulink model.

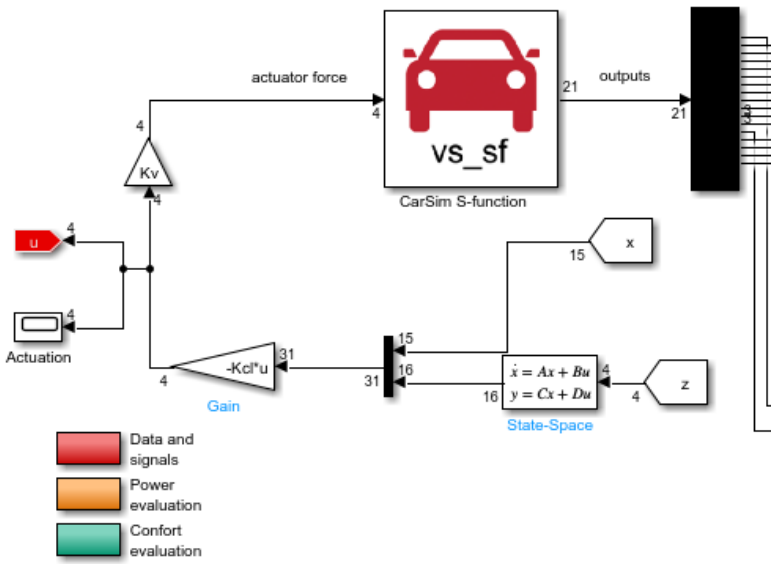

Figure 5.16: Simulink model of the LQ control with CarSim S-function

CarSim allows to export a single block called "CarSim S-function" that implements the equations of the vehicle dynamics. The generators and controllers are the same as for the full-car scheme in section 5.2.8.8. Since CarSim uses units of measurement different from those of the SI (e.g. Km/h for speed and g for acceleration), it is necessary to pre-process the data before giving them.

Three simulations have been carried out to test the behaviour of the car in different situations:

- A straight driving road at 70 km/h constant speed.
- A common double lane changing handling test at 70 km/h constant speed.
- Sine bumps at 20 km/h constant speed.

Total electrical power harvested with CarSim			
	RI=0.25	**RI=0.47**	**RI=0.70**
RD	-105[W]	-105[W]	-105[W]
H_2 MIPC	-125[W]	-251[W]	-520[W]
LQR	-157[W]	-363[W]	-661[W]

Table 5.21: Test 1: Total electrical power harvested with CarSim

5.3.2 Test 1: Straight driving road at 70 km/h constant speed

The road profile has a medium roughness as depicted in Fig.5.17.

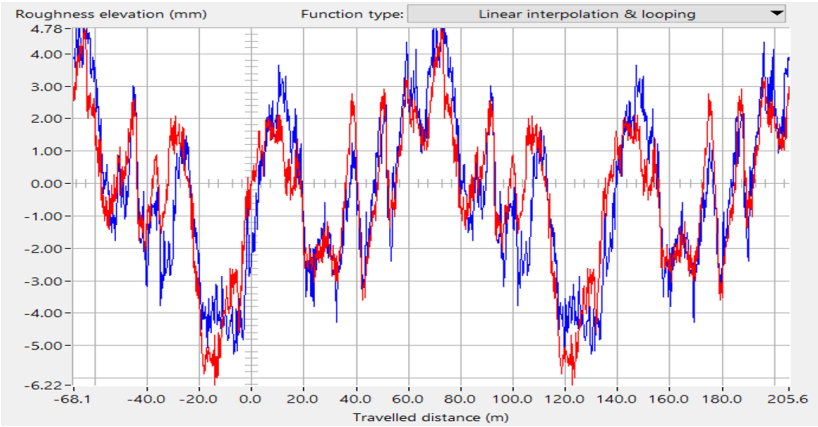

Figure 5.17: Straight driving road's roughness

The resulting plots with the LQR are presented in Figs.B.1-B.8 while the plots for the MIPC H_2 are depicted in Figs.B.9-B.16 of the appendix B. In these figures, we prioritize the comfort.

For the LQR control, the actuators currents, suspension deflections and tire deflections are maintained at fairly small values (see Figs.B.6,B.5, B.4 of the appendix B) thus also guaranteeing good road holding and negligible dissipation due to the negligible Joule effect. The same remark can be formulated for the MIPC H_2. For the LQR control, we have a roll's inclination of $[-0.1; 0.25]$ deg and a pitch's inclination of $[-0.4; 0.4]$ deg while the MIPC H_2 gives greater values of roll and pitch motions $[-0.6; 0.6]$ deg. The results for the three RI are summarized in Table 5.21. In all cases, the LQR outperforms the H_2 MIPC.

5.3.3 Test 2: A common double lane changing handling test at 70 km/h constant speed

The road profile roughness is depicted in Fig.5.18.

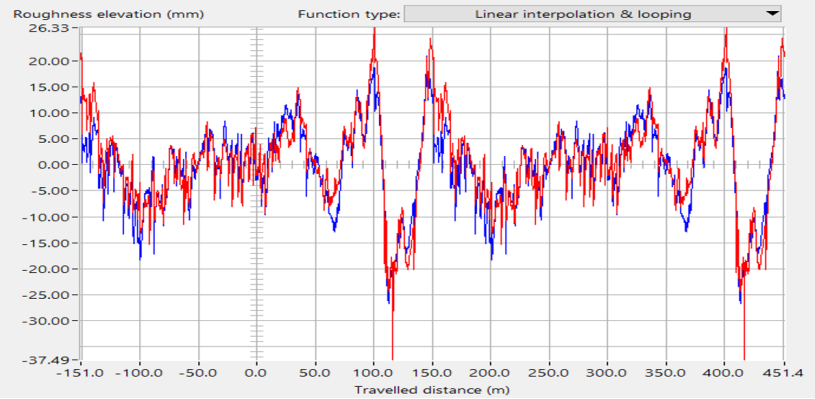

Figure 5.18: Double lane changing road's roughness

Test 2: Total electrical power harvested with CarSim			
	RI=0.25	**RI=0.47**	**RI=0.70**
H_2 MIPC	-47[W]	-93[W]	-146[W]
LQR	-71[W]	-122[W]	-350[W]

Table 5.22: Test 2: Total electrical power harvested with CarSim

The plots for the LQR are presented in Figs.B.17-B.24 of the appendix B while the plots for the MIPC H_2 are depicted in Figs.B.25-B.32 of the appendix B. In these figures, we prioritize the comfort.

For the LQR control, we notice that the actuators currents, suspension deflections and tire deflections have been increased (Figs.B.22,B.21, B.20) compared to Test 1's results. We also remark that the MIPC H_2 stabilizes the system faster than the LQ (see Figs.B.17, B.19, B.25, B.27). However, the MIPC H_2 provides greater roll and pitch's inclination than the LQR. The powers harvested for different RI are summarized in Table 5.22. In all cases, the LQR outperforms the H_2 MIPC.

5.3.4 Test 3: Sine bumps at 20 km/h constant speed

The road profile has a different roughness as depicted in Fig.5.19.

The plots for the LQR are presented in Figs.B.33-B.40 of the appendix B while the plots for the MIPC H_2 are depicted in Figs.B.41-B.48 of the appendix B. In these figures, we prioritize energy harvesting.

For the LQR control, we notice that the acceleration and the actuators currents have been increased $[-30; 40]$ m/s^2 and $[-60; 60]$ A respetively (see Figs.B.33 and B.38). The suspension deflections and tire deflections have been increased (Figs.B.37 and B.36) too but they remain within realistic limits. We note pitch and roll inclinations of $[-2; 2]$ deg and $[-2; 2.5]$ deg respectively which are great values.

For the MIPC H_2, we notice that the acceleration is similar to the one obtained with the LQ. Actuators currents are lower than what we have with

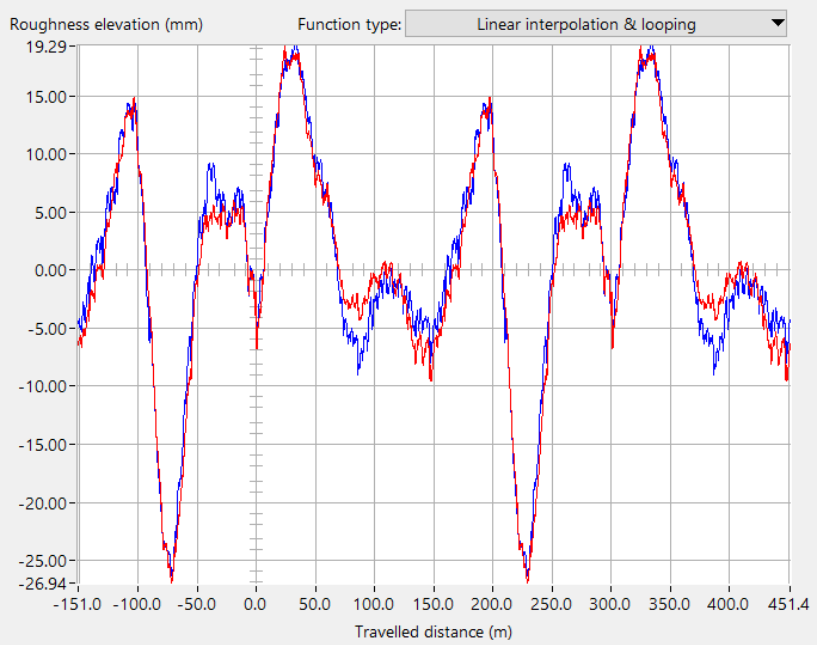

Figure 5.19: Sine bumps roughness

the LQR $[-25; 20]$ A (see Figs.B.41 and B.46). The suspension deflections and tire deflections have been increased too (Figs.B.45 and B.44) but they remain within realistic limits. We note pitch and roll inclinations of $[-2.5; 2.5]$ deg which are greater than the ones obtained with the MIPC H_2.

For both control laws, we obtain a $RI = 3$ which corresponds to "uncomfortable". The total electrical powers harvested are -4026 W and -3850 W for the LQR and the MIPC H_2 respectively.

5.4 Wave energy converters

5.4.1 WEC state space realization

For safe operation purpose, a set of constraints are imposed on the WEC's heave position (buoy's displacement), heave velocity (buoy's velocity) and control input (actuator's force), which can be expressed by

$$|z_v| \leq d_{max} \tag{5.56}$$

$$|\dot{z}_v| \leq v_{max} \tag{5.57}$$

$$|u| \leq u_{max} \tag{5.58}$$

where d_{max}, v_{max} and u_{max} are the maximal allowed heave position, heave velocity and control input respectively.

The WEC controller design objective is to maximize the energy output for a period of time subject to constraints. The standard state-space model

for a WEC can be established by

$$\begin{cases} \dot{x} &= A_c x + B_{uc} f_u + B_{wc} w \\ z &= C_z x \end{cases} \tag{5.59}$$

where $w{:=}z_w$, $z{:=}\dot{z}_v$,$x{:=}$ $[z_v,\dot{z}_v,x_r,\tilde{x}_e\ ]$. We recall that $w{:=}z_w$ is the wave elevation as described in section 3.4.

$$A_c = \begin{bmatrix} 0 & 1 & 0 & 0 \\ -\frac{k_s}{m} & 0 & -\frac{C_r}{m} & \frac{C_e}{m} \\ 0 & B_r & A_r & 0 \\ 0 & 0 & 0 & A_e \end{bmatrix} \quad B_{wc} = \begin{bmatrix} 0 \\ 0 \\ 0 \\ B_e \end{bmatrix} \quad B_{uc} = \begin{bmatrix} 0 \\ \frac{1}{m} \\ 0 \\ 0 \end{bmatrix} \quad C_z = \begin{bmatrix} 0 & 1 & 0_{1*(n_r+n_e)} \end{bmatrix} \tag{5.60}$$

with $m{:=}m_s + m_\infty$. Here, n_r and n_e are the number of states associated with radiation force and excitation force respectively. The coefficients (A_r, B_r, C_r, 0) and (A_e, B_e, C_e, 0) have been introduced in Eq.3.7 and Eq.3.9.

The vertical velocity of the buoy $\dot{z}_v$ can be assumed equal to the relative velocity of the stator/rotor within the generator. The control force f_u and $\dot{z}_v$ are related to the current and voltage as

$$f_u = K_i i; v_{out} = K_v \dot{z}_v \tag{5.61}$$

with K_v and K_i as constants depending on the generator.

Without loss of generality, the system input in Eq.5.59 can be easily re-defined in terms of the current i as input and v_{out} as output, by re-stating

$$B'_u = B_{uc} K_i; C'_z = K_v C_z \tag{5.62}$$

in order to include the simplified generator dynamics. We obtain the new state space representation:

$$\begin{cases} \dot{x} &= A_c x + B'_u i + B_{wc} w \\ z &= C'_z x \end{cases} \tag{5.63}$$

5.4.2 H_2 MIPC for WEC

We recall that the mechanical power provided by the PTO of a WEC is given by

$$P_m(t) = -f_u(t) v(t) \tag{5.64}$$

and the corresponding mechanical energy is

$$E_m = \int_{T_1}^{T_2} -f_u(t) v(t) dt \tag{5.65}$$

When the actuator acts as a generator ($P_m < 0$), the electrical power P_e is the useful power that can be harvested because it is a fraction of the mechanical power.

Let P_s denote the power the device exchanges with the waves. By applying the MIPC strategy to the wave energy field, P_s is given by

$$P_s(t) = -f_e(t)\dot{z}_v(t) \tag{5.66}$$

Therefore, if $f_e(t) = 0$, no power can be harvested.

The following power balance holds

$$\dot{E}(t) = P_s(t) + P_m(t) \tag{5.67}$$

where $\dot{E}(t)$ represents the instantaneous power stored into or dissipated by the WEC. Next, the same considerations made in the power flow analysis in section 2.4 can be used here. In fact, the power flowing from the road is replaced by the power flowing from the waves.

As explained in section 5.2.7.1 for MIPC in regenerative suspension systems, it could be convenient to optimize P_s as sign-defined and large as desired regardless of P_m as $P_s(t) < 0$ at all times would provide a barrier for the internal potential energy from flowing back towards the waves.

We could state that if

$$\dot{z}_v(t) = \mu f_e(t) \tag{5.68}$$

remained true at all time instants, then $P_s(t)$ would be negative sign-defined. That would lead to

$$P_s(t) = -\mu f_e(t)^2 \tag{5.69}$$

Similarly to section 5.2.7.1 for MIPC in regenerative suspensions, the power coming from the waves would be flowing into the system at all times and it could be made as large as required by choosing suitable values for μ. In practice, this is obviously not possible as the current $i(t)$ would increase as well and this would make the Joule losses too large over a certain threshold, where the harvested energy would be reduced instead of increasing further.

We introduce the following performance output

$$z_0(t) = \dot{z}_v(t) - \mu f_e(t) \tag{5.70}$$

given that it is simply not possible to find a dynamics for z_v such as Eq.5.68 is perfectly satisfied.

The energy harvesting goal is precisely that of minimizing z_0. This objective is pursued as a H_2 norm minimization of the transfer function (with s as Laplace variable) built between the output $z_o(t)$ and the input $f_e(t)$. It can be stated that, by minimizing the H_2 norm of such transfer function, the energy/power of $z_0(t)$ is minimized as well, provided that $f_e(t)$ has finite energy.

The state-space realization is the following

$$\begin{cases} \dot{x}(t) &= A_c x(t) + B_u' i(t) + E f_e(t) \\ z_0(t) &= Cx(t) + Di(t) + F f_e(t) \end{cases} \tag{5.71}$$

where the matrices A_c, B'_u have been previously defined in Eq.5.63 and

$$E = \begin{bmatrix} 0 \\ \frac{1}{m} \\ 0_{(n_r+n_e)*1} \end{bmatrix} \quad C = \begin{bmatrix} 0 & 1 & 0_{1*(n_r+n_e)} \end{bmatrix} \quad D = 0 \quad F = -\mu \tag{5.72}$$

As in section 5.2.7.1, it is good practice to add a filter for the input f_e with the aim of localizing the energy of the disturbance on specific frequency bands. Let W_d of Eq.5.55 be the corresponding low-pass filter, we obtain the following augmented state:

$$x_g = \begin{bmatrix} x^T & x_d^T \end{bmatrix} \tag{5.73}$$

and the extended state space representation:

$$\begin{cases} \dot{x}_g(t) &= A_g x_g(t) + B_{g2} i(t) + B_{g1} f_e(t) \\ z_0(t) &= C_{g1} x_g(t) + D_{g12} i(t) + D_{g11} f_e(t) \\ z_C(t) &= C_{gC} x_g(t) + D_{gC2} i(t) \end{cases} \tag{5.74}$$

where $i(t)$ is the control input current, $z_0(t)$ is the variable that responds to that control action. $z_C(t)$ is the vector of constrained outputs which contains all constraints of 5.56,5.57 and 5.58.

The corresponding matrices are the following:

$$A_g = \begin{bmatrix} A_c & EC_d \\ 0_{1\times 6} & A_d \end{bmatrix}, \quad B_{g2} = \begin{bmatrix} B'_u \\ 0 \end{bmatrix},$$

$$B_{g1} = \begin{bmatrix} ED_d \\ B_d \end{bmatrix}, \quad C_{g1} = \begin{bmatrix} C & FC_d \end{bmatrix}, \tag{5.75}$$

$$D_{g11} = FD_d, \quad D_{g12} = D$$

$$C_{gC} = \begin{bmatrix} 0_{1\times 4} & 1 & 0 & 0 & 0 \\ 0_{1\times 4} & 0 & 1 & 0 & 0 \\ 0_{1\times 4} & 0 & 0 & 0 & 0 \end{bmatrix}, \quad D_{gC2} = \begin{bmatrix} 0 \\ 0 \\ 1 \end{bmatrix},$$

with A_d, B_d, C_d, D_d being the minimal state-space realization of the filter W_d.

Then we look for a feedback control law

$$i = K_2 x_g \tag{5.76}$$

where K_2 is the H_2 optimal state feedback controller gain. By substituting the state feedback control law in Eq.5.74, we obtain

$$\begin{array}{lcl} \dot{x}_g(t) &=& (A_g + B_{g2}K_2)x_g(t) + B_{g1} f_e(t) \\ z_0(t) &=& (C_{g1} + D_{g12}K_2)x_g(t) + D_{g11} f_e(t) \\ z_C(t) &=& (C_{gC} + D_{gC2}K_2)x_g(t) \end{array} \tag{5.77}$$

The control design consists in the minimization of the H_2 norm of the following transfer function (between the performance output z_0 and the uncontrolled input f_e).

$$H(s) = (C_{g1} + D_{g12}K_2)(sI - (A_g + B_{g2}K_2))^{-1}B_{g1} + D_{g11} \tag{5.78}$$

Then, a multi-objective H_2 control law can be determined by solving the following LMI optimization problem.

$$\begin{cases} [X_2, Y_2] = \min_{X,Y,Q,\gamma} \ \gamma \\ s.t \\ Q > 0; \\ \gamma > 0; \\ tr(Q) \leq \gamma; \\ X = X^T > 0; \\ \begin{bmatrix} A_gX + B_{g2}Y + (A_gX + B_{g2}Y)^T & B_{g1} \\ * & -I \end{bmatrix} < 0; \\ \\ \begin{bmatrix} X & (C_{g1}X + D_{g12}Y)^T \\ * & Q \end{bmatrix} > 0 \end{cases} \tag{5.79}$$

If a solution exists, the optimal controller is given by

$$K_2 = Y_2X_2^{-1} \tag{5.80}$$

We can include constraints into the MIPC H_2 scheme. By defining a matrix $Q = X^{-1}$ with a quadratic storage function as $V(x_g) = x_g^TQx_g$, we can show that the feasibility of 5.79 guarantes that the closed loop system is asymptotically stable and that

$$\frac{d}{dt}V(x_g(t)) - ||f_e(t)||^2 < 0 \tag{5.81}$$

After integration [101], we obtain:

$$V(x_g(t)) - V(x_g(0)) < \int_0^t ||f_e(t)||^2 d\tau \tag{5.82}$$

In addition, the assumption of bounded disturbance energy gives

$$V(x_g(t)) \leq V(x_g(0)) + \int_0^t ||f_e(t)||^2 d\tau \leq V(x_g(0)) + f_{e,max} \tag{5.83}$$

for any $t > 0$. This implies that the closed loop trajectory stays in an ellipsoid defined by

$$\Omega(Q, \kappa) := \{x_g \in \mathbb{R}^n | V(x_g) \leq \kappa\} \tag{5.84}$$

with n being the number of states in the extended representation and $\kappa := V(x_g(0)) + f_{e,max}$.

In order to cast the time-domain constraints in 5.56,5.57 and 5.58 as LMIs, we can say that the ellipsoid $\Omega(Q,\kappa)$ contains the set of all reachable states for the closed-loop system with disturbances whose energy is bounded by $f_{e,max} := \kappa$ ($V(x_g(0)) = 0$ is assumed) [102].

We can state that

$$\begin{aligned}\max_{t\geq 0}|i(t)|^2 &= \max_{t\geq 0}|(YX^{-1})x_g(t)|^2 \\ &\leq \max_{x_g\in\Omega}|(YX^{-\frac{1}{2}})x_g|^2 \leq \kappa||YX^{-\frac{1}{2}}||_2^2\end{aligned} \tag{5.85}$$

$$\begin{aligned}\max_{t\geq 0}|z_{Ci}(t)|^2 &= \max_{t\geq 0}|(C_{gC}+D_{gC2}YX^{-1})_i x_g(t)|^2 \\ &\leq \max_{x_g\in\Omega}|(C_{gC}+D_{gC2}YX^{-1})_i x_g|^2 \\ &\leq \kappa||(C_{gC}X+D_{gC2}Y)X^{-\frac{1}{2}})_i||_2^2\end{aligned} \tag{5.86}$$

where the Cauchy-Schwarz inequality is used. Then, if the matrices X and Y furthermore satisfy that

$$\begin{gathered}\begin{bmatrix}\frac{1}{\kappa}Z & Y\\ Y^T & X\end{bmatrix}\geq 0; \\ Z\leq i_{max}^2; \\ \begin{bmatrix}\frac{1}{\kappa}N & (C_{gC}X+D_{gC2}Y)\\ * & X\end{bmatrix}\geq 0; \\ N_{ii}\leq z_{i,max}^2\end{gathered} \tag{5.87}$$

for some symmetric matrices Z and N then the constraints are satisfied. $z_{1,max}$ and $z_{2,max}$ are the bounds on heave position and heave velocity respectively.

Ultimately, the constrained MIPC H_2 is solved by computing

$$[X_2,Y_2] = \min_{X=X^T,Y,Z=Z^T,N=N^T,\gamma}\ \gamma\ \ s.t\ \ 5.79\ \ and\ \ 5.87 \tag{5.88}$$

The full state-feedback control gain K_2 is computed offline using MOSEK solver.

5.4.3 LQR design for WEC

In this section, we design two LQ strategies for WECs.

5.4.3.1 First method: using an augmented state including the excitation substates

The first strategy is sea state dependent (its optimal tuning will change when the sea condition change). This means that when the sea state changes, the configuration chosen for the controller will no longer be optimal and a new configuration should be found and studied for the controller to work at its best.

That's why we cast the state space 5.63 and the excitation force subsystem 3.9 together so that LQ optimizes on the sea properties as well.

We obtain the following extended state representation

$$\dot{x}_a(t) = A_a x_a(t) + B_a i(t) + E_a w(t) \tag{5.89}$$

where $x_a(t)$ is the augmented state including the excitation substates and

$$A_a = \begin{bmatrix} A_c & B'_u C_e \\ 0_{5\times5} & A_e \end{bmatrix}, \quad B_a = \begin{bmatrix} B'_u \\ 0 \end{bmatrix}, \quad E_a = \begin{bmatrix} 0 \\ B_e \end{bmatrix},$$

The controlled input vector is once again the current $i(t)$. It is determined by finding a feedback matrix K_{LQ} such that

$$i(t) = K_{LQ} x_a(t) \tag{5.90}$$

Such matrix is found using the strategy detailed in section 5.2.5 and by solving the same LMI of Eq.5.27.

5.4.3.2 Second method: using the system's steady state response to the disturbance

The second LQR strategy is developed in discrete time using the system's steady-state response to the wave disturbance. Denoting the control input as $u(k)$=$Kx(k)$ $\forall k \in \mathbb{I}_{[0,N_T-1]}$, we obtain the following equality:

$$x(k+1) = (A_d + B_d K)x(k) + E_d w(k) \tag{5.91}$$

The transfer function between the disturbance and the states is

$$H(z) = (zI - (A_d + B_d K))^{-1} E_d \tag{5.92}$$

For a sinusoidal disturbance of the form

$$w(k) = acos(\omega k) + bsin(\omega k)$$

the steady state response is

$$\bar{x}(k) = Re(H(e^{j\omega}))acos(\omega k) + Im(H(e^{j\omega}))bsin(\omega k) \tag{5.93}$$

where Re and Im denote the real part and imaginary part of the complex number $H(e^{j\omega})$ respectively. Those quantities can be calculated using the Euler's formula for complex numbers and conjugate. We can reuse the result of section 5.2.5. Indeed, under stationary conditions, the electrical power is given by

$$P_e := 2v_{out}^T N_a i + i^T R_a i \tag{5.94}$$

with $N_a = 0.5$ and R_a being the armature's resistance and the power in the inductance being negligible.

Knowing that $i = Kx$ and

$$v_{out} = K_v \dot{z}_v \tag{5.95}$$

$$\dot{z}_v = G^T x, \text{with } G^T = [0,\ 1,\ 0_{1\times(n_r+n_e)}] \tag{5.96}$$

the electrical power is computed as follows

$$P_e(k) = \bar{x}(k)^T (G^T N_a K K_v + K^T R_a K)\bar{x}(k) \tag{5.97}$$

Then we calculate the mean power.

$$P_{mean} = \lim_{T\to+\infty} \left[\frac{\sum_{t=0}^{T-1} P_e(k)}{T} \right] \tag{5.98}$$

One notices that the mean power obtained is a function of the controller gain K. The final step is to find the stabilizing value of K that gives us the maximum power.

5.4.4 Results and discussions

In this section, the wave signal used for simulation is the small wave signal depicted in Fig.3.11 of significant wave height of $H_s = 0.5m$ and a peak period of $T_p = 15.38s$. The WEC's parameters can be found in [46] and they are summarized in Table A.9 of the appendix A. In fact, this point absorber is not appropriate for bigger waves due to its dimensions and components.

The input force limit in N can be converted to the current limit in A through Eq.5.61 and vice versa. The actuator's data are presented in Table A.8 of the appendix A.

The dynamic modeling of the radiation force 3.7 and excitation force 3.9 of this WEC are given respectively by

$$A_r = \begin{bmatrix} 0 & 0 & -17.9 \\ 1 & 0 & -17.7 \\ 0 & 1 & -4.41 \end{bmatrix} \quad B_r = \begin{bmatrix} 36.5 \\ 394 \\ 75.1 \end{bmatrix} \quad C_r = \begin{bmatrix} 0 & 0 & 1 \end{bmatrix} \tag{5.99}$$

and

$$A_e = \begin{bmatrix} 0 & 0 & 0 & 0 & -400 \\ 1 & 0 & 0 & 0 & -459 \\ 0 & 1 & 0 & 0 & -226 \\ 0 & 0 & 1 & 0 & -64 \\ 0 & 0 & 0 & 1 & -9.96 \end{bmatrix} \quad B_e = \begin{bmatrix} 1549886 \\ -116380 \\ 24748 \\ -644 \\ 19.3 \end{bmatrix} \quad C_e = \begin{bmatrix} 0 & 0 & 0 & 0 & 1 \end{bmatrix} \tag{5.100}$$

In the WEC context [103], interest is mainly focused on the absorbed energy which is the mechanical energy developed by the PTO. The mechanical energy developed for $\lambda = 0$ is $-1.5 * 10^5 J$ and the electrical energy harvested with this actuator is $3 * 10^5 J$, λ being the bound on γ in the LQR's LMI in Eq.5.27. The mechanical energy being negative means that the system is absorbing energy but the positive value of electrical energy means that the system looses too much energy through Joule effects. One would want

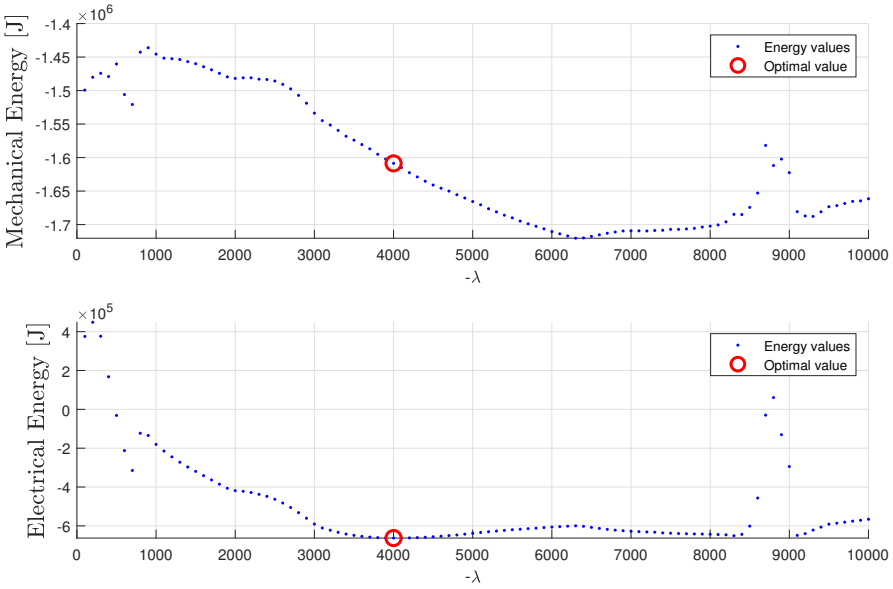

Figure 5.20: Average mechanical and electrical energies with respect to λ

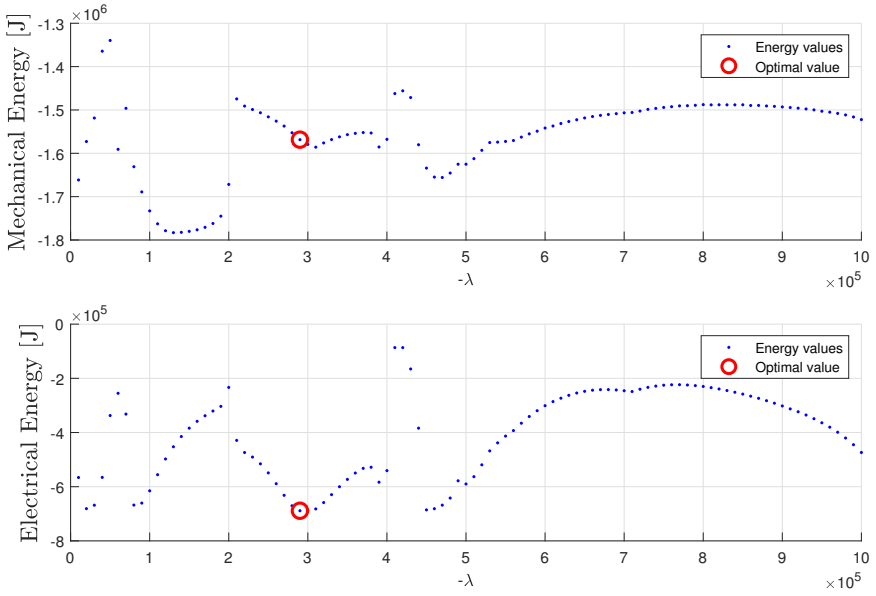

Figure 5.21: Average mechanical and electrical energies with respect to bigger values of λ

to obtain the optimal value of λ corresponding to both negative values of mechanical energy and electrical energy. Figs.5.20 and 5.21 depict the average mechanical and electrical energies developed with respect to the parameter λ which is the bound on γ in the LMI. Fig.5.20 gives an optimal value of $\lambda = -4000$ and Fig.5.21 an optimal value of $\lambda = -2.9 * 10^5$ which corresponds to both negative electrical and mechanical energies.

The optimal value is chosen to be $\lambda = -2.9 * 10^5$.

Table 5.23 depicts all the results obtained with LQR first strategy (LQR

Table 5.23: LQR and MIPC H_2 for a WEC

	LQR 1	LQR 2	Unconstrained H_2	Constrained H_2
Mechanical Energy E_m[J]	-3.32*10^6	-5.66*10^4	-5.18*10^5	-5.3*10^4
Electrical Energy E_e[J]	-1.46*10^6	-4.09*10^4	2.18*10^8	4.06*10^6
Control input force f_u[N]	[-2794;2754]	[-228;228]	[-2.7*10^4;2.9*10^4]	[-2786;4860]
Heave position z_v[m]	[-21.5;27.8]	[-1.3;1.3]	[-8;9]	[-0.1;0.6]
Heave velocity $\dot{z}_v$[m/s]	[-11.62;12]	[-5;5]	[-4;4]	[-0.15;0.15]

1), LQR second strategy (LQR 2), unconstrained H_2 MIPC and constrained H_2 MIPC.

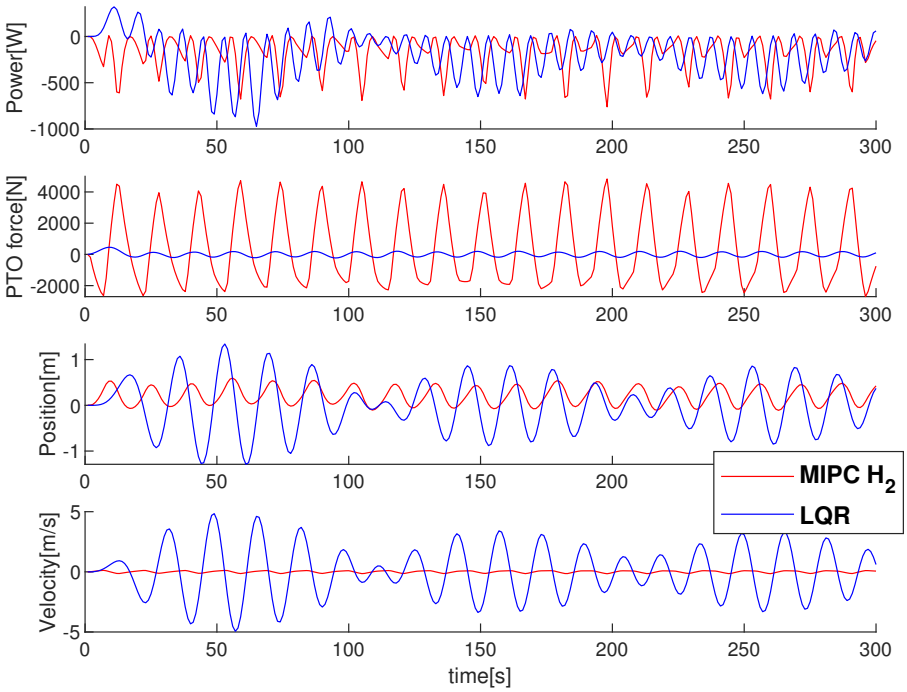

Figure 5.22: Absorbed power, PTO force, heave position and heave velocity obtained with the small WEC

The LQR first strategy allows the greatest energy harvesting of both mechanical and electrical energy. It allows an excellent energy harvesting but it is not applicable to this WEC. In fact, it exceeds the heave position and heave velocity limits (see Table A.9) but the control input force is within operational limits.

In terms of absorbed energy, the second strategy is the unconstrained H_2 but it exceeds all the limits on the control input force, heave position and heave velocity. In addition, we notice that the electrical energy is positive. This means that with the chosen actuator, the MIPC H_2 can't allow an electrical energy recovery. These results for the unconstrained

H_2 are obtained for $\mu = 10^{-1}$ which is found to be the best MIPC tuning parameter's value. Unfortunately many values of the MIPC parameter μ lead to numerical issues so it is not possible to plot the electrical and mechanical energies with respect to the values of μ.

The third strategy is the LQR second strategy. Its control input force is good but it exceeds heave position and heave velocity limits. The strategy that satisfies all constraints specifications is the constrained MIPC H_2 and it allows the smallest absorbed energy.

Fig.5.22 displays the absorbed power, PTO force, heave position and heave velocity obtained with the constrained MIPC H_2 and the LQR second strategy.

5.5 Conclusion

In this chapter, we introduced a LQR approach with a non standard cost and we applied it to vehicles regenerative suspension systems and wave energy converters. We found that this strategy allows to recover more energy than other strategies usually considered for the same purpose. In addition, it is possible to introduce a constraint on passengers comfort requiring few tuning parameters making the LQR approach more suitable for real time implementation than other existing control strategies. However it is not possible to incorporate constraints on suspension stroke and road handling into the LQR formulation even though these characteristics are not significantly deteriorated with this approach. In the same way, we found that the LQR approach also outperforms the H_2 MIPC strategy for energy harvesting in wave energy converters but LQR doesn't allow constraints incorporation like the constrained H_2 MIPC. In the next chapter, we will see how to deal with more constraints requirements using the same LQR cost function and model predictive control techniques.

Chapter 6

Economic Model Predictive Control (EMPC)

Contents

6.1 Introduction 119
6.2 EMPC design for vehicles regenerative suspension systems 120
6.3 EMPC design for Wave Energy Converters 140
6.4 Conclusion 157

6.1 Introduction

This chapter introduces the design and analysis of an Economic Model Predictive control based on the same non standard cost function for vehicles regenerative suspensions and wave energy converters. In the regenerative suspension context, we design a stochastic Model Predictive Control considering the unpredictability of the road's disturbance. This strategy aims to optimize energy harvesting while ensuring recursive feasibility at each time step and satisfying the control requirements (suspension stroke, road handling and ride comfort).

In the wave energy converter context, this EMPC strategy is applied to optimize energy harvesting and to ensure recursive feasibility at each time step and safe operative constraints (limitation on the buoy's displacement, buoy's velocity and actuator's force). Wave prediction is incorporated into the controller and many investigations are undertaken using different models of wave energy converters and wave scenarios.

The chapter is organized as follows. Section 6.2 presents the EMPC design for vehicles regenerative suspension systems, section 6.3 presents the EMPC design for wave energy converters and a small conclusion ends the chapter in section 6.4.

6.2 EMPC design for vehicles regenerative suspension systems

6.2.1 Linear Quadratic formulation in discrete time

In this section, a Linear Quadratic Regulator is designed that is instrumental to build up the proposed EMPC scheme. To this end, the regenerative quarter-car suspension model of Figure 6.1 and the moving-magnet linear actuator (Eq.(2.9)) are modeled by the state space representation of Eq.5.3.

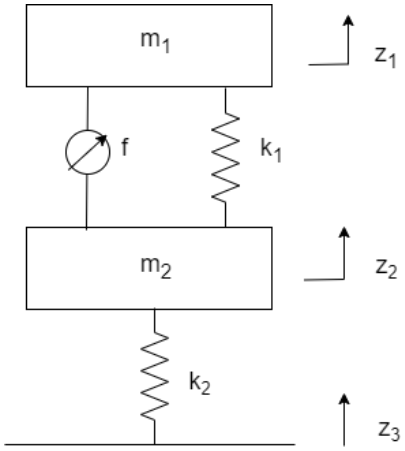

Figure 6.1: Regenerative quarter car model

By recalling that P_e represents the fraction of mechanical power P_m produced when the actuator operates as a generator (that is, $P_m(t) < 0$), the goal of maximizing the harvested energy can be converted in the minimization of the expected value of P_e [54]

$$J = E(2v_{emf}^T N_a i + i^T R_a i) \tag{6.1}$$

where v_{emf} is the back EMF voltage and $E(\cdot) := E[\cdot|x(0) = x]$ is the expected value under stationary conditions.

Notice also that N_a is a cross coupled weighting matrix and $R_a > 0$ the generator resistance. Under stationary conditions, the expected value of the electrical power is given by [104]

$$J = E(v_{emf} i + R_a i^2) \tag{6.2}$$

where $N_a = 0.5$. By denoting i=u for simplicity and noting that

$$v_{emf} = K_a(\dot{z_1} - \dot{z_2}) \tag{6.3}$$

$$\dot{z_1} - \dot{z_2} = G^T x, \text{with } G^T = [0,\ 0,\ 1,\ 0,\ -1] \tag{6.4}$$

we obtain

$$J = E(x^T G N_a K_a u + u^T R_a u) \tag{6.5}$$

After discretization with a sampling time $T_s = 0.1s$, the system (5.3) is recast as

$$x(k+1) = A_d x(k) + B_d u(k) + E_d w(k) \tag{6.6}$$

Based on Eq.(6.5), we can now define the infinite horizon cost to be minimized in the design procedure of the LQR gain for energy harvesting

$$J_\infty = \lim_{T \to +\infty} E\left[\frac{\sum_{k=0}^{T-1} \ell(x(k), u(k))}{T}\right] \tag{6.7}$$

where

$$l(x(k), u(k)) = x(k)^T G N_a K_a u(k) + u(k)^T R_a u(k) \tag{6.8}$$

$$\ell(x(k), u(k)) = [x(k)^T, u(k)^T]\, M \begin{bmatrix} x(k) \\ u(k) \end{bmatrix} \tag{6.9}$$

for some suitable symmetric matrix M.

The following result establishes how to design a stabilizing feedback gain for Eq.(6.6).

Proposition 6.2.1

Given the system (6.6)*, a stabilizing feedback gain that minimizes* J_∞ *can be found by solving the following LMI optimization problem*

$$\begin{cases} [\Pi_*, Y_*] = argmin_{\Pi, Y} \gamma \\ s.t \\ \begin{bmatrix} \Pi & (\Pi A_d^T + Y^T B_d^T) \\ (A_d \Pi + B_d Y) & \Pi - E_d \Sigma E_d^T \end{bmatrix} \geq 0 \\ \begin{bmatrix} Z & M_{22}^{1/2} Y \\ Y^T M_{22}^{1/2} & \Pi \end{bmatrix} \geq 0 \\ Tr\left(M_{11}\Pi + Y^T M_{12}^T + M_{12} Y\right) + Z \leq \gamma \\ \gamma \geq 0 \end{cases} \tag{6.10}$$

where $\Sigma = E[w(k)w(k)^T]$*,* γ *and* Z *are scalars while* Y *and* $\Pi = \Pi^T > 0$ *matrices.*

If a solution exists, the controller's gain is given by

$$K_{LQ} = Y_* \Pi_*^{-1} \tag{6.11}$$

□

Proof: By defining $X(k) := E[x(k)x(k)^T]$ and letting $u(k) = Kx(k)$, the following equation is achieved:

$$X(k+1) = (A_d + B_d K) X(k) (A_d + B_d K)^T + E_d \Sigma E_d' \tag{6.12}$$

Since K is stabilizing, $X(k) \to \Pi$ as $k \to +\infty$. Accordingly,

$$\begin{aligned} J_\infty &= E\left[\lim_{T\to+\infty} \frac{\sum_{k=0}^{T-1} x(k)^T [I, K^T] M \begin{bmatrix} I \\ K \end{bmatrix} x(k)}{T}\right] \\ &= E\left[\lim_{T\to+\infty} \frac{\sum_{k=0}^{T-1} tr\left([I, K^T] M \begin{bmatrix} I \\ K \end{bmatrix} x(k)x(k)^T\right)}{T}\right] \\ &= tr\left([I, K^T] M \begin{bmatrix} I \\ K \end{bmatrix} \Pi\right). \end{aligned} \tag{6.13}$$

By rearranging M as a block matrix

$$M = \begin{bmatrix} M_{11} & M_{12} \\ M_{12}^T & M_{22} \end{bmatrix} \tag{6.14}$$

we get the following expression for J_∞

$$J_\infty = Tr\left((M_{11} + K^T M_{12}^T + M_{12}K + K^T M_{22} K)\Pi\right) \tag{6.15}$$

To verify the correctness of the solution, the stability condition for the discrete-time Lyapunov equation

$$\Pi = (A_d + B_d K)\Pi(A_d + B_d K)^T + E_d \Sigma E_d' \tag{6.16}$$

should be satisfied. Then the following *Bilinear Matrix Inequalities* (BMI) optimization is obtained where the equilibrium condition (6.16) has been relaxed as in (6.17)

$$\begin{aligned} &\min_{\Pi,K} Tr\left((M_{11} + K^T M_{12}^T + M_{12}K + K^T M_{22} K)\Pi\right) \\ &\Pi \geq 0 \\ &\Pi \geq (A_d + B_d K)\Pi(A_d + B_d K)^T + E_d \Sigma E_d^T \end{aligned} \tag{6.17}$$

By applying Schur's complement on the BMI conditions and by defining the new variable $Y = K\Pi$, the latter optimization problem can be recast as

$$\begin{aligned} &\min_{\Pi,Y} Tr\left(M_{11}\Pi + Y^T M_{12}^T + M_{12} Y\right) + M_{22}^{1/2} Y \Pi^{-1} Y^T M_{22}^{1/2} \\ &\begin{bmatrix} \Pi & (\Pi A_d^T + Y^T B_d^T) \\ (A_d\Pi + B_d Y) & \Pi - E_d \Sigma E_d^T \end{bmatrix} \geq 0 \end{aligned} \tag{6.18}$$

In order to get an LMI formulation, it is useful to define an auxiliary upperbounding scalar $Z \geq M_{22}^{1/2} Y \Pi^{-1} Y^T M_{22}^{1/2}$ and linearize the previous

optimization problem as follows:

$$\min_{\Pi,Y} Tr\left(M_{11}\Pi + Y^T M_{12}^T + M_{12}Y\right) + Z \tag{6.19}$$

$$\begin{bmatrix} \Pi & (\Pi A_d^T + Y^T B_d^T) \\ (A_d\Pi + B_d Y) & \Pi - E_d \Sigma E_d^T \end{bmatrix} \geq 0 \tag{6.20}$$

$$Z \geq M_{22}^{1/2} Y \Pi^{-1} Y^T M_{22}^{1/2} \tag{6.21}$$

Finally by resorting again to Schur's complement, the following LMI optimization problem is achieved

$$\begin{cases} min_{(\Pi,Y)} Tr\left(M_{11}\Pi + Y^T M_{12}^T + M_{12}Y\right) + Z \\ s.t \\ \begin{bmatrix} \Pi & (\Pi A_d^T + Y^T B_d^T) \\ (A_d\Pi + B_d Y) & \Pi - E_d \Sigma E_d^T \end{bmatrix} \geq 0 \\ \begin{bmatrix} Z & M_{22}^{1/2} Y \\ Y^T M_{22}^{1/2} & \Pi \end{bmatrix} \geq 0 \end{cases} \tag{6.22}$$

that can be recast as in (6.10).

However, due to the unboundedness of the cost function, many controllers can be determined with costs arbitrarily large by adding additional conditions on P_e in (6.10). This can be done by introducing a bound λ on the cost and by reformulating the LMI design optimization problem (6.10) as follows

$$\begin{cases} [\Pi_*, Y_*] = argmin_{\Pi,Y}\gamma \\ s.t \\ \begin{bmatrix} \Pi & (\Pi A_d^T + Y^T B_d^T) \\ (A_d\Pi + B_d Y) & \Pi - E_d \Sigma E_d^T \end{bmatrix} \geq 0 \\ \begin{bmatrix} Z & M_{22}^{1/2} Y \\ Y^T M_{22}^{1/2} & \Pi \end{bmatrix} \geq 0 \\ Tr\left(M_{11}\Pi + Y^T M_{12}^T + M_{12}Y\right) + Z \leq \gamma \\ \gamma \geq \lambda \end{cases} \tag{6.23}$$

6.2.2 Economic Model Predictive Control

This section presents the Economic Model Predictive Control (EMPC) framework adopted in this work. We first introduce notation and admissible constraint sets. We then formulate the finite-horizon stochastic EMPC problem and summarize the assumptions required to guarantee well-posedness, recursive feasibility, and closed-loop stability.

6.2.2.1 Notation and constraints

Let $\mathbb{I}_{[a,b]}$ denote the set of integers from a to b, $\mathbb{R}^n$ the n-dimensional Euclidean space, and $\mathbf{I}_n$ the $n \times n$ identity matrix. The system is subject to constraints of the form

$$x \in \mathbb{X}, \qquad u \in \mathbb{U}. \tag{6.24}$$

The admissible input set is

$$\mathbb{U} := \{u \in \mathbb{R} : |u| \leq u_{\max}\}, \tag{6.25}$$

where $u_{\max} > 0$ is the maximum allowable magnitude of the actuator current. The state constraint set $\mathbb{X}$ depends on the adopted constraint-handling strategy and is specified in Section 6.2.2.4.

6.2.2.2 Stochastic EMPC formulation

To explicitly account for stochastic road excitation, predictions are carried out in terms of expected values. The applied control input is decomposed as

$$u = v + K\,\mathbb{E}[x], \tag{6.26}$$

where v is the online decision variable computed by the EMPC optimizer, and K is the stabilizing LQR gain obtained offline (Section 6.2.1). This structure separates economic optimization and constraint handling (through v) from stabilization (through K), which is instrumental to guarantee closed-loop stability while retaining flexibility in the economic objective.

Over a horizon of length N_T, define

$$z(k) := \begin{bmatrix} \mathbb{E}[x(k)] \\ v(k) \end{bmatrix}, \qquad k \in \mathbb{I}_{[0,N_T-1]}. \tag{6.27}$$

Economic stage cost. Recalling the energy-oriented instantaneous power term in (6.5), the EMPC stage cost is defined as the electrical power associated with the applied input $u = v + K\mathbb{E}[x]$, i.e.,

$$\ell(x, v) = x^\top G N_a K_a (v + K\mathbb{E}[x]) + (v + K\mathbb{E}[x])^\top R_a\,(v + K\mathbb{E}[x]). \tag{6.28}$$

Taking expectation yields an affine-quadratic function of $\mathbb{E}[x]$ and v, plus a constant term depending on the covariance:

$$\mathbb{E}[\ell(x, v)] = z^\top H z + \mathrm{Tr}\Big(Q\,\tilde{X}\Big), \tag{6.29}$$

where $\tilde{X}$ is the state covariance matrix

$$\tilde{X} := \mathbb{E}\Big[(x - \mathbb{E}[x])(x - \mathbb{E}[x])^\top\Big] = \mathbb{E}[xx^\top] - \mathbb{E}[x]\mathbb{E}[x]^\top, \tag{6.30}$$

and

$$Q := \Big(G N_a K K_a + K^\top R_a K\Big), \qquad H := \begin{bmatrix} G^\top N_a K_a K + K^\top R_a K & G^\top N_a K_a + K^\top R_a \\ R_a K & R_a \end{bmatrix}. \tag{6.31}$$

Covariance recursion. Under the stabilizing feedback term, the covariance evolves according to the Lyapunov recursion

$$\begin{aligned} \tilde{X}(k+1) &= (A_d + B_d K)\tilde{X}(k)(A_d + B_d K)^\top + E_d \Sigma E_d^\top, \\ \tilde{X}(0) &= 0, \qquad k \in \mathbb{I}_{[0,N_T-1]}, \end{aligned} \tag{6.32}$$

with $\Sigma = \mathbb{E}[w(k)w(k)^\top]$. Notably, (6.32) depends only on the closed-loop matrix $(A_d + B_d K)$ and the disturbance statistics, hence it is independent of the EMPC decision variable $v(k)$.

This modeling choice is deliberate and reflects an engineering trade-off: by fixing the state covariance through a stabilizing energy-oriented feedback law, the proposed EMPC formulation avoids online uncertainty propagation, thereby preserving convexity and real-time tractability, at the cost of not actively shaping the uncertainty through the economic input. This design prioritizes robustness, computational efficiency, and real-time implementability over optimal uncertainty shaping, which is a common and acceptable trade-off in automotive control applications [105].

Finite-horizon problem. The EMPC optimization problem is formulated as

$$\begin{cases} \min\limits_{\{v(k)\}_{k=0}^{N_T-1}} & \sum\limits_{k=0}^{N_T-1} \Big(z(k)^\top H z(k) + \mathrm{Tr}\Big(Q\,\tilde{X}(k)\Big)\Big) + \mathbb{E}\Big(x(N_T)^\top \Phi x(N_T)\Big) \\ \text{s.t.} & \mathbb{E}[x(k+1)] = (A_d + B_d K)\,\mathbb{E}[x(k)] + B_d v(k), \quad \forall k \in \mathbb{I}_{[0,N_T-1]}, \\ & \mathbb{E}[x(k)] \in \mathbb{X}, \quad u(k) \in \mathbb{U}, \quad \forall k \in \mathbb{I}_{[0,N_T-1]}, \\ & \mathbb{E}[x(0)] = x(t), \\ & \mathbb{E}\Big(x(N_T)^\top \Phi x(N_T)\Big) \le \alpha, \\ & \tilde{X}(0) = 0, \quad \tilde{X}(k) \text{ satisfies (6.32)}. \end{cases} \tag{6.33}$$

The terminal cost and terminal constraint employ the same weighting matrix $\Phi = \Phi^\top \succ 0$. Using the second-moment decomposition,

$$\mathbb{E}\Big(x(N_T)^\top \Phi x(N_T)\Big) = \mathbb{E}[x(N_T)]^\top \Phi\, \mathbb{E}[x(N_T)] + \mathrm{Tr}\Big(\Phi\, \tilde{X}(N_T)\Big). \tag{6.34}$$

At each sampling instant, once the optimal sequence $\{v(0), \ldots, v(N_T-1)\}$ has been computed, only the first input is applied,

$$u(t) = v(0) + K\,\mathbb{E}[x(t)], \tag{6.35}$$

and the procedure is repeated in a standard receding-horizon fashion.

6.2.2.3 Assumptions

Closed-loop stability and recursive feasibility hold under the following assumptions.

Assumption 6.2.1

The terminal matrix Φ is symmetric positive definite and there exists a stabilizing feedback $u(k) = Kx(k)$ such that, for all $x(k) \in \mathbb{R}^n$,

$$x(k)^\top \Phi x(k) \geq \begin{bmatrix} x(k) \\ u(k) \end{bmatrix}^\top M \begin{bmatrix} x(k) \\ u(k) \end{bmatrix} + \mathbb{E}_{x(k)}\Big[x(k+1)^\top \Phi x(k+1)\Big]. \quad (6.36)$$

Hence, $x^\top \Phi x$ acts as a stochastic Lyapunov function under $u(k) = Kx(k)$. □

Assumption 6.2.2

The parameter α is selected such that any initial state distribution satisfying $\mathbb{E}\Big(x(0)^\top \Phi x(0)\Big) \leq \alpha$ yields state trajectories that remain in the admissible region under the applied inputs. □

In the next subsection, we detail the investigated constraint-handling strategies and the corresponding definitions of $\mathbb{X}$.

6.2.2.4 Approaches to Constraint Handling

This subsection compares alternative constraint-handling strategies within the proposed EMPC framework. The goal is to quantify how different definitions of the admissible state and input sets affect the trade-off among harvested energy, ride comfort, and road handling, while preserving computational tractability. Four configurations are considered, ranging from input-only saturation to increasingly structured state-constraint enforcement.

- Constrained EMPC 0: Input saturation only

  The first configuration is intended to isolate the effect of actuator saturation on the closed-loop behavior. Only a constant bound on the control input is enforced, and no explicit constraints are imposed on the state. The admissible input set is

  $$\mathbb{U} := \{u \in \mathbb{R} : |u| \leq u_{\max}\}, \quad (6.37)$$

  where $u_{\max}$ denotes the maximum allowable actuator current. This case serves as a baseline, highlighting the maximum energy-harvesting capability achievable when performance is limited solely by actuator constraints.

- Constrained EMPC 1: Constant bounds on deflections, acceleration, and input

  The second configuration enforces constant bounds on the main performance variables introduced in Section 1—namely suspension deflection, tire deflection, and sprung-mass acceleration—in addition to input saturation. The admissible state set is defined as

  $$\mathbb{X} := \Big\{\mathbb{E}[x] \in \mathbb{R}^5 : |z_1 - z_2| \leq g_1,\ |z_2 - z_3| \leq g_2,\ |\ddot{z}_1| \leq g_3\Big\}, \quad (6.38)$$

where g_1, g_2, and g_3 are prescribed bounds on suspension stroke, tire deflection, and vertical acceleration, respectively, while $\mathbb{U}$ is given by (6.37). This is a conservative yet transparent formulation that uniformly enforces physical limitations and comfort requirements over time.

- Constrained EMPC 2: Variance-aware deflection bounds with input saturation

  The third configuration introduces time-varying bounds on suspension and tire deflection to account for uncertainty in the state. Since both quantities depend linearly on the state, they can be written as

$$\begin{aligned} z_1 - z_2 &= F_x\, \mathbb{E}[x(k)], \\ z_2 - z_3 &= G_x\, \mathbb{E}[x(k)], \end{aligned} \tag{6.39}$$

  where F_x and G_x are selection matrices. The associated standard deviations are computed from the covariance $\tilde{X}(k)$ as

$$\begin{aligned} \sigma_1(k) &= \sqrt{\mathrm{Tr}\Big(F_x^\top F_x\, \tilde{X}(k)\Big)}, \\ \sigma_2(k) &= \sqrt{\mathrm{Tr}\Big(G_x^\top G_x\, \tilde{X}(k)\Big)}. \end{aligned} \tag{6.40}$$

  The admissible state set is then defined through tightened (variance-dependent) bounds:

$$\mathbb{X} := \Big\{ \mathbb{E}[x] \in \mathbb{R}^5 : |z_1 - z_2| \le g_1 - \sigma_1(k),\ |z_2 - z_3| \le g_2 - \sigma_2(k) \Big\}, \tag{6.41}$$

  while $\mathbb{U}$ remains (6.37). Compared with constant bounds, this approach reduces conservativeness by explicitly allocating a probabilistic safety margin via the state covariance. A similar tightening is not introduced for the acceleration constraint, since its variance depends explicitly on both the state and the applied input.

- Constrained EMPC 3: Comfort-oriented constraint with input saturation

  The fourth configuration enforces a bound only on the sprung-mass acceleration, together with input saturation. Since $\ddot{z}_1$ depends on both the state and the control input, constraining acceleration indirectly shapes suspension stroke and tire deflection. The admissible sets are

$$\mathbb{U} := \{ u \in \mathbb{R} : |u| \le u_{\max} \}, \tag{6.42}$$

$$\mathbb{X} := \Big\{ \mathbb{E}[x] \in \mathbb{R}^5 : |\ddot{z}_1| \le g_3 \Big\}. \tag{6.43}$$

  This case isolates the impact of a single comfort-driven constraint and provides insight into the coupling between body acceleration, suspension travel, and tire dynamics within the EMPC framework.

Although explicit constraints on suspension stroke and tire deflection provide direct physical guarantees, the results suggest that bounding the sprung-mass acceleration alone can act as an effective surrogate for regulating multiple performance variables, owing to the strong coupling between acceleration, suspension dynamics, and tire–road interaction in vehicle vertical motion.

6.2.3 Results and discussions

A simulation study was conducted to evaluate the performance of the proposed control architectures. Comparisons were performed using MATLAB R2022b on a 64-bit Windows 10 system equipped with a 2.1GHz Intel® Core™ i3-10110U CPU and 16GB of RAM. The optimization problems were solved using the MOSEK solver. In the simulations, a driving speed of 70km/h on a straight Class C road was assumed. A prediction horizon of $N_T = 10$ and a sampling time of $T_s = 0.1$s were employed.

The vehicle selected for simulation and performance evaluation is a standard Class C car, with its parameters detailed in Tables A.2 and A.3 of the appendix A. After comparing linear actuators typically used in regenerative suspension systems [106]−[107], the moving magnet linear actuator of [106] was chosen. Its data are presented in Table A.8 of the appendix A. To effectively characterize the road profile, the signal shown in Fig.6.2 was considered.

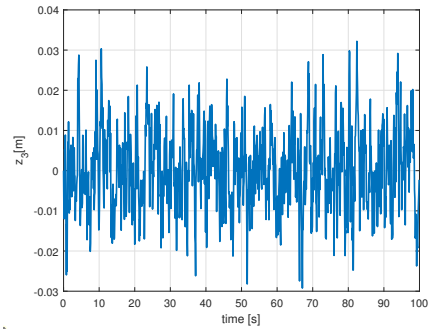

Figure 6.2: Signal characterizing the road profile.

The values of ϕ and α used in the terminal cost and terminal constraint are given by

$$\phi = \begin{bmatrix} 1 & 0 & 0 & 0 & 0 \\ 0 & 1 & 0 & 0 & 0 \\ 0 & 0 & 1 & 0 & 0 \\ 0 & 0 & 0 & 1 & 0 \\ 0 & 0 & 0 & 0 & 1 \end{bmatrix} \quad \alpha = 10, \tag{6.44}$$

which satisfy Assumptions 1 and 2.

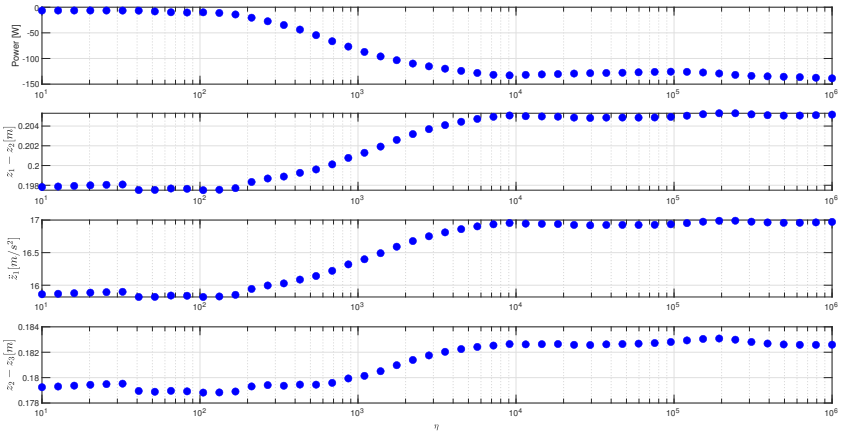

Figure 6.3: Performance with respect to λ, $\lambda \in [0; 10^6]$

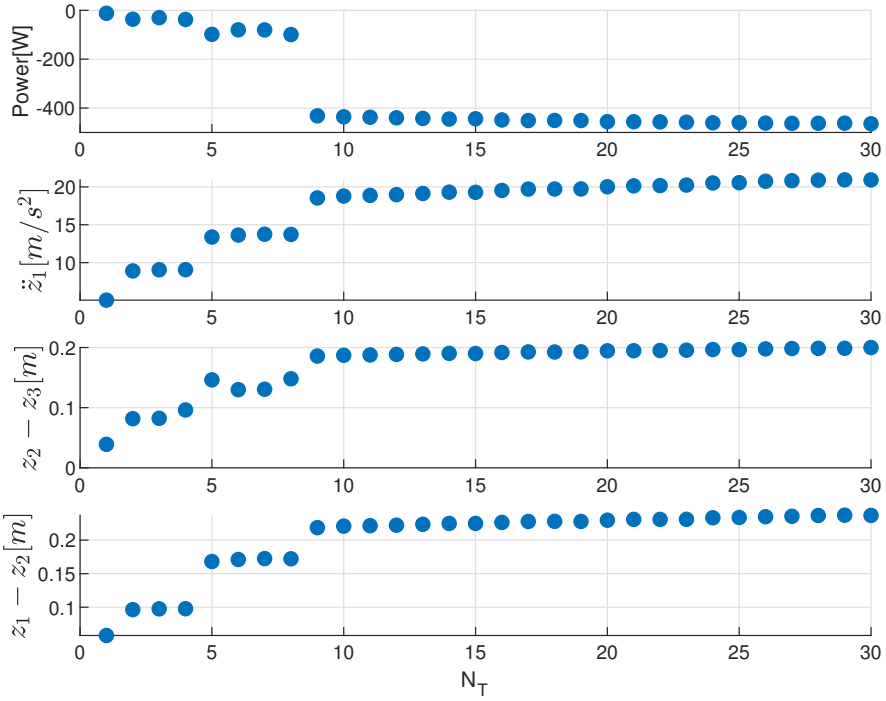

Figure 6.4: Performance with respect to N_T, $N_T \in [1; 30]$ with a step of 1

6.2.3.1 Energy-Oriented LQR Tuning

As discussed in Section 6.2.1, the performance of the energy-oriented LQR controller depends on the parameter λ, which bounds the LQR cost in (6.23). Different values of λ yield stabilizing controllers characterized by distinct trade-offs between harvested energy and physical performance. Figure 6.3 reports the mean harvested power together with the ranges of suspension deflection, tire deflection, and vertical acceleration for increasing values of $-\lambda$. While harvested power initially increases with $-\lambda$, saturation effects

are observed beyond specific thresholds, accompanied by a degradation of physical performance. Overall, this analysis confirms that an LQR strategy exclusively optimized for energy recovery may lead to unacceptable suspension excursions and accelerations. Based on this trade-off, the value $\lambda = -1000$ is selected for all subsequent simulations, as it provides a reasonable compromise between energy harvesting and physical feasibility.

6.2.3.2 Prediction Horizon Selection

The prediction horizon N_T is selected to balance performance and computational complexity. Figure 6.4 illustrates the effect of N_T on harvested power and physical performance indices. The harvested power increases with N_T up to $N_T = 30$. A similar trend is observed for acceleration, suspension deflection and tire deflection indicating reduced ride comfort and road-holding performance. One notices that for horizons $N_T \leq 8$, the nonlinear recursive feasibility condition (6.34) is not binding because the prediction horizon is not long enough. As a result, the optimizer only minimizes the quadratic stage cost over the short horizon without worrying about long-term feasibility. At $N_T = 9$, the recursive feasibility condition (6.34) becomes active. The rolled covariance and terminal penalty now force the optimizer to plan differently. The jump in power at $N_T = 9$ occurs because the horizon becomes long enough for the nonlinear recursive-feasibility condition to turn binding, which pushes the optimizer to a different solution with much larger regenerative electrical power.

Based on these results, a prediction horizon $N_T = 10$ is adopted. This choice is sufficiently long to capture the dominant system dynamics while ensuring computational feasibility for real-time implementation. In what follows, four simulation scenarios corresponding to the aforementioned constrained EMPC strategies of section 6.2.2.4, are presented.

6.2.3.3 Comparison of Control Strategies

The LQR controller and the four constrained EMPC strategies introduced in Section 6.2.2.4 are compared in terms of harvested energy, physical performance, and constraint satisfaction.

Figure 6.5 shows the time histories of harvested power, control input, vertical acceleration, tire deflection, and suspension stroke for the LQR and Constrained EMPC 0. While Constrained EMPC 0 achieves significantly higher energy recovery, it does so at the expense of physical performance, yielding suspension excursions and accelerations that are incompatible with practical vehicle operation.

Introducing additional constraints (Constrained EMPC 1–3) progressively improves ride comfort and road handling while reducing harvested energy. Tables 6.1, 6.3, 6.5, 6.7 summarize the active constraints, while Tables 6.2, 6.4, 6.6, 6.8 report the corresponding performance metrics.

Table 6.1: Active constraints in LQR and Constrained EMPC 0

Constraints	LQR	EMPC
Control Input [A]	—	[-3; 3]
Accelerations [m/s^2]	—	—
Tire Deflection [m]	—	—
Suspension Deflection [m]	—	—

Explicit constraint management via EMPC enables substantial energy recovery gains over LQR while preserving ride comfort and safety, provided that constraints are selected to exploit the intrinsic coupling of vehicle vertical dynamics rather than over-constraining individual physical variables.

6.2.3.4 Computational Complexity

Table 6.9 reports the mean harvested power and average computation times for all control strategies. The offline computation of the LQR gain represents the most expensive step (approximately 1.02 s), but it is performed once and does not affect online execution.

During real-time operation, the most demanding EMPC strategy (Constrained EMPC 2) requires approximately 42 ms per optimization, which is well below the available sampling interval of 100 ms. Therefore, all proposed EMPC strategies are compatible with real-time implementation.

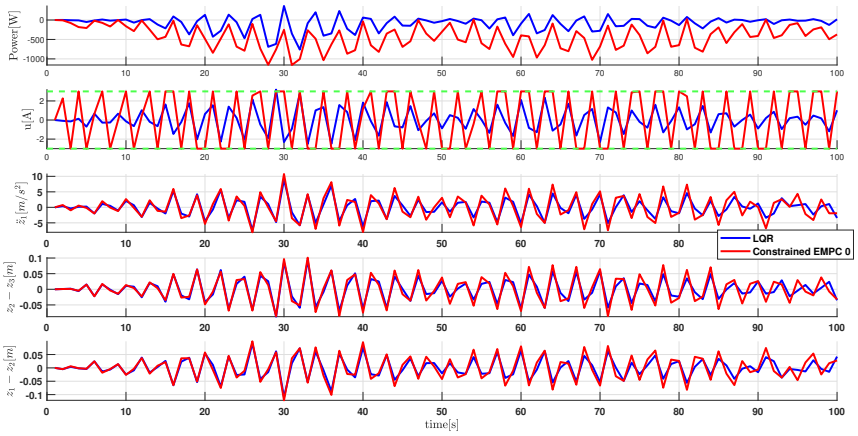

Figure 6.5: Constrained EMPC 0 vs. LQR

6.2.3.5 Comments to the simulation results

The simulation results highlight the effectiveness of the proposed EMPC framework in balancing energy harvesting and vehicle dynamic performance under stochastic road excitation. The energy- oriented LQR provides a useful baseline and confirms that maximizing harvested power alone leads to

Table 6.2: Outputs of LQR and Constrained EMPC 0

	LQR	EMPC
Mean Power [W]	-83	-436
Control Input Range [A]	[-2.5; 3.2]	[-3; 3]
Accelerations Range [m/s^2]	[-7.4; 9.0]	[-8; 10]
Tire Deflection Range [m]	[-0.09; 0.09]	[-0.08; 0.1]
Suspension Deflection Range [m]	[-0.11; 0.09]	[-0.12; 0.1]

Table 6.3: Active constraints in LQR and Constrained EMPC 1

Constraints	LQR	Constrained EMPC 1
Control Input [A]	—	[-30; 30]
Accelerations [m/s^2]	—	[-3; 3]
Tire Deflection [m]	—	[-0.06; 0.06]
Suspension Deflection [m]	—	[-0.07; 0.07]

Table 6.4: Outputs of LQR and Constrained EMPC 1

	LQR	Constrained EMPC 1
Mean Power [W]	-83	-138
Control Input Range [A]	[-2.5; 3.2]	[-22.1; 29.8]
Accelerations Range [m/s^2]	[-7.4; 9.0]	[-3; 3]
Tire Deflection Range [m]	[-0.09; 0.09]	[-0.04; 0.05]
Suspension Deflection Range [m]	[-0.11; 0.09]	[-0.05; 0.06]

Table 6.5: Active constraints in LQR and Constrained EMPC 2

Constraints	LQR	Constrained EMPC 2
Control Input [A]	—	[-30; 30]
Accelerations [m/s^2]	—	—
Tire Deflection [m]	—	[-0.06 - σ_2; 0.06 - σ_2]
Suspension Deflection [m]	—	[-0.07 - σ_1; 0.07 - σ_1]

Table 6.6: Outputs of LQR and Constrained EMPC 2

	LQR	Constrained EMPC 2
Mean Power [W]	-83	-147
Control Input Range [A]	[-2.5; 3.2]	[-27.8; 30]
Accelerations Range [m/s^2]	[-7.4; 9.0]	[-5.2; 4.5]
Tire Deflection Range [m]	[-0.09; 0.09]	[-0.04; 0.05]
Suspension Deflection Range [m]	[-0.11; 0.09]	[-0.05; 0.06]

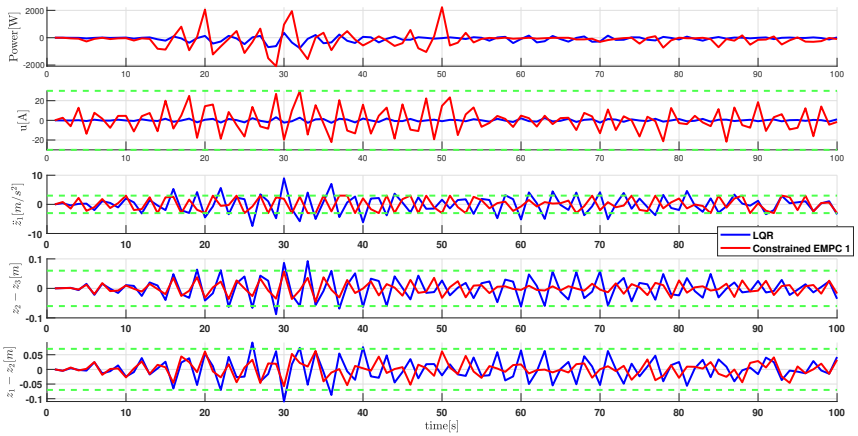

Figure 6.6: Constrained EMPC 1 vs. LQR

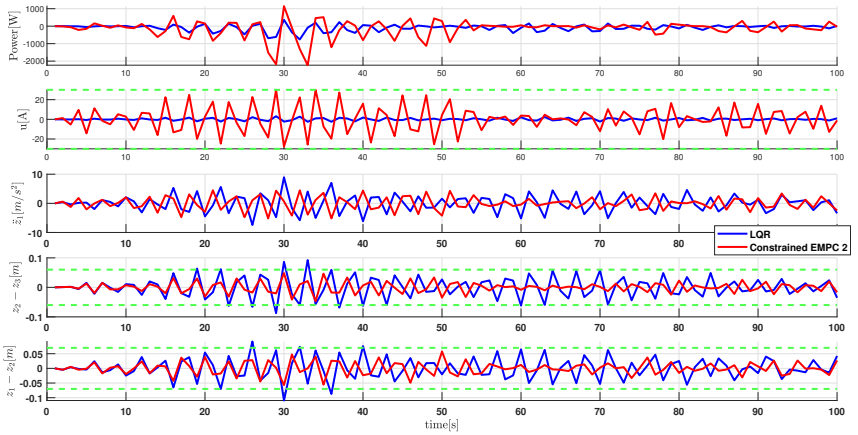

Figure 6.7: Constrained EMPC 2 vs. LQR

Table 6.7: Active constraints in LQR and Constrained EMPC 3

Constraints	LQR	Constrained EMPC 3
Control Input [A]	—	[-30; 30]
Accelerations [m/s^2]	—	[-3; 3]
Tire Deflection [m]	—	—
Suspension Deflection [m]	—	—

aggressive control actions and degraded physical behavior when constraints are not explicitly enforced.

Among the EMPC strategies, Constrained EMPC 0 achieves the highest energy recovery but violates comfort- and safety-related requirements, making it unsuitable for practical vehicle applications. Introducing explicit physical constraints (Constrained EMPC 1–3) progressively improves ride comfort, suspension stroke, and road handling at the cost of reduced

Table 6.8: Outputs of LQR and Constrained EMPC 3

	LQR	Constrained EMPC 3
Mean Power [W]	-83	-138
Control Input Range [A]	[-2.5; 3.2]	[-22.1; 29.8]
Accelerations Range [m/s^2]	[-7.4; 9.0]	[-3; 3]
Tire Deflection Range [m]	[-0.09; 0.09]	[-0.04; 0.05]
Suspension Deflection Range [m]	[-0.11; 0.09]	[-0.05; 0.06]

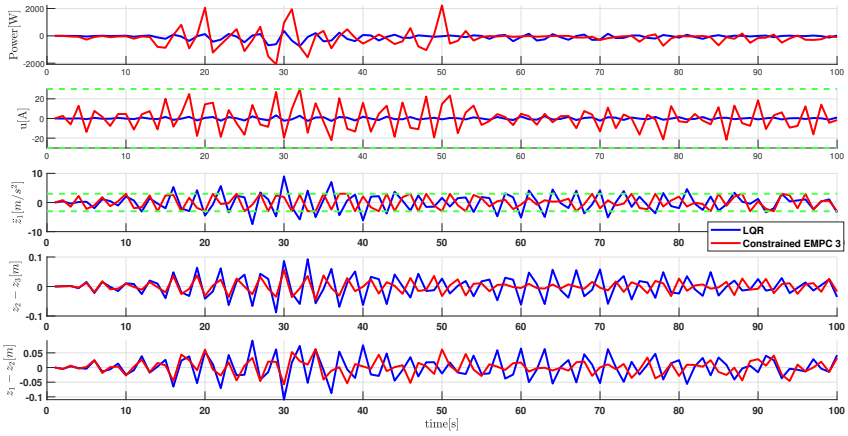

Figure 6.8: Constrained EMPC 3 vs. LQR

harvested energy. In particular, Constrained EMPC 1 and Constrained EMPC 3 offer the most balanced trade-off, achieving substantial energy recovery while strictly satisfying all imposed constraints.

Time-varying constraint tightening based on state covariance (Constrained EMPC 2) reduces conservativeness with respect to constant bounds, but incurs higher computational effort and does not consistently outperform simpler constraint formulations. Notably, constraining only the sprung-mass acceleration (Constrained EMPC 3) implicitly regulates suspension stroke and tire deflection due to the strong coupling of vertical vehicle dynamics, yielding performance comparable to more restrictive strategies with lower computational cost.

Overall, the results demonstrate that explicit economic optimization combined with judicious constraint selection enables EMPC to outperform traditional LQR control in terms of energy recovery while maintaining real-time feasibility and physically meaningful vehicle behavior.

6.2.3.6 Robustness of the control laws

It is well known that real vehicles never match the exact nominal parameters (mass, damping, stiffness...). Small deviations can significantly affect suspension dynamics : vehicle load changes alter sprung mass, tire pressure

Table 6.9: Summary of the results

Approach	Mean power $[W]$	Mean computation time$[s]$
LQR	-83	1.02
Constrained EMPC 0	-436	0.015
Constrained EMPC 1	-138	0.039
Constrained EMPC 2	-147	0.042
Constrained EMPC 3	-138	0.036

or wear changes effective stiffness. Moreover, ISO road profiles range from smooth highways (A class) to very rough rural roads (H class) as explained in Table 5.1 and controllers must adapt across this spectrum. Therefore, the robustness of the control laws to vehicle parameters variation and to road signal variation is investigated in the following paragraphs.

To evaluate the robustness of the control laws under vehicle parameters uncertainties, new simulations are undertaken. While unstructured uncertainty is not modeled in the system matrices, a sensitivity analysis is performed by modifying key parameters of the quarter-car model:

- The sprung mass is increased from $m = 1274$kg to $m = 1374$kg,
- The front wheels mass is increased from $m_f = 35.5$kg to $m = 45.5$kg,
- The suspension stiffness is reduced from $k_f = 27$kN/m to $k_f = 23$kN/m.

Table 6.10 shows the obtained results with constrained EMPC 0 while Table 6.12 shows the obtained results with constrained EMPC 1 under the new parameters set. The constraints applied in constrained EMPC 1 are presented in Table 6.11. The corresponding plots are depicted in figure 6.9 for constrained EMPC 0 and figure 6.10 for constrained EMPC 1. The values of ϕ and α used in the terminal cost and constraint for constrained EMPC 0 are given by (6.45)

$$\phi = \mathbf{I}_5 \quad \alpha = 28 * Tr(\phi \tilde{X}(N_T)) \tag{6.45}$$

while the values of ϕ and α for constrained EMPC 1 are given by (6.46)

$$\phi = 10^4 * \mathbf{I}_5 \quad \alpha = 20 * Tr(\phi \tilde{X}(N_T)) \tag{6.46}$$

It is shown in Table 6.10 that constrained EMPC 0 recovers twice the energy harvested by the LQR within the same control input range and it exhibits almost the same physical characteristics as the LQR. Constrained EMPC 1 achieves more energy harvesting than the LQR with ride comfort and deflections improvement while needing greater control inputs as shown in Table 6.12. Despite the changes in vehicle parameters, the LQR and EMPC strategies remain effective, confirming their robustness to moderate vehicle parameters uncertainties.

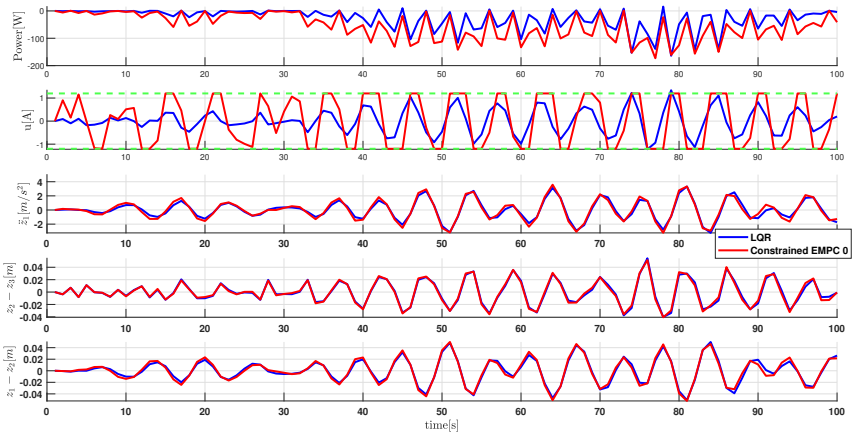

Figure 6.9: Constrained EMPC 0 vs. LQR for vehicle parameters variations

Table 6.10: Constrained EMPC 0 results obtained with vehicle parameters variations

	LQR	Constrained EMPC 0
Mean Power [W]	-27.66	-54.41
Control Input Range [A]	[-1.2; 1.3]	[-1.2; 1.2]
Accelerations Range [m/s^2]	[-3.2; 3.3]	[-3.2; 3.6]
Tire Deflection Range [m]	[-0.04; 0.05]	[-0.04; 0.04]
Suspension Deflection Range [m]	[-0.05; 0.05]	[-0.05; 0.05]

Table 6.11: Active constraints in LQR and Constrained EMPC 1 with vehicle parameters variations

Constraints	LQR	Constrained EMPC 1
Control Input [A]	—	[-10; 10]
Accelerations [m/s^2]	—	[-1.5; 1.5]
Tire Deflection [m]	—	[-0.04; 0.04]
Suspension Deflection [m]	—	[-0.04; 0.04]

Table 6.12: Constrained EMPC 1 results obtained with vehicle parameters variations

	LQR	Constrained EMPC 1
Mean Power [W]	-27.66	-48.2
Control Input Range [A]	[-1.2; 1.3]	[-9.6; 9.4]
Accelerations Range [m/s^2]	[-3.2; 3.3]	[-1.5; 1.5]
Tire Deflection Range [m]	[-0.04; 0.05]	[-0.03; 0.04]
Suspension Deflection Range [m]	[-0.05; 0.05]	[-0.03; 0.03]

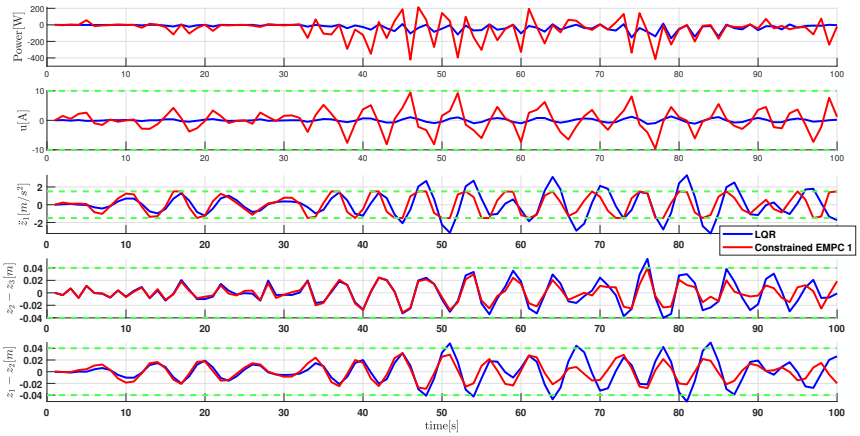

Figure 6.10: Constrained EMPC 1 vs. LQR for vehicle parameters variations

Table 6.13: Active constraints in LQR and Constrained EMPC 3 for $n_{00} = 0.1m^{-1}$

Constraints	LQR	Constrained EMPC 3
Control Input [A]	—	[-10; 10]
Accelerations [m/s^2]	—	[-1; 1]
Tire Deflection [m]	—	—
Suspension Deflection [m]	—	—

Table 6.14: Constrained EMPC 3 results obtained for $n_{00} = 0.1m^{-1}$

	LQR	Constrained EMPC 3
Mean Power [W]	-14.45	-38.84
Control Input Range [A]	[-0.8; 1]	[-8.6; 6.9]
Accelerations Range [m/s^2]	[-2.54; 3.32]	[-1; 1]
Tire Deflection Range [m]	[-0.03; 0.03]	[-0.02; 0.02]
Suspension Deflection Range [m]	[-0.04; 0.03]	[-0.03; 0.02]

Another robustness investigation has been carried out. Indeed, the road signal's parameters have been modified to analyze the performance of the controllers under new road signals.

- The minimal boundary frequency $n_{00} = 0.033m^{-1}$ is increased to $n_{00} = 0.1m^{-1}$. The constraints applied in this scenario are described in Table 6.13 and the corresponding results are presented in Table 6.14. It is shown that the constrained EMPC 3 outperforms LQR in terms of energy harvesting and physical characteristics while needing greater control inputs.
- The road roughness $G(n_0) = 80 \times 10^{-6}$ corresponding to a C class road (average roughness) is decreased to $G(n_0) = 20 \times 10^{-6}$ corresponding to a B class road (good roughness) with respect to ISO 8608 standard

Table 6.15: Active constraints in LQR and Constrained EMPC 3 for $G(n_0) = 20 \times 10^{-6}$

Constraints	LQR	Constrained EMPC 3
Control Input [A]	—	[-14; 14]
Accelerations [m/s^2]	—	[-1; 1]
Tire Deflection [m]	—	—
Suspension Deflection [m]	—	—

Table 6.16: Constrained EMPC 3 results obtained for $G(n_0) = 20 \times 10^{-6}$

	LQR	Constrained EMPC 3
Mean Power [W]	-28.8	-28.9
Control Input Range [A]	[-1.14; 1.44]	[-13.7; 11.6]
Accelerations Range [m/s^2]	[-3.8; 4.6]	[-1; 1]
Tire Deflection Range [m]	[-0.04; 0.05]	[-0.03; 0.03]
Suspension Deflection Range [m]	[-0.06; 0.05]	[-0.04; 0.02]

as shown in Table 5.1. The constraints applied in this scenario are described in Table 6.15 and the corresponding results are presented in Table 6.16. It is shown that the constrained EMPC 3 harvests the same energy as the LQR but with better physical characteristics while needing greater control inputs.

The values of ϕ and α used in the terminal cost and constraint for constrained EMPC 3 are given by (6.47)

$$\phi = \mathbf{I}_5 \quad \alpha = 28 * Tr(\phi \tilde{X}(N_T)) \tag{6.47}$$

In the above results, it has been shown that the designed control strategies are effective when faced with the inevitable variability of vehicles and roads.

6.2.3.7 Application to a full car model

A quarter car model analyzes the vertical motion of the vehicle only while neglecting its other motions. A more accurate model is needed to investigate the potentialities of the controllers. By considering a full-car model, the complex dynamics of the vehicle can be analyzed involving its vertical motion (z_s), its pitch motion (θ_s) and its roll motion (φ_s) as depicted in Chapter 2. The continuous time state equation for a full-car model is given by (6.48):

$$\dot{x}_f(t) = A_f x_f(t) + B_f u_f(t) + E_f \dot{z}_r(t) \tag{6.48}$$

where the matrices A_f, B_f, E_f are of appropriate dimensions, $x_f(t)$ is the full-car state, $u_f(t)$ the input and $\dot{z}_r(t)$ the exogenous input corresponding

to the following system vectors

$$x_f = \begin{bmatrix} z_{s_1} - z_{u_1} \\ z_{s_2} - z_{u_2} \\ z_{s_3} - z_{u_3} \\ z_{s_4} - z_{u_4} \\ \dot{\varphi}_s \\ \dot{\theta}_s \\ \dot{z}_s \\ z_{u_1} - z_{r_1} \\ z_{u_2} - z_{r_2} \\ z_{u_3} - z_{r_3} \\ z_{u_4} - z_{r_4} \\ \dot{z}_{u_1} \\ \dot{z}_{u_2} \\ \dot{z}_{u_3} \\ \dot{z}_{u_4} \end{bmatrix} \quad u_f = \begin{bmatrix} i_1 \\ i_2 \\ i_3 \\ i_4 \end{bmatrix} \quad \dot{z}_r = \begin{bmatrix} \dot{z}_{r_1} \\ \dot{z}_{r_2} \\ \dot{z}_{r_3} \\ \dot{z}_{r_4} \end{bmatrix} \tag{6.49}$$

This state equation directly uses $\dot{z}_r$ as the disturbance to the system but a state equation similar to (5.3) is needed where the only disturbance signal is the Gaussian white noise w. In this full-car configuration and following (5.2), the road profile is given by:

$$\dot{z}_r = \alpha_1 V z_r + \beta_1 \sqrt{V} w, \tag{6.50}$$

By solving the differential equation (6.50) characterizing the road profile, a solution is obtained :

$$\dot{z}_r(t) = \beta_1 \sqrt{V} w(t) + \alpha_1 V \beta_1 \sqrt{V} \int_0^t e^{\alpha_1 V (t-\tau)} w(\tau) d\tau \tag{6.51}$$

which results to (6.52) in convolution form :

$$\dot{z}_r(t) = [\beta_1 \sqrt{V} \delta(t) + \alpha_1 V \beta_1 \sqrt{V} e^{\alpha_1 V t} unit(t)] w(t) \tag{6.52}$$

where *unit* is the unit step function and δ is the Dirac delta function. By using (6.52) in (6.48), a state space representation using directly the Gaussian white noise w as a disturbance signal is achieved. After discretization, LQR and constrained EMPC 1 are investigated. The constraints applied in constrained EMPC 1 are presented in Table 6.17. For this simulation, the original C road signal and vehicle parameters are employed. The values of ϕ and α used in the terminal cost and constraint for constrained EMPC 1 are given by (6.53)

$$\phi = \mathbf{I}_{15} \quad \alpha = 28 * Tr(\phi \tilde{X}(N_T)) \tag{6.53}$$

The results are presented in Table 6.18 and Table 6.19 for the LQR and constrained EMPC 1 respectively. One notices that the constrained EMPC 1 still outperforms the LQR strategy in terms of power harvested and all the constraints are satisfied. Moreover, the power harvested in this full-car scenario is a little bit greater than 4 times the power harvested on a quarter-car model due to the all the dynamics neglected in section 6.2.3.3.

Table 6.17: Active constraints in LQR and Constrained EMPC 1 for a full-car model

Constraints	LQR	Constrained EMPC 1
Control Input [A]	—	[-20; 20]
Accelerations [m/s^2]	—	[-3; 3]
Tire Deflection [m]	—	[-0.05; 0.05]
Suspension Deflection [m]	—	[-0.15; 0.15]

Table 6.18: LQR on a full car model

LQR				
Total Power [W]	-403.4			
Average $\ddot{z}_s$ [m/s^2]	[-6; 4]			
	Wheel 1	Wheel 2	Wheel 3	Wheel 4
Average u [A]	[-9.3 ; 10.9]	[-7.3 ; 8.01]	[-10.39 ; 13.46]	[-8.21 ; 8.23]
Average $z_u - z_r$ [m]	[-0.03 ; 0.03]	[-0.03 ; 0.03]	[-0.04 ; 0.04]	[-0.03; 0.03]
Average $z_s - z_u$ [m]	[-0.11; 0.10]	[-0.1 ; 0.08]	[-0.14 ; 0.14]	[-0.1 ; 0.1]

Table 6.19: Constrained EMPC 1 on a full car model

Constrained EMPC 1				
Total Power [W]	-627.4			
Average $\ddot{z}_s$ [m/s^2]	[-3; 3]			
	Wheel 1	Wheel 2	Wheel 3	Wheel 4
Average u [A]	[-16 ; 17]	[-12.9; 9.8]	[-15.5; 13.8]	[-11.4 ; 11.1]
Average $z_u - z_r$ [m]	[-0.03 ; 0.03]	[-0.03 ; 0.03]	[-0.04 ; 0.04]	[-0.03 ; 0.03]
Average $z_s - z_u$ [m]	[-0.11 ; 0.10]	[-0.1; 0.09]	[-0.14; 0.14]	[-0.09 ; 0.1]

6.3 EMPC design for Wave Energy Converters

The control requirements are energy harvesting, control input's restriction, heave position and heave velocity's restriction. This restriction depends on the WEC and the wave characteristics. For instance in [73], the linear PTO AWS has a stroke of $7m$ ($[-3.5; 3.5]m$) . For larger waves, the restriction on heave position becomes difficult to maintain while harvesting energy. Generally, the goal is to maintain a heave displacement smaller than the wave peaks as in [57]. The heave velocity and control input should be maintained as small as possible. In the following subsections we present some control approaches to deal with such requirements. We will use the same notations as in the previous section.

6.3.1 EMPC formulation

n being the number of states, the state and input constraints are represented by $x \in \mathbb{X}$ and $u \in \mathbb{U}$ with

$$\mathbb{X} := \{x \in \mathbb{R}^n : |z_v| \leq d_{max} \ \& \ |\dot{z}_v| \leq v_{max}\} \tag{6.54}$$

$$\mathbb{U} := \{u \in \mathbb{R}^n : |u| \leq u_{max}\} \tag{6.55}$$

After discretizing the WEC's state space model of Eq.(5.63) with a sampling time T_s, we obtain the following state space model

$$\begin{cases} x(k+1) &= A_d x(k) + B_d u(k) + E_d w(k) \\ z_d(k) &= C_z' x(k), \forall k \in \mathbb{I}_{[0,N_T-1]} \end{cases} \tag{6.56}$$

where N_T is the prediction horizon. The optimization variable $z(k)$ is chosen

$$z(k) = \begin{bmatrix} x(k) \\ u(k) \end{bmatrix}, \forall k \in \mathbb{I}_{[0,N_T-1]} \tag{6.57}$$

The problem to solve is to design a control law acting on the input $u(k)$ with the aim of maximizing the harvested energy while preserving constraints fulfilment. We recall that the harvested electrical power can be computed as follows using a linear generator:

$$P_e(t) = R_a i^2(t) + L_a \frac{di(t)}{dt} i(t) + K_a v(t) i(t) \tag{6.58}$$

where R_a is the resistance, L_a the inductance, K_a the voltage constant, $v(t)$ the speed. Following the reasoning of section 5.2.5, the objective of maximizing the harvested energy can be converted in the minimization of the expected value of P_e. We have the following cost index:

$$J := E(2v_{emf}^T N_a i + i^T R_a i) \tag{6.59}$$

where v_{emf} is the back EMF voltage and $E(.)$ is the expected value under stationary conditions. Notice that N_a is a cross coupled weighting matrix. Under stationary conditions, the expected value of the electrical power is given by

$$J := E(v_{emf} i + R_a i^2) \tag{6.60}$$

The two previous equations express the same cost index J. One finds $N_a = 0.5$. By noting that

$$v_{emf} = K_a \dot{z}_v \tag{6.61}$$

$$\dot{z}_v = G^T x, \text{with } G^T = [0,\ 1,\ 0_{1\times(n_r+n_e)}] \tag{6.62}$$

We can rewrite the objective cost to minimize as:

$$l(x,u) = x^T G N_a K_a u + u^T R_a u \tag{6.63}$$

The linear EMPC optimization problem can be formulated as follows:

$$\begin{cases} min_{u(k)} \sum_{k=0}^{N_T-1} \ell(x(k), u(k)) \\ s.t \\ x(k+1) = A_d x(k) + B_d u(k) + E_d w(k), k \in \mathbb{I}_{[0,N_T-1]} \\ x(k) \in \mathbb{X}, u(k) \in \mathbb{U}, k \in \mathbb{I}_{[0,N_T-1]} \\ x(0) = x(t) \\ x(N_T) = x_F(t \bmod T) \end{cases} \tag{6.64}$$

where $w(k)$ is predicted through the Harvey's model [61] and $x(t)$ are initial states obtained from sensors. Moreover, the term $x_F(t)$, appearing in the terminal equality constraint, is a sample of a periodic sequence $\mathbf{x_F}$ that is offline determined by assuming to know the period T of the disturbance signal $w(t)$. It can be obtained by computing the best steady-state periodic solution of $\ell(\cdot)$ according to the following problem

$$\begin{cases} min_{x_F, u_F} \sum_{k=0}^{T-1} \ell(x_F(k), u_F(k)) \\ s.t \\ x_F(k+1) = A_d x_F(k) + B_d u_F(k) + E_d w(k), k \in \mathbb{I}_{[0,T-1]} \\ x_F(k) \in \mathbb{X}, u(k) \in \mathbb{U}, k \in \mathbb{I}_{[0,T-1]} \\ x_F(0) = x_F(T) \end{cases} \tag{6.65}$$

As proven in [108], if the above solution is used as terminal ingredient in (6.64), then the recursive feasibility of (6.64) is guaranteed. In fact, $x_F(t)$ are the states corresponding to a single frequency signal, maximizing the energy harvesting and satisfying the constraints. Moreover, as customary in receding horizon control, it is assumed that only the first element of the minimizing control sequence computed at time t, is actually applied to the plant and the whole optimization program reruns at the subsequent sampling time.

6.3.2 Other control laws used for comparison

6.3.2.1 Linear noncausal optimal control

The *Linear Noncausal Optimal Control* (LNOC) is computed through the following optimization problem [103].

$$min_{u(k)} \frac{\sum_{k=0}^{N_T-1} l(x(k), u(k))}{N_T} \tag{6.66}$$

$$\begin{aligned} s.t \quad & x(k+1) = A_d x(k) + B_d u(k) + E_d w(k) \\ & z_d(k) = C_z' x(k), \forall k \in \mathbb{I}_{[0,N_T-1]} \end{aligned} \tag{6.67}$$

where the stage cost $l(x(k), u(k))$ is given by

$$l(x(k), u(k)) := \frac{1}{2}x(k)^T Q x(k) + \frac{1}{2}ru(k)^2 + z_d(k)u(k)$$

In this equation, the first two terms are used to penalize the state and control input respectively; the weights Q and r can be used as tuning parameters to influence the stability and robustness of the system. $z_d(k)u(k)$ represents the power at time step k that can be absorbed by the PTO mechanism.

When constraints are inactive, the infinite dimensional optimization problem can be tackled by the following linear noncausal optimal control policy without performance degradation:

$$u(k) = K_x x(k) + K_d w(k) \tag{6.68}$$

where $w(k)$ is the N_T-step of wave prediction and $x(k)$ is the current state. K_x and K_d are calculated following the rules in [103].

The aforementioned control strategies (EMPC and LNOC) are designed based on the assumption that the full information of x is available. However, in many cases, direct measurements of all states of a WEC are not realistic, e.g. the states associated with the radiation force and excitation force. Thus a state observer needs to be designed. We assume the measured states are the buoy's velocity (also called heave velocity) and the buoy's displacement (also called heave postion) such as:

$$y(k) = [\dot{z}_v, z_v]^T = Cx(k) \tag{6.69}$$

with C the corresponding matrix and (A, C) is assumed to be observable. A Kalman filter observer is designed with the form of

$$\tilde{x}(k+1) = A_d\tilde{x}(k) + B_d u(k) + E_d w(k) + L(y(k) - C\tilde{x}(k)) \tag{6.70}$$

where $\tilde{x}$ is the estimated state and $\tilde{w}$ is the measured current wave elevation.

At each time step, with the wave prediction w provided by the wave prediction technology and the state estimation $\tilde{x}$ provided by the estimator, the optimization is derived through the following algorithm.

Algorithm: *The control strategies can be implemented by recursively going through the following procedure at each time step:*

1: *Wave prediction w from wave prediction device.*
2: *State estimation updates:*

$$\tilde{x}(k) = \tilde{x}(k/k-1) + L(y(k) - C\tilde{x}(k/k-1)) \tag{6.71}$$

where $\tilde{x}(k/k-1)$ represents $\tilde{x}(k)$ estimated at time $k-1$ and L is the Kalman gain which can be computed offline as [103]

$$L = -PC^T(CPC^T + R_v)^{-1} \tag{6.72}$$

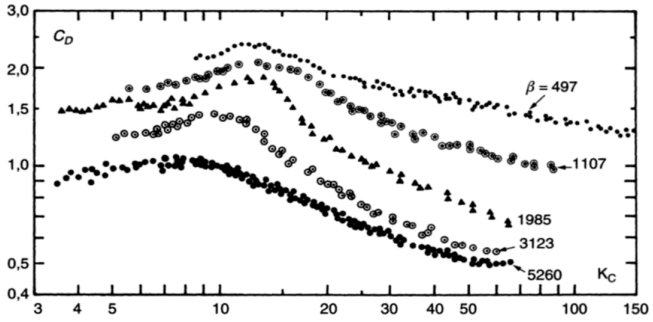

Figure 6.11: Drag coefficient

where P is the solution of Discrete time Algebraic Ricatti Equation (DARE)

$$P = A_d P A_d^T - A_d P C^T (C P C^T + R_v)^{-1} C P A_d^T + Q \tag{6.73}$$

where R_v and Q are tuning matrices.

3: *Control input update $u(k)$ with respect to $\tilde{x}(k)$*

4: *Estimator updates.*

$$\tilde{x}(k+1/k) = A_d \tilde{x}(k/k) + B_d u(k/k) + E_d w(k) \tag{6.74}$$

6.3.2.2 Nonlinear model predictive control using the moment domain approach

The NMPC is a moment domain based approach which includes nonlinearities often neglected in WEC control strategies. The dynamics equation of WEC in Eq.3.3 becomes [109]

$$(m_s + m_\infty)\ddot{z}_v + k\dot{z}_v + k_s z_v - F^{nl} = f_e - f_u \tag{6.75}$$

where k is the radiation impulse response function containing the memory effect of the fluid response. It is also called the damping coefficient. F^{nl} represents all nonlineartities exerting on the device. In particular, we consider two main hydrodynamic forces: viscous effects F_v and a nonlinear restoring force F_r^{nl}.

The Morison equation describes the total force on a fixed body in an oscillatory flow [110] therefore the viscous effects F_v are defined as [109]:

$$F_v(\dot{z}_v) = -\beta_v |\dot{z}_v| \dot{z}_v \tag{6.76}$$

where $\beta_v = \frac{1}{2}\, \rho\, C_D\, D$, ρ being the water's density, C_D the drag coefficient and D the characteristic area of the device. Notwithstanding the simplicity of Eq.(6.76), the definition of the drag coefficient represents a challenge.

Ideally, specific experimental tests can be performed in order to identify C_D, as in [111]. However, accessing wave tank facilities is often not a feasible option, due to high costs of experimental testing. Furthermore, a prototype

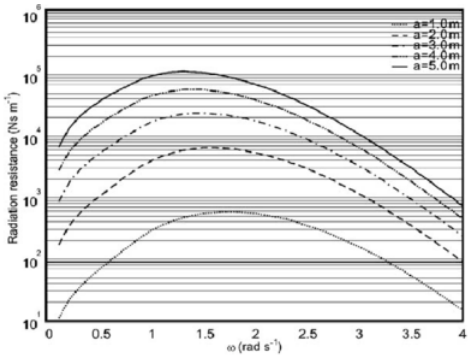

Figure 6.12: Radiation resistance

of the device needs to be available for testing. Such problems may be overcome by performing the identification of C_D in a numerical wave tank, using Computational Fluid Dynamics simulations, as in [112]. On the other hand, when simple geometries are considered, it is possible to approximate C_D based on data available in the literature [113]. In the case of heaving floating buoys, the dimensionless Keulegan Carpenter number K_C can be used, which is the ratio between the drag and inertia forces acting on a body in an oscillatory fluid flow [114]. In the case of sinusoidal motion, the K_C number can be computed as:

$$K_C = 2\pi \frac{A}{L_c} \tag{6.77}$$

where A is the amplitude of motion and L_c is a characteristic length scale, for example the diameter for a sphere. With the value of K_C, it is possible to obtain the drag coefficient using experimental graphs like Fig.6.11. This figure depicts the drag coefficient with respect to the Keulegan-Carpenter number K_C and the Reynolds number β [115].

The nonlinear restoring force F_r^{nl} is computed based on experimental results on the WEC. One can write [109]:

$$F_r^{nl}(z_v) = \beta_{r1} z_v^2 + \beta_{r2} z_v^3 \tag{6.78}$$

The coefficients β_{r1} and β_{r2} are determined through experimental results on the device [109]. Another important parameter needed for this NMPC strategy is the radiation resistance R of the device which can be obtained using Fig.6.12. This figure displays the radiation resistance with respect to the angular velocity of the device and different device's radii.

It is assumed that the excitation force f_e can be written as a finite sum L of harmonics of the peak frequency ω_p. The wave excitation force f_e and the control input f_u can be expressed as a function of the extended signal generator as in [109]:

$$\begin{cases} \dot{\bar{\epsilon}} = \overline{S}\bar{\epsilon} \\ f_e = \overline{L}_e \bar{\epsilon} \\ f_u = \overline{L}_u \bar{\epsilon} \end{cases} \tag{6.79}$$

where $\overline{\epsilon(t)} \in \mathbb{R}^L$ and

$$\overline{S} = \oplus_{f=1}^{L/2} \begin{bmatrix} 0 & f\omega_p \\ -f\omega_p & 0 \end{bmatrix} \tag{6.80}$$

$\overline{L}_e$ and $\overline{L}_u$ are user-defined such that the triple of matrices ($\overline{L}_e$-$\overline{L}_u$, $\overline{S}$,$\overline{\epsilon(0)}$) is minimal, i.e observable and excitable.

The energy maximizing problem can be converted to a convex optimization problem such as:

$$\begin{cases} min_{z\in\mathbb{R}^{1*L}} \overline{J}_{QP}(z) + \overline{J}_{nl}(z) \\ s.t \\ A_x z \leq B_x \\ A_{\dot{x}} z \leq B_{\dot{x}} \\ A_u z + N_u(z) \leq B_u \end{cases} \tag{6.81}$$

with

$$\overline{J}_{QP}(z) = \frac{1}{2}(z^T \overline{\phi}^{-1} z - z^T \overline{L}_e^T) \tag{6.82}$$

$$\overline{J}_{nl}(z) = \frac{1}{2} z^T \overline{\phi}^{-1} \phi_\Omega vec(F_{nl}(g(z))) \tag{6.83}$$

$$\begin{gathered} A_x = \overline{S}^{-1}\overline{\Delta}, \quad B_x = X_{max}\mathbf{1}_{1*2N_p} \\ A_{\dot{x}} = \overline{\Delta}, \quad B_{\dot{x}} = V_{max}\mathbf{1}_{1*2N_p} \\ A_u = -\overline{\phi}^{-T}\overline{\Delta}, \quad B_u = U_{max}\mathbf{1}_{1*2N_p} + \overline{L}_e * A_u \\ N_u(z) = -vec(F_{nl}(g(z)))^T \phi_\Omega^T A_u \end{gathered} \tag{6.84}$$

The parameters $\overline{\phi}$, $\overline{\Delta}$, ϕ_Ω are given in [109]. Eq.6.84 denotes the set of constraints with X_{max}, V_{max},U_{max} being the bounds on the heave position, heave velocity and actuator force respectively. $\overline{J}_{QP}$ represents the quadratic cost function and $\overline{J}_{nl}$ the nonlinear cost function. F_{nl} and g functions are explicited in [109].

6.3.3 Results and discussions

6.3.3.1 Perfect wave prediction and imperfect wave prediction

In this section, we present comparison results between the LNOC, EMPC and LQR based approach of section 5.4.3.2. Many works that incorporate wave prediction in the control laws design use the assumption that $w(k)$ is provided by a wave prediction device at each time step. However in practice, it might not be possible to have an estimation of the wave signal at each time step k because the wave signal is the sum of many harmonics of different frequencies. It could be difficult for a wave prediction device to estimate all these frequencies at each time step. Therefore, in this section, we use two configurations. We consider the ideal case where we have a perfect estimation of the wave signal at each time step in our controller. In the

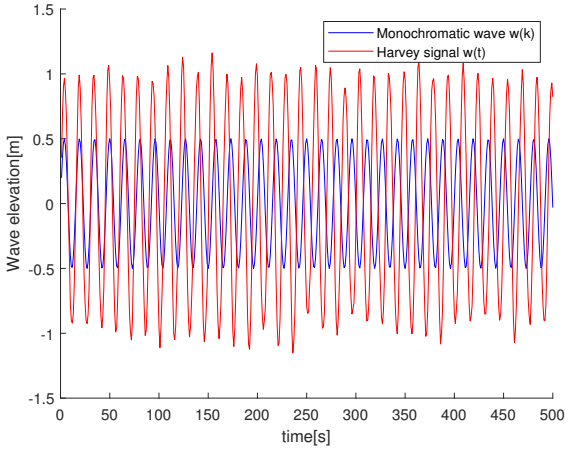

Figure 6.13: Monochromatic wave $w(k)$ vs Harvey's model wave $w(t)$

Table 6.20: Ideal case: values obtained without constraints

	LQR	EMPC	LNOC
Mean Power P_e/P_m[W]	-81/-119	-173/-300	n.a./-373
Input current range u[A]	[-4;8]	[-26;9]	[-17;116]
Heave position range z_v [m]	[-1.1;1.1]	[-0.7;0.7]	[-2.1;2.9]
Heave velocity range $\dot{z}_v$ [m/s]	[-4;4]	[-3;3]	[-8;7]

second case, we use a monochromatic signal as the prediction of the wave. This monochromatic signal must be in phase with the real wave signal as depicted in Fig.6.13.

As we can see on the figure, the monochromatic signal used in the controller $w(k)$ for the non ideal case is lower than the signal used in the simulations $w(t)$. In fact, we decided to understimate the wave signal's prediction at each time step in the controller. The results obtained with underestimation are more reliable than the ones one could have obtained by overestimating the wave signal in the predictions. If one overestimates the wave prediction to be used in the controller, surely one could obtain more power than the ideal case but these results would be unrealistic.

The simulations are presented based on the same point absober introduced in section 5.4.4 (Table A.9 of the appendix A). We use a sampling time T_s=0.1 s and a prediction Horizon N_T=10 as in [103] and [116].

Table 6.20 presents the performance obtained with the three control laws in the ideal case with the only goal to maximize energy harvesting. In other words, no constraints have been added to the EMPC optimization problem. For the LQR and EMPC, the electrical power P_e and the absorbed (mechanical) power P_m are presented. The absorbed power is greater than the electrical power because the electrical power considers the generator's losses. For the LNOC, only the absorbed power is presented. Indeed, the electrical

Table 6.21: Ideal case: values obtained with constraints

	LQR	EMPC	LNOC
Mean Power P_e/P_m[W]	-81/-119	-87/-318	n.a./-185
Input current range u[A]	[-4;8]	[-85;14]	[-26;75]
Heave position range z_v[m]	[-1.1;1.1]	[-0.5;0.5]	[-1.4;1.4]
Heave velocity range $\dot{z}_v$[m/s]	[-4;4]	[-2;2]	[-5;5]

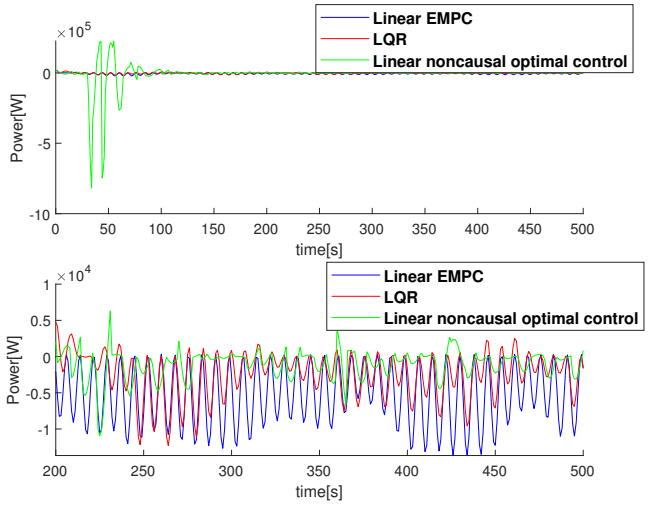

Figure 6.14: Power for the ideal case during 500 s simulation (a) and in the interval [200-500] s (b)

power P_e generated by the LNOC can't be computed because this approach doesn't incorporate the generator's dynamics like the others. We compare the absorbed powers as it is common in WEC literature [103],[38],[39]. We know that the LQR can't handle constraints so the heave position obtained is equal to the wave peak (1.1 m approximately as we can see in Fig.6.13). The LNOC can be tuned to obtain a certain performance through trial and error procedure. The tuning parameters are $Q = 2 \times 10^6$ and $r = 3$. We note that the power obtained with the LNOC is the greatest but with bad heave position. It also needs the greatest control input. In terms of energy harvesting, it is followed by the EMPC which has the best heave position and heave velocity among the three control laws. In addition, the EMPC recovers more energy than the LQR strategy. Fig.6.14 displays the power obtained with the three control laws during 500 s simulation and an emphasis has been put on the [200-500] s interval which represents the steady state. Fig.6.15 displays the heave position and heave velocity obtained with the three control laws.

Table 6.21 presents the performance obtained with the three control laws with the goal to maximize energy harvesting while satisfying physical limits. The tuning parameters for the LNOC are $Q = 1 \times 10^6$ and $r = 3$. When we compare these results to the unconstrained case, we note that the control

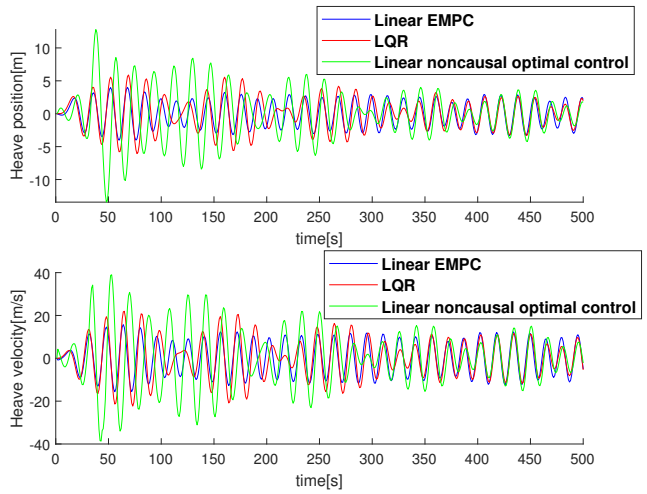

Figure 6.15: Ideal case: Heave position (a) and Heave velocity (b)

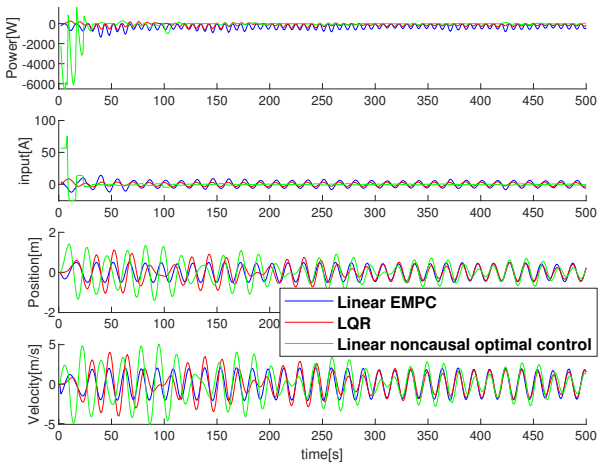

Figure 6.16: Ideal case constrained: Absorbed power, control input, heave position and heave velocity

input has been increased to satisfy the bounds. We note that the EMPC is the best control strategy in terms of constraints satisfaction and energy harvesting. It is followed by the LNOC in terms of energy harvesting but with physical characteristics worse than those obtained with the LQR. The LQR control input is the smallest among the three control laws. Fig.6.16 depicts the absorbed power, control input, heave position and heave velocity obtained with the three control laws when we apply constraints.

Table 6.22 shows the results obtained with the only goal to maximize energy harvesting considering a non ideal case. We note that the results obtained with the LQR are not different from the results obtained in the ideal case. It is due to the fact that the LQR control law doesn't use wave predictions. The tuning parameters for the LNOC are Q=2×10^6 and $r = 3$.

Table 6.22: Non ideal case: values obtained without constraints

	LQR	EMPC	LNOC
Mean Power P_e/P_m[W]	-81/-119	-170/-291	n.a./-344
Input current range u[A]	[-4;8]	[-26;9]	[-170;77]
Heave position range z_v[m]	[-1.1;1.1]	[-0.7;0.7]	[-2.1;2.1]
Heave velocity range $\dot{z}_v$[m/s]	[-4;4]	[-3;3]	[-7;7]

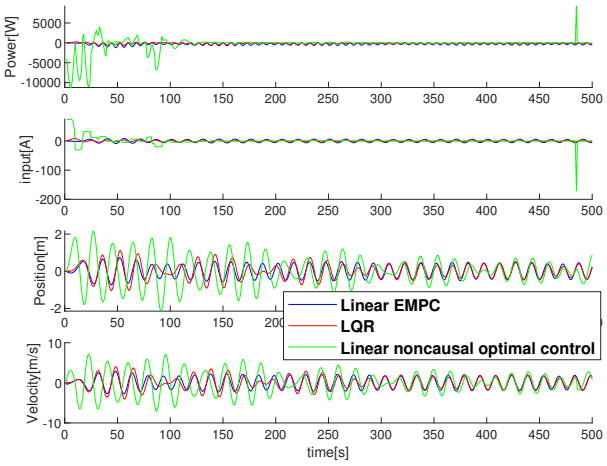

Figure 6.17: Non ideal case: Absorbed power, control input, heave position and heave velocity

Table 6.23: Non ideal case: values obtained with constraints

	LQR	EMPC	LNOC
Mean Power P_e/P_m[W]	-81/-119	-84/-316	n.a./-96
Input current range u[A]	[-4;8]	[-85;14]	[-1.3;65.6]
Heave position range z_v[m]	[-1.1;1.1]	[-0.5;0.5]	[-1.1;1.5]
Heave velocity range $\dot{z}_v$[m/s]	[-4;4]	[-2;2]	[-4.2;4]

We note that the power obtained with the LNOC is the greatest but with worst heave position and heave velocity. In terms of energy harvesting, it is followed by the EMPC which gives the best heave position and heave velocity among the three control laws. Fig.6.17 shows the corresponding plots.

Table 6.23 presents the results while satisfying physical limits in the non ideal case. The tuning parameters for the LNOC are $Q = 10^6$ and $r = 3$. Fig.6.18 shows the corresponding plots. The results are quite similar to the ones obtained in the ideal case. In all cases, the input force limit is respected. Among all three control laws, the EMPC seems to be the best control strategy suitable for energy harvesting in the WEC. On a computational

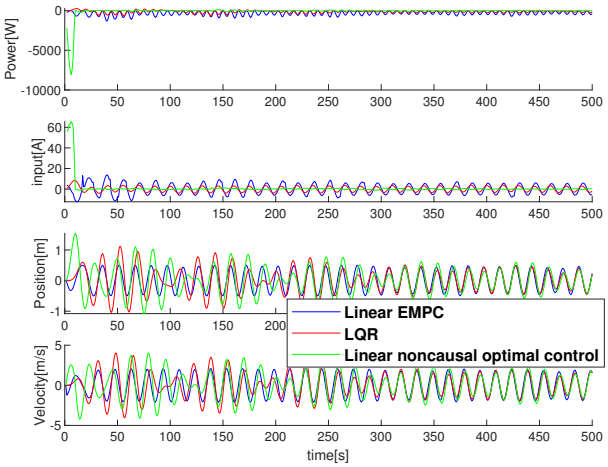

Figure 6.18: Non ideal case constrained: Absorbed power, control input, heave position and heave velocity

complexity point of view, one can say the LQR is computed faster than the other strategies. It requires 2 seconds approximately while the EMPC and the LNOC require 5 minutes of computation. Indeed, this difference in computational complexity is due to the noncausal nature of the EMPC and LNOC.

6.3.3.2 Simulation on two models of WEC

In this section, we perform comparisons between the EMPC, NMPC and MIPC H_2 detailed in section 5.4.2. For simplicity, we assume that all simulations are undertaken with a perfect prediction of the wave signal $w(k)$ in the controller at each time step. We use a sampling time T_s=0.1 s and a prediction Horizon N_T=10 as in [103] and [116]. For the NMPC approach, we use 2 collocation points per second of simulation [109] to decrease the computational burden of the approach [109]. However we find that even using 10 collocation points per second of simulation doesn't modify the obtained results. Two WECs are considered. The first device is a small WEC. In particular, it is the standard Point Absorber used in the previous sections whose parameters can be found in Table A.9 of the appendix.

The second one is a full-scale CorPower-like wave energy device oscillating in heave (translational motion). The actual CorPower device is a wave energy system currently under development by the Swedish company CorPower Ocean. Note that this type of device is often considered as a case study, due to its intrinsic geometrical complexity. Fig.6.19 shows a schematic of the CorPower-like WEC, along with its corresponding hydrodynamic characterization. The dimensions of the device are shown in Table A.10 of the appendix.

The same actuator is used in the two devices and its data are presented

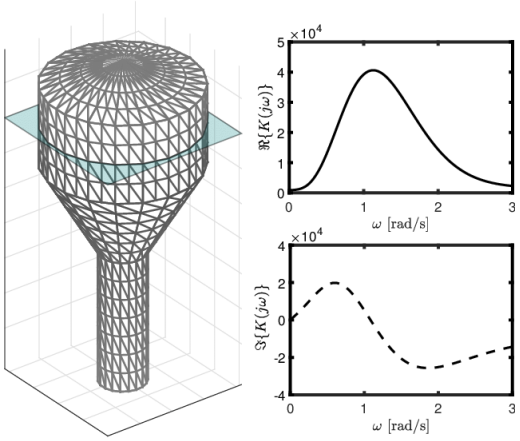

Figure 6.19: Corpower WEC Device

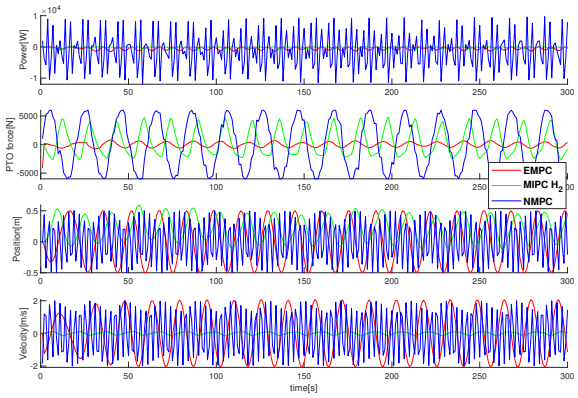

Figure 6.20: Absorbed power, PTO force, heave position and heave velocity obtained with the small WEC

Table 6.24: Values obtained with the small WEC

	EMPC	MIPC H_2	NMPC
Power $P_{absorbed}$[W]	-542	-177	-1318
Input force f_u[N]	[-4077;794]	[-3000;5000]	[-6000;6000]
Heave position z_v[m]	[-0.5;0.5]	[-0.1;0.58]	[-0.5;0.5]
Heave velocity $\dot{z}_v$[m/s]	[-2;2]	[-0.15;0.15]	[-2;2]

in Table A.8 of the appendix. We recall that the input force limit in N can be converted to the current limit in A through Eq.5.61 and vice versa.

- **Small WEC: Point Absorber**

  We use the first wave signal (see Fig.3.11) in this case study because this WEC point absorber has not been designed to handle bigger waves. Fig.6.20 and Table 6.24 display the results obtained in this configuration.

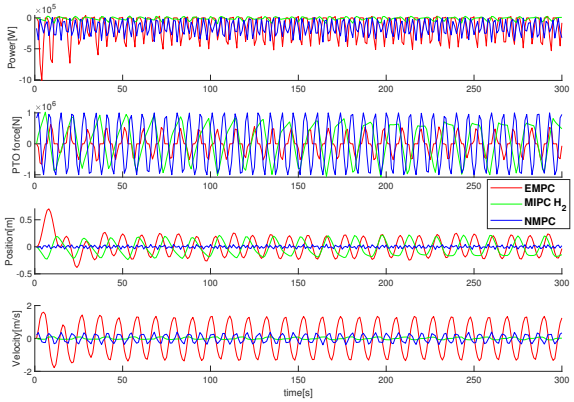

Figure 6.21: Absorbed power, PTO force, heave position and heave velocity obtained with the big WEC

One notices that only EMPC and NMPC perfectly satisfy the constraints on heave position and velocity. The control input force required by the EMPC is less than that required by the two other control laws. In terms of energy harvesting, NMPC gives the best result and it is followed by the EMPC then by the MIPC H_2. These energy harvesting results are explained by the fact that the NMPC approach considers all nonlinearities applied to the WEC. The control input force needed by the NMPC is greater than the one needed by the EMPC approach while remaining within the imposed bounds. Moreover, NMPC needs 2 hours of computation while EMPC and MIPC H_2 only need 5 minutes and 3 minutes of computation respectively. This emphasizes the fact that including nonlinearities in the controller increases a lot the computational burden. Even though MIPC H_2 gives the smallest heave position and heave velocity, one notices that it needs more control input force than the EMPC. It should be also noted that MIPC H_2 is the fastest control strategy illustrating the speed of causal control strategies.

- **Big WEC : Corpower device**

  To apply the control laws to this big WEC, we use a reduced-order model, which is derived using a static excitation coefficient D_e and a static radiation coefficient D_r to approximate the dynamical realizations of Eq.3.7 and Eq.3.9. This results in a 2^{nd}-order state space model (Eq.5.59) with the following matrices:

$$A_c = \begin{bmatrix} 0 & 1 \\ -\frac{k_s}{m} & -\frac{D_r}{m} \end{bmatrix} \quad B_{wc} = \begin{bmatrix} 0 \\ \frac{D_e}{m} \end{bmatrix} \quad B_{uc} = \begin{bmatrix} 0 \\ \frac{1}{m} \end{bmatrix} \quad C_z = \begin{bmatrix} 0 & 1 \end{bmatrix} \tag{6.85}$$

  where $w{:=}z_w$, $z{:=}\dot{z}_v$, $x{:=}\,[z_v,\dot{z}_v]$.

  Fig.6.21 and Table 6.25 display the results obtained. Only EMPC and NMPC satisfy the constraints on heave position, velocity and

Table 6.25: Values obtained with the big WEC

	EMPC	MIPC H_2	NMPC
Power $P_{absorbed}$[W]	-1.48*10^5	-1.44*10^4	-1.58*10^5
Input force f_u[N]	[-6.61;6.27]*10^5	[-1.1;1.05]*10^6	[-10^6;10^6]
Heave position z_v[m]	[-0.4;0.7]	[-0.24;0.24]	[-0.1;0.1]
Heave velocity $\dot{z}_v$[m/s]	[-1.8;1.6]	[-0.1;0.1]	[-0.5;0.5]

Table 6.26: Mean value of the computation time for each time step

	EMPC	NMPC
Small WEC	0.0921[s]	417[s]
Big WEC	0.0212[s]	253[s]

control input force. In terms of energy harvesting, NMPC gives the best result and it is followed by the EMPC. However, the control input force needed by the NMPC is greater than the one needed by the EMPC approach while remaining within the imposed bounds. As for the first WEC, NMPC needs 2 hours of computation while EMPC and MIPC H_2 only need 5 minutes and 3 minutes computation respectively. Table 6.26 depicts the mean values of the computation times needed at each step of the optimization problems. One notices the huge computational burden of the NMPC making it non suitable for real time implementation. Although NMPC achieves the greatest energy harvesting while satisfying the constraints, its computational burden is high (2 hours of computation on MATLAB). This high computational burden might be decreased by using other numerical optimization methods or softwares. Furthermore, the NMPC approach requires many experimental results and approximations making it more difficult to implement than the other control strategies.

6.3.3.3 Simulation under various sea conditions (Northwest coast of Ireland 23/05/2020-23/11/2020)

In this section, we investigate the potentialities of the EMPC under various sea conditions. The site chosen is an area of the sea to the North West of Ireland. Data is collected over a period of six months between May and November 2020. The data is taken from official measurements [117]. Fig.6.22 shows the probability (%) of sea conditions for the chosen site. Among all sea conditions, an operational region has been highlighted. Only within that region (shown in Fig.6.22 with a black rectangle), the device is supposed to be harnessing power. Therefore, those are the sea state combinations that will be simulated. We use the big WEC for these simulations.

Figs.6.23, 6.24, 6.25 and 6.26 show the results obtained under the selected sea conditions when constraints are applied to the EMPC scheme. We note

		Data from AMETS Berth B Wave Buoy offhore north west coast of Ireland (23/05/2020-23/11/2020)									
Significant Wave Height[m]	9.092	0	0	0	0	0	0	0	0.04788	0.07181	0
	8.176	0	0	0	0	0.01197	0.02394	0.03591	0.1915	0.09575	0.01197
	7.26	0	0	0	0.01197	0.1197	0.1696	0.05984	0.08378	0.01197	0
	6.344	0	0	0	0.1556	0.5266	0.5386	0.08378	0.1556	0	0
	5.428	0	0	0.01197	0.6463	1.676	1.137	0.2035	0.1676	0	0
	4.512	0	0	0.07181	1.209	4.105	1.616	0.1915	0	0	0
	3.596	0	0.01197	0.5027	4.129	5.577	0.6463	0.02394	0	0	0
	2.68	0	0.5147	3.184	14.29	7.313	1.161	0.1795	0.08378	0	0
	1.764	0.1436	2.657	8.055	13.57	3.758	0.4907	0.05984	0.1795	0.01197	0
	0.848	0.2633	2.501	8.438	6.882	1.46	0.371	0.02394	0.07181	0	0
		4.1795	6.0785	7.9775	9.8765	11.7755	13.6745	15.5735	17.4725	19.3715	21.2705
		Peak Period[s]									

Figure 6.22: Probability (%) of sea conditions for the chosen site (data from AMETS Berth B wave buoy offshore north west coast of Ireland).

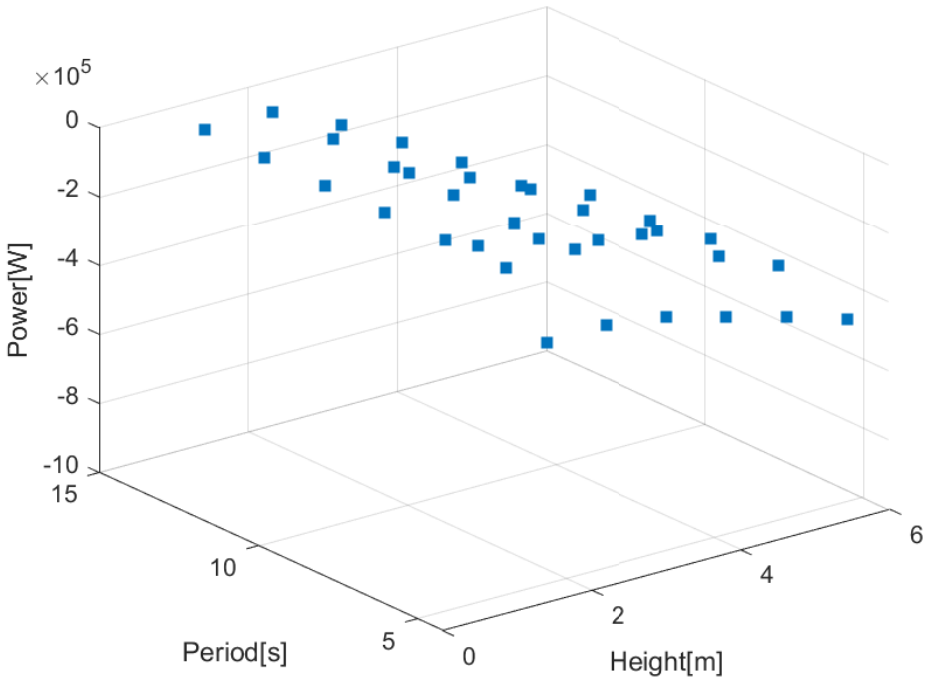

Figure 6.23: Power absorbed with the constrained EMPC under various sea conditions

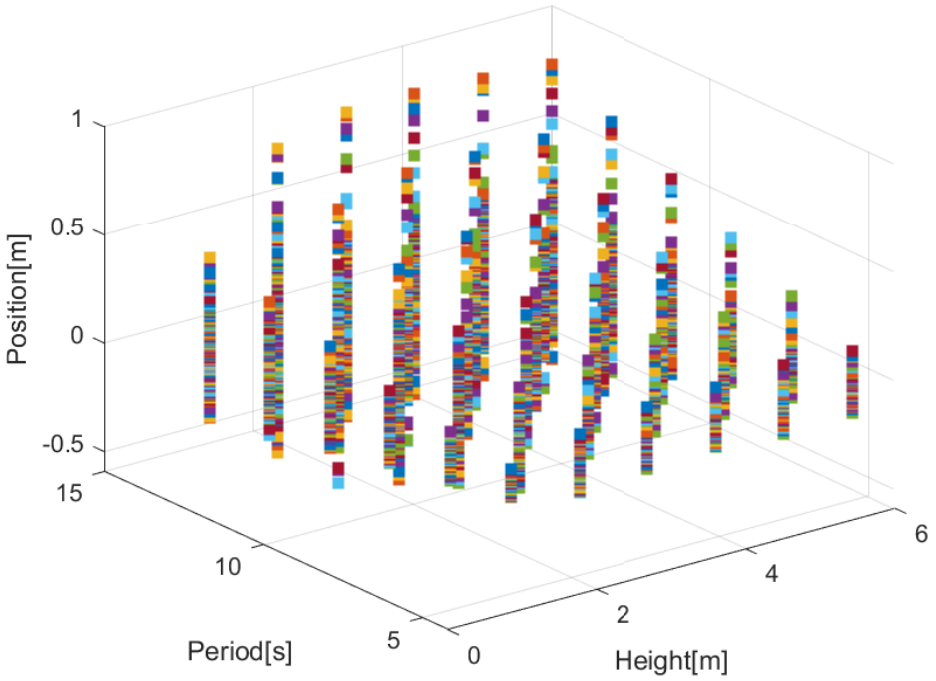

Figure 6.24: Position obtained with the constrained EMPC under various sea conditions

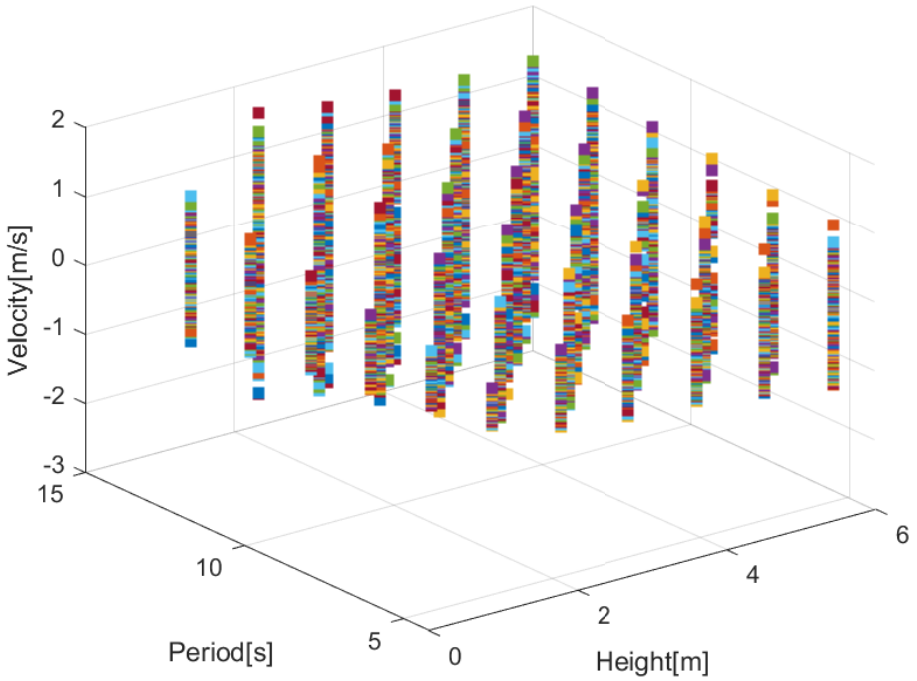

Figure 6.25: Velocity obtained with the constrained EMPC under various sea conditions

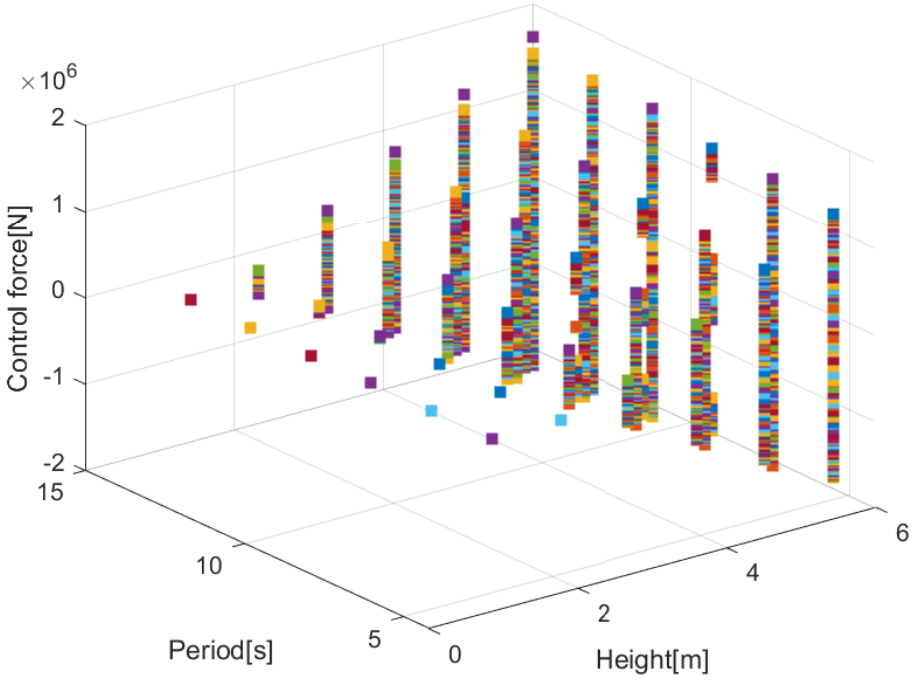

Figure 6.26: Control input force obtained with the constrained EMPC under various sea conditions

that the lowest absorbed power is -3.13 W which corresponds to $H_s = 0.848$ m and $T_p = 4.1795$ s. The greatest absorbed power is -8.87*10^5W which corresponds to $H_s = 5.428$ m and $T_p = 13.6745$ s. The velocity $\dot{z}_v$ belongs to the range [-2;2] m/s, the displacement z_v to the range [-0.6;0.9] m and the control input force f_u to [-1.82;1.97]$*10^6$N.

We note that the constraints on the displacement and the velocity are satisfied in all scenarios but the control input force sometimes exceeds the imposed bounds. This could be explained by the fact that the WEC in our case study can't work perfectly with all the waves recorded in the North West of Ireland. Indeed, wave heights of 3.596 m,4.512 m,5.428 m have been recorded in the region while the maximum limit on the buoy's displacement is $d_{max} = 2$ m. The differences between the significant wave height and the buoy's displacement may be too huge for the constraints to be satisfied in all scenarios while harvesting energy.

6.4 Conclusion

This chapter has introduced a novel stochastic Economic Model Predictive Control (EMPC) framework for regenerative suspension systems that employs a non-standard cost function to directly maximize harvested energy while ensuring ride comfort, road handling, and suspension stroke. Simulation results on a quarter-car model and a full-car model demonstrate that the

proposed EMPC outperforms the LQR controller in energy recovery and allows for flexible trade-offs among conflicting performance objectives through various constraint handling approaches. In addition, recursive feasibility is ensured in this new stochastic EMPC framework and the robustness of the two control laws to model parameters variation is investigated. Overall, the results highlight the potential of the EMPC strategy to achieve improved energy harvesting and enhanced vehicle dynamics, paving the way for future investigations into more complex scenarios and real-world implementations.

On the other side, we introduced a noncausal Economic Model Predictive Control for energy harvesting in wave energy converters (WECs) using the same non-standard cost function. A comparison with the Linear Non-Causal Optimal Control (LNOC) strategy, which also incorporates wave prediction in its design, has highlighted the advantages of explicitly considering wave prediction in control law design. When physical constraints are included, the Economic Model Predictive Control (EMPC) outperforms the LNOC in terms of energy harvested. We also noticed through the NMPC approach that includes nonlinearities into the controller's design significantly increases energy harvesting but also increases the computational burden of the approach. The EMPC approach needs 5 minutes of computation while the NMPC needs 2 hours of computation. Finally, simulations results across many wave scenarios have been shown. It has been highlighted that the EMPC approach satisfies both energy recovery and compliance with physical constraints in most of the waves scenarios. Only the control input's constraint is not satisfied for wave heights significantly higher than the physical limit on the buoy's displacement.

Chapter 7

Conclusions and future works

VII

7.1 Summary of the thesis

The main aim of this thesis was to formulate novel optimal control strategies which could be implemented in real time on vehicles regenerative suspension systems and wave energy converters devices. The objectives were to develop causal and noncausal strategies suitable for energy harvesting optimization and constraints satisfaction, and to investigate their performance by simulations on the devices. Here are the main results.

In chapter 2, we stated that there are three models of suspension modeling namely the quarter-car model which focuses on the dynamics of a single wheel (only the vertical motion), the half-car model which focuses on the dynamics of half the vehicle (either roll and vertical motion or pitch and vertical motion) and the full-car model which considers all dynamics of the vehicle (roll, pitch and vertical motion). We presented the main actuators used in regenerative suspensions literature or *Energy Harvesting Shock Absorbers* (EHSAs) namely the LPMA, RPEHSA, SPEHSA and IPVA. It is important to recall that these actuators have been designed to operate as generators. We conducted the power flow analysis in the car model focusing on the IPVA actuator. Indeed, the energy from road profile is converted to mechanical energy through the suspension systems then it is converted to electrical energy through the actuator. We noticed an energy transfer from the road profile to the electrical batteries with small losses.

In chapter 3, we introduced the different categories of point absorbers namely one-body point absorbers and multi-body point absorbers, a point absorber being a kind of wave energy converter (WEC). We presented the different kinds of Power Take Off (PTO) mechanisms used to convert energy from marine waves into mechanical energy. These are hydraulic PTO mechanisms, mechanical PTO mechanisms and direct drive PTO mechanisms. We also investigated point absorber dynamic modeling which allows us to have a clear overview of the different forces (radiation force, excitation force...) acting on the device. Furthermore, we introduced two wave forecasting models : Harvey's model and DHR and we justified the use of Harvey's model for wave's prediction in this thesis.

In chapter 4, we designed a H_∞ and a H_2 Maximum Induced Power Control (MIPC) dynamic output feedback for each actuator mentioned for vehicle's regenerative suspension systems. These are two causal control strategies and the intention was to find the best actuator for vehicle's regenerative suspension systems and the best control strategy. Simulations have been undertaken on MATLAB to obtain the three values of the *Ride Index* (RI) describing the level of desired passenger's comfort with respect to ISO-2631 standard. It has been found that the H_2 MIPC dynamic output feedback control outperforms its H_∞ counterpart for all Ride Index scenarios and actuators configurations. Rotary EHSAs induce larger electrical currents than linear EHSAs due to their great angular speeds. This outcome is a direct result of the Faraday-Neumann-Lenz law, which governs the generation of electromotive force in response to the rotational motion in the magnetic field. The IPVA offers the highest potential for energy recovery due to its superior conversion of linear to rotary motion, allowing it to achieve higher power outputs. Among the rotary EHSAs aforementioned, the IPVA stands out as the best actuator for regenerative suspensions under the two designed control strategies.

In chapter 5, the goal was to find an approach superior to the classical LQR formulation which is not well suited for energy harvesting optimization and constraints satisfaction. Another goal was to ensure that this novel approach outperforms some existing control strategies used for vehicle's regenerative suspensions and wave energy converters. Therefore, we designed a novel multi-objective LQR control which is also a causal control strategy. In the regenerative suspensions case, the results demonstrate that the novel LQR controller, designed with a specific non standard cost function, allows better performance in terms of energy harvesting and comfort satisfaction with respect to two famous control strategies of the literature. The first one is the regenerative viscous damper which is the simplest control strategy developed for regenerative suspensions. The second one is the static state feedback H_2 MIPC control strategy which optimizes energy harvesting along with ride comfort, road handling and suspension stroke. Ride comfort requirements are integrated into the novel LQR scheme through an H_∞ constraint on the Ride Index, leading to an LMI-based semidefinite optimization problem for LQR gain synthesis. Although constraints on suspension stroke and road handling are not integrated into the LQR design, it has been found that the LQR strategy optimizes energy harvesting and passengers comfort without deteriorating suspension stroke and road handling. A comparative study of the three control strategies has been done under varying road excitations and car models. MATLAB Simulink and CarSim softwares have also been used for simulations. The results demonstrate the superiority and robustness of the novel LQR approach under sensor noise, actuator saturation, variation in models parameters and disturbance signals. Moreover, it is important to note that the novel LQR approach requires only two tuning parameters, as opposed to the four required by H_2 MIPC. This reduction decreases computational complexity and calibration effort, enhancing both robustness

and practical applicability.

A similar study has been done for a WEC point absorber. The LQR approach has been reformulated in two ways: using an augmented state including the excitation substates and using the system's steady state response to the disturbance. H_2 MIPC state feedback strategy has also been reformulated for wave energy converters and a constraint approach has been included to optimize the buoy's displacement, buoy's velocity and actuator's force. The two formulations of the novel LQR approach have been compared to the unconstrained H_2 MIPC and the constrained H_2 MIPC. It has been found that the LQR first formulation allows the greatest energy harvesting in the wave energy converter but it exceeds all operational limits of the device. This is due to the fact that this LQR formulation doesn't consider constraints on buoy's displacement, buoy's velocity and actuator's force. The strategy that satisfies all constraints specifications in the wave energy converter is the constrained H_2 MIPC but it allows the smallest energy harvesting.

In chapter 6, we designed a novel stochastic EMPC for regenerative suspension systems. The aim was to develop a causal strategy that maximizes energy harvesting while ensuring precise constraints satisfaction on suspension stroke, road handling and ride comfort. The LQR strategy developed in chapter 5 includes ride comfort constraint but it doesn't incorporate directly constraints on suspension stroke and road handling. That is why this novel stochastic EMPC needed to be designed. A comparative study between this EMPC approach and the LQR strategy has been done on several scenarios. Due to the absence of road's preview, a particular recursive feasibility condition had to be found. Simulation results on a quarter-car model and a full-car model demonstrate that the proposed stochastic EMPC outperforms the LQR controller in energy recovery and allows for flexible trade-offs among the conflicting performance objectives (suspension stroke, road handling and ride comfort) through various constraint handling approaches. In addition, recursive feasibility is ensured in this new stochastic EMPC framework and the robustness of the two control laws to model parameters variation is investigated. Overall, the results highlight the potential of the stochastic EMPC strategy to achieve improved energy harvesting and enhanced vehicle dynamics, paving the way for future investigations into more complex scenarios and real-world implementations.

In the second part of chapter 6, we developed a noncausal EMPC for WECs. The aim was to investigate the improvement in the results when the exogenous signal's prediction is incorporated into the controller scheme. It has been found that the incorporation of wave's prediction allows to recover more energy than causal strategies while being more computationally expensive. Comparative studies have been undertaken with two control strategies of the literature: the LNOC(Linear noncausal Optimal Control) and the NMPC(Nonlinear Model Predictive Control) which are two different model predictive control techniques. Firstly, the EMPC has been compared to the LNOC and the LQR assuming a perfect wave's prediction

and an imperfect wave's prediction. The superiority of the EMPC has been proven. In fact, when physical constraints are included, the EMPC outperforms the LNOC in terms of energy harvested. Across all scenarios investigated, the EMPC consistently surpasses the LQR in both energy recovery and compliance with physical constraints. Secondly, the EMPC has been compared to NMPC and H_2 MIPC on two wave energy converters: a standard Point Absorber and the Corpower device. It has been found that H_2 MIPC shows good performances within 3 minutes computation. EMPC strategy satisfies the constraints and energy harvesting requirements within 5 minutes computation. Even though NMPC achieves the greatest energy harvesting while satisfying the constraints, its computational burden is high (2 hours computation on MATLAB). This high computational burden might be decreased by using other numerical optimization methods or softwares. Furthermore, the NMPC approach requires many experimental results and approximations in its computation making it more difficult to implement than the other control strategies. This high computational burden is a reason why linear controllers are preferred in the literature. Thirdly, the EMPC strategy has been tested under various sea conditions recorded on the Northwest coast of Ireland. It has been found that the constraints on buoy's displacement and velocity are satisfied in all scenarios but the control input force sometimes exceeds the imposed bounds. This could be due to the presence of too huge waves in some scenarios. However in most cases, all constraints are satisfied with the EMPC while ensuring energy harvesting. Therefore, this strategy represents a promising solution for future energy harvesting systems, effectively balancing energy efficiency and physical constraint satisfaction.

In other words, we can summarize the main findings of the thesis as follows:

- we designed causal control strategies which don't need future information on the system's dynamics. This reduces the computational burden and operational costs in comparison to control architectures which necessitate the use of forecasting systems.
- we also designed noncausal control strategies which outperform the causal ones despite the increase of the computational burden.
- all the control methods are readily applicable to real devices, given their compatibility with processors in industry and limitations to mechanical/electrical components.

7.2 Future works

Despite the results obtained in this thesis, more investigations are required due to some drawbacks:

- As explained in section 5.2.8.5, balancing safety and performance in control systems is a challenge that involves finding the right balance between keeping things safe and making sure they work well. It could be interesting to investigate fault tolerant control design methods on regenerative suspensions and wave energy converters to ensure safety.
- The tuning parameters in this thesis were chosen with respect to grid search methodology. It could be interesting to investigate adaptive parameters tuning via reinforcement learning. Even though this strategy is more computationally expensive than the grid search methodology, this will constitute an improvement for the controllers designed in this thesis.
- When performing complex tasks, some renewable energy systems need *Linear Parameters Varying* (LPV) modeling. In this thesis, we work under the assumption of *Linear Time Invariant* (LTI) systems which are easier to implement. LPV systems could provide more accurate modeling and control potentially leading to improved performance and stability so their investigation constitutes a research axis for the future.
- While the proposed control strategies demonstrate robustness to variations in excitation signals and models parameters, structured or parametric uncertainty modeling is not explicitly included in this thesis. However, we acknowledge the potential benefits of incorporating parametric uncertainty - e.g., via interval models, fuzzy sets, or probabilistic bounds - and we consider this a valuable direction for future extensions of our work, especially for robustness analysis and controller synthesis under uncertainty.
- In chapter 5, the LQR approach is compared to the MIPC-based framework that has already been experimentally implemented and validated in prior works. In those studies, electromagnetic suspension systems with DC actuators were tested under H_∞-based MIPC control and it was later demonstrated that the H_2 variant can increase the controller performance. Our contribution extends this framework by introducing a novel LQR formulation with a non-standard cost function and a Ride Index constraint, which outperforms even the MIPC H_2 strategy in terms of energy harvesting. In order to partially address the lack of experimental results for vehicle's regenerative suspensions, we run several simulations with the mechanical simulation software CarSim. However, we fully agree on the importance of experimental validation and we intend to implement this LQR and EMPC approaches in a future work through *Hardware-in-the-Loop* (HIL) laboratory experimentation. The car model will be installed on a rig for dynamic tests of mechanical structures. This will enable the simulation of real conditions by disturbing investigated suspension with kinematic excitation. Research will be conducted for comparing

the various control algorithms on the active unit and analyze the trade-offs between energy recovery and constraints satisfaction. The same investigation will be conducted for wave energy converters.

Appendices

Appendix A

Vehicles, actuators and wave energy converters data

Contents

A.1 Vehicles data 168
A.2 Actuators data 169
A.3 Wave Energy Converters data 169

A.1 Vehicles data

The vehicles data used for simulations throughout this thesis are summarized in Tables A.1,A.2 and A.3.

Table A.1: Vehicle 1 data

Parameter	Symbol	Value
Sprung mass	m_s	1136 kg
Front wheels'mass	m_{uf}	63 kg
Rear wheels'mass	m_{ur}	60 kg
Roll's Inertia	I_p	2400 $kg.m^2$
Pitch Inertia	I_r	400 $kg.m^2$
Front suspension stiffness	k_f	36297 N/m
Rear suspension stiffness	k_r	19620 kN/m
Front tire stiffness	k_{tf}	182470 N/m
Rear tire stiffness	k_{tr}	182470 N/m
Distance rear's left side and center of mass	t_f	0.505 m
Distance front's left side and center of mass	t_r	0.557 m
Damping of the front shock absorbers	b_f	3924 $N \times s/m$
Damping of the rear shock absorbers	b_r	2943 $N \times s/m$
Distance front and center of mass	a	1.15 m
Distance rear and center of mass	b	1.65 m

Table A.2: Vehicle 2 data

Parameter	Symbol	Value
Sprung mass	m	1274 kg
Front wheels'mass	m_{uf}	35.5 kg
Rear wheels'mass	m_{ur}	35.5 kg
Roll's Inertia	I_p	606.1 $kg.m^2$
Pitch Inertia	I_r	1523 $kg.m^2$
Front suspension stiffness	k_f	27 kN/m
Rear suspension stiffness	k_r	30 kN/m
Front tire stiffness	k_{tf}	228 kN/m
Rear tire stiffness	k_{tr}	228 kN/m
Distance between the rear's left side and the center of mass	t_f	0.7 m
Distance between the front's left side and the center of mass	t_r	0.7 m
Damping of the front shock absorbers	b_f	1140 $N \times s/m$
Damping of the rear shock absorbers	b_r	1250 $N \times s/m$
Distance between the front and the center of mass	a	1.4 m
Distance between the rear and the center of mass	b	1.47 m

Table A.3: Quarter car parameters

Parameter	Value
Sprung mass	$m_s = m/4$
Unsprung mass	$m_u = m_{ur}$
Suspension stiffness	$k_s = k_f$
Tire stiffness	$k_u = k_{tf}$

A.2 Actuators data

The actuators data used for simulations throughout this thesis are summarized in Tables A.4,A.5, A.6,A.7 and A.8.

Table A.4: LPMA data.

Parameter	Symbol	Value
Force constant	K_e	938 N/A
Armature Resistance	R	0.7 Ω
Armature Inductance	L	5 mH

A.3 Wave Energy Converters data

The wave energy converters data used for simulations throughout this thesis are summarized in Table A.9 and Table A.10.

Table A.5: RPEHSA data.

Parameter	Symbol	Value
EMF constant	K_e	938 N/A
Pinion gear radius	r	2 cm
Inertia moment	J_m	8000 $kg.m^2$
Torque constant	K_t	300 $N.m/(rad/s)$
Armature Resistance	R	0.7 Ω
Armature Inductance	L	5 mH

Table A.6: SPEHSA data

Parameter	Symbol	Value
EMF constant	K_e	938 N/A
Torque constant	K_t	300 $N.m/(rad/s)$
Armature Resistance	R	0.7 Ω
Armature Inductance	L	5 mH
Power Pulley radius	r_{pp}	2 cm
Free Pulley radius	r_{pl}	0.8 cm
Generator Inertia Moment	J_{gen}	1210 $kg.m^2$
Multiplier Inertia Moment	J_{mul}	1000 $kg.m^2$
Power Pulley Inertia Moment	J_{pp}	810 $kg.m^2$
Free Pulley Inertia Moment	J_{pl}	2330 $kg.m^2$
Power Pulley Performance	η_{pp}	0.98
Bevel gear Performance	η_{ec}	0.95
Multiplier Performance	η_{mul}	0.87
Multiplier multiplication factor	k_{mul}	13.5

Table A.7: IPVA data

Parameter	Symbol	Value
EMF constant	K_e	938 N/A
Pendulum radius	r	8.97 cm
Distance pendulum-support's center	R_p	11.7 cm
Damping coefficient of the electrical generator	c_e	0.225 $N/(rad/s)$
Pendulum mass	m	≈ 0 kg
Inertia moment	J_m	1210 $kg.m^2$
Torque constant	K_t	300 $N.m/(rad/s)$
Resistance	R_a	0.7 Ω
Inductance	L_a	5 mH

Table A.8: Actuator data

Parameter	**Symbol**	**Value**
Force constant	K_v/K_a	48 N/A
Resistance	R_a	6 Ω
Inductance	L_a	3 mH

Table A.9: The parameters used for the small WEC

Description	Notation	Values
Stiffness	k_s	3866 N/m
Float mass	m_s	242 kg
Added mass	m_a	83.5 kg
Total mass	m	325.5 kg
Cylinder's radius	r	0.35 m
Cylinder's draught	h	0.63 m
Input force limit	f_u	6 kN
Heave position limit	d_{max}	0.5 m
Heave velocity limit	v_{max}	2 m/s
Radiation coefficient	D_r	4*10^1 kg/s

Table A.10: The parameters used for the big WEC

Description	Notation	Values
Stiffness	k_s	5.43*10^5 N/m
Float mass	m_s	7.8*10^4 kg
Added mass	m_a	7*10^4 kg
Total mass	m	14.8*10^4 kg
Cylinder's radius	r	4.2 m
Cylinder's draught	h	18 m
Input force limit	f_u	1000 kN
Heave position limit	d_{max}	2 m
Heave velocity limit	v_{max}	2 m/s
Radiation coefficient	D_r	2*10^4 kg/s
Excitation coefficient	D_e	9*10^5 kg/s

Appendix B

Plots on CarSim 2025.1

IX

This section presents the plots obtained using the mechanical simulation software CarSim 2025.1.

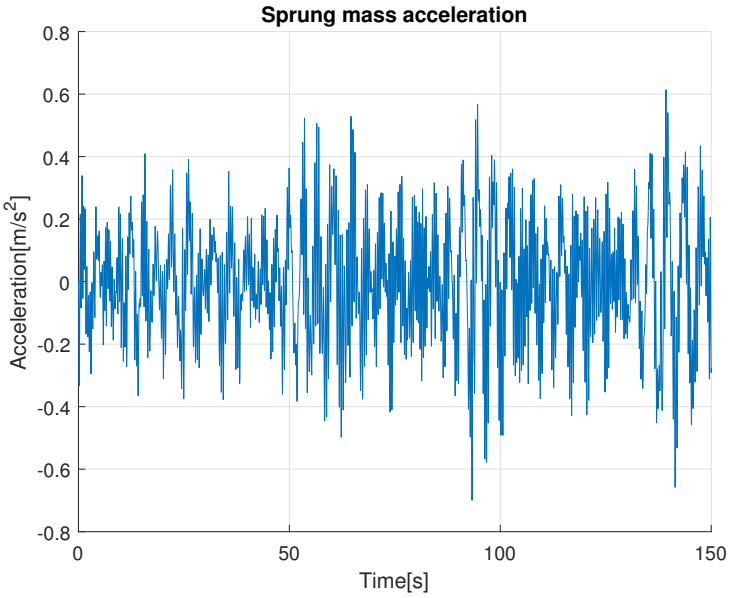

Figure B.1: Test 1- Chassis acceleration with LQ

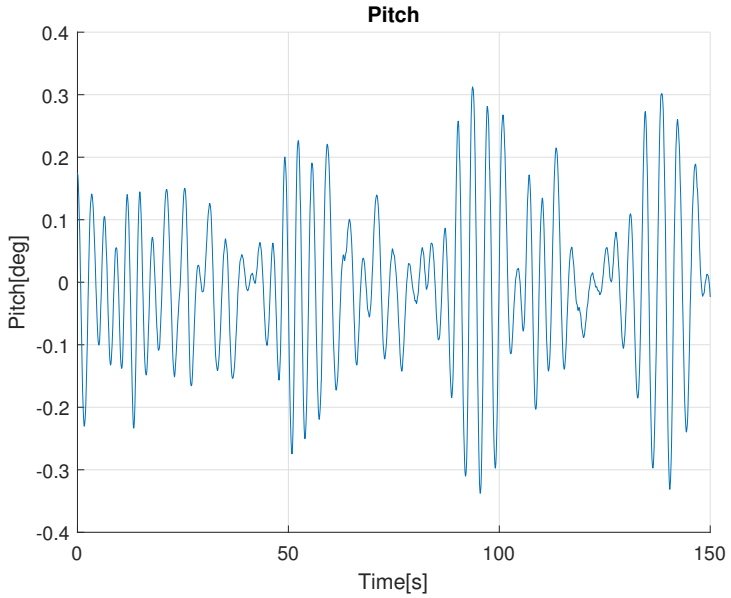

Figure B.2: Test 1- Pitch with LQ

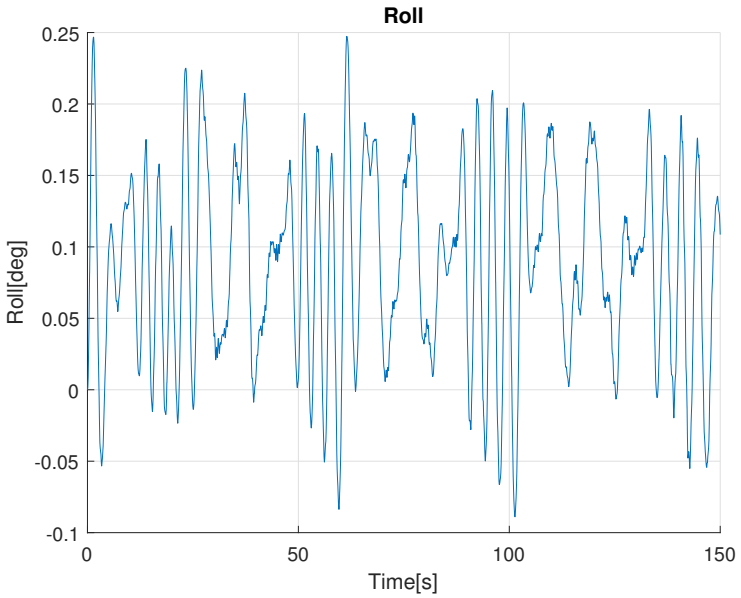

Figure B.3: Test 1- Roll with LQ

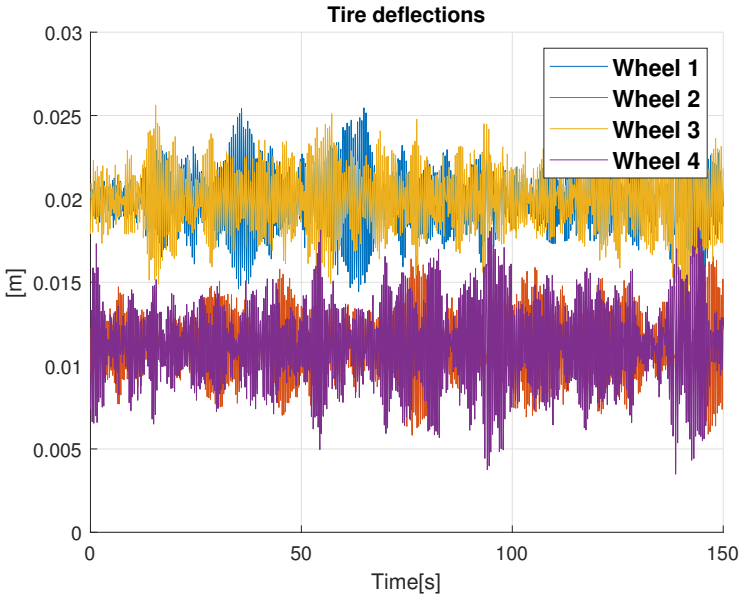

Figure B.4: Test 1- Tire deflections with LQ

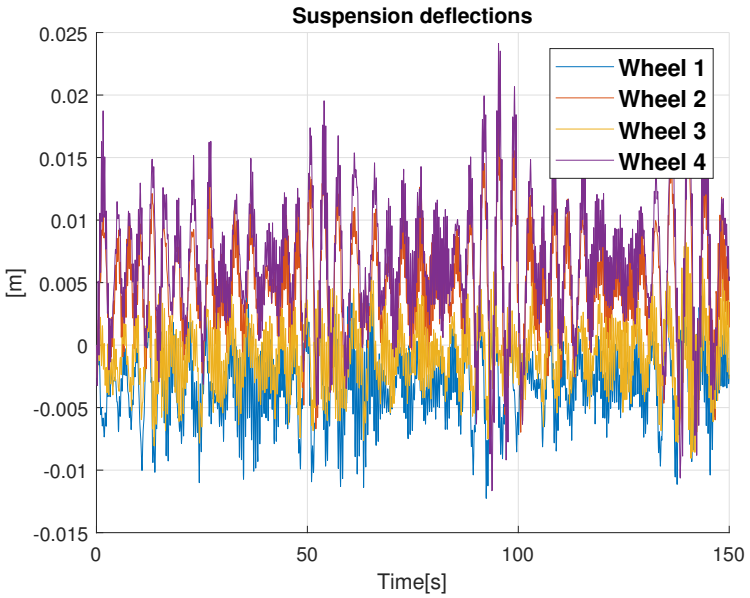

Figure B.5: Test 1- Suspension deflections with LQ

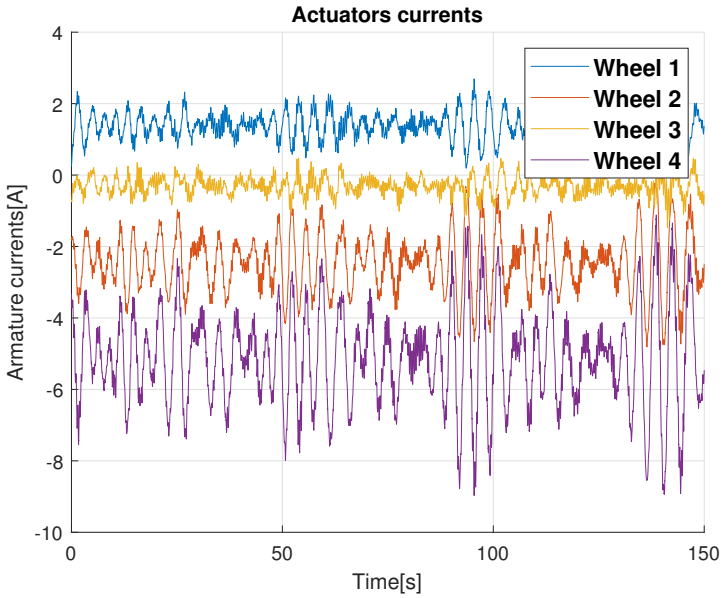

Figure B.6: Test 1- Actuation currents with LQ

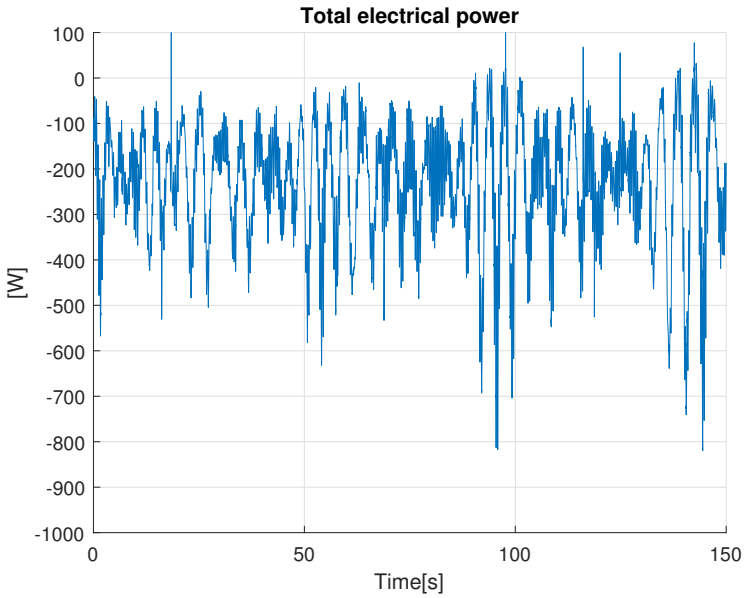

Figure B.7: Test 1- Electrical power with LQ

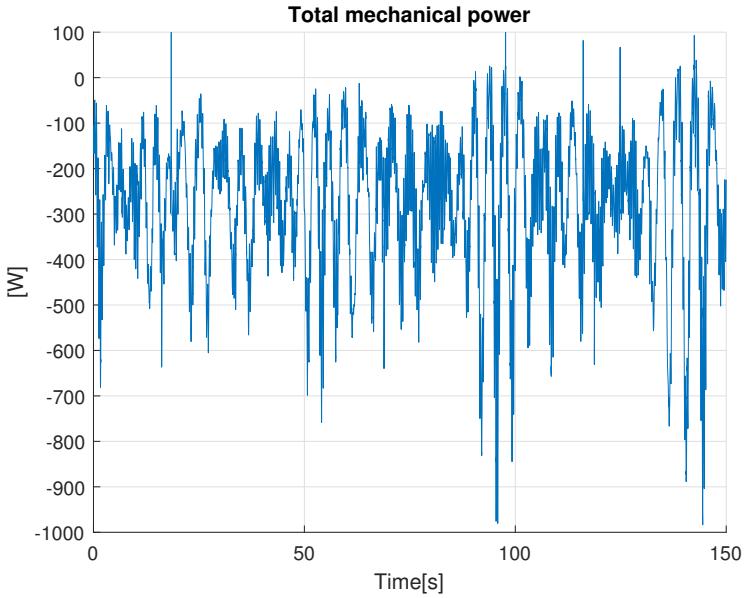

Figure B.8: Test 1- Mechanical power with LQ

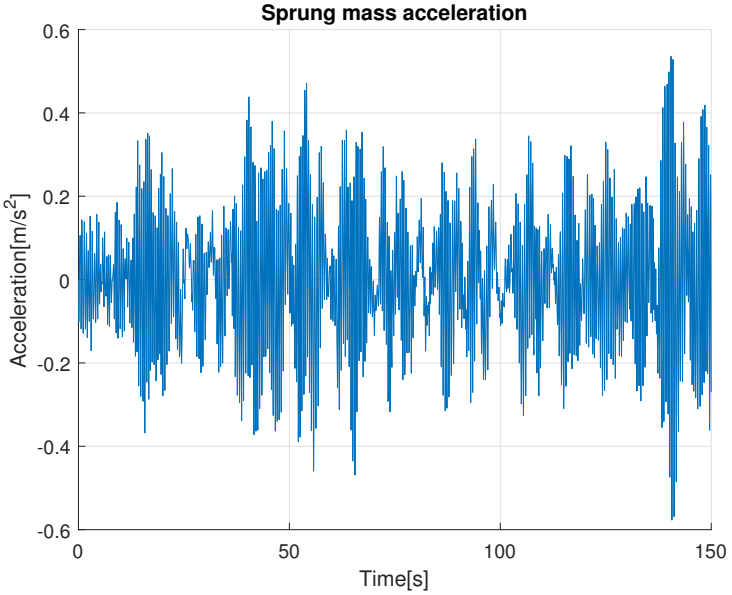

Figure B.9: Test 1- Chassis acceleration with MIPC H_2

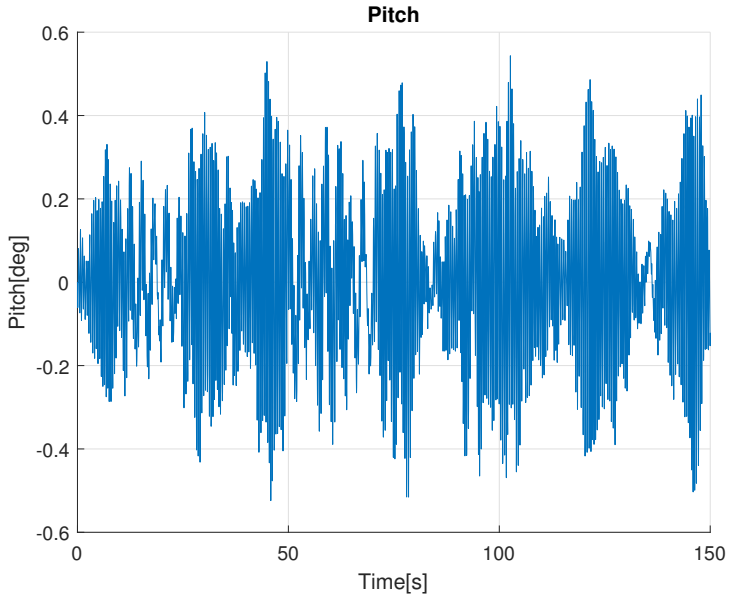

Figure B.10: Test 1- Pitch with MIPC H_2

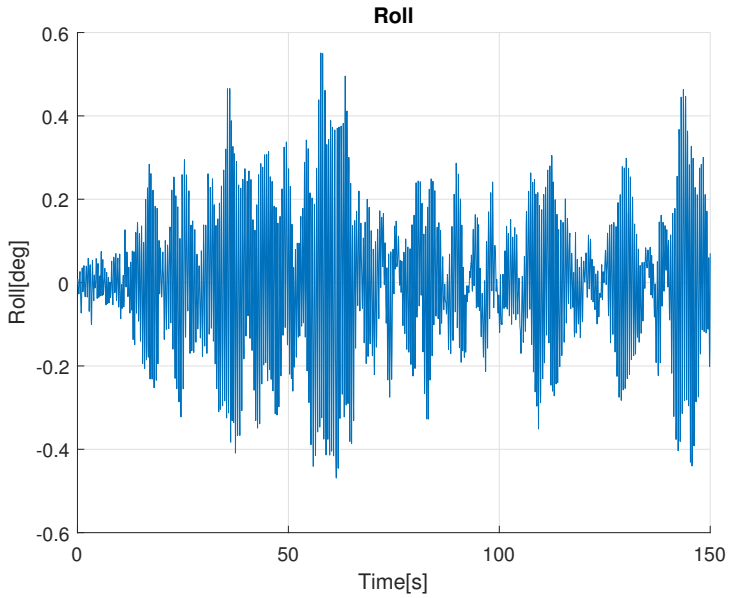

Figure B.11: Test 1- Roll with MIPC H_2

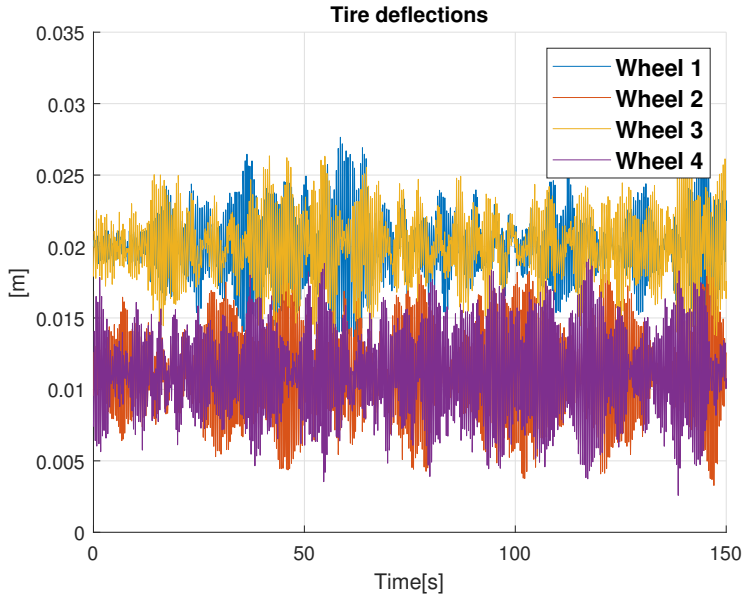

Figure B.12: Test 1- Tire deflections with MIPC H_2

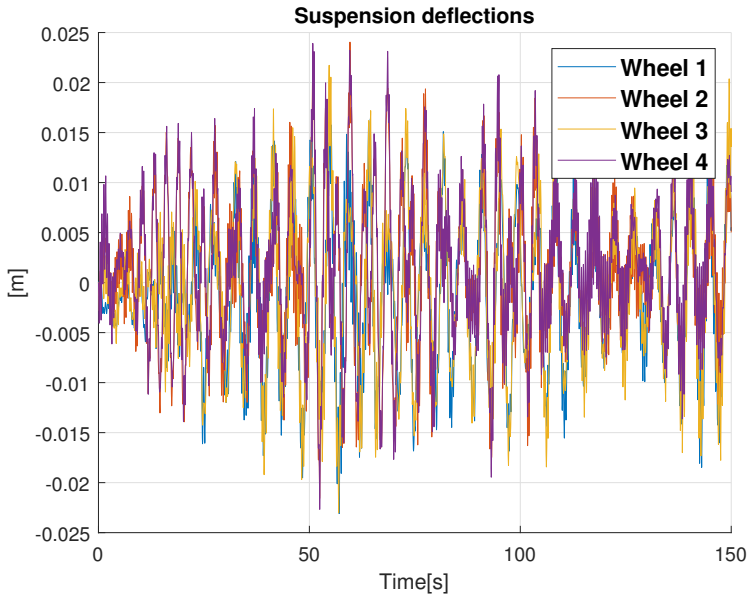

Figure B.13: Test 1- Suspension deflections with MIPC H_2

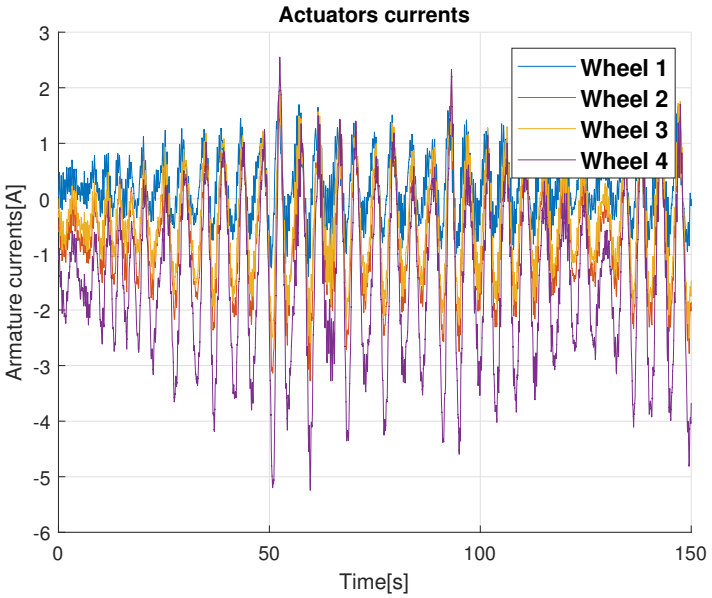

Figure B.14: Test 1- Actuation currents with MIPC H_2

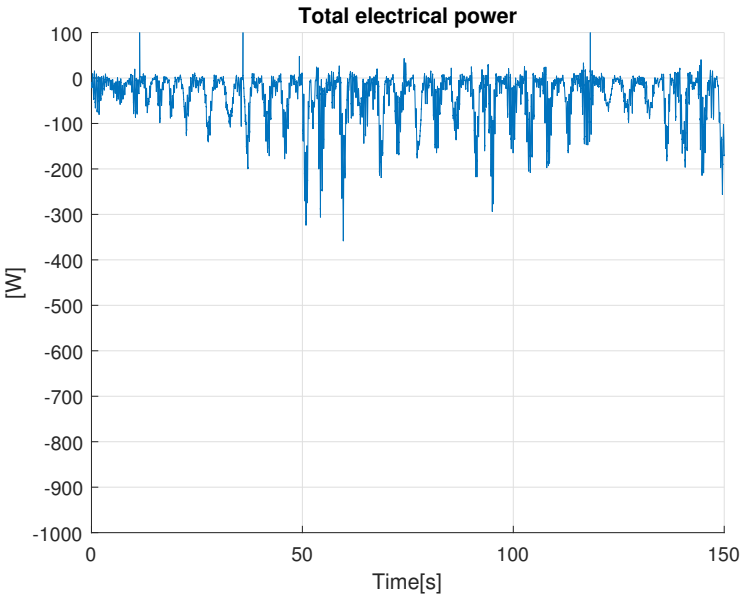

Figure B.15: Test 1- Electrical power with MIPC H_2

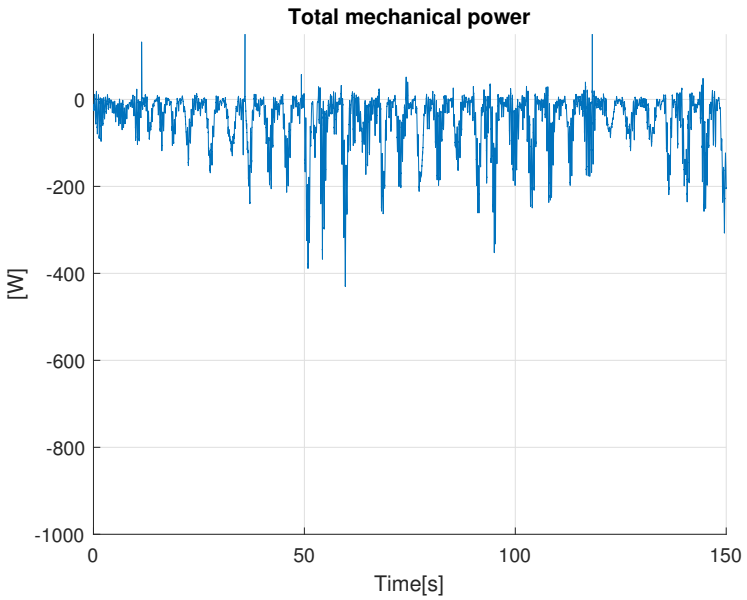

Figure B.16: Test 1- Mechanical power with MIPC H_2

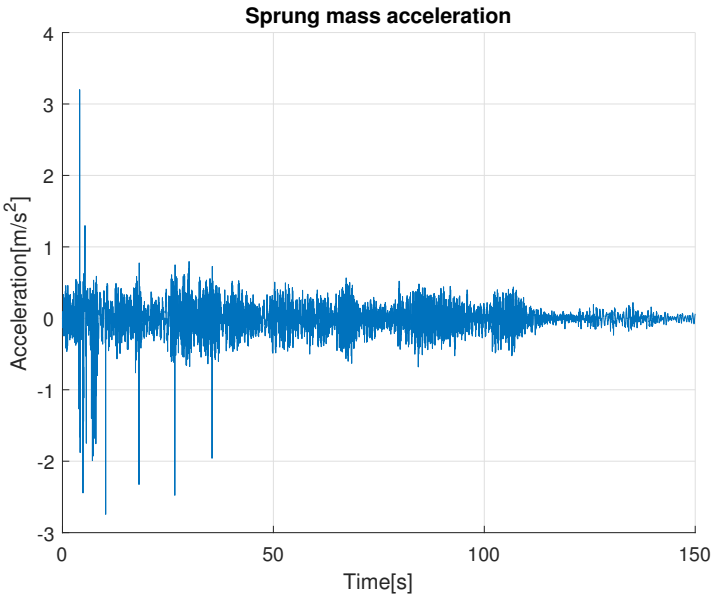

Figure B.17: Test 2- Chassis acceleration with LQ

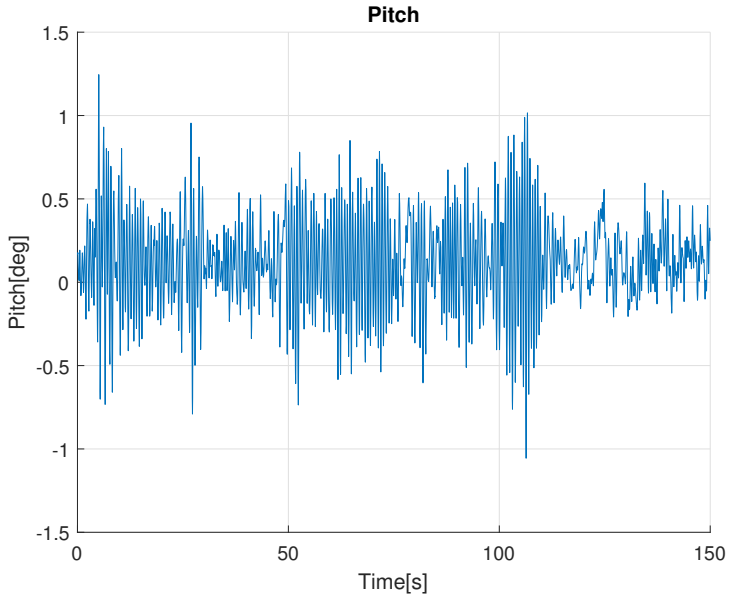

Figure B.18: Test 2- Pitch with LQ

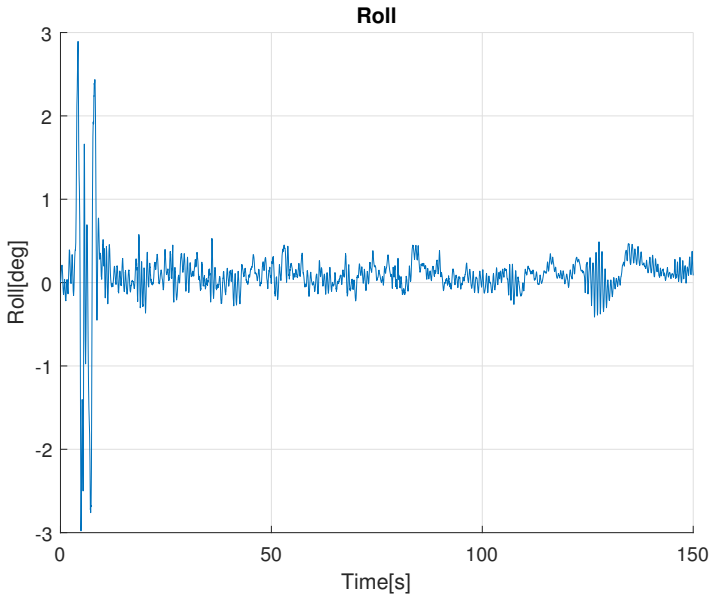

Figure B.19: Test 2- Roll with LQ

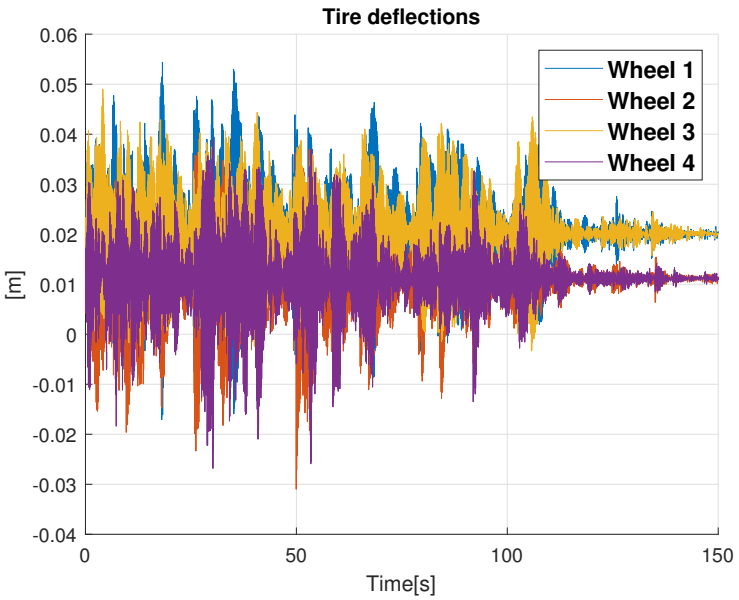

Figure B.20: Test 2- Tire deflections with LQ

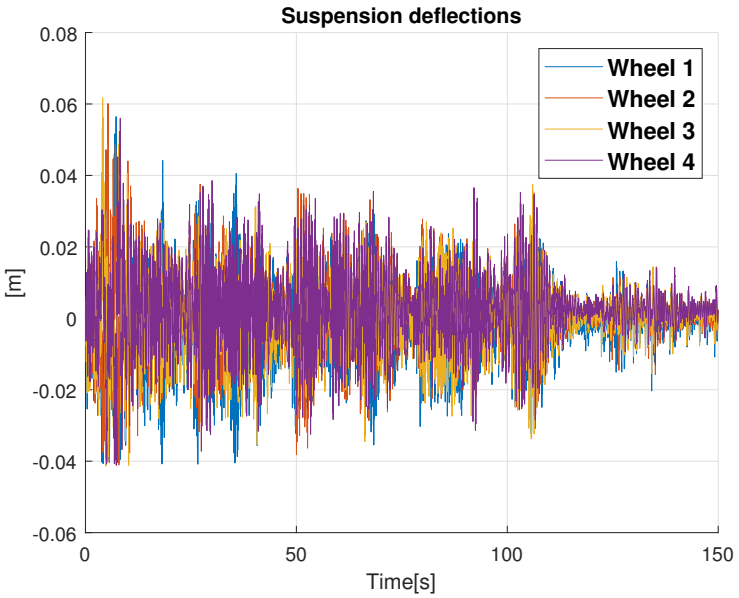

Figure B.21: Test 2- Suspension deflections with LQ

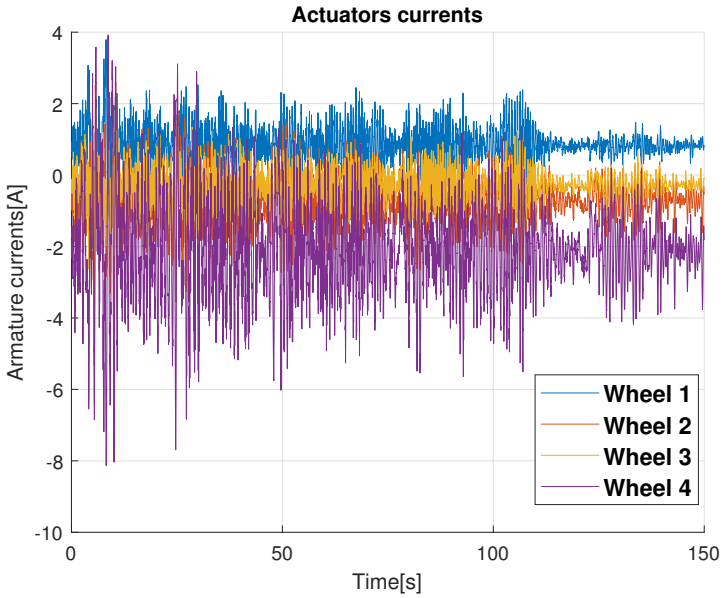

Figure B.22: Test 2- Actuation currents with LQ

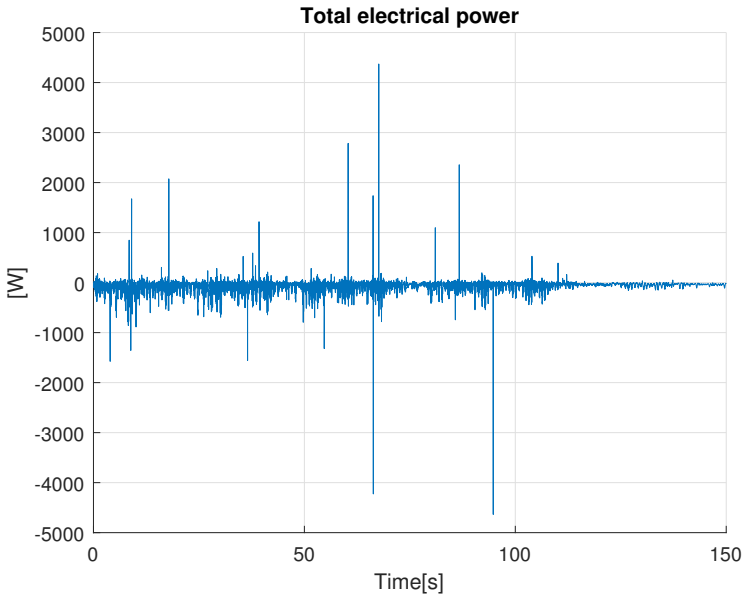

Figure B.23: Test 2- Electrical power with LQ

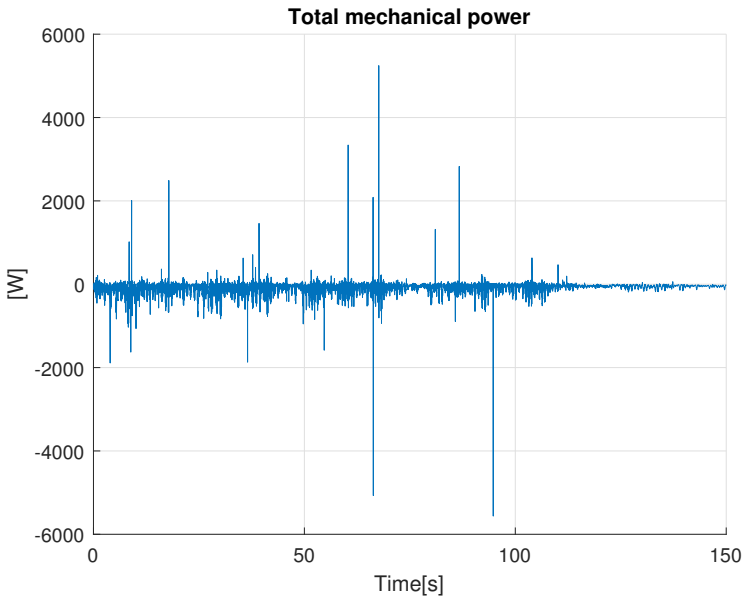

Figure B.24: Test 2- Mechanical power with LQ

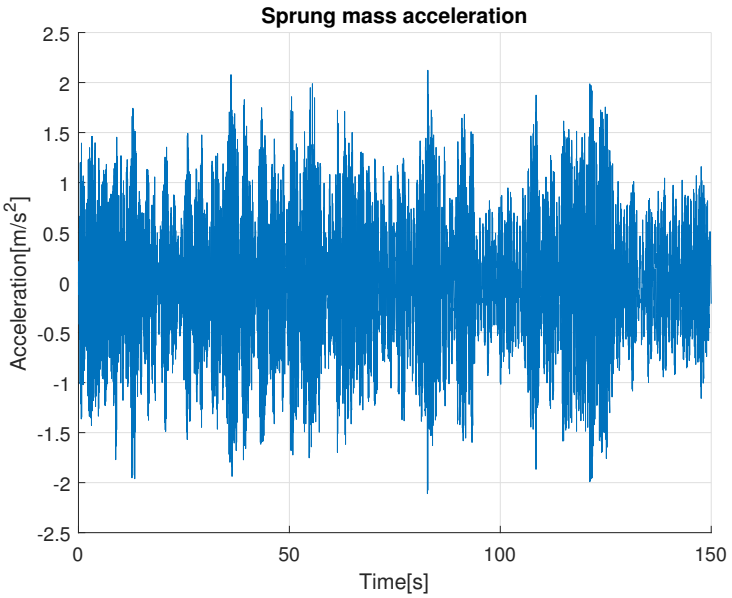

Figure B.25: Test 2- Chassis acceleration with MIPC H_2

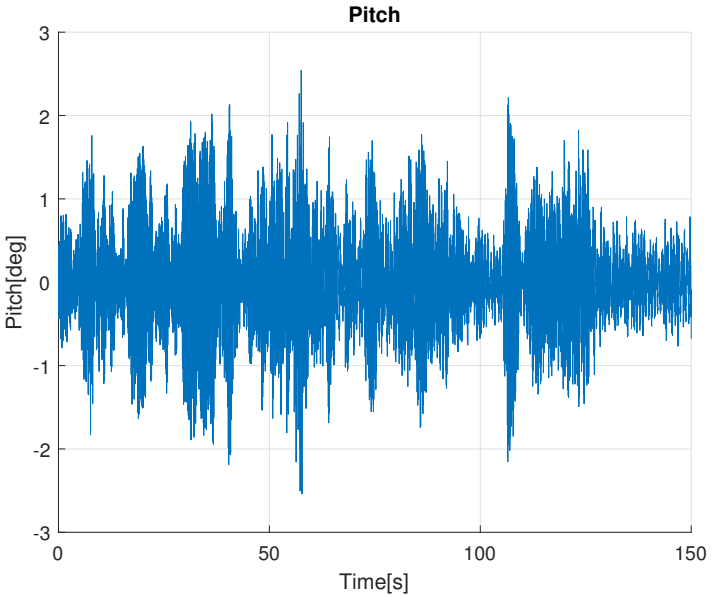

Figure B.26: Test 2- Pitch with MIPC H_2

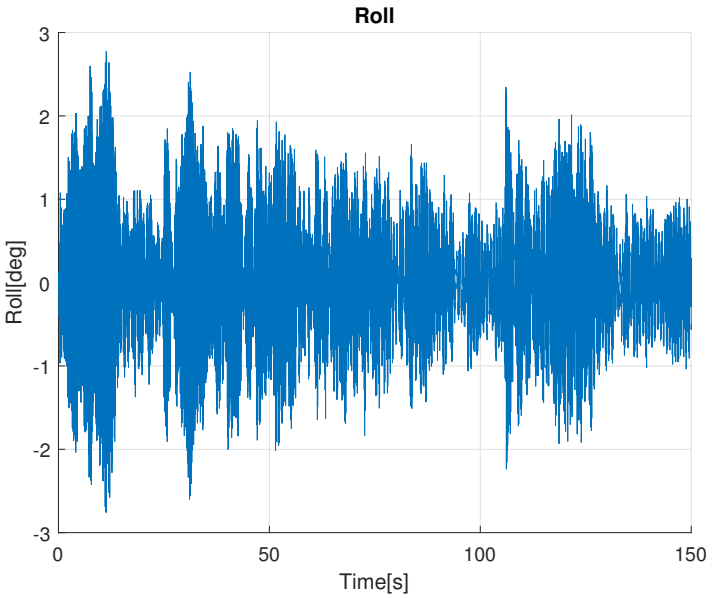

Figure B.27: Test 2- Roll with MIPC H_2

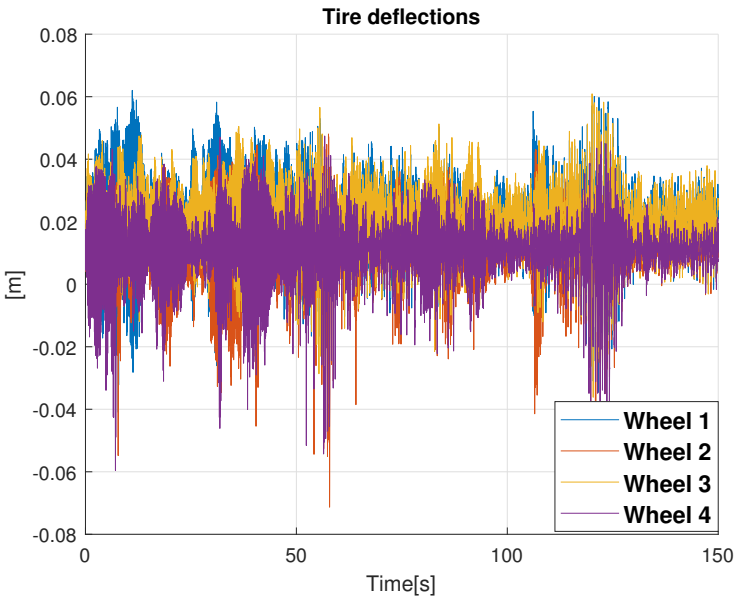

Figure B.28: Test 2- Tire deflections with MIPC H_2

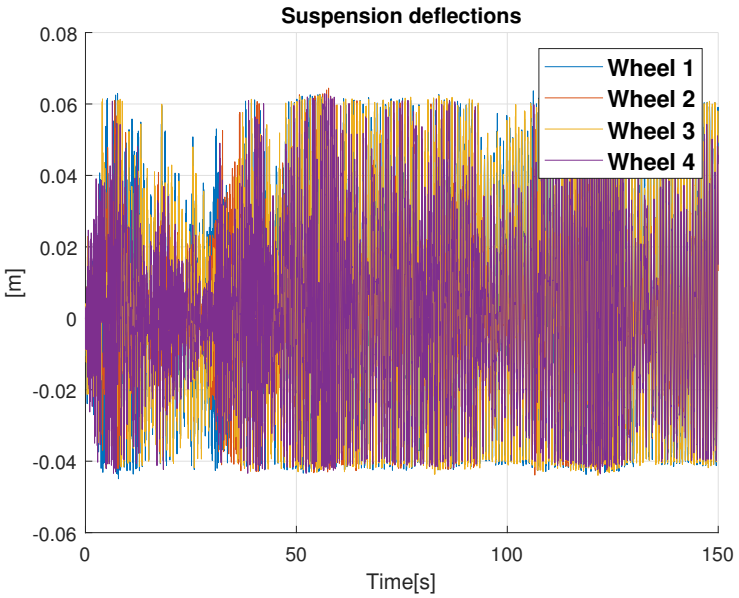

Figure B.29: Test 2- Suspension deflections with MIPC H_2

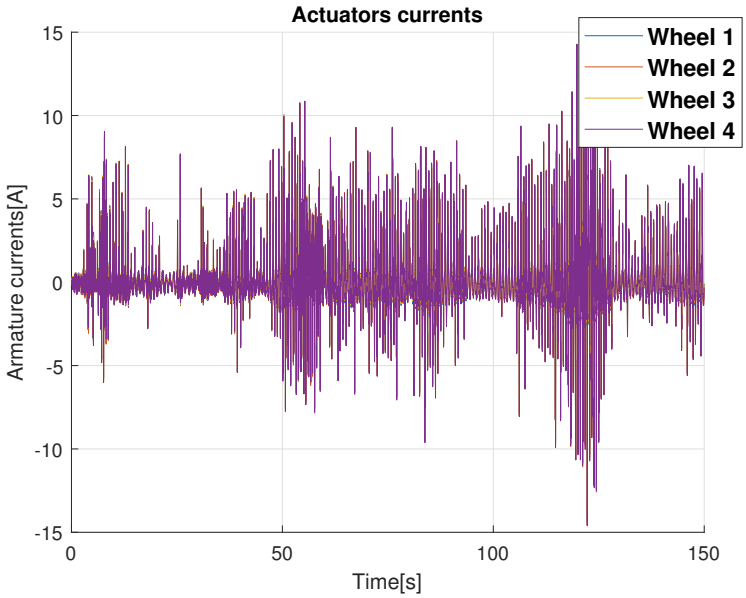

Figure B.30: Test 2- Actuation currents with MIPC H_2

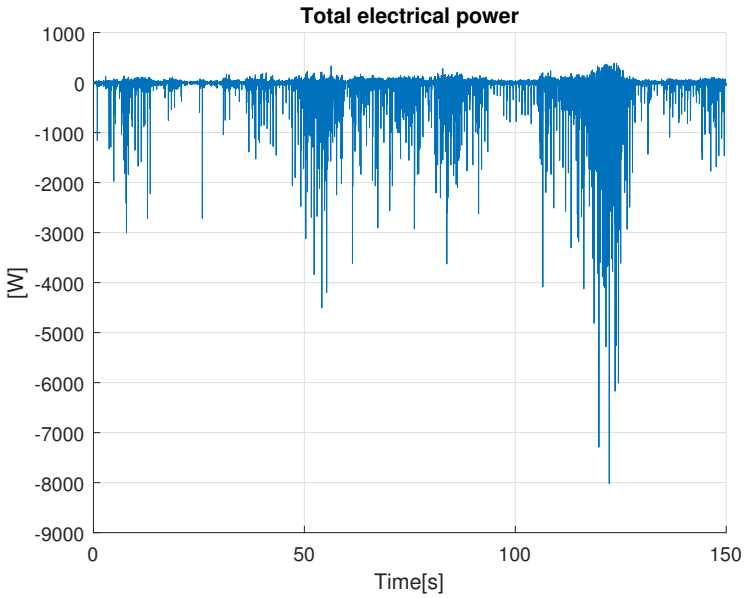

Figure B.31: Test 2- Electrical power with MIPC H_2

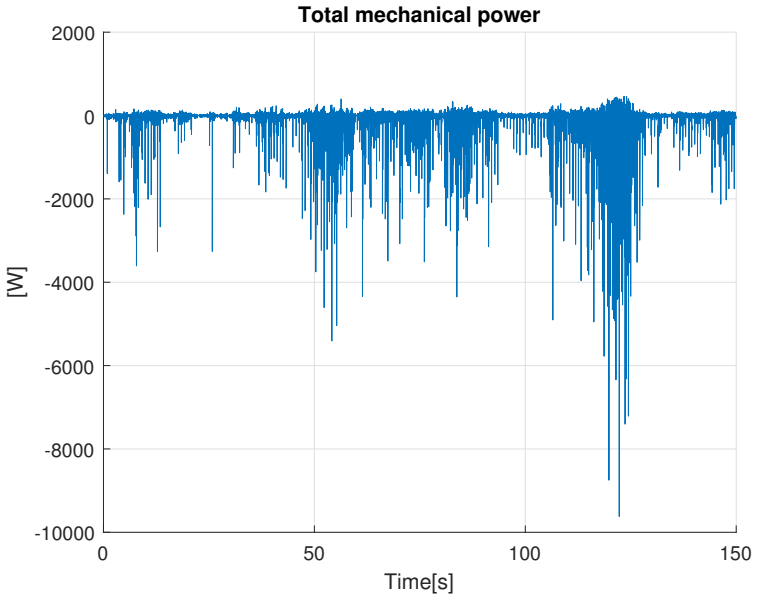

Figure B.32: Test 2- Mechanical power with MIPC H_2

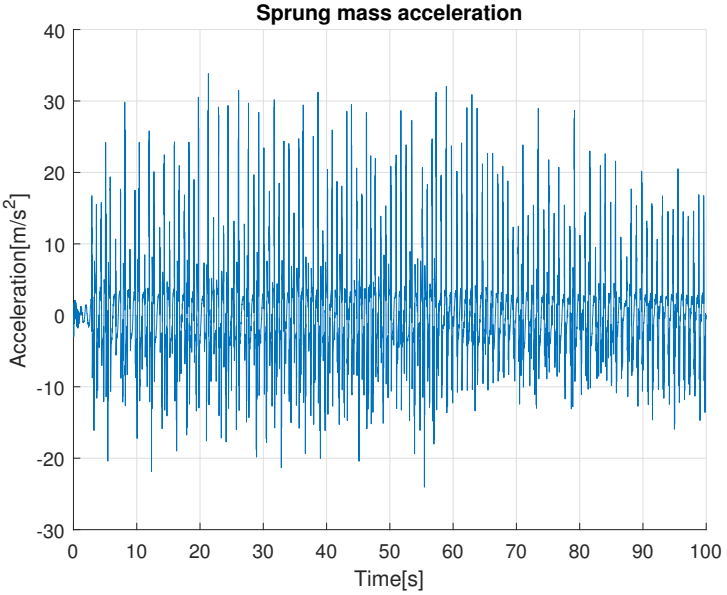

Figure B.33: Test 3- Chassis acceleration with LQ

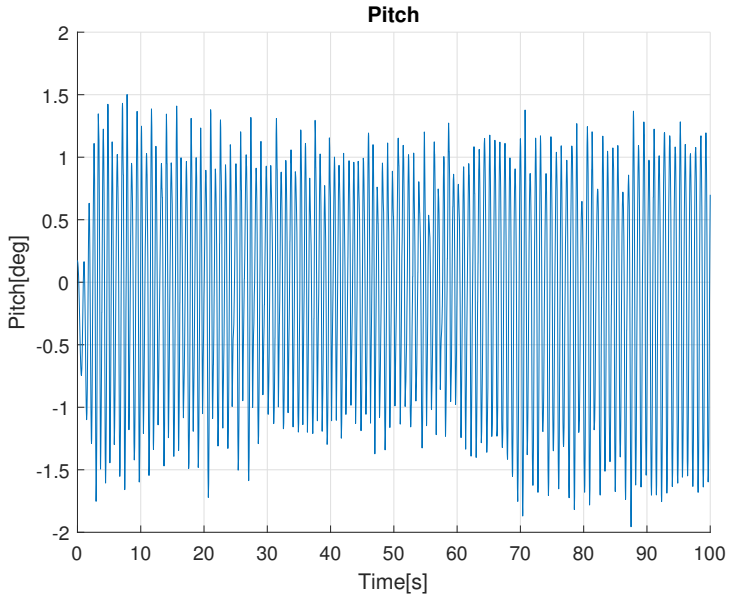

Figure B.34: Test 3- Pitch with LQ

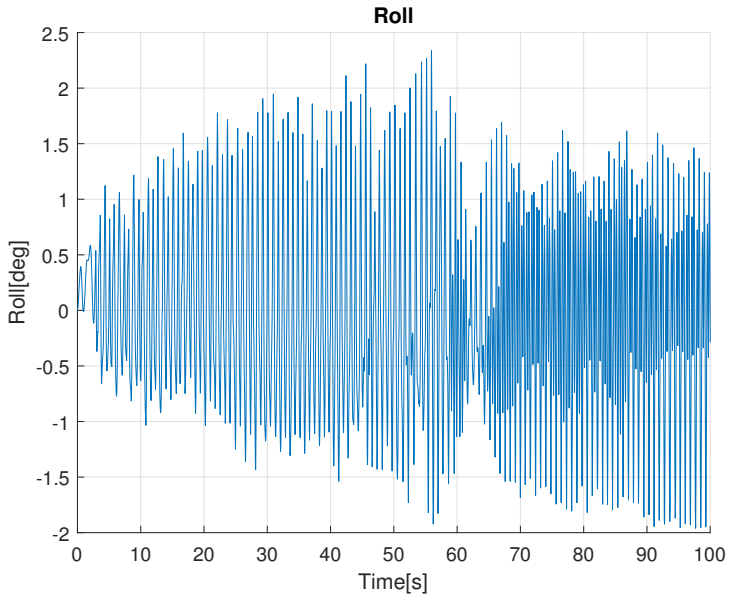

Figure B.35: Test 3- Roll with LQ

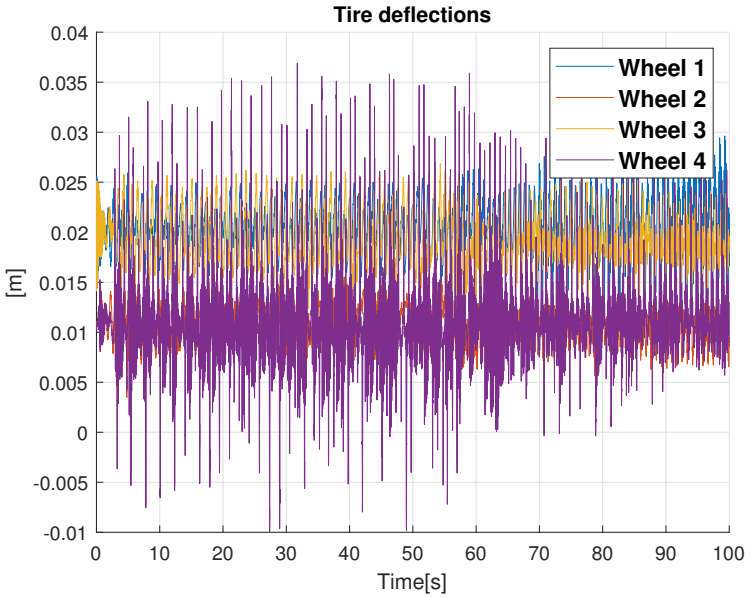

Figure B.36: Test 3- Tire deflections with LQ

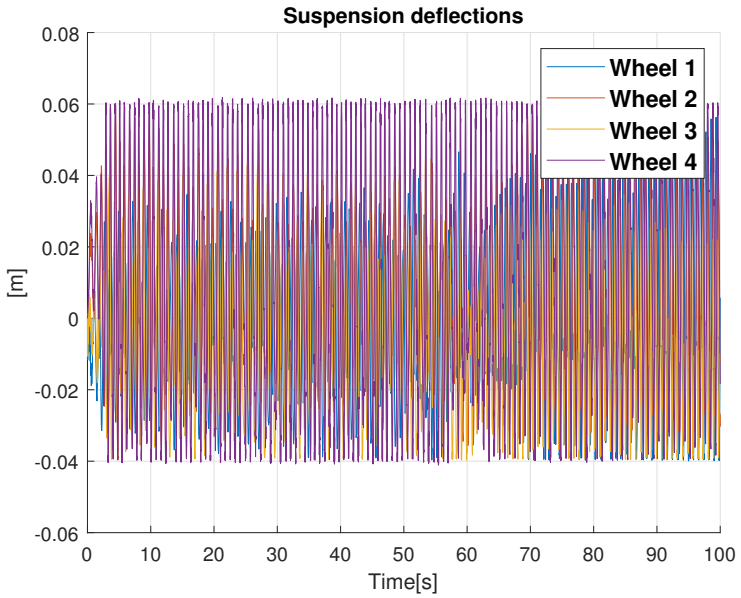

Figure B.37: Test 3- Suspension deflections with LQ

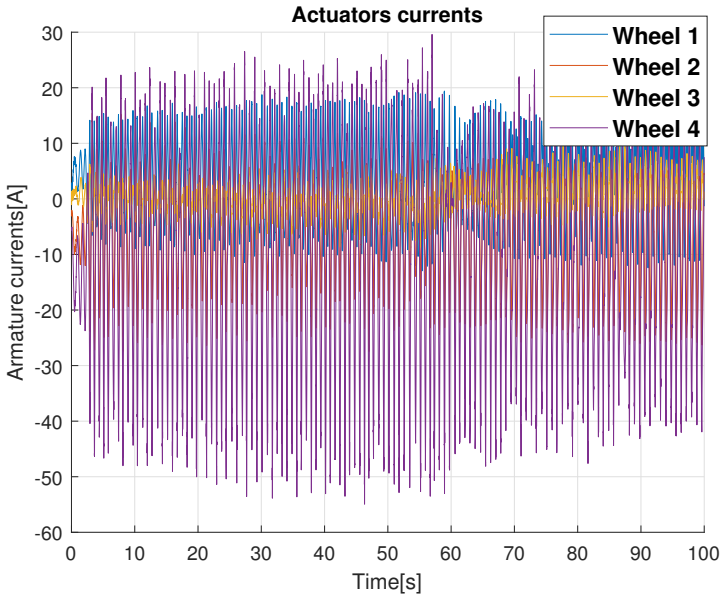

Figure B.38: Test 3- Actuation currents with LQ

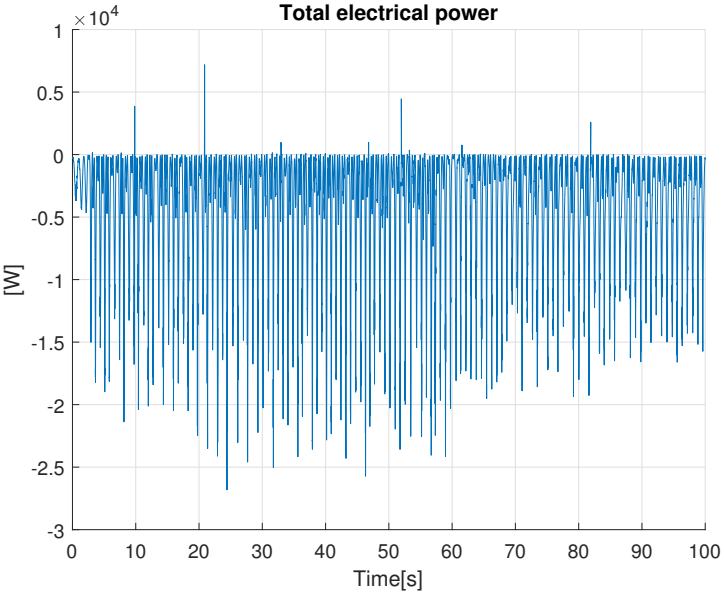

Figure B.39: Test 3- Electrical power with LQ

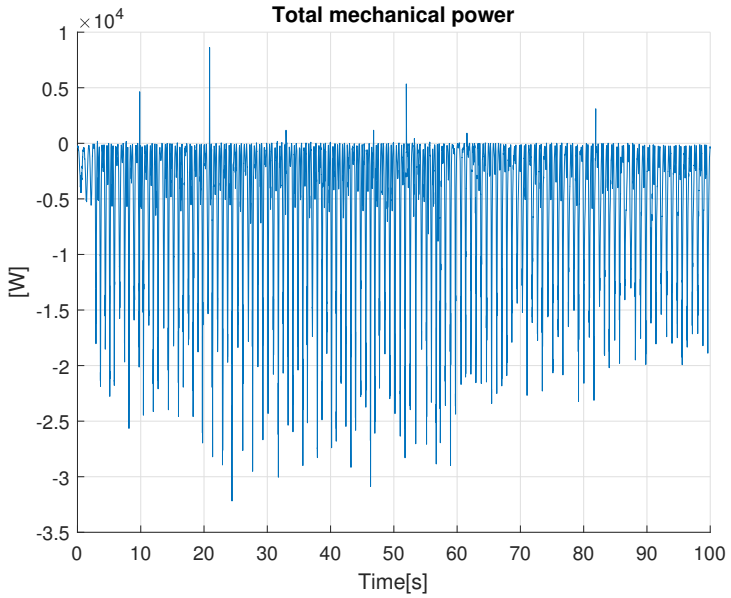

Figure B.40: Test 3- Mechanical power with LQ

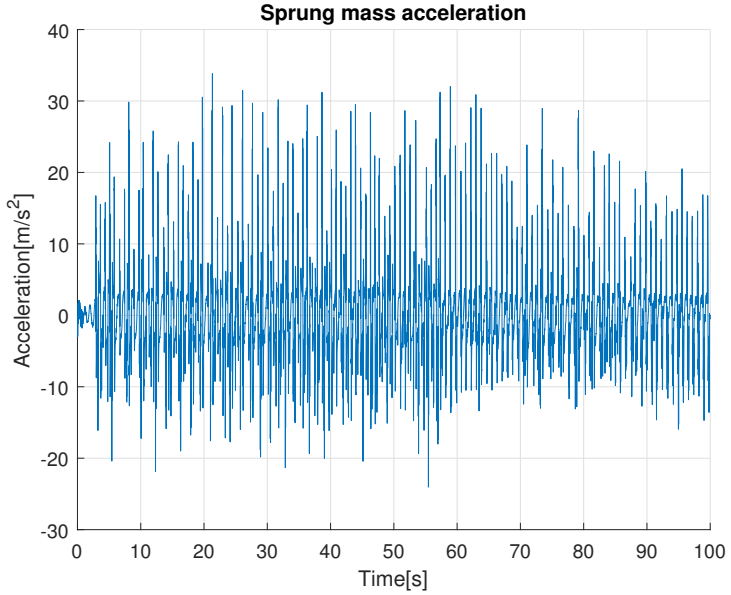

Figure B.41: Test 3- Chassis acceleration with MIPC H_2

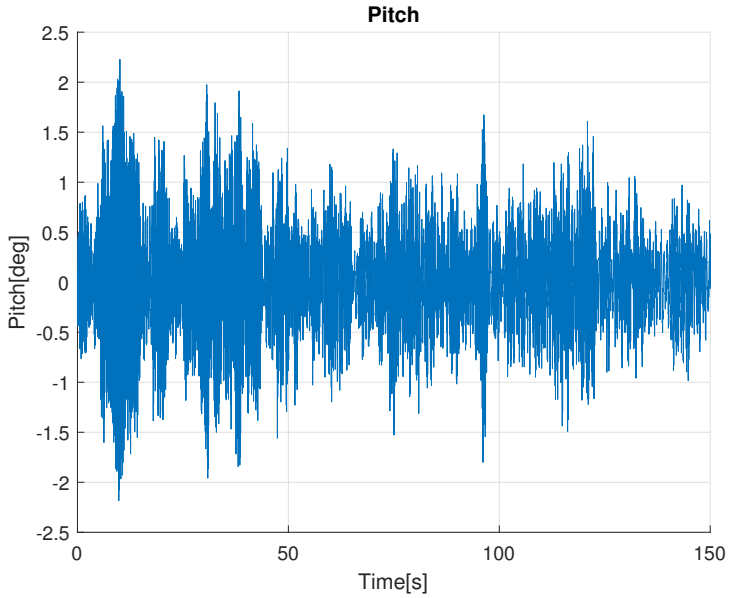

Figure B.42: Test 3- Pitch with MIPC H_2

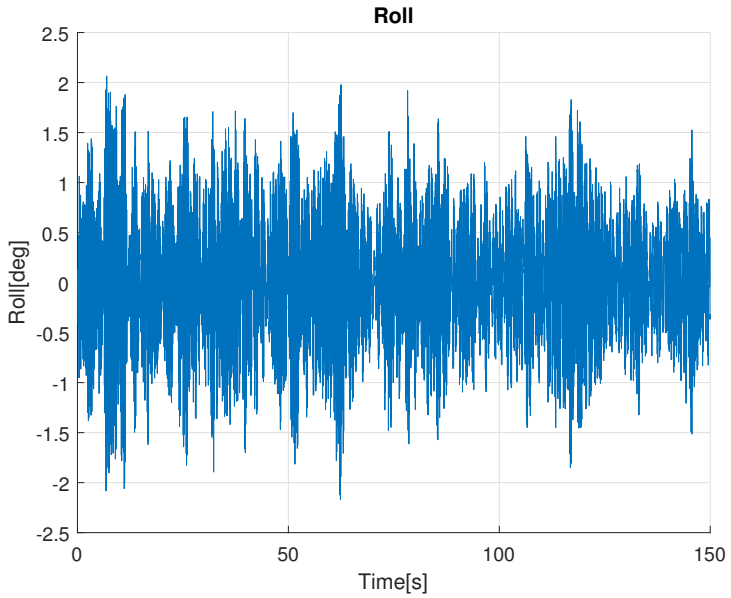

Figure B.43: Test 3- Roll with MIPC H_2

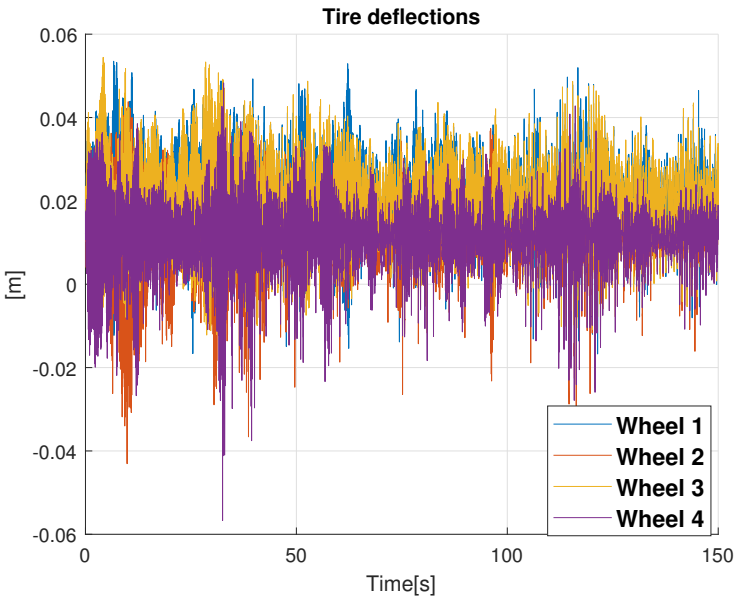

Figure B.44: Test 3- Tire deflections with MIPC H_2

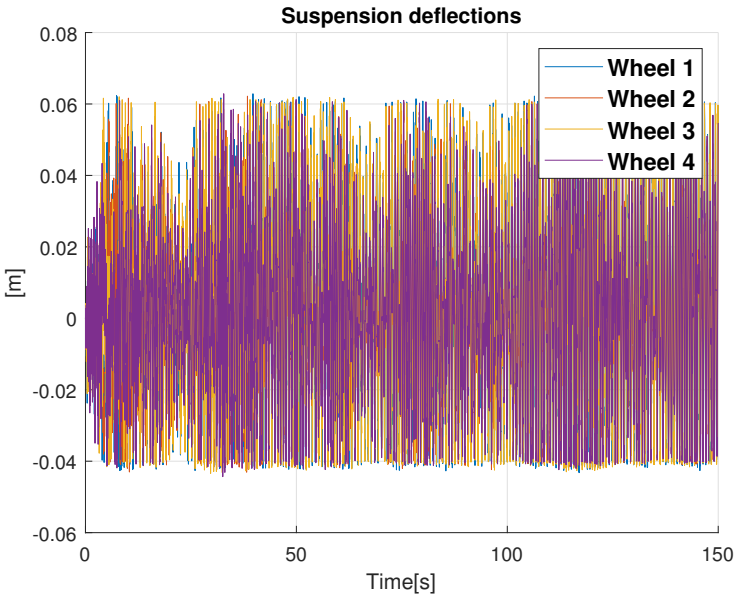

Figure B.45: Test 3- Suspension deflections with MIPC H_2

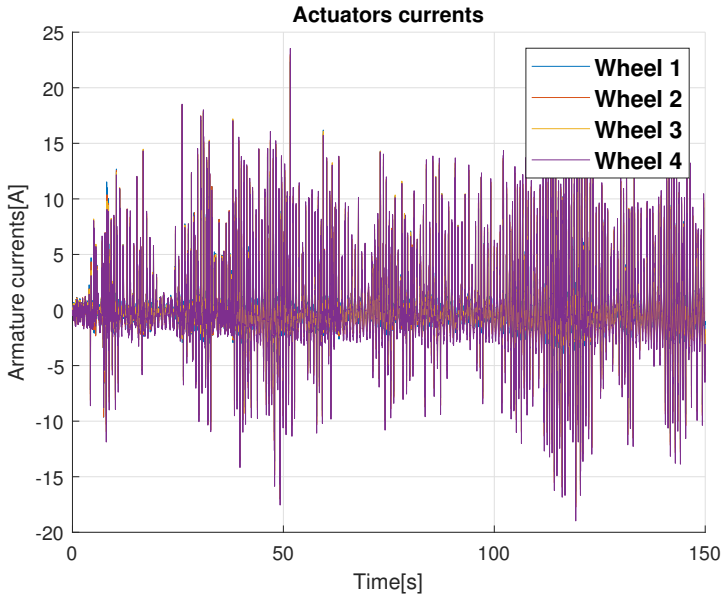

Figure B.46: Test 3- Actuation currents with MIPC H_2

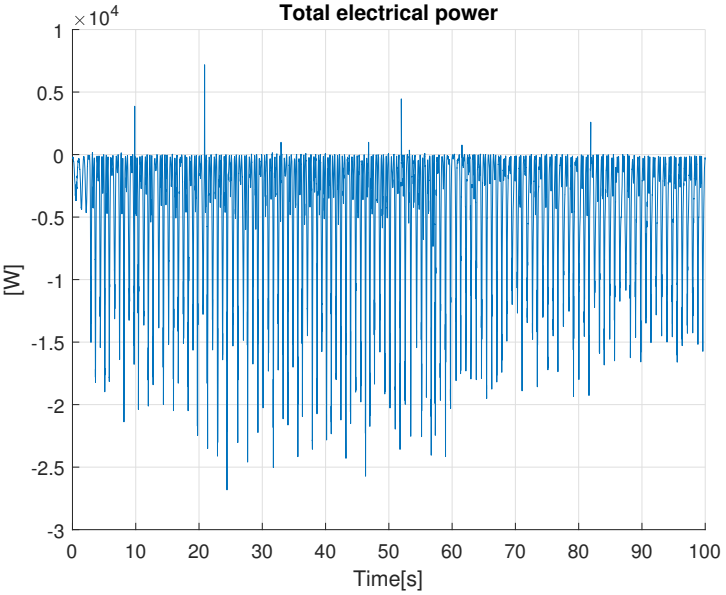

Figure B.47: Test 3- Electrical power with MIPC H_2

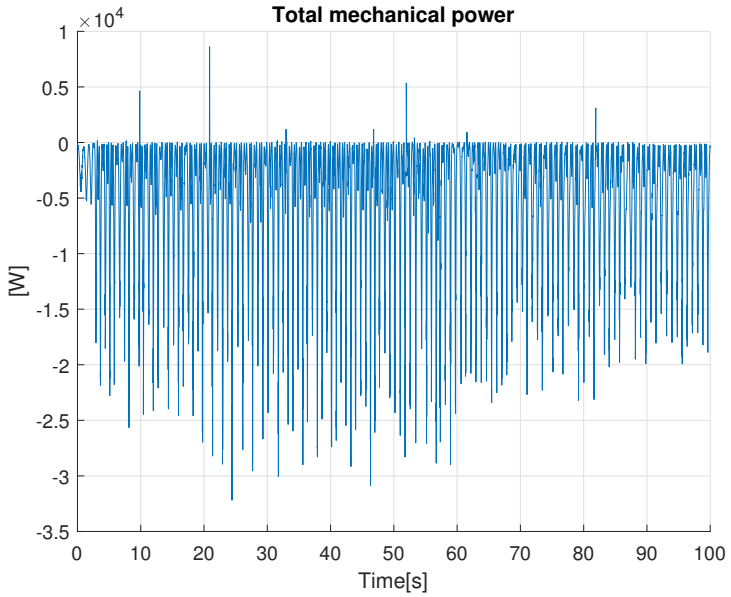

Figure B.48: Test 3- Mechanical power with MIPC H_2

References

[1] V.Nitin and N.Sarika, "Hybrid electromagnetic shock absorber for energy harvesting in a vehicle suspension," *Journal of Mechanical Engineering Science*, vol. 231, no. 8, pp. 1500–1517, 2017. DOI: https://doi.org/10.1177/0954406216663577.

[2] H.Tseng and D.Hrovat, "State of the art survey: active and semi-active suspension control," *Vehicle System Dynamics*, vol. 53, no. 7, pp. 1034–1062, 2015.

[3] autoblog, "On the Rebound: Scientists invent regenerative shocks," *[Online;accessed 02-August-2025]*, 2025. DOI: https://www.autoblog.com/news/on-the-rebound-scientists-invent-regenerative-shocks.

[4] Research, S. B. and Innovation, "Stony Brook Scientists on Front Line of an Energy Revolution," *[Online;accessed 02-August-2025]*, 2025. DOI: https://www.stonybrook.edu/commcms/innovation/news/Stony20Brook20Energy20Revolution.

[5] Audiworld, "The innovative shock absorber system from Audi: New technology saves fuel and enhances comfort," *[Online;accessed 02-August-2025]*, 2025. DOI: https://www.audiworld.com/articles/innovative-shock-absorber-system-audi-new-technology-saves-fuel-enhances-comfort.

[6] M.Canale, M. and Z.Ahmad, "Semi-active suspension control using "Fast" Model Predictive Control," *American Control Conference*, 2005. DOI: https://doi.org/10.1109/ACC.2005.1469945.

[7] B.Drew, A. and M.Sahinkaya, "A review of wave energy converter technology," *Journal of Power and Energy*, vol. 223, no. 8, pp. 887–902, 2009. DOI: https://doi.org/10.1243/09576509JPE782.

[8] A.Khaligh and O.Onar, "Energy Harvesting: Solar, Wind, and Ocean Energy Conversion Systems," *CRC Press*, 2009. DOI: https://doi.org/10.1201/9781439815090.

[9] C.Khairallah, E. and P.Rahme, "Development of a Wave Buoy Device For Energy Harvesting," *Fourth International Conference on Advances in Computational Tools for Engineering Applications*, 2019. DOI: https://doi.org/10.1109/ACTEA.2019.8851089.

[10] A.Mohamed, M. and L.Zuo, "Vibration energy harvesting in automotive suspension system: A detailed review.," *Applied Energy*, vol. 229, pp. 672–699, 2018. DOI: https://doi.org/10.1016/j.apenergy.2018.08.030.

[11] X.Lv, Y. and L.Zhang, "Research Review of a Vehicle Energy Regenerative Suspension System," *energies*, vol. 13, no. 2, p. 441, 2020. DOI: https://doi.org/10.3390/en13020441.

[12] K.Ahmad and M.Alam, "Design and simulated analysis of regenerative suspension system with hydraulic cylinder, motor and dynamo," *SAE Technical Paper*, 2017. DOI: https://doi.org/10.4271/2017-01-1284.

[13] R.Zhang, X. and S.John, "A Comprehensive Review of the Techniques on Regenerative Shock Absorber Systems.," *Energies*, vol. 11, no. 5, p. 1167, 2018. DOI: https://doi.org/10.3390/en11051167.

[14] A.Gonzalez, J. and M.Izquierdo, "An Innovative Energy Harvesting Shock Absorber System for Motorbikes.," *IEEE/ASME Transactions on Mechatronics*, vol. 27, no. 5, pp. 3110–3120, 2022. DOI: doi: 10.1109/TMECH.2021.3109383.

[15] A.Gupta and W.Tai, "Broadband and enhanced energy harvesting using inerter pendulum vibration absorber," *International Design Engineering Technical Conferences and Computers and Information in Engineering Conference, American Society of Mechanical Engineers*, vol. 83969, V007T07A007, 2020. DOI: https://doi.org/10.1115/DETC2020-22200.

[16] Di.Iorio and A.Casavola, "A multiobjective H_∞ control strategy for energy harvesting while damping for regenerative vehicle suspension systems.," *2012 American Control Conference (ACC)*, pp. 491–496, 2012. DOI: doi:10.1109/ACC.2012.6314772.

[17] A.Casavola, D. and F.Tedesco, "A multiobjective H_∞ control strategy for energy harvesting in regenerative vehicle suspension systems.," *International Journal of Control*, vol. 91, no. 4, pp. 741–754, 2017. DOI: https://doi.org/10.1080/00207179.2017.1293298.

[18] J.Lee, Y. and B.Park, "An Energy-Harvesting System Using MPPT at Shock Absorber for Electric Vehicles.," *energies*, vol. 14, no. 2552, pp. 726–731, 2021. DOI: https://doi.org/10.3390/en14092552.

[19] M.Hajidavalloo, A. and Z.Li, "MPC-Based Vibration Control and Energy Harvesting using Stochastic Linearization for a New Energy Harvesting Shock Absorber.," *IEEE Conference on Control Technology and Applications (CCTA)*, pp. 38–43, 2021. DOI: https://doi.org/10.1109/CCTA48906.2021.9658755.

[20] L.Zuo and P-S.Zhang, "Energy Harvesting, Ride Comfort and Road Handling of Regenerative Vehicle Suspensions.," *Journal of Vibration and Acoustics*, vol. 135, no. 1, p. 011 002, 2011. DOI: https://doi.org/10.1115/1.4007562.

[21] A.Sultoni, I. and A.Pramono, "H_∞ Multi-Objective Implementation for Energy Control of Electromagnetic Suspension.," *International Review of Mechanical Engineering (I.RE.M.E.)*, vol. 9, no. 6, pp. 542–547, 2015.

[22] A.Casavola, D. and F.Tedesco, "Gain-scheduling control of electromagnetic regenerative shock absorbers for energy harvesting by road unevenness.," *IEEE American Control Conference*, pp. 2114–2119, 2014. DOI: https://doi.org/10.1109/ACC.2014.6858638.

[23] A.Casavola, F. and P.Vaglica, "H_2 and H_∞ Optimal Control Strategies for Energy Harvesting by Regenerative Shock Absorbers in Cars.," *Vibration*, vol. 3, no. 2, pp. 99–115, 2020. DOI: https://doi.org/10.3390/vibration3020009.

[24] M.Hajidavalloo, J. and Z.Song, "Simultaneous Suspension Control and Energy Harvesting through Novel Design and Control of a New Nonlinear Energy Harvesting Shock Absorber," *IEEE Transactions on Vehicular Technology*, vol. 71, no. 6, pp. 6073–6087, 2022. DOI: https://doi.org/10.1109/TVT.2022.3159734.

[25] S.Mudduluru and M.Chizari, "Quarter and Full Car Models Optimization of Passive and Active Suspension System Using Genetic Algorithm," *School of Physics, Engineering and Computer Science, University of Hertfordshire, Hatfild, UK*, DOI: https://doi.org/10.48550/arXiv.2101.12629.

[26] M.Fauzy, F. and M.Talip, "Enhancing Ride Comfort of Quarter Car Semi-active Suspension System Through State-Feedback Controller," *Proceedings of the Second International Conference on the Future of ASEAN (ICoFA)*, vol. 2, pp. 827–837, 2017. DOI: https://doi.org/10.1007/978-981-10-8471-3_81.

[27] H.Shi, L. and L.Liu, "Research on Energy Regenerative Performance of Suspension System with Semi active Control," *Journal of Vibration Engineering and Technologies*, vol. 7, no. 5, pp. 465–475, 2018. DOI: https://doi.org/10.1007/s42417-019-00144-x.

[28] C.Liang, J. and L.Zuo, "Design, fabrication, simulation and testing of an ocean wave energy converter with mechanical motion rectifier," *Ocean Engineering*, vol. 136, pp. 190–200, 2017. DOI: https://doi.org/10.1016/j.oceaneng.2017.03.024.

[29] A.Falcao, J. and R.Gomes, "Air turbine choice and optimization for flating oscillatingwater-column wave energy converter," *Ocean Engineering*, vol. 75, pp. 148–156, 2014. DOI: https://doi.org/10.1016/j.oceaneng.2013.10.019.

[30] A.Falcao, "Wave energy utilization: a review of the technologies," *Renewable Sustainable Energy Revue*, vol. 14, pp. 899–918, 2010. DOI: https://doi.org/10.1016/j.rser.2009.11.003.

[31] E.Lejerskog, L. and M.Leijon, "Experimental results on power absorption from a wave energy converter at the Lysekil wave energy research site," *Renewable Energy*, vol. 77, pp. 9–14, 2015. DOI: https://doi.org/10.1016/j.renene.2014.11.050.

[32] L.Xiaofan, C. and Z.Lei, "A compact mechanical power take-of for wave energy converters: Design, analysis, and test verifiation," *Applied Energy*, vol. 278, p. 115 459, 2020.

[33] T.Aderinto and H.Li, "Review on Power Performance and Effiency of Wave Energy Converters," *Energies*, vol. 12, no. 22, p. 4329, 2019. DOI: https://doi.org/10.1016/j.apenergy.2020.115459.

[34] F.Fusco and J.Ringwood, "Short-term wave forecasting for real-time control of wave energy converters," *IEEE Transactions on Sustainable Energy*, vol. 1, no. 2, pp. 99–106, 2010. DOI: https://doi.org/10.1109/TSTE.2010.2047414.

[35] S.Sirigu, L. and G.Mattiazzo, "TechnoEconomic Optimization for a Wave Energy Converter via Genetic Algorithm," *Journal of Marine Science and Engineering*, vol. 8, no. 7, p. 482, 2020. DOI: https://doi.org/10.3390/jmse8070482.

[36] J.Xie and L.Zuo, "Dynamics and control of o cean wave energy converters," *International Journal of Dynamics and control*, vol. 1, pp. 262–276, 2013. DOI: https://doi.org/10.1007/s40435-013-0025-x.

[37] G.Bacelli and R.Coe, "Comments on Control of Wave energy Converters," *IEEE TRANSACTIONS ON CONTROL SYSTEMS TECHNOLOGY*, vol. 29, no. 1, pp. 478–481, 2021. DOI: https://doi.org/10.1109/TCST.2020.2965916.

[38] S.Zhan, J. and B.Wang, "Adaptive Model Predictive Control of Wave Energy Converters," *IEEE TRANSACTIONS ON SUSTAINABLE ENERGY*, vol. 11, no. 1, pp. 229–238, 2020. DOI: https://doi.org/10.1109/TSTE.2018.2889767.

[39] S.Zhan, G. and C.Bailey, "Economic Feedback Model Predictive Control of Wave Energy Converters," *IEEE TRANSACTIONS ON INDUSTRIAL ELECTRONICS*, vol. 67, no. 5, pp. 3932–3943, 2020. DOI: https://doi.org/10.1109/TIE.2019.2922947.

[40] M.Penalba and J.Ringwood, "A Review of Wave-to-Wire Models for Wave Energy Converters," *Energies*, vol. 9, no. 7, p. 506, 2016. DOI: https://doi.org/10.3390/en9070506.

[41] N.Faedo, G. and J.Ringwood, "Energy- maximising control of wave energy converters using a moment-domain representation," *Control Engineering Practice*, vol. 81, pp. 85–96, 2018. DOI: https://doi.org/10.1016/j.conengprac.2018.08.010.

[42] A.Merigaud and J.Ringwood, "Improving the Computational Performance of Nonlinear Pse udo sp ectral Control of Wave Energy Converters," *IEEE Transactions on sustainable energy*, vol. 9, no. 3, pp. 1419–1426, 2018. DOI: https://doi.org/10.1109/TSTE.2017.2786045.

[43] Y.Zhang and G.Li, "Non- Causal Linear Optimal Control of Wave Energy Converters With Enhanced Robustness by Sliding Mode Control," *IEEE Transactions on sustainable energy*, vol. 11, no. 4, pp. 2201–2209, 2020. DOI: https://doi.org/10.1109/TSTE.2019.2952200.

[44] J.Nao, B. and W.He, "Nonlinear Constrained Optimal Control of Wave Energy Converters With Adaptive Dynamic Programming," *IEEE Transactions on industrial electronics*, vol. 66, no. 10, pp. 7904–7915, 2019. DOI: https://doi.org/10.1109/TIE.2018.2880728.

[45] J.Na, G. and S.Zhan, "Robust Optimal Control of Wave Energy Converters Bas ed on Adaptive Dynamic Programming," *IEEE Transactions on sustainable energy*, vol. 10, no. 2, pp. 961–970, 2019. DOI: https://doi.org/10.1109/TSTE.2018.2856802.

[46] Z.Yu and J.Falnes, "State-space modelling of a vertical cylinder in heave," *Applied Ocean Research*, vol. 17, no. 5, pp. 265–275, 1995. DOI: https://doi.org/10.1016/0141-1187(96)00002-8.

[47] D.Evans, "A theory for wave-power absorption by oscillating bodies," *Journal of Fluid Mechanics*, vol. 77, no. 1, pp. 1–25, 1976. DOI: https://doi.org/10.1017/S0022112076001109.

[48] A.Kody, N. and J.Scruggs, "Model Predictive Control of a Wave Energy Converter Using Duality Techniques," *American Control Conference (ACC)*, pp. 5444–5451, 2019. DOI: https://doi.org/10.23919/ACC.2019.8814715.

[49] B.Paula, G. and M.Molinas, "Real time passive control of wave energy converters using the Hilbert-Huang Transform," *International Federation of Automatic Control*, vol. 50, no. 1, pp. 14 705–14 710, 2017. DOI: https://doi.org/10.1016/j.ifacol.2017.08.2502.

[50] A.Babarit and A.Clément, "Optimal latching control of a wave energy device in regular and irregular waves," *Applied Ocean Research*, vol. 28, no. 2, pp. 77–91, 2006. DOI: https://doi.org/10.1016/j.apor.2006.05.002.

[51] U.Korde, "Latching control of deep water wave energy devices using an active reference," *Ocean Engineering*, vol. 29, no. 11, pp. 1343–1355, 2002. DOI: https://doi.org/10.1016/S0029-8018(01)00093-2.

[52] K.Budal, "Model experiment with a phase-controlled point absorber," *Proceedings 2nd International Symposium on Wave Tidal Energy*, vol. 29, no. 11, pp. 191–206, 1981. DOI: https://doi.org/10.1016/S0029-8018(01)00093-2.

[53] A.Babarit, M. and A.Clément, "Declutching control of a wave energy converter," *Ocean Engineering*, vol. 36, no. 12, pp. 1015–1024, 2009. DOI: https://doi.org/10.1016/j.oceaneng.2009.05.006.

[54] J.Scruggs, S. and I.Cassidy, "Optimal causal control of a wave energy converter in a random sea," *Applied Ocean Research*, vol. 42, pp. 1–15, 2013. DOI: https://doi.org/10.1016/j.apor.2013.03.004.

[55] S.Nielse, Q. and Z.Zhang, "Optimal control of nonlinear wave energy point converters," *Ocean Engineering*, vol. 72, pp. 176–187, 2013. DOI: https://doi.org/10.1016/j.oceaneng.2013.06.029.

[56] S.Zhan and L.Guang, "Linear Optimal Noncausal Control of Wave Energy Converters," *IEEE Transactions on control systems technology*, vol. 27, no. 4, pp. 1526–1536, 2019. DOI: https://doi.org/10.1109/TCST.2018.2812740.

[57] S.Zhan, G. and W.He, "Feedback noncausal model predictive control of wave energy converters," *Control Engineering Practice*, vol. 85, pp. 110–120, 2019. DOI: https://doi.org/10.1016/j.conengprac.2018.12.015.

[58] G.Li, G. and M.Belmont, "Wave energy converter control by wave prediction and dynamic programming," *Renewable Energy*, vol. 48, pp. 392–403, 2012. DOI: https://doi.org/10.1016/j.renene.2012.05.003.

[59] M.Aleix, J. and G.Izaskun, "Control Strategies Applied to Wave Energy Converters: State of the Art," *energies*, vol. 12, no. 16, p. 3115, 2019. DOI: https://doi.org/10.3390/en12163115.

[60] M.Belmont and J.Christmas, "An examination of the feasibility of linear determ inistic sea wave prediction in multidirectional seas using wave profiing radar:Theory, simulation, and sea trials," *Journal of Atmospheric Ocean Technology*, vol. 31, no. 7, pp. 1601–1614, 2014. DOI: https://doi.org/10.1175/JTECH-D-13-00170.1.

[61] A.Harvey, "Structural Time Series Models and the Kalman Filter," *Cambridge University Press*, 1989.

[62] A.Darwish and A.Aggidis, "A review on Power Electronic Topologies and Control for Wave Energy Converters," *energies*, vol. 15, no. 23, p. 9174, 2022. DOI: https://doi.org/10.3390/en15239174.

[63] C.Kim and P.Ro, "An Accurate Full Car Ride Model Using Model Reducing Techniques.," *J. Mech. Des.*, vol. 124, no. 4, pp. 697–705, 2002. DOI: https://doi.org/10.1115/1.1503065.

[64] Z.Wang, C. and Y.Qiu, "Advancements in Semi-Active Automotive Suspension Systems with Magnetorheological Dampers: A Review.," *Applied Sciences*, vol. 14, no. 7866, p. 1167, 2024. DOI: https://doi.org/10.3390/app14177866.

[65] A.Do, O. and L.Dugard, "An LPV control approach for semi-active suspension control with actuator constraints.," *Proceedings of the 2010 American control conference*, pp. 4653–4658, 2010.

[66] S.Savaresi, C. and O.Sename, "Semi-Active Suspension Control Design for Vehicles.," *Butterworth-Heinemann*, 2010. DOI: https://doi.org/10.1016/B978-0-08-096678-6.00014-6.

[67] Z.Li, L. and G.Luhrs, "Energy-harvesting shock absorber with a mechanical motion rectifier," *SMART MATERIALS AND STRUCTURES*, vol. 22, no. 2, p. 025 008, 2013. DOI: DOI 10.1088/0964-1726/22/2/025008.

[68] L.Bowen, J. and J.Otero, "An Innovative Energy Harvesting Shock Absorber System Using Cable Transmission.," *IEEE/ASME Transactions on Mechatronics*, vol. 24, no. 2, pp. 689–699, 2019. DOI: https://doi.org/10.1109/TMECH.2019.2892824.

[69] G.Gagliardi, P. and A.Casavola, "Performance Analysis of Linear and Rotary Energy Harvesting Shock Absorber Systems.," *IEEE Vehicle Power and Propulsion Conference (VPPC)*, pp. 1–6, 2023. DOI: https://doi.org/10.1109/VPPC60535.2023.10403168.

[70] P.Ricci, J. and A.Falcao, "Control strategies for a simple point absorber connected to a hydraulic power take-off," *Proceedings of the European Wave and Tidal Energy Conference*, pp. 746–755, 2009.

[71] I.Lopez, J. and I.Kortabarria, "Review of wave energy technologies and the necessary power-equipment," *Renew. Sustain. Energy Rev*, vol. 27, pp. 413–434, 2013. DOI: https://doi.org/10.1016/j.rser.2013.07.009.

[72] K.Budar and J.Falnes, "A resonant point absorber of ocean-wave power," *Nature*, vol. 256, pp. 478–479, 1975. DOI: https://doi.org/10.1038/256478a0.

[73] B.Guo, T. and Y.Zhao, "A Review of Point Absorber Wave Energy Converters," *Journal of marine science and engineering*, vol. 10, no. 10, p. 1534, 2022. DOI: https://doi.org/10.3390/jmse10101534.

[74] Y.Lin, J. and D.Zhang, "Review of hydraulic transmission technologies for wave power generation," *Renew. Sustain. Energy Rev.*, vol. 50, pp. 194–203, 2015. DOI: https://doi.org/10.1016/j.rser.2015.04.141.

[75] X.Li, C. and L.Zuo, "A compact mechanical power take-off for wave energy converters: Design, analysis, and test verification," *Applied Energy*, vol. 278, no. 115459, pp. 194–203, 2020. DOI: https://doi.org/10.1016/j.apenergy.2020.115459.

[76] M.Mueller and N.Baker, "Direct drive electrical power take-off for offshore marine energy converters," *Proc. Inst. Mech. Eng. Part A J. Power Energy*, vol. 219, no. 3, pp. 223–234, 2005. DOI: https://doi.org/10.1243/095765005X7574.

[77] W.Liu, L. and T.Cheng, "Torus structured triboelectric nanogenerator array for water wave energy harvesting," *Nano Energy*, vol. 58, pp. 499–507, 2019. DOI: https://doi.org/10.1016/j.nanoen.2019.01.088.

[78] R.Henderson, "Design, simulation, and testing of a novel hydraulic power take-off system for the Pelamis wave energy converter," *Renew. Energy*, vol. 31, no. 2, pp. 271–283, 2006. DOI: https://doi.org/10.1016/j.renene.2005.08.021.

[79] F.Antonio, "Phase control through load control of oscillating-body wave energy converters with hydraulic PTO system," *Ocean Eng*, vol. 35, no. 3-4, pp. 358–366, 2008. DOI: https://doi.org/10.1016/j.oceaneng.2007.10.005.

[80] T.Omholt, "A wave activated electric generator," *In Proceedings of the OCEANS,Washington*, pp. 585–589, 1978. DOI: https://doi.org/10.1109/OCEANS.1978.1151091.

[81] M.Mueller and N.Baker, "A low speed reciprocating permanent magnet generator for direct drive wave energy converters," *In Proceedings of the International Conference on Power Electronics Machines and Drives*, pp. 468–473, 2002. DOI: https://doi.org/10.1049/cp:20020162.

[82] P.Khatri and X.Wang, "Comprehensive review of a linear electrical generator for ocean wave energy conversion," *IET Renew. Power Gener.*, vol. 14, no. 6, pp. 949–958, 2020. DOI: https://doi.org/10.1049/iet-rpg.2019.0624.

[83] K.Rhinefrank, J. and A.Schacher, "Development and characterization of a novel direct drive rotary wave energy point absorber," *In Proceedings of the OCEANS*, pp. 1–5, 2009. DOI: https://doi.org/10.23919/OCEANS.2009.5422344.

[84] M.Mueller, H. and N.Bakerr, "Current and novel electrical generator technology for wave energy converters," *In Proceedings of the IEEE International Conference on Electric Machines and Drives (IEMDC)*, vol. 2, pp. 1401–1406, 2007. DOI: https://doi.org/10.1109/IEMDC.2007.383634.

[85] M.Leijon, O. and O.Agren, "An electrical approach to wave energy conversion," *Renewable Energy*, vol. 31, no. 9, pp. 1309–1319, 2006. DOI: https://doi.org/10.1016/j.renene.2005.07.009.

[86] R.Genest, F. and A.Babarit, "Effect of non-ideal power take-off on the energy absorption of a reactively controlled one degree of freedom wave energy converter," *Applied Ocean Research*, vol. 48, pp. 236–243, 2014. DOI: https://doi.org/10.1016/j.apor.2014.09.001.

[87] H.Polinder, B. and M.Mueller, "Conventional and TFPM linear generators for direct-drive wave energy conversion," *Appl. Ocean Res.*, vol. 20, pp. 260–267, 2005. DOI: https://doi.org/10.1109/TEC.2005.845522.

[88] H.Polinder, M. and F.Gardner, "Linear PM generator system for wave energy conversion in the AWS," *IEEE Trans. Energy Convers*, vol. 19, no. 3, pp. 583–589, 2004. DOI: https://doi.org/10.1109/TEC.2004.827717.

[89] Mara, F. N., "Marine Data Centre," *[Online; accessed 13-October-2024]*, 2024. DOI: https://www.marine.ie/site-area/data-services/real-time-observations/wave-buoys-0.

[90] ISO, *ISO 2631-4: Human Exposure to Mechanical Vibration and Shock. Part 4: Guidelines for the evaluation of the effects of vibration and rotational motion on passenger and crew comfort in fixed-guideway transport systems*. 2001.

[91] C.Scherer, P. and M.Chilali, "Multiobjective Output-Feedback Control via LMI Optimization.," *IEEE Transactions on Automatic Control*, vol. 42, no. 7, pp. 896–911, 1997. DOI: https://doi.org/10.1109/TMECH.2019.2892824.

[92] T.Rao and G.Rao, "Parametric Sensitivity Analysis of a heavy duty Passenger vehicle Suspension System," *ARPN Journal of Engineering and Applied Sciences*, vol. 4, 2009.

[93] Z.Zhao, T. and T.Wang, "Energy Harvesting from Vehicle Suspension System by Piezoelectric Harvester," *Mathematical Problems in Engineering*, no. 1, p. 1 086 983, 2019. DOI: https://doi.org/10.1155/2019/1086983.

[94] C.Olalla and R.Leyva, "Robust LQR Control for PWM Converters: An LMI Approach," *IEEE Transactions on Industrial Electronics*, vol. 56, no. 7, pp. 2548–2558, 2009. DOI: https://doi.org/10.1109/TIE.2009.2017556.

[95] H.Trentelman, "The regular free-endpoint linear quadratic problem with indefinite cost," *SIAM Journal on Control and Optimization*, vol. 27, no. 1, pp. 27–42, 1989. DOI: https://doi.org/10.1137/0327003.

[96] A.Rantzer, "On the Kalman-Yakubovich-Popov lemma," *Systems & Control Letters*, vol. 28, no. 1, pp. 7–10, 1996. DOI: https://doi.org/10.1016/0167-6911(95)00063-1.

[97] A.Abassi and A.Seifi, "Simultaneous Integrated stochastic electrical and thermal energy expansion planning," *IET Generation, Transmission & Distribution*, vol. 8, no. 6, pp. 1017–1027, 2014. DOI: https://doi.org/10.1049/iet-gtd.2013.0710.

[98] A.Abassi and R.Khoramini, "A new intelligent method for optimal allocation of D-STATCOM with uncertainty," *Journal of Intelligent & Fuzzy Systems*, vol. 29, no. 5, pp. 1881–1888, 2015. DOI: https://doi.org/10.3233/IFS-151666.

[99] Chaubey, Y. and C.Sandeep, "Failure Analysis of Suspension System: Case Study-Tata Indica," *International Journal for Scientific Research and Development*, vol. 3, no. 9, pp. 1085–1090, 2015.

[100] Yu, M. and D.Daniele, "Advances in active suspension systems for road vehicles," *Engineering*, vol. 33, pp. 160–177, 2014. DOI: https://doi.org/10.1016/j.eng.2023.06.014.

[101] S.Boyd, L. and V.Balakrishnan, "Linear Matrix Inequalities in System and Control Theory," *Studies in Applied Mathematics*, vol. 15, 1994.

[102] M.Ma and H.Chen, "Constrained H_2 control of active suspensions using LMI optimization," *Chinese Control Conference*, pp. 702–707, 2006. DOI: doi: 10.1109/CHICC.2006.280723.

[103] S.Zhan and L.Guang, "Linear Optimal Noncausal Control of Wave Energy Converters," *IEEE Transactions on control systems technology*, vol. 27, no. 4, pp. 1526–1536, 2019. DOI: https://doi.org/10.1109/TCST.2018.2812740.

[104] R.Coe and D.Wilson, "A comparison of control strategies for wave energy converters," *International Journal of Marine Energy*, vol. 20, pp. 45–63, 2017. DOI: https://doi: 10.1016/j.ijome.2017.11.001.

[105] J.Rawlings and D.Mayne, "Model Predictive Control Theory and Design 2nd edition.," *Nob Hill Publishing*, 2009.

[106] J.Seok, J. and S.Lee, "Dynamic Characteristic Analysis and Experiments of Moving-Magnet Linear Actuator With Cylindrical Halbach Array," *IEEE Transactions on Magnetics*, vol. 41, no. 10, pp. 3814–3816, 2005. DOI: https://doi.org/10.1109/TMAG.2005.854931.

[107] A.Hassan, A. and I.Lazoglu, "Dynamic Analysis of a Novel Moving Magnet Linear Actuator," *IEEE Transactions on Industrial Electronics*, vol. 64, no. 5, pp. 3758–3766, 2017. DOI: https://doi.org/10.1109/TIE.2016.2645506.

[108] D.Angeli, A. and F.Tedesco, "On Average Performance of Economic Model Predictive Control with Time-Varying Cost and Terminal Constraints," *American Control Conference (ACC)*, pp. 2974–2979, 2015. DOI: https://doi.org/10.1109/ACC.2015.7171187.

[109] N.Faedo, G. and J.Ringwood, "Nonlinear Energy Maximizing optimal control of Wave Energy Systems: A Moment Based Approach," *IEEE Transactions on Control Systems Technology*, vol. 29, no. 6, pp. 2533–2547, 2021. DOI: https://doi.org/10.1109/TCST.2020.3047229.

[110] J.Morison, J. and S.Schaaf, "The force exerted by surface waves on piles," *J. Pet. Technol.*, vol. 2, no. 5, pp. 149–154, 1950.

[111] K.Lok, T. and N.Jenkins, "Optimisation of a clutch-rectified power take off system for a heaving wave energy device in irregular waves with experimental comparison," *Int. J. Mar. Energy*, vol. 8, pp. 1–16, 2014.

[112] M.Bhinder, A. and P.Ferrant, "Assessment of viscous damping via 3d-cfd modelling of a floating wave energy device," *Proceedings of the 9th European Wave and Tidal Energy Conference*, 2011.

[113] G.Giorgi and J.Ringwood, "Nonlinear Froude-Krylov and viscous drag representations for wave energy converters in the computation/fidelity continuum," *Ocean Engineering*, vol. 141, pp. 164–175, 2017.

[114] G.Keulegan and L.Carpenter, "Forces on Cylinders and Plates in an Oscillating Fluid," *US Department of Commerce, National Bureau of Standards*, 1956.

[115] B.Molin, "Hydrodynamique des structures offshore," *Editions Technip*, 2002.

[116] P.Tesso, D. and A.Casavola, "Novel LQR and Economic MPC Control Strategies for Energy Harvesting in Wave Energy Converters," *Joint Mechatronics 2025 and Robotics 2025 Symposia*, 2025.

[117] Mara, F. N., "Marine Data Centre," *[Online; accessed 19-July-2020]*, 2020. DOI: http://www.marine.ie/Home/site-area/ data-services/real-time-observations/real-time-observations.